A FRAMEWORK FOR EFFICIENT MODULATION TECHNIQUES FOR VISIBLE LIGHT COMMUNICATION UNDER INDOOR ENVIRONMENT BASED IOT APPLICATIONS

Thesis

Submitted in partial fulfillment of the requirements
for the award of the degree of

DOCTOR OF PHILOSOPHY

by

Salvi Sanket Sarang

DEPARTMENT OF INFORMATION TECHNOLOGY
NATIONAL INSTITUTE OF TECHNOLOGY KARNATAKA
SURATHKAL, MANGALORE - 575 025

June, 2023

DECLARATION

I hereby declare that the Research Thesis entitled "**A Framework for Efficient Modulation Techniques for Visible Light Communication under Indoor Environment based IoT Applications**", which is being submitted to **National Institute of Technology Karnataka, Surathkal** in partial fulfilment of the requirements for the award of the degree of **Doctor of Philosophy** in **Information Technology** is a bonafide report of the research work carried out by me. The material contained in this Research Thesis has not been submitted to any University or Institution for the award of any degree.

Place : NITK - Surathkal

Date : June 16, 2023

SALVI SANKET SARANG

Reg. No. : 177045IT001,

Department of IT,

NITK Surathkal.

CERTIFICATE

This is to certify that the Research Thesis entitled, "**A FRAMEWORK FOR EFFICIENT MODULATION TECHNIQUES FOR VISIBLE LIGHT COMMUNICATION UNDER INDOOR ENVIRONMENT BASED IOT APPLICATIONS**", submitted by **SALVI SANKET SARANG (Reg.no. 177045IT001)**, as the record of research work carried out by him, *is accepted as the Research Thesis* submission in partial fulfillment of the requirements for the award of the degree of **Doctor of Philosophy** in **Information Technology**.

Place : NITK - Surathkal

Date : June 16, 2023

Dr. Geetha V

Research Guide,

Assistant Professor,

Department of IT,

NITK Surathkal.

Chairman, DRPC,

Head of IT,

NITK Surathkal.

CHAIRMAN - DRPC
Department of Information Technology
NITK Surathkal, Srinivasnagar P.O.
Mangaluru 575 025, INDIA

I dedicate my thesis to my wife, mother, father and brother and to all who were my LIGHT

Acknowledgements

I take the privilege to express my heartfelt gratitude to all the people who have been a constant support to me throughout my doctoral research. Foremost, my sincere thanks to my research guide Dr. Geetha V, Department of Information Technology, NITK Surathkal, for her valuable guidance, enthusiasm, inspiration, and dedication throughout my research. This research work is a result of her being open to the most out-of-the-box ideas, timely suggestions, and firm decisions. I extend my gratitude to Dr. Sowmya Kamath and Dr. Sidney Rosario for providing me an opportunity to relearn the basics and stay updated with the technology.

I sincerely thank the RPAC members, Dr. Aparna P and Dr. Biju R Mohan, for their apt and timely suggestions and valuable reciprocations. I would also like to thank all the teaching, technical, administrative, and non-teaching staff who have been very kind and helpful throughout my research. Further, I extend my gratitude to Prof. Sanjay H A, HoD, Department of ISE, MSRIT, who motivated me to do research at NITK Surathkal.

I also thank my parents and family for their exhaustive encouragement and support. I extend my special thanks to my wife, Dr. Mrunali Borkar, for her cooperation, love, suggestions, and constant encouragement at every point in time.

I extend my gratitude to my dear ones Shashank, Tulasi, Ranjith, Pragnesh, Natesha, Gokul, Sanjay, Manjunath, Karthik, Rajesh, Sunil, and my other co-researchers and also my brother Laukik who made my journey more enjoyable and fun. Never to forget, the most exciting place for doctoral research with updated technologies usable for research and advanced resources made readily available, facilitating a convenient study, my heartfelt gratitude to NITK Surathkal for making this research memorable and possible.

Salvi Sanket Sarang

Abstract

The Internet of Things has paved the way for several smart applications, which broadly include smart homes, smart cities, smart transports, etc. The underlying architecture of these systems typically involves sensor devices communicating data over the internet to provide some useful insight. However, as the number of devices connected to the internet is increasing, the existing backbone network infrastructure is experiencing considerable challenges in the allocation of channel bandwidth for communicating devices. Moreover, it is also widely debated that prolonged exposure to high radio-frequency spectrum is harmful to living bodies. Thus, there is a need to have an alternative to existing radio-frequency-based communication techniques. Visible light communication is a sub-domain of optical wireless communication which uses an unlicensed visible light spectrum for communication. However, the domain is new and requires more work to be done with respect to designing testbeds and integration with existing Internet of Things infrastructure. Thus, there is a scope to design low-cost testbeds to test various modified versions of existing modulation techniques as well as to build new modulation techniques specific to light characteristics.

This research thesis proposes various low-cost testbeds to implement existing modulation techniques and compares them with the standard implementation of their simulated counterparts. The work also proposes a few new modulation techniques and describes their integration with Internet of Things applications. Depending upon the type of the receivers and the features used for generating signals, the modulation techniques were divided into three major categories namely photodiode-based modulation, rolling-shutter-based optical camera communication modulation, and pattern-based optical camera communication.

The work also proposes photodiode-based modulation and shows an implementation of a low-cost visible light communication testbed. It also highlights the implementation of On-Off keying and pulse duration modulation techniques on the proposed testbed. The work also evaluates the performance of the implemented system with its equivalent standard implementation using Matlab simulation. The

work shows the performance of the proposed testbed is in line with the performance of the simulated counterpart with respect to the trend of increasing error rate with increasing distance. It also shows that the performance of pulse duration modulation is consistently better than that of On-Off keying in terms of the success of reception (%). The work also highlights an extension by building an image transmission application using the proposed visible light communication testbed.

The research work in the thesis involves the design and implementation of the visible light communication system which uses the camera as the receiver. It highlights the use of the concept of a rolling shutter to modulate signals in terms of the blink frequency of the transmitter LED. The work proposes a novel hybrid frequency shift pulse duration modulation technique that modulated the data in terms of the duration of frequencies. The work also highlights the performance comparison of the proposed technique with other standard implementations of the modulation techniques such as On-Off keying and binary frequency shift on-off keying. An indoor positioning system application built using the testbed was also described in this work.

As a part of the work on pattern-based optical camera communication modulation techniques, the work proposes two novel modulation techniques, one inspired by the nested structure of textures and the other inspired by quantum physics. The implementation of both proposed modulation techniques uses the same testbed setup. It evaluates the performance of the proposed techniques based on the visibility of the patterns, the amount of data that can be encoded, signal-to-noise ratio, and bit-error rate (%). The work also highlights the performance comparison of the proposed techniques with the other existing techniques. Finally, the testbed setup was also used to propose and build an Internet of Things application that communicates temperature and humidity data over a non-radio-frequency medium.

KEYWORDS: Optical Wireless Communication, Internet of Things, Visible Light Communication, Optical Camera Communication, On-Off Keying, Pulse Duration Modulation, Modulation, Testbed, Pattern-based Modulation.

Contents

List of Figures

List of Tables

Abbreviations

2D 2 Dimensional

3D 3 dimensional

ACO-OFDM Asymmetrically Clipped Optical-OFDM

ADO-OFDM Asymmetrically Clipped DC biased Optical OFDM

BER Bit-Error-Ratio

BFS-OOK Binary Frequency Shift OOK

BHIPC Binary Hierarchical Image Pattern Classification

bps bits-per-second

CCR Continuous Current Reduction

CCTV Closed-circuit television

CEO-OFDM Clipping-enhanced Optical OFDM

CIM Color Intensity Modulation

CIR Channel Impulse Response

CISK Color Intensity Shift Keying

CSK Color Shift Keying

DC Direct Current

DCO-OFDM DC-baised Optical-OFDM

DD Direct Detection

DFT Discrete Fourier Transform

DHT Discrete Hartley Transformation

DHT11 digital humidity temperature

DMT Discrete Multitone

DPPM Differential PPM

DST-OFDM discrete sine transform-based OFDM

FDM Frequency Division Multiplexing

FFF Flicker Free Frequency

FFT Fast Fourier Transform

FoV Field-of-View

FPS frames per second

fps frames per second

FS-OOK Frequency Shift OOK

FSK Frequency Shift Keying

FWHT fast Walsh-Hadamard transformation

GLCM Gray level Co-occurrence Matrix

GPS Global Positioning System

GS Global Shutter

HCM Hadamard Coded Modulation

HDAP-OFDM Hybrid DC-biased asymmetrically-clipped PAM OFDM

HFSPDM Hybrid Frequency Shift Pulse Duration Modulation

IDE integrated development environment

IEEE Institute of Electrical and Electronics Engineers

IFFT Inverse Fast Fourier Transform

IM Intensity Modulated

IoT Internet of Things

IP inner pattern

IPS Indoor Positioning System

IR Infrared

IS Image Sensor

LACO-OFDM Layered ACO-OFDM

LCD liquid crystal display

LED Light Emitting Diodes

Li-Fi Light Fidelity

LoS Line-of-Sight

MAC media access control

M-PPM Multipulse PPM

M-QAM M-ary QAM

MCM Multicarrier Modulation

MIMO Multiple Input Multiple Output

MN Mobile Node

MPPM Multiple PPM

MSE Mean Squared Error

NIR Near Infrared

NLoS Non Line-of-Sight

NRZ Non Return to Zero

OCC Optical Camera Communication

OFDM Orthogonal Frequency Division Multiplexing

OMPPM Overlapped MPPM

OOK On-Off Keying

OP outer pattern

OPPM Overlapping PPM

ORWP Orientation-based Random Waypoint

OWC Optical Wireless Communication

OWC Optical Wireless Communication

PAM-DMT PAM-Discrete Multitone

PAM Pulse Amplitude Modulation

PAM Pulse Amplitude Modulation

PAPR Peak Amplitude to Power Ratio

PCM Pulse Coded Modulation

PD Photodiode

PDM Pulse Duration Modulation

PER Packet Error Ratio

PET positron emission tomography

PFFR Percentage Frequency Frame Ratio

PPM Pulse Position Modulation

PSNR Peak Signal to Noise Ratio

PTM Pulse Time Modulation

PVC Poly-Vinyl-Chloride

PWM Pulse Width Modulation

QAM Quadrature Amplitude Modulation

QCD-OCC Quantum Chromodynamics based OCC

QCD Quantum Chromodynamics

QR Quick Response

RC Repetition Code

RF Radio-Frequency

RGB red-green-blue

RoI Region of Interest

RS Rolling Shutter

RSS Receive Signal Strength

Rx Receiver

RZ Return to Zero

SCM Single Carrier Modulation

SE Spectral Efficiency

SISO Single Input Single Output

SM Spatial Modulation

SMD surface-mounted device

SMP Spatial Multiplexing

SNR Signal-to-Noise-Ratio

TDM Time Division Multiplexing

TG7r1 Task Group 802.15.7r1

TG7m Task Group 802.15.7m

Tx Transmitter

U-FSOOK Undersampled FS-OOK

U-OFDM Unipolar OFDM

UV ultra-violet

VLC Visible Light Communication

VLCA Visible Light Communication Association

VLCC VLC Consortium

VPPM Variable PPM

WDM Wavelength Division Multiplexing

WDM Wavelength Division Multiplexing

WPDM Wavelet Packet Division Multiplexing

Notations

D	distance between receiver and transmitter
r	radius of receiver aperture
α	receiver oritentation angle
β	source normal
θ_{max}	maximum half angle
Ω_r	receiver solid angle
Ω_{max}	beam solid angle
A_r	receiver area
I_0	axial intensity
$g_s(\theta)$	normalized distributed function
F_s	Transmitted Luminous intensity
F_r	Received Luminous intensity
L_L	Luminous path loss
$\Phi_{1/2}$	half illuminance
$P_{rSignal}$	received signal power
σ_{total}	total noise variance
σ_{shot}	shot noise variance
$\sigma_{thermal}$	thermal noise variance
q	electronic charge
B	noise bandwidth
I_2	noise bandwidth factor rectangular transmitter pulse shape
G	open-loop voltage gain
η	fixed capacitance of photodetector per unit area
Γ	absolute temperature of the environment
g_m	PET transconductance
I_3	noise bandwidth factor for a full raised-cosine equalized pulse shape
$fs(i)$	the sum of the values of the last s pixels at point i
y_i	grayscale value of a pixel at point i
$\mathbf{T}$	quick adaptive threshold
$N_{Stripes}$	the number of stripes
$F1$	delimiter blink frequency 1
$F2$	blink frequency 2
$F3$	blink frequency 3
$W1$	stripe width for frequency 1

$W2$	stripe width for frequency 2
$W3$	stripe width for frequency 3
T_{F2}	total number of frames between successive start frames containing $F2$ frequency
N_{Frames}	total number of frames between successive start frames
P_{F2}	percentage of $F2$ frequency frames
P_{ij}	pixel intensity of gray scaled image at position i, j
A_i	image frame containing active transmitter
B_i	image frame containing inactive transmitter
BER_e	BER for the existing technique
BER_p	BER for the proposed technique
N_{Err}	the number of error bits
N_{bits}	the total number of bits transmitted
A	the signal power
P	the pixel brightness intensity
$Packets_{Err}$	Error packets
$Packets_{tot}$	Total packets
$Gray_{i,j}$	grayscale pixel value at i, j
$R_{i,j}$	red channel pixel value at i, j
$G_{i,j}$	green channel pixel value at i, j
$B_{i,j}$	blue channel pixel value at i, j
$Intensity_{max}$	maximum pixel intensity in the grayscaled image
$B_{i,j}$	binary pixel value at i, j
$strel_n$	square structuring element
BA	list of binary blobs
BM	largest binary blob
R_S	resized image 8×8 image
R	red channel
$\hat{R}$	anti-red channel
G	green channel
$\hat{G}$	anti-green channel
B	blue channel
$\hat{B}$	anti-blue channel
W	white channel
$D1$	data stream 1
$D2$	data stream 2
$D3$	data stream 3
I_{ac}	image frame containing active transmitter
I_{in}	image frame containing inactive transmitter
N_{LEDs}	Number of LEDs
$N_{ColorBits}$	number of bits used to represent a color
$N_{AnchorLEDs}$	number LEDs used to represent anchor pattern
$L1$	length of binary stream 1
$L2$	length of binary stream 2
$L3$	length of binary stream 3
L_{max}	maximum length of binary stream

Z_i	number zero bits padded
R_{8x8}^{Tx}	red channel transmitter side 8×8 pattern
G_{8x8}^{Tx}	green channel transmitter side 8×8 pattern
B_{8x8}^{Tx}	blue channel transmitter side 8×8 pattern
R_{8x8}^{Rx}	red channel receiver side 8×8 pattern
G_{8x8}^{Rx}	green channel receiver side 8×8 pattern
B_{8x8}^{Rx}	blue channel receiver side 8×8 pattern
O_{8x8x3}^{Tx}	overall transmitter side pattern
O_{8x8x3}^{Rx}	overall receiver side pattern
F_r	camera frame rate
D_r	data rate
$S(i)$	skip image i

Chapter 1

Introduction

With the emergence of the Internet of Things (IoT), an increasing number of devices are becoming connected to the network. The IoT is widely recognized as an essential element in the process of revolutionizing industries, cities, and agriculture, as stated by Zhou *et al.* (2021). The applications of IoT span a broad range, encompassing both indoor and outdoor scenarios. In a general sense, an IoT system consists of entities capable of sensing the environment, generating data, and communicating it over the internet. These entities can include various electronic devices, microcontroller units, plants, animals, and humans.

However, the rapid proliferation of network-connected devices has resulted in a significant challenge for current communication technologies, namely the insufficient provisioning of bandwidth to accommodate all these devices. This issue has led to the saturation of the Radio-Frequency (RF) spectrum. Consequently, intelligent frequency allocation has become increasingly complex, as highlighted by Librino and Santi (2021). Moreover, researchers are actively exploring alternative communication technologies, particularly in environments such as hospitals, schools, and other places involving older people, children, and patients. This is due to the concerns regarding the adverse effects of RF waveforms on human health, as discussed by Miller *et al.* (2019).

One potential solution to address both the frequency allocation problem and human health concerns lies within the optical spectrum. Optical Wireless Communication (OWC) technologies, including Visible Light Communication (VLC), Light Fidelity (Li-Fi), Optical Camera Communication (OCC), and free-space optical communication, offer promising prospects for high data rates and communication distances over short to long ranges. These technologies harness the power of light to enable efficient and secure communication.

1.1 History

The concept of long-distance communication using light dates back to the 17th century when light towers were employed to warn localities of events or potential invasions. These towers used specific colors of flame or patterns, and the method was known as the optical telegraph or semaphore telegraph (Wikipedia 2018*c*).

In the late 19th century, Alexander Graham Bell introduced the Photophone, which revolutionized wireless communication by utilizing electromagnetic waves transmitted through sunlight (Wikipedia 2018*b*). While the Photophone was an impressive achievement for its time, it eventually gave way to other wireless communication systems operating at lower frequencies, as it did not gain widespread popularity. Throughout the 20th century, information transmission through the air primarily relied on waves with frequencies lower than visible light.

In contemporary times, however, light has become a common medium for data transport, especially in fiber optic networks. Building upon Alexander Graham Bell's pioneering work, visible light communication has emerged as a novel approach to transferring data across free space. Unlike Bell's era, we now possess more advanced technologies, such as photodiodes, cameras, and Light Emitting Diodes (LED)s, enabling more efficient and reliable visible light communication.

1.2 Basics of Data Communication in Visible Light Spectrum

The wavelength range under the electromagnetic spectrum between 380 and 700 nanometers which can be seen by human eyes is called as visible light spectrum. To achieve communication using this spectrum, the underlying data transmission and reception techniques should use the various properties of light for modulation. Typically, any type of digital data can be decomposed into individual bits of 1's and 0's. These bits can be represented as a low or high signal. Thus, while using a light source for communication the digital signal can be simply converted into the presence and absence of light, i.e., by turning the light 'on' and 'off'. This type of modulation is called On-Off Keying (OOK). There are more advanced ways for modulating signals to achieve higher data rates, and better quality of reception, which are elaborated on in Chapter 2. In general, the ability to switch between 'on-off' states is critical for data transfer rates, as it limits achievable data rates. Traditional light sources similar to tungsten filament bulb and compact fluorescent

bulb does not support fast switching between 'on-off' states thus, making LED ideal for VLC. Although the concept is not new, however, due to recent technological advancements concerning reduced sensor sizes, faster and power-efficient LEDs, low-cost hardware, and faster processors, the concept is revived to serve the current situation (Pang *et al.* 1999; Tanaka *et al.* 2001). The theoretical limit of OOK using specialized LEDs is 100 Gbps (Chowdhury *et al.* 2018).

1.3 VLC Architecture

A general architecture of VLC system is as shown in Figure 1.1 which shows a VLC-Transmitter (Tx), free space medium, and a VLC-Receiver (Rx). At the Tx side, the input binary data passes through an optical signal modulator to map the bit value with voltage level as per the requirement. These voltage values are used for modulating the physical state of connected LEDs using LED driver. These, changes in light intensities are sensed at Rx side using either a photodiode or a camera sensor. The sensed values undergo pre-processing to reconstruct the received signal. Finally, the output is generated at the Rx side by performing suitable demodulation.

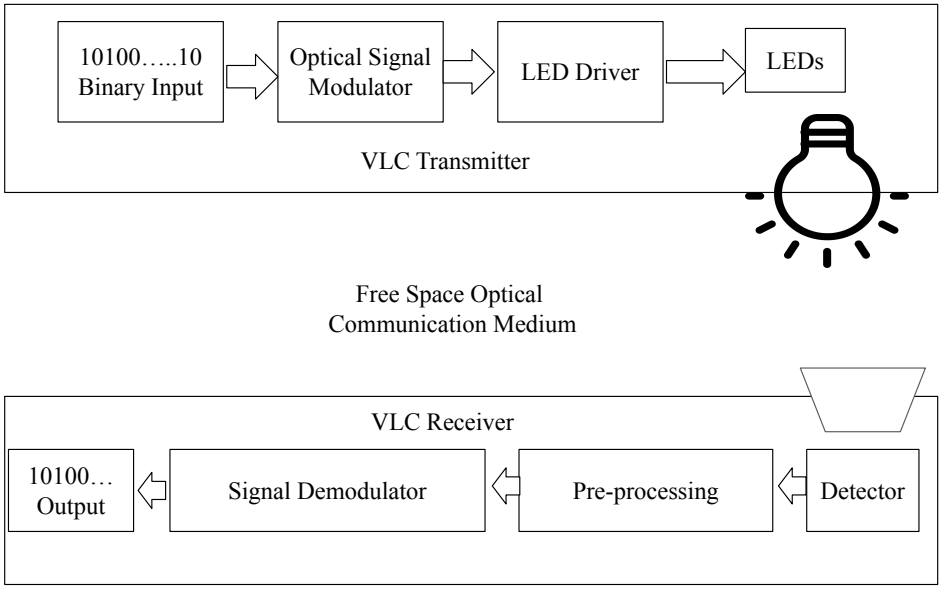

Figure 1.1: Generic VLC System

Depending upon the type of the Rx, i.e., photodiode or camera, the underlying architecture for Rx will change. In Li-Fi and VLC, photodiodes are used widely as the detectors that receive the light intensity from transmitting LEDs. The modu-

lation techniques used will be generally based on Intensity Modulated (IM)/Direct Detection (DD). Whereas, in OCC, image sensors serve as the detectors that receive data. The demodulation schemes in OCC undergo an additional image processing step to detect the Tx and decode the data. A suitable OCC modulation scheme is designed based on the type of camera and usage of LED features.

1.4 Standards

Standardization efforts such as Visible Light Communication Association (VLCA) standards and Institute of Electrical and Electronics Engineers (IEEE) 802.15.7 shows that VLC would augment existing wireless networks in coming years. In 2003, a VLC Consortium (VLCC) was formed to speed up the research and commercialization of VLC. The VLCC proposed two standards by 2007; JEITA CP-1221 (VLC system)(JEITA 2007*a*) and JEITA CP-1222 (VL ID system)(JEITA 2007*b*) which was later accepted by the Japan Electronics and information technology industries association (JEITA). CP-1223(JEITA 2013) was introduced as a visible light beacon system in 2013. Both these standards have meager data rates of up to 4.8 Kbps.

Due to the growing interest of researchers in VLC, VLCC introduced the first IEEE 802.15.7 standard (Standards 2011). This standard defines physical and media access control (MAC) layer parameters for short-range optical wireless communications. This includes network topology, modulation domain spectrum, MAC protocol specification, collision avoidance, addressing, performance, quality indicator, dimming support, color status indicator, and stabilization. This standard proposes OOK, Color Shift Keying (CSK), and Variable PPM (VPPM) techniques for indoor and outdoor communications (Roberts *et al.* 2011). The highest achievable data rate for indoor communication is up to 96 Mb/s. However, by using Multiple Input Multiple Output (MIMO) systems and other modulation schemes, the data rate can be greatly increased.

The IEEE 802.15.7 standard was initially formulated in 2011 for VLC without considering the Image Sensor (IS)-based Rx (Standards-IEEE 2018*b*). In 2014, however, OCC was included in the revised IEEE 802.15.7r1 standard (Standards-IEEE 2018*a*), which was managed by the Task Group 802.15.7r1 (TG7r1) task group and covered wider light spectra such as Near Infrared (NIR) and near ultraviolet (UV). OCC is currently organized by the updated task group Task Group 802.15.7m (TG7m) that finalized the initial draft in 2018 (Nguyen *et al.* 2018).

1.5 Applications

VLC exhibits two distinct application scenarios based on operational range. The first scenario encompasses outdoor environments, where communication distances can extend up to a few meters. Applications falling within this category include vehicle-to-vehicle communication and pedestrian/vehicle-to-street light communication. Conversely, the second scenario pertains to indoor environments, involving shorter communication distances ranging from a few centimeters to 2 meters. Devices such as refrigerators, washing machines, and study lamps, which remain stationary, fall under this category. Notably, VLC can also facilitate internet connectivity in aircraft through the utilization of LED reading lamps.

Indoor geolocation emerges as another compelling application for VLC systems, particularly due to the limitations of Global Positioning System (GPS) functionality within buildings. Leveraging the diverse array of lights present in a VLC system, triangulation techniques can be employed to precisely locate devices within a room. This capability proves particularly valuable in hazardous situations where it becomes necessary to locate individuals inside a building. As long as the VLC system remains intact and an unobstructed view of the room is maintained, it becomes possible to identify devices containing people, thereby aiding firefighters in their rescue efforts.

The rapid development of compact electronic devices integrated with cameras has created a demand for affordable, efficient, and feature-rich camera systems. Consequently, various types of cameras, including Closed-circuit television (CCTV), drone cams, and car dashcams, are being deployed. Furthermore, these cameras can be enhanced to provide communication capabilities through minor software modifications (Ali *et al.* 2021).

VLC systems can also be seamlessly integrated into traffic lights and vehicle dashboards, presenting an opportunity to transmit real-time traffic information directly to vehicle drivers. This integration enhances the functionality of traffic lights, similar to highway signs that warn drivers about forthcoming traffic conditions, with the distinction that VLC transmits traffic information directly to screens inside vehicles. This incorporation of VLC into traffic lights significantly improves the efficiency and convenience of the overall traffic system. Figure 1.2 provides a comprehensive overview of the diverse applications encompassed by VLC.

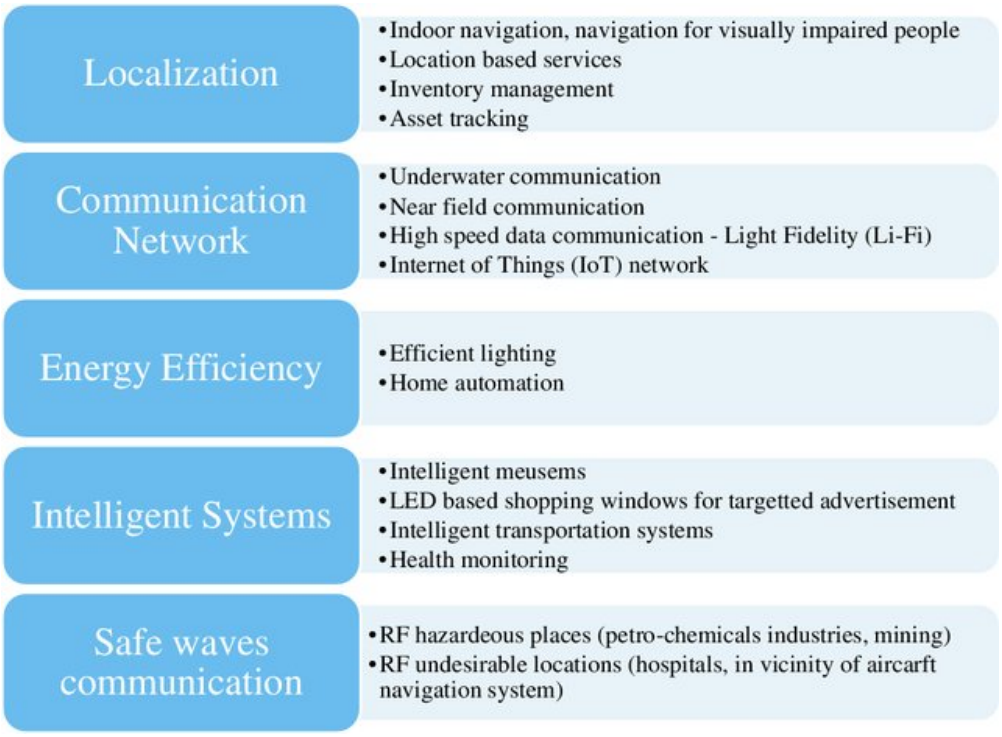

Figure 1.2: VLC Applications Summary (Saadi and Wuttisittikulkij 2019)

1.6 Motivation

The continuous rise in network-connected devices indicates a clear trajectory towards an even greater number of interconnected devices in the near future. However, this upward trend presents notable challenges for the existing spectrum, which is already grappling with congestion, leading to a surge in cross-talks and interference. Furthermore, the introduction of bandwidth-intensive applications such as streaming platforms and the metaverse further exacerbates the demand for higher bandwidth capacities.

Conversely, the implications of overexposure to high-density RF signals on human health remain a subject of debate. As researchers delve into the potential effects of prolonged exposure to such signals, the quest for a solution becomes imperative. Leveraging the inherent properties of light stands as the primary motivation driving this endeavor, as it holds the potential to address these issues effectively. By capitalizing on the unique characteristics of light, an alternative approach can be devised to mitigate the challenges posed by RF signals, thereby ensuring a more robust and health-conscious communication environment.

1.7 Problem Statement

To design and develop an Efficient Modulation Technique for Visible Light Communication in Indoor Environment with respect to Data Rate, Error Rate, and Distance for IoT Applications.

1.8 Research Objectives

- To design and develop an efficient Photodiode based Visible Light Communication Prototype and Modulation Technique

  - **Publications based on Objective 1**

    1. S. Salvi and V. Geetha, "*Design and Implementation of a Lowcost Testbed for LiFi Modulation Techniques and Experimental Evaluation using Matlab Simulation*" ISBM ICT4SD Bangkok 2023 [Scopus] (Submitted)
    2. S. Salvi and V. Geetha, "From Light to Li-Fi: Research Challenges in Modulation, MIMO, Deployment Strategies and Handover," 2019 International Conference on Data Science and Engineering (ICDSE), Patna, India, 2019, doi: 10.1109/ICDSE47409.2019.8971475 [Scopus]

- To design and develop efficient Optical Camera Communication Prototype and Modulation Technique

  - **Publications based on Objective 2**

    1. S. Salvi and V. Geetha, "*An Optical Camera Communication using Hybrid Frequency Shift and Pulse Width Modulation Technique for Li-Fi*" MDPI Computation Volume 10 Issue 7, Page No. 110; https://doi.org/10.3390/computation10070110 [Scopus, ESCI]
    2. S. Salvi and V. Geetha, "*A Nested Texture Inspired Novel Image Pattern Based Optical Camera Communication*", in IEEE Access, vol. 10, pp. 109056-109067, 2022, doi: 10.1109/ACCESS.2022.3213701. [Scopus, SCIE]
    3. S. Salvi and V. Geetha, "*Quantum Chromodynamics Inspired Optical Camera Communication for User-Centric MIMO*" Special Issue

on Optical Camera Communication, MDPI Applied Sciences, Volume 12(20), 10204; https://doi.org/10.3390/app122010204 [Scopus, SCIE]

- To design and develop efficient Visible Light Communication based technique with respect to Data Rate, Error Rate, and Distance for IoT Applications

  – **Publications based on Objective 3**

  1. S. Salvi, V. Geetha and S. Sowmya Kamath, "Jamura: A Conversational Smart Home Assistant Built on Telegram and Google Dialogflow," TENCON 2019 - 2019 IEEE Region 10 Conference (TENCON), Kochi, India, 2019, pp. 1564-1571. doi: 10.1109/TENCON.2019.8929316 [Scopus]

  2. S. Salvi, V. Geetha, H. Maru, N. Kumar and R. Ahmed, "An Image Transmission Technique using Low-Cost Li-Fi Testbed," 2021 2nd International Conference on Secure Cyber Computing and Communications (ICSCCC), 2021, pp. 114-119, doi: 10.1109/ICSCCC51823.2021.9478124. [Scopus]

  3. S. Salvi, V. Geetha, K. Praveen, K. C and V. J. Nayaka, "LiCamPos : An Indoor Positioning System using Light to Camera Communication," 2021 2nd International Conference on Secure Cyber Computing and Communications (ICSCCC), 2021, pp. 261-266, doi: 10.1109/ICSCCC51823.2021.9478134. [Scopus]

  4. S. Salvi and V. Geetha, "LiCamIoT: An 8x8 LED Matrix Pattern to Camera Communication for LiFi-IoT Applications", 2022 IEEE Silchar Subsection Conference (SILCON), Silchar, India, 2022, pp. 1-6, doi: 10.1109/SILCON55242.2022.10028869. [Scopus]

  5. S. Salvi and V. Geetha, "A Novel 2D LED Matrix and Aztec Pattern Inspired Optical Camera Communication for Industrial IoT", 2022 IEEE 19th India Council International Conference (INDICON), Kochi, India, 2022, pp. 1-6, doi: 10.1109/INDICON56171.2022.10040141 [Scopus]

1.9 Framework for Modulation Techniques for VLC in Indoor Environment IoT Applications

The proposed framework for VLC modulation techniques in indoor IoT applications, as shown in Figure 1.3, encompasses a transmitter and receiver for VLC with integrated modulation techniques. The transmitter generates data and selects the appropriate modulation technique, while the receiver utilizes a photodiode for VLC or a camera for OCC.

The VLC modulator path embodies a series of essential components and techniques that synergistically manipulate the properties of light for efficient data transmission. An LED driver assumes control over the LED, while a repertoire of techniques refines and modulates the transmitted light to encode the data. Through the medium of free space, the modulated light propagates, and its intensities are discerned by a photodiode at the receiver end. The application of thresholding algorithms aids in the seamless demodulation and reconstruction of the original data. To further exemplify the versatility of the proposed framework, an image transmission application has been implemented, showcasing the successful integration of VLC into a low-cost testbed setup.

The OCC modulator path, an integral part of the comprehensive framework, presents a diverse range of techniques catering to specific requirements. Prominent techniques such as Binary Hierarchical Image Pattern Classification (BHIPC), Quick Response (QR)-Code-OCC, and Aztec-Code-OCC effectively exploit the shared hardware setup to facilitate data transmission. The ingenious employment of the rolling shutter effect in the Hybrid Frequency Shift Pulse Duration Modulation (HFSPDM) technique, coupled with an LED driver, maximizes the capabilities of the camera in transmitting data. Additionally, OCC techniques based on an 8x8 LED pattern contribute to the diversity of transmission options. Notably, the HFSPDM setup extends its functionalities to include beacon signal transmission, enabling precise indoor positioning. In industrial IoT applications, the adoption of QR-code and Aztec-code-based OCC systems facilitates seamless sensor data transmission. Furthermore, the Quantum Chromodynamics (QCD)-OCC technique has been proposed, implemented, and meticulously evaluated, underscoring its potential for future applications within the framework.

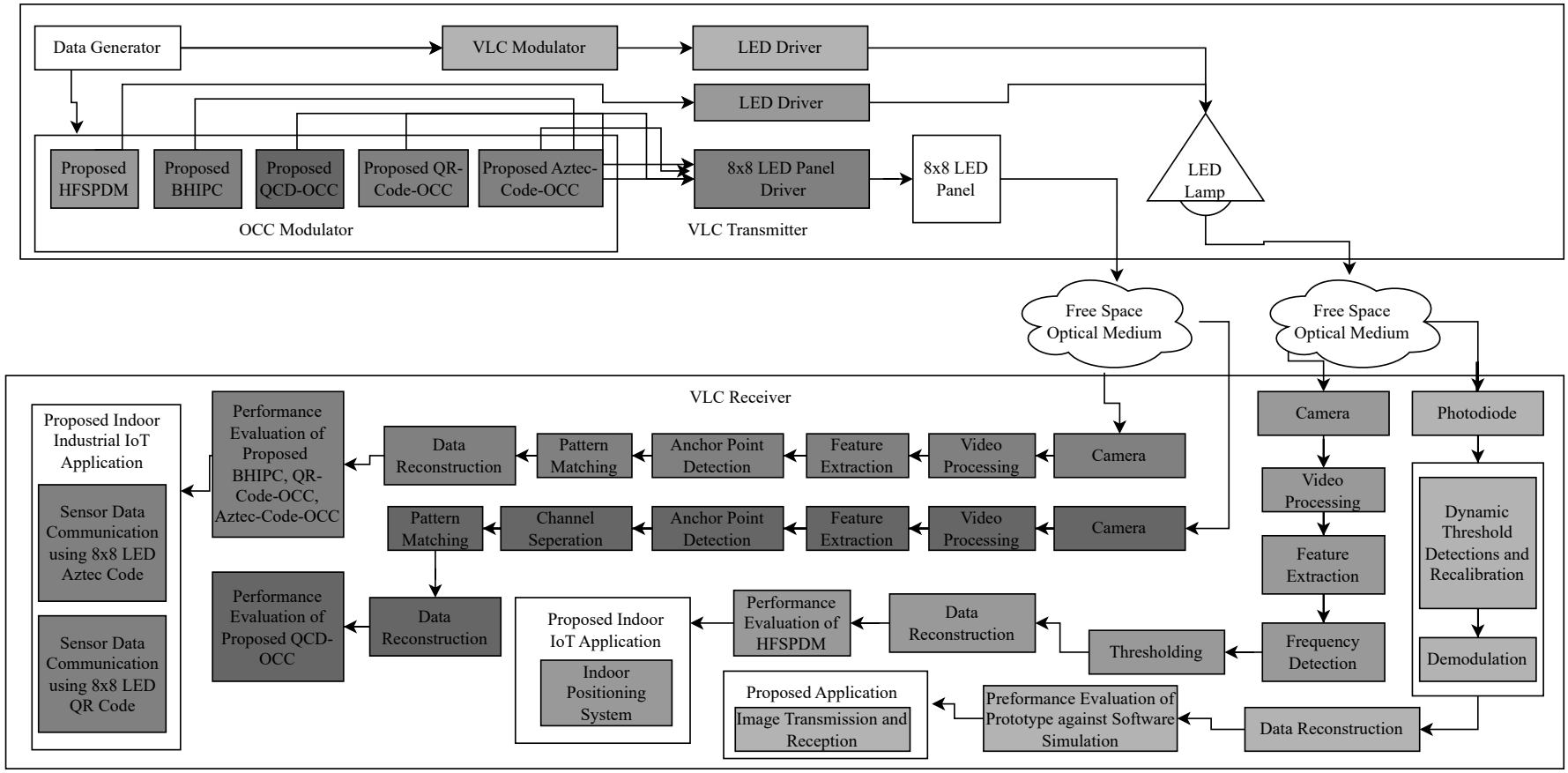

Figure 1.3: A Proposed Framework for Modulation Techniques for VLC in Indoor Environment IoT Applications

1.10 Organization of the Thesis

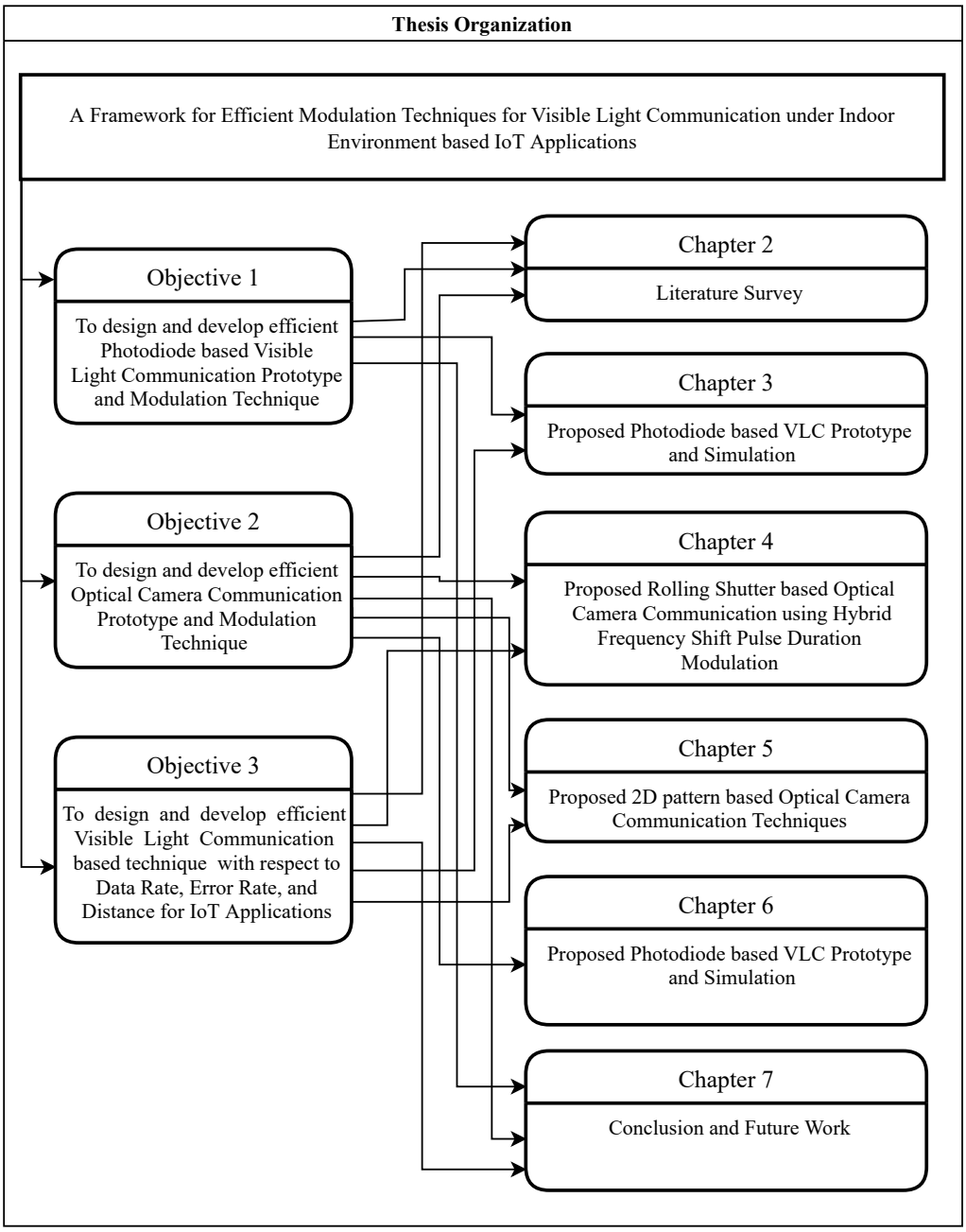

Figure 1.4: Thesis Organization

The remainder of the thesis is organized as follows. Chapter 2 reviews the related work on visible light communication. It also highlights various challenges and issues pertaining to modulation techniques, channel model, receiver design, and MIMO. It provides a detailed summary of various existing modulation techniques, access point deployment strategies, and handover strategies. Based on the

outcome of the literature survey, the problem statement and research objectives are defined.

Chapter 3 describes the proposed low-cost VLC testbed. It provides a detailed explanation of the implementation of the proposed testbed. It also explains the channel model simulation for VLC. The performance of standard modulation techniques implemented on the testbed is also evaluated with the simulated channel model. The testbed is further used to build and evaluate the proposed image transmission technique using VLC.

Chapter 4 focuses on the implementation of a rolling shutter-based optical camera communication technique using the proposed hybrid frequency shift pulse duration modulation. The implemented OCC testbed is also used for implementing existing modulation techniques to evaluate the performance of the proposed modulation technique. The chapter also highlights the proposed Indoor Positioning System (IPS) using implemented testbed.

Chapter 5 focuses on increasing the robustness of previously implemented modulation techniques by using 2 Dimensional (2D) pattern designs. The chapter highlights the proposed nested pattern based OCC and provides a comparison with other pattern-based communication techniques. The chapter also provides details on the two IoT applications built using the proposed testbed.

Chapter 6 describes the proposed novel Quantum Chromodynamics inspired OCC. The proposed technique provides the capability to address multiple users simultaneously with multiple parallel channel streams. The performance of the proposed technique is also compared with existing techniques.

Finally, Chapter 7 summarizes the contributions of the research work and highlights the possible future directions in enhancing the performance of VLC and OCC.

1.11 Summary

The chapter introduces visible light communication as a complementary technology to mitigate RF spectrum saturation problem. It also highlights the brief history of light-based communication and provides a basic understanding of the working principle. The basic architecture of a generic VLC system is described to introduce various components involved. Current standards and applications of the VLC technology is also highlighted in this chapter. Finally, the motivation behind this research work is discussed along with the outline of the thesis. The next chapter provides details on the existing literature.

Chapter 2

Literature Survey

Recently, there has been an observed increase in the number of internet-connected devices. Various new technologies and methods are emerging, especially those that utilize light to provide high-speed communication and efficient utilization of available bandwidth. This is because light communication is faster than any other wired or wireless communication. One such technology, a smaller division of Optical Wireless Communication (OWC) known as Visible Light Communication (VLC), is being strongly considered for integration into 5G technology. Light-Emitting Diodes (LEDs), traditionally used solely for illumination purposes, can also be used for communication under VLC. This increases spectral usage and provides opportunities to explore and innovate various navigation, positioning, and data communication applications in both indoor and outdoor scenarios.

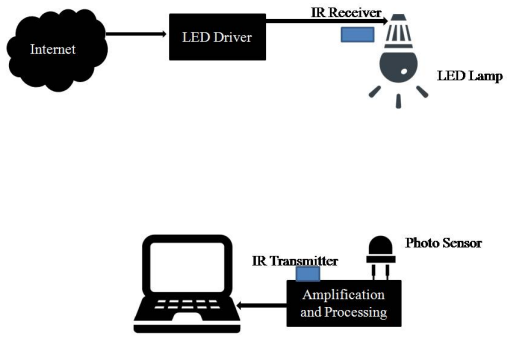

Figure 2.1: Basic LiFi Architecture

As VLC is a form of wireless communication, its underlying backbone architecture remains the same with significant modifications concerning the access points and receiver designs. VLC systems are a simple form of communication typically

used for broadcasting information. Traditionally, a light fixture is mounted on the ceiling, which serves as the transmitter, while non-illuminating devices are placed under the ceiling as receivers facing toward the transmitter. However, bidirectional communication can be achieved by using VLC for data downlink and Infrared (IR) communication for data uplink. This type of system is called "Li-Fi," a term coined by Prof. Harald Haas for Light Fidelity (Haas *et al.* 2016).

Figure 2.1 shows the underlying architecture of a Li-Fi system which consists of backbone internet, LED driver, IR-Rx, LED lamp, photo-sensor, IR-Tx, amplification and processing unit, and any connecting device such as laptop, desktop or mobile. Here, the light fixture is capable of sending and receiving data using LEDs and IR, respectively. Such a light fixture is called Li-Fi access point. An LED driver is used to convert back-end network data to corresponding light pulses by incorporating suitable modulation and encoding scheme. Photodiodes, image sensors, and/or cameras are used as receivers with respective demodulation and decoding scheme to reproduce data. Existing LEDs are commonly used only for illumination, however, to support communication, it has to overcome several research challenges. These challenges majorly include the adoption of existing RF modulation schemes for Li-Fi limited IM/DD scheme while maintaining illumination standards.

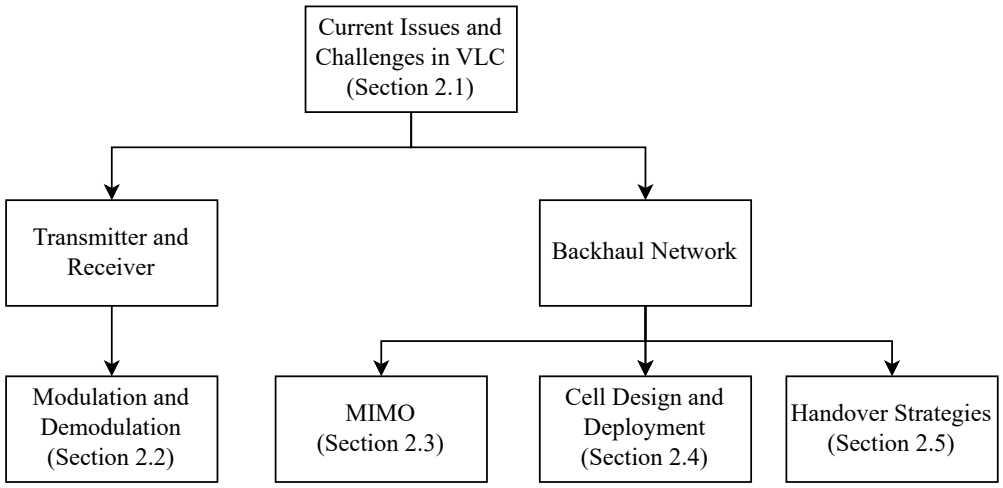

Figure 2.2: Literature Survey Orgaanization

The major challenges in VLC are with respect to modulation and demodulation to increase data rate and in developing scalable communication systems. Based on this literature survey is conducted with respect to TransmitterReciever and Backhaul Networks. The areas considered for further study are shown in Figure 2.2.

2.1 Current Issues and Challenges

LEDs are the most suitable candidates for implementation of Li-Fi system mainly due to its fast response time, long operational lifetime, and low cost (Haruyama 2013). However, it also imposes a few limitations. This section provides a brief insight into various issues and challenges faced while building a Li-Fi system. Table.2.1 highlights the literature on issues and challenges in VLC.

2.1.1 Transmitter (Tx) and Modulation Technique:

The current commercial Li-Fi communication (Lifi-Lighting 2017) (Purelifi 2016) can offer a maximum working distance range of 1 to 50 meters. However, since Li-Fi is inherently Line-of-Sight (LoS) communication, this distance is significantly less compared to the radio frequency counterpart. Also, the achievable data rates by using Li-Fi is limited to a few Mbps. However, active research is going on in this field to improve data rates by using different materials and techniques on LED and photo-sensors. By using a modulation scheme that has high Spectral Efficiency (SE) and bandwidth, high-speed communication can be achieved even in Li-Fi (Omura *et al.* 2018). By using tri-chromatic LEDs instead of phosphorescent LEDs has shown improvement in throughput by a factor of three (Ahn and Kwon 2012). Figure 2.3, shows basic building blocks of Wavelength Division Multiplexing (WDM) which provides better spectral efficiency by using multi-color LEDs over phosphorescent LEDs. It consists of a modulator, signal generator, LEDs, color filters, photodiodes, oscilloscope, and demodulator. In this system, the symbol to be transmitted is encoded and modulated using a modulator, which is then mapped to a specific colored LED. Using a signal generator, the specific LED will be controlled. This allows the simultaneous operation of three transmitters allowing three channels for sending data. On the receiver side, by using chromatic filters, light intensity across each channel will be gathered, and data is reconstructed by demodulation.

Table 2.1: Literature Survey on Issues and Challenges in VLC

Paper	**Methodology**	**Related Parameters**
Haruyama (2013)	LED suitability for Li-Fi system	Fast response time, long operational lifetime, low cost
Lifi-Lighting (2017), Purelifi (2016)	Commercial Li-Fi communication	Maximum working distance range: 1-50 meters cost
Omura *et al.* (2018)	Modulation scheme for high-speed Li-Fi	High spectral efficiency, high bandwidth
Ahn and Kwon (2012)	Use of tri-chromatic LEDs	Improvement in throughput
Sarbazi *et al.* (2014), Li *et al.* (2022)	Study of CIR for NLoS communication	Delays between direct/reflected rays, impact of room characteristics
Kharraz and Forsyth (2013)	Comparison of photodiodes	Avalanche photodiodes for Li-Fi communication
Singh *et al.* (2015*b*)	Selection of receiver devices	Photodiodes for stationary receivers, image sensors for mobile receivers
Albraheem *et al.* (2018)	Trade-off between speed and complexity	Use of photodiodes or image sensors
Zeng *et al.* (2009)	Challenges of applying traditional RF MIMO techniques	Intelligent transmitter deployment-based modulation schemes
Wang and Haas (2015)	Optimization of cross-layer parameters	Two-tier buffer structure, data rates improvement
Galati and Greenhalgh (2010)	User mobility modeling	User movement in shopping mall scenarios
Garg and Parikh (2017)	Impact of receiver orientation	Data rate affected by Li-Fi receiver orientation
Dehghani Soltani *et al.* (2019), Purwita *et al.* (2018)	Evaluation of performance metrics	Bit error rate, signal-to-noise ratio based on device orientation
Soltani *et al.* (2019)	Orientation-based random waypoint model	Handover rate assessment under realistic scenarios

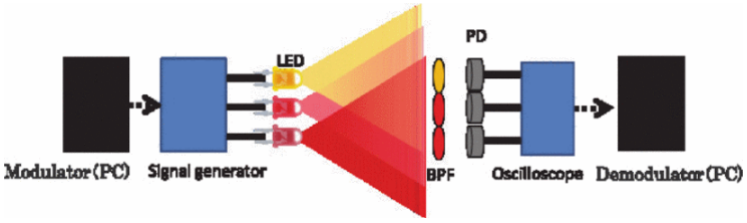

Figure 2.3: OFDM Based WDM-MIMO VLC System (Omura *et al.* 2018)

2.1.2 Optical Wireless Indoor Communication Channel

The Li-Fi communication system is restricted to LoS type of communication, and any misalignment results in drastic degradation of the performance. However, the shadowing effect caused by blocking the direct ray path between the transmitter and photo-sensor can be used for the reconstruction of data using Non Line-of-Sight (NLoS) communication channels. In Sarbazi *et al.* (2014); Li *et al.* (2022), Channel Impulse Response (CIR) is obtained by studying delays between direct /reflected rays, which is affected by wall pain material, furniture, and the size of the room. Obtained CIR can be used for recalibrating the receiver to work in NLoS communication channel.

2.1.3 Receiver Device and its Properties

The pattern of change in light intensities is detected using photosensors at the receiver side. These photosensors could be image sensors or photodiodes. The photodiode converts detected light intensity into photo-current. By comparing the performance of various photodiodes, it was found that avalanche photodiodes can be used for Li-Fi communication due to their smaller size, low cost, and faster response time (Kharraz and Forsyth 2013). However, due to interference from sunlight and other light fixture, the performance of Li-Fi system may get compromised. Thus, by using specific filters and selecting the proper receiver design, the effects of interference can be reduced significantly. It was observed that photodiodes for stationary receivers and image sensors for mobile receivers are well suited in Li-Fi communication system (Singh *et al.* 2015*b*). Image sensors can provide faster data rates by using the rolling shutter effect. However, Li-Fi using image sensors is resource inefficient because it requires more complex computation and power compared to photodiodes. Thus, a suitable trade-off between the speed and complexity should be considered while using photodiodes or camera (Albraheem *et al.* 2018).

2.1.4 MIMO Optical Wireless Communications

Applying traditional RF MIMO techniques for Li-Fi has a major challenge due to the design limitation of narrow beam-width at receivers. It degrades the communication quality even with slight misalignment. Therefore, efficient receivers and intelligent transmitter deployment-based modulation schemes to support MIMO is a potential research area (Zeng *et al.* 2009).

2.1.5 Cross-layer load Balancing

As the network traffic has to be converted either from Li-Fi to RF or vice-versa suitable load balancing should be created. A central unit design of load balancing by using the two-tier buffer structure requires the optimization of cross-layer (MAC layer and Physical Layer) parameters. Efficient cross-layer load balancing will improve the performance in terms of data rates (Wang and Haas 2015).

2.1.6 User Movement Modelling

While designing Li-Fi network, user movement and device orientation should be considered and modeled to study and provide seamless connectivity. The random waypoint model is popularly used to simulate user mobility, however, it is impractical in real scenarios. Users in a shopping mall have a different moving performance from those in the office scenarios (Galati and Greenhalgh 2010). In addition, the random orientations of Li-Fi receiver will affect the user data rate, which should be carefully modeled (Garg and Parikh 2017). In Dehghani Soltani *et al.* (2019) and Purwita *et al.* (2018), performance metrics such as Bit-Error-Ratio (BER) and Signal-to-Noise-Ratio (SNR) are evaluated based on the characterization of device orientation. An Orientation-based Random Waypoint (ORWP) (Soltani *et al.* 2019) mobility model was specifically modeled for Li-Fi mobile devices and it is assessed based on the handover rate under realistic scenarios.

2.1.7 Illumination Requirements

An ideal Li-Fi system must have provision for supporting various dimming levels. There are two techniques that can be used to achieve dimming in indoor Li-Fi systems either by Continuous Current Reduction (CCR) or by Pulse Width Modulation (PWM) (Roberts *et al.* 2011). In CCR, the 'on/off' levels of the LED are redefined based on the selected dimming level and maintain the same data

rate. However, it was studied that it not only affects the reliability of communication at low dimming levels but also the color rendering property of LED becomes non-linear and unpredictable under continuous low power (Zafar *et al.* 2015). In PWM based dimming, additional 'on/off' pulses are inserted according to desired dimming level. More 'off' pulses provide dimmer light and more 'on' pulses provide brighter light. It is considered that the frequency of combined pulses for transmission of a symbol is higher than Flicker Free Frequency (FFF). As studied in papers by Pathak *et al.* (2015) and Jovicic *et al.* (2013) 50% dimming level provides maximum data rate, further decreasing or increasing the brightness of the LED results in a decrease in data rate. Thus, it shows that communication efficiency with PWM based dimming in Li-Fi is a triangular function with peak performance at 50% brightness. It also suggests that the modulation scheme to be used should have an equal distribution of bits to avoid flickering.

2.2 Modulation Techniques

At the core of any communication technique is the usage of different properties of the concerned medium. These properties are modulated and demodulated to send information across the channel. This section discusses modulation techniques used in Li-Fi/VLC, some of which are adapted from their RF counterparts and some unique to their nature. The modulation techniques under Li-Fi are classified as Single Carrier Modulation (SCM), Multicarrier Modulation (MCM), and Li-Fi Specific Color-based Modulation.

2.2.1 Single Carrier Modulation (SCM)

In SCM the information is transmitted using a single channel. Widely used SCM schemes for Li-Fi/VLC include OOK, Pulse Position Modulation (PPM) and Pulse Amplitude Modulation (PAM). Table.2.2 highlights the literature on single carrier modulations in VLC.

2.2.1.1 On-Off Keying (OOK)

In OOK, for transmitting data bits, the LED is switched 'on' and 'off' for bits 1 and 0 respectively. In some variations of OOK, the LED is dimmed instead of completely turning it 'off'. Generally, the level of minimum light intensity that can be detected is determined by the sensitivity of the photosensor. Thus, if sensitivity is high, the minimum light intensity can be closer to the full brightness of the LED.

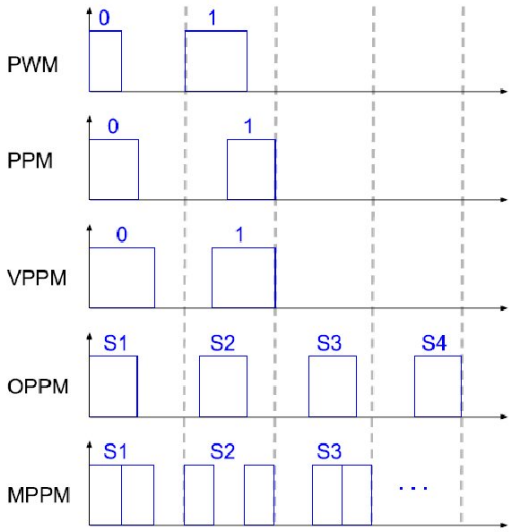

Figure 2.4: Various Pulse Position Modulation Techniques (Lee and Park 2011)

It also gives a better wider range of Peak Amplitude to Power Ratio (PAPR) and thus supports various dimming levels. Although it is easy to implement the major issue is with the limited bandwidth as the response time of white LED is slow.

The proposed Non Return to Zero (NRZ)-OOK modulation in S *et al.* (2007) demonstrated a 10Mbps VLC link using white LEDs and P-I-N photodiode. Based on the same premise, further improvements in the performance were achieved by using a blue filter and a combination of a blue filter with analog equalization to gain bandwidth of 40 Mbps and 125 Mbps respectively (Vucic *et al.* 2009). However, by using Avalanche photodiode at the receiver side, better performance in terms of bandwidth, i.e., 230 Mbps was achieved. It was due to the high sensitivity and fast response time offered by avalanche photodiode (Kharraz and Forsyth 2013). It was also observed that using red-green-blue (RGB) LED for modulation at the transmitter and Avalanche photodiode at receiver bandwidth of up to 477 Mbps is achievable (Fujimoto and Mochizuki 2013).

2.2.1.2 Pulse Position Modulation (PPM)

In PPM, symbol duration is kept constant and divided into a certain number of slots. Figure 2.4 represents various pulse modulation techniques. The symbol is decoded depending on the presence of a pulse in a particular slot. Although PPM is more power efficient compared to OOK, the bandwidth consumed is higher to provide the same data rates. Thus, due to limitations of lower data rates and SE, several other modifications have been suggested over time. The proposed Differential PPM (DPPM) by Tsonev *et al.* (2014) provides improved power and

SE gains; however, due to the unequal distribution of power for different symbols, considerable flickering was observed affecting the illumination performance. An improvement over DPPM was proposed by Sevincer *et al.* (2013) by adding a layer of bit encoding to ascertain even distribution of duty cycle across various symbols. Although it solves the flickering problem, the attainable data rate was lesser compared to DPPM.

An alternative method to implement VPPM by Rajagopal *et al.* (2012) showed better data rate and support for dimming by using PWM methods for dimming. Due to these advantages of VPPM, it is considered one of the standard modulations for VLC (IEEE 2018). In Lee and Park (2011) Multiple PPM was compared with VPPM to observe that Multiple PPM (MPPM) achieves better spectral efficiency in comparison with VPPM. Other PPM methods such as Overlapping PPM (OPPM) (Gancarz *et al.* 2015) and Multipulse PPM (M-PPM) (Siddique and Tahir 2014) allowed transmission of symbols at higher data rate due to the inclusion of multiple pulse levels and a group of pulses respectively. The combination of best of OPPM and MPPM was also considered called Overlapped-MPPM (Ohtsuki *et al.* 1993) which performed better compared to MPPM in terms of spectral efficiency under the specific condition of fewer pulse slots and more pulse per symbol duration. Another particular modulation scheme named Trellis-Coded Overlapped MPPM (OMPPM) (Long *et al.* 2017) was explicitly used to combat the error rate.

If the symbol is transmitted using the amplitude of the pulse, it is called PAM which provides higher spectral efficiency. A combination of PAM and VPPM was proposed by Yi and Lee (2014), which on comparison with other dimmable modulation schemes like OPPM, VPPM, and Return to Zero (RZ)-OOK was found to provide better bandwidth efficiency at the cost of more power. Another variation proposed by Zeng *et al.* (2015) provided and more power-efficient model. Under the controlled environment proposed in Li *et al.* (2016*a*) and Lu *et al.* (2017) 40 Gbps and 56 Gbps data, the rate was achieved by using M-ary variation of PAM (Nishikawa 1973). It was also studied that by converting Multicarrier Orthogonal Frequency Division Multiplexing (OFDM) to SCM by using Discrete Fourier Transform (DFT) and Inverse Fast Fourier Transform (IFFT), (Shi *et al.* 2016) and (Li *et al.* 2019) non-linearity tolerance is improved at the receiver.

Table 2.2: Literature Survey on Single Carrier Modulation

Paper	Methodology	Related Parameters
S *et al.* (2007), Vucic *et al.* (2009), Kharraz and Forsyth (2013), Fujimoto and Mochizuki (2013)	On-Off Keying (OOK)	Data rate: 10 Mbps, 40 Mbps, 125 Mbps, 230 Mbps, 477 Mbps
Tsonev *et al.* (2014)	Differential Pulse Position Modulation (DPPM)	Improved power and spectral efficiency
Sevincer *et al.* (2013)	Enhanced DPPM (DPPM+)	Even distribution of duty cycle across symbols, reduced flickering
Rajagopal *et al.* (2012)	Variable Pulse Position Modulation (VPPM)	Support for dimming, higher data rates
Lee and Park (2011)	Multiple Pulse Position Modulation (MPPM)	Better spectral efficiency
Gancarz *et al.* (2015)	Overlapping Pulse Position Modulation (OPPM)	Higher data rates with multiple pulse levels
Siddique and Tahir (2014)	M-ary Pulse Position Modulation (M-PPM)	Higher data rates with a group of pulses
Ohtsuki *et al.* (1993)	Overlapped M-ary Pulse Position Modulation (OMPPM)	Better spectral efficiency
Long *et al.* (2017)	Trellis-Coded Offset M-ary Pulse Position Modulation (OMPPM)	Error rate reduction
Yi and Lee (2014), Zeng *et al.* (2015)	Pulse Amplitude Modulation (PAM)	Higher spectral efficiency, power efficiency, bandwidth efficiency
Li *et al.* (2016*a*), Lu *et al.* (2017)	M-ary PAM	Data rates: 40 Gbps, 56 Gbps
Shi *et al.* (2016), Li *et al.* (2019)	Conversion of Multicarrier OFDM to SCM	Improved non-linearity tolerance at the receiver

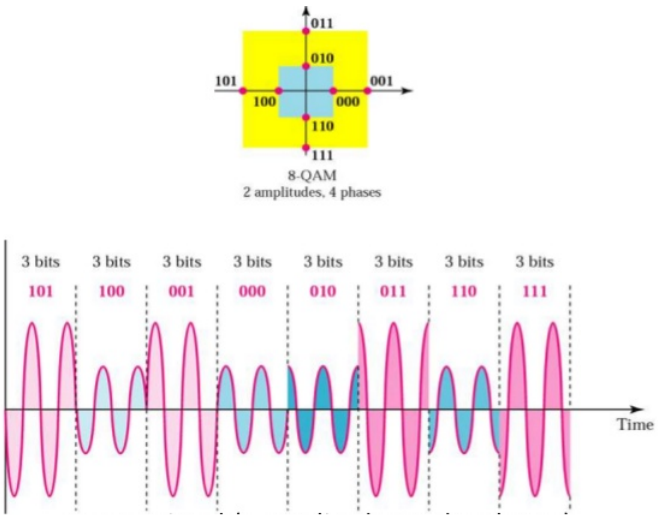

Figure 2.5: 8-QAM Signal 4 Phases 2 Amplitudes (David Quilindo-Méndez *et al.* 2020)

2.2.2 Multi-carrier Modulation (MCM)

SCM techniques requires intricate equalization methods at faster data rates (Zhang *et al.* 2012). On the other hand, MCM techniques such as OFDM can be applied in IM/DD domain by adding a computationally efficient single tap equalizer. Here, OFDM transmitter first modulates incoming bits into modulation format such as M-ary QAM (M-QAM). Table.2.3 and Table.2.4 highlights the literature on multiple carrier modulations in VLC.

Figure 2.5, shows 8-Quadrature Amplitude Modulation (QAM) signal with two Amplitudes and four Phases. The M-QAM (David Quilindo-Méndez *et al.* 2020) modulated bits are then loaded over orthogonal sub-carriers and by using Inverse Fast Fourier Transform multiple symbols are then multiplexed into the time domain. However, as the output of OFDM is bipolar and complex, it cannot be directly applied to the IM/DD system. Hence, these signals are first converted into unipolar real values by using the Hermitian Symmetry property. Depending on the methods used for exploiting this property few variants with their advantages and disadvantages are as follows:

2.2.2.1 DC-baised Optical-OFDM (DCO-OFDM)

An addition of Direct Current (DC) bias to the real part of the bipolar OFDM signal offers better BER and SE (Zhang and Zhang 2014). However, high PAPR of OFDM Signal results in clipping distortion leading to undesirable electrical and optical spikes.

Table 2.3: Literature Survey on Multicarrier Modulation (Part 1)

Paper	Methodology	Related Parameters
Zhang *et al.* (2012)	Multi-carrier Modulation (MCM)	SCM techniques require intricate equalization methods at faster data rates.
David Quilindo-Méndez *et al.* (2020)	M-QAM Modulation	Modulated bits are loaded over orthogonal sub-carriers and multiplexed into the time domain using Inverse Fast Fourier Transform.
Zhang and Zhang (2014)	DCO-OFDM	Addition of DC bias to the real part of the bipolar OFDM signal offers better BER and SE.
Vappangi and Mani (2019)	DST-OFDM	Provides computationally efficient signal transmission without the need to comply with Hermitian symmetry criteria.
Namei Yin *et al.* (2017)	ACO-OFDM	Only odd sub-carriers of the original OFDM frame are used for information transmission, allowing negative samples to pass through without distortion.
Chen *et al.* (2017)	ADO-OFDM	Combination of ACO-OFDM and DCO-OFDM, utilizing both even and odd sub-carriers for data transmission.
Lee *et al.* (2009)	PAM-DMT	Similar to ACO-OFDM but uses all sub-carriers of OFDM, providing better spectral efficiency.
Ghassemlooy *et al.* (2017)	OFDM-PTM	Converts bipolar OFDM signal into digital PCM formats (PWM, PPM, DPIM) for improved BER.

Table 2.4: Literature Survey on Multicarrier Modulation (Part 2)

Paper	Methodology	Related Parameters
Taherkhani and Kiasaleh (2018)	Reed Solomon-OFDM	Uses Reed Solomon encoding to filter redundant parts that cross the clipping range and recreate data at the receiver.
Wang *et al.* (2015)	Layered ACO-OFDM	Multiple ACO-OFDM signals are mapped to different layers of the time-divided input data signal.
Islam and Mondal (2019)	HDAP-OFDM	Combination of DCO-OFDM, ACO-OFDM, and PAM-DMT for power efficiency.
Tsonev *et al.* (2012); Zhou and Zhang (2018)	U-OFDM	Applies Hermitian symmetry over the input signal of M-QAM symbols and unfolds it into two time-domain frames.
Lian *et al.* (2019)	VPW-OFDM	Uses variable width pulses to convey the magnitude and phase information based on clipping distortion and noise.
Lian and Brandt-Pearce (2018), Lian and Brandt-Pearce (2019)	CEO-OFDM	Clipped information due to peak power constraint is transmitted via extra time slots or multiple slots for reduced clipping distortion.

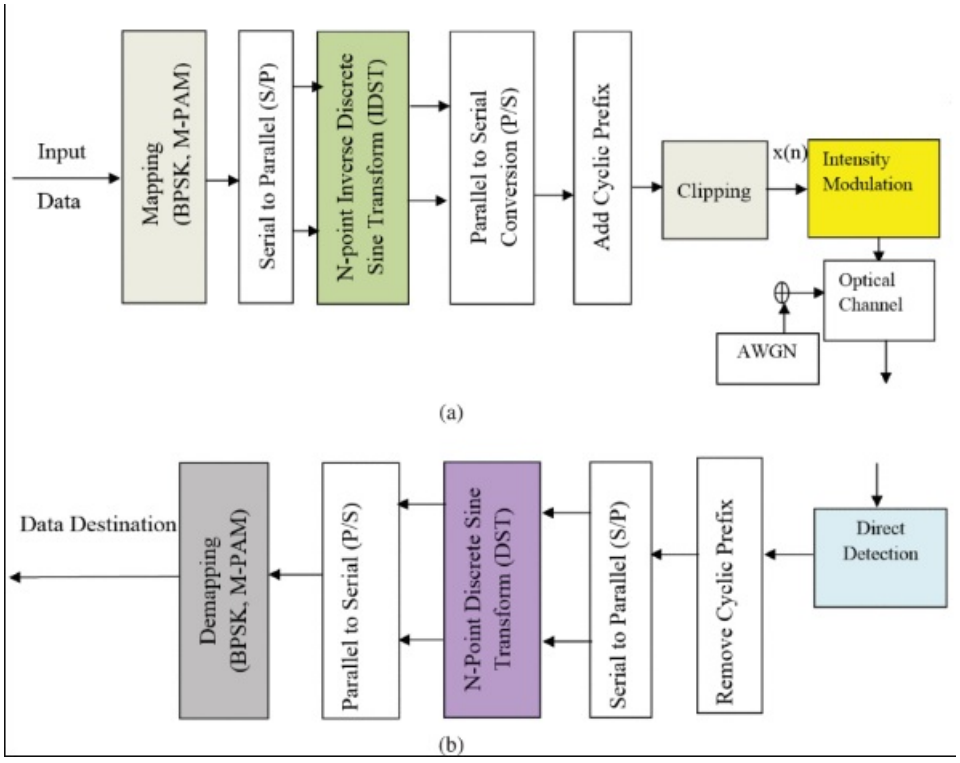

Figure 2.6: DST-based DCO-OFDM/ACO-OFDM system model for VLC. (a) The transmitter of DST-DCO/ACO-OFDM system for VLC. (b) The receiver of DST-DCO/ACO-OFDM system for VLC (Vappangi and Mani 2019)

2.2.2.2 Asymmetrically Clipped Optical-OFDM (ACO-OFDM)

In ACO-OFDM (Namei Yin *et al.* 2017), even sub-carriers of the original OFDM frame is skipped and information is added only to the odd sub-carrier. This creates symmetry allowing negative samples to pass through without any distortion. However, this reduces the available bandwidth by half as compared to DCO-OFDM.

2.2.2.3 Asymmetrically Clipped DC biased Optical OFDM (ADO-OFDM)

Combination of the best of ACO-OFDM and DCO-OFDM is considered in ADO-OFDM (Chen *et al.* 2017). It applies DCO-OFDM on the even sub-carriers and odd sub-carriers are modulated by using ACO-OFDM. This provides utilization of even as well as odd sub-carriers for data transmission. ADO-OFDM provides better power efficiency compared to DCO-OFDM and better bandwidth compared to ACO-OFDM at the cost of increased computational complexity.

2.2.2.4 PAM-Discrete Multitone (PAM-DMT)

PAM-DMT proposed by Lee *et al.* (2009) is similar to ACO-OFDM in terms of transmission of the positive part of Discrete Multitone (DMT) and asymmetric clipping at zero. However, it provides better spectral efficiency as it uses all the sub-carriers of OFDM. It was also observed that the detection performance at the receiver could be improved by exploiting the nonlinear distortions of PAM-DMT (Vasconcelos *et al.* 2014). The authors in Islim *et al.* (2015) proposed a modulation technique which overlaps multiple unipolar streams of PAM-DMT. In Hybrid ACO-OFDM (Wang *et al.* 2018*a*), PAM-DMT is used for transmission of data on the even sub-carriers and ACO-OFDM is transmitted on the odd sub-carriers. In PAM-based hybrid optical OFDM(PHO-OFDM) (Zhang *et al.* 2018) a hybrid high order QAM is used to replace 1-dimensional PAM in order to compensate for data capacity of PAM-DMT providing better BER at the cost of reduced PAPR.

In Ghassemlooy *et al.* (2017) a hybrid OFDM-Pulse Time Modulation (PTM) scheme is proposed, where a bipolar Optical OFDM signal is converted into digital Pulse Coded Modulation (PCM) formats (PWM, PPM, Digital Pulse Interval Modulation(DPIM)). It is done by generating a PWM signal of varying width or PPM signal corresponding to input discrete OFDM sample. It showed improved BER compared to ACO-OFDM. In Reed Solomon-OFDM (Taherkhani and Kiasaleh 2018) after encoding data using RS codeword, the redundant part which crosses the clipping range is filtered and the redundancy left is used at the receiver to recreate data. In layered ACO-OFDM (Wang *et al.* 2015), multiple ACO-OFDM signals are mapped to different layers of the time-divided input data signal. It was observed that Layered ACO-OFDM (LACO-OFDM) gives better performance in terms of SNR for two-layer compared to more layers.

Hybrid DC-biased asymmetrically-clipped PAM OFDM (HDAP-OFDM) (Islam and Mondal 2019) and discrete sine transform-based OFDM (DST-OFDM) (Vappangi and Mani 2019) were proposed to achieve power efficiency. HDAP-OFDM is a combination of three OFDM formats (DCO-OFDM, ACO-OFDM, PAM-DMT). It uses higher order sub-carriers to carry ACO-OFDM on the odd-index, PAM-DMT on the event, and DCO-OFDM on remaining lower order sub-carriers. DST-OFDM provides computationally efficient signal transmission as real-valued signals are achieved without the need to comply with Hermitian symmetry criteria. Figure 2.6, shows the basic architecture of DST-OFDM modulation. It can be used with the DCO-OFDM or ACO-OFDM technique.

2.2.2.5 Unipolar OFDM (U-OFDM)

The U-OFDM (Tsonev *et al.* 2012; Zhou and Zhang 2018) applies Hermitian symmetry over the input signal of M-QAM symbols. The bipolar signal thus obtained is unfolded into two time-domain frames. The first frame represents positive values, and the second represents the negative value from the original bipolar signal. DC biasing is not needed as the resultant signal consists of only non-negative values. At the receiver side, the subtraction of the second frame from the first one results in the reconstruction of the original bipolar signal. However, since it uses two frames for conveying the same amount of data as in conventional DCO-OFDM, its bandwidth is half that of DCO-OFDM.

In an improvement over U-OFDM, a variable pulse width-U-OFDM (Lian *et al.* 2019) was proposed. It uses variable width pulses for conveying magnitude and phase information which are adjusted based on clipping distortion and noise.

Figure 2.7(a) and 2.7(b), shows examples of two different pulse width signals. The width of the magnitude component of pulse in 2.7(b) is wider than that in 2.7(a). The OFDM symbol duration can be calculated as $Ts{=}N(Tm + Tp)$. In Figure 2.7(a), the signals exceeding the maximum transmitted power must be hard clipped for the magnitude part. However, as the phase part is normalized and limited between 0 to $Pmax$, there is no clipping distortion while transmitting the phase component.

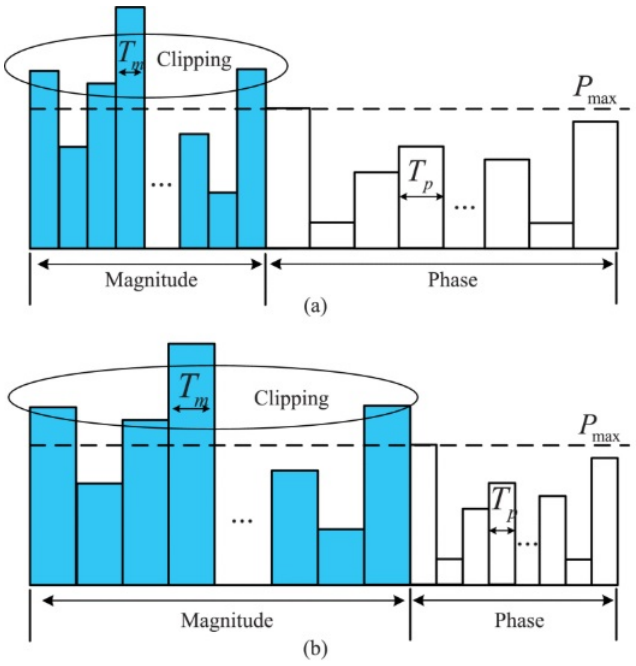

Figure 2.7: An illustration of VPW-OFDM (Lian *et al.* 2019)

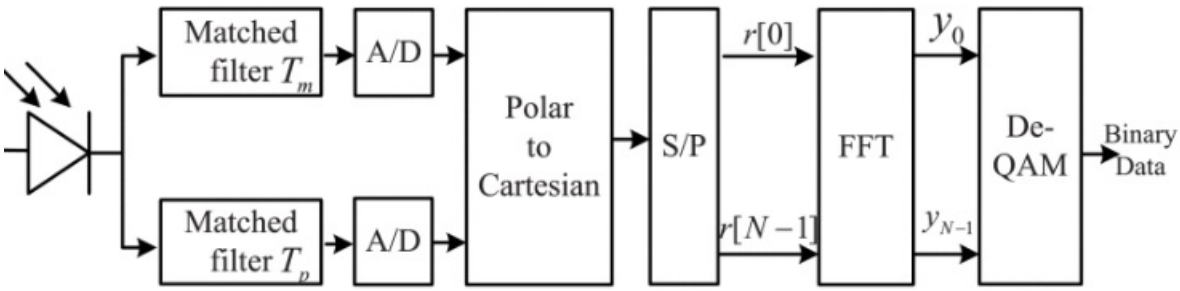

Figure 2.8: A block diagram of VPW-OFDM Receiver (Lian *et al.* 2019)

The received optical signal is converted into an electrical signal and matched filters with pulse widths Tm and Tp are used to detect the magnitude and phase components respectively as shown in Figure 2.8. After sampling and conversion from polar to Cartesian, serial data is converted to parallel and passed to Fast Fourier Transform (FFT) followed by M-QAM decoder. However, the required bandwidth is more, and it underperforms severely in low bandwidth conditions.

In another U-OFDM based modulation technique, the clipped information due to peak power constraint is transmitted via extra time slots. This (Lian and Brandt-Pearce 2018) achieves better SNR at the cost of bandwidth. An improvement over Clipping-enhanced Optical OFDM (CEO-OFDM) was proposed in the form of L-slot CEO-OFDM (Lian and Brandt-Pearce 2019) as illustrated in Figure 2.9 where $Pmax$ is peak transmitted power constraint. Figure 2.9(a) shows an illustration of a bipolar real OFDM signal which uses Hermitian symmetry. Figure 2.9(b) shows one-slot CEO-OFDM signal, in which positive, negative, and its respective clipped parts are transmitted in time slots 1,2, and three, respectively. It reduces clipping distortion while retaining important information. However, for a higher modulation index, the third time slot can also experience clipping. Thus by generalizing the idea for L-slots, the effects of clipping distortion can reduce by delaying the slot containing clipped signals. As shown in figure 2.9(c) where L is several slots. It was observed that L-slot CEO-OFDM techniques provide better BER at higher data rates and better support for dimming compared to ACO-OFDM and DCO-OFDM.

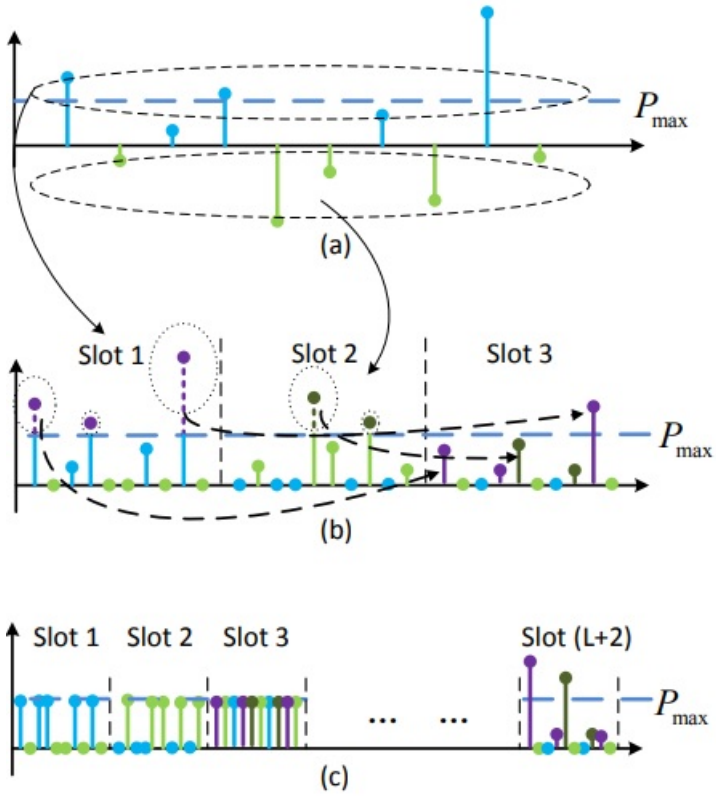

Figure 2.9: Principle of multi-slot CEO-OFDM. (a) bipolar OFDM signal, (b) One-slot CEO-OFDM signal, (c) L-CEO-OFDM signal (Lian and Brandt-Pearce 2019)

2.2.3 Other Multicarrier Multiplexing

OFDM uses FFT based transformation for providing Multi-Carrier Multiplexing. Few other transformations such as Hadamard Coded Modulation (HCM), Discrete Hartley Transformation (DHT), and Spatial Modulation (SM) are also considered for Li-Fi channels. Table. 2.5 highlights the literature survey on other multicarrier modulation techniques.

2.2.3.1 HCM

In HCM (Noshad and Brandt-Pearce 2014) fast Walsh-Hadamard transformation (FWHT) is used as an alternative to traditional FFT used in OFDM. Although HCM is reported to achieve better performance gains at higher illumination levels compared to ACO-OFDM and DCO-OFDM, an alternative DC reduced HCM (Noshad and Brandt-Pearce 2016) was proposed to reduce the power consumption and support dimming.

Table 2.5: Literature Survey on Other Multicarrier Modulation

Paper	Methodology	Related Parameters
Noshad and Brandt-Pearce (2014)	HCM	FWHT is used as an alternative to traditional FFT used in OFDM. Achieves better performance gains at higher illumination levels.
Noshad and Brandt-Pearce (2016)	DC reduced HCM	DC reduced HCM proposed to reduce power consumption and support dimming.
Wong *et al.* (1997)	WPDM	Multiple signals encoded into a waveform using wavelet packet basis functions. Provides channel capacity improvement and maintains orthogonality.
Huang *et al.* (2014)	WPDM	Clipping distortion observed.
Moreolo *et al.* (2010)	DHT	DHT used in multicarrier IM/DD system. Less computationally intensive and improves SE compared to ACO-OFDM.
Jeganathan *et al.* (2008)	SM	One light fixture transmits symbols using any modulation scheme, others provide regular illumination.
Wang *et al.* (2018*b*),	SM-LACO-OFDM	GenSM technology combined with LACO-OFDM.
Mao *et al.* (2017), Rajesh Kumar and Jeyachitra (2017), Yesilkaya *et al.* (2017)	LED Index Modulation	Generalized LED Index Modulation for OFDM-based VLC systems.

2.2.3.2 Wavelet Packet Division Multiplexing (WPDM)

WPDM (Wong *et al.* 1997) transmits multiple signals which are encoded into a waveform using wavelet packet basis functions. It provides channel capacity improvement compared to Frequency Division Multiplexing (FDM) and Time Division Multiplexing (TDM) as it allows time and frequency overlapped signals. Also, it maintains orthogonality of the resultant wave, which can be separated by using correlator at receiver. However, clipping distortion is observed (Huang *et al.* 2014).

2.2.3.3 DHT

DHT is one of the Fourier related transforms, which is Discrete version of Hartley Transform. It produces real-valued output for real-valued input, unlike FFT. By applying this transform, a multicarrier IM/DD system was proposed (Moreolo *et al.* 2010). To achieve unipolar output, asymmetrical clipping and DC-biasing can be applied. As it does not require Hermitian symmetry to be satisfied, it is computationally less intensive and improves SE compared to ACO-OFDM. However, since it accepts only real-valued input like multilevel-PAM, the SE is lower than DCO-OFDM.

2.2.3.4 Spatial Modulation

In traditional SM (Jeganathan *et al.* 2008) only one light fixture will be transmitting symbols using any underlying modulation scheme at a given instance, while others will provide regular illumination. The selection of fixture for transmission would be based on the symbol to be transmitted. At the receiver, side depending on the direction and received data, the symbol will be decoded. In the Spatially Modulated version of LACO-OFDM (Wang *et al.* 2018*b*) generalized spatial modulation (GenSM) technology is combined with LACO-OFDM. In Yesilkaya *et al.* (2017), Mao *et al.* (2017) and Rajesh Kumar and Jeyachitra (2017) a generalized LED Index Modulation for OFDM-based VLC systems is discussed with focus on minimizing losses incurred due to time and frequency shaping of OFDM. It integrates location information of single or group (constellation) of LEDs along with spatial modulation to transmit data to single or multiple users.

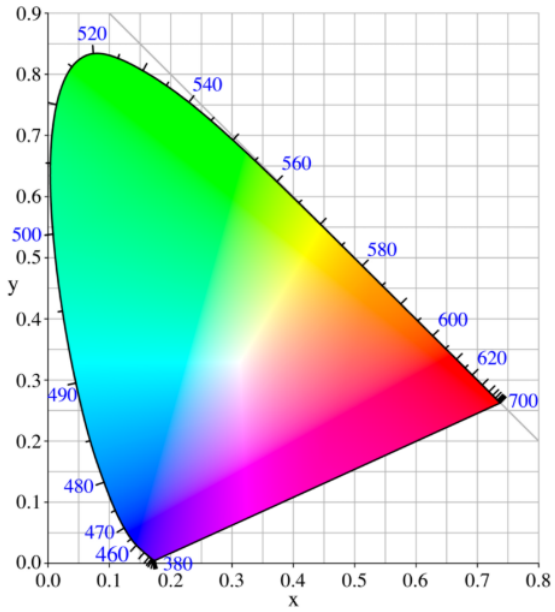

Figure 2.10: International Commission on Illumination CIE 1931 (Wikipedia 2018*a*)

2.2.4 Color Domain Modulation

Color is one of the unique characteristics of the light which can be exploited for achieving extra dimension while bit encoding, thus, making color domain modulation techniques specific to OWC. This section highlights a class of modulation techniques based on chromatic characteristics of LED. Table. 2.6 highlights the literature survey in color domain modulation.

2.2.4.1 Color Shift Keying

In Li-Fi modulation frequency does not represent carrier frequency, since carrier frequency is dependent on the LED. All previously mentioned modulation methods were baseband, which makes it difficult to modulate the carrier frequency of LEDs. However, the limitation of baseband communication can be overcome by using the color property of light. In figure 2.10, x and y-axis determine chromaticity of the color. Chromaticity is an objective specification of the quality of a color regardless of its luminance. Multiple combinations of colors can be used to keep the overall intensity of output color constant.

Table 2.6: Literature Survey of Color Domain Modulation

Paper	Methodology	Related Parameters
Monteiro and Hranilovic (2014)	Color Shift Keying: LEDs transmit data using different colors. Chromatic filters detect color on the receiver side.	Symbol mapping optimization for maximum distance between symbols and minimum inter-symbol interference
Singh *et al.* (2014) Liang *et al.* (2017)	Symbol mapping optimization for maximum distance between symbols and minimum inter-symbol interference	Use of quad-LED for simple symbol mapping with quadrilateral constellation shape
Okumura *et al.* (2018)	PWM-based modulation for brightness control without changing color	Reduced brightness without changing color
Ahn and Kwon (2012)	Color Intensity Modulation: Intensity of the color used as a modulating parameter	Dimming for efficient illumination
Chen *et al.* (2018)	Combination of Color Shift Keying and Non-Zero Level-PAM	Power efficiency with freedom of varied brightness
Bian *et al.* (2019)	Experimental evaluation of a Li-Fi system with 15.73 Gb/s data rate and 16.m distance	Use of WDM for higher spectral efficiency
Atta and Bermak (2018)	Modulation using the polarization of light	Dimming support and low data rate support without flickering
Liu *et al.* (2022)	Optical Camera Communication (OCC) system using image sensor and lens	- Communication range up to a kilometer in outdoor environments
Matus *et al.* (2021)	OCC for image capturing increases the communication range in outdoor environments	Use of image processing, long sampling duration, and lenses

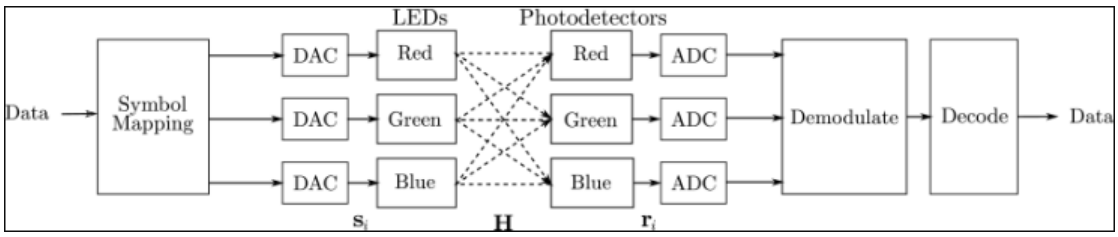

Figure 2.11: General block diagram for CSK modulation in Li-Fi (Monteiro and Hranilovic 2014)

As shown in figure 2.11, each color LED transmits the data, and it is controlled independently depending on the symbol to be transmitted. On the receiver side, chromatic filters are used before photodiode to detect color, and the respective signal is demodulated to set of bits (Monteiro and Hranilovic 2014). However, deciding the constellation for the symbol to be transmitted requires optimization in which the distance between symbols should be maximum with minimum inter-symbol interference. This problem was discussed in Singh *et al.* (2014) and Liang *et al.* (2017), possible solution in terms of use of quad-LED was proposed, which allows simple symbol mapping due to quadrilateral constellation shape. Also, in order to remove the limitation imposed by amplitude dimming, (Okumura *et al.* 2018) proposed PWM based modulation, which ensures reduced brightness without a change in color.

2.2.4.2 Color Intensity Modulation (CIM)

In another color-based Modulation intensity of the color is used as a modulating parameter. CIM (Ahn and Kwon 2012) was proposed to overcome the complexity of CSK to achieve dimming for efficient illumination. A hybrid of CSK and CIM called Color Intensity Shift Keying (CISK) (Chen *et al.* 2018) was proposed which uses CSK and Non-Zero Level-PAM to achieve power efficiency with freedom of varied brightness. By maintaining a constant average transmit power, it relaxes the requirement of constant power constraint for CSK which fulfills the illumination requirement of non-flickering.

However, due to the cost and complexity involved in Color Domain Modulation concerning the separation of the colors, there is a lack of specific design standards for receivers compared to OFDM. Hence, this area still has sufficient scope for designing efficient modulation techniques, which are computationally less intensive.

In Bian *et al.* (2019), an experimental evaluation of a Li-Fi system with a 15.73

Gb/s data rate and 16.m distance was performed. Four low-cost monochromatic LEDs were selected to modulate four wavelengths in the visible light spectrum. WDM was used for higher spectral efficiency in addition to OFDM with adaptive bit loading to provide a higher data rate.

Apart from the modulation techniques discussed in this section, many other techniques are always under modification. Out of these techniques, one using the polarization of light as modulation was also proposed in Atta and Bermak (2018). This method provides dimming support and low data rate support without flickering as it uses the polarity of light for modulation.

2.2.5 Optical Camera Communication Modulation

VLC system using IS is known according to the standard as OCC which does not require any hardware changes. A MIMO can be realized by using a IS with a large array of micro-scale photodiodes in combination with a lens. Additionally, a camera-based Rx can capture information not only from multiple Txs but also from digital displays such as liquid crystal display (LCD) and organic LED screens (Liu *et al.* 2022).

Furthermore, an OCC image capturing increases the communication range in outdoor environments up to a kilometer, due to the use of image processing, long sampling duration, and lenses (Matus *et al.* 2021). Nevertheless, most OCC schemes reported in the literature are intended for indoor applications because of smart-devices availability and a lower intensity of ambient light in indoor environments.

With regard to the OCC, it is important to note that OCC-based systems are mainly targeted for a low-rate transmission, due to the reception-sampling rate, which is determined by the camera frame rate, which is typically in the range of 30 to 60 frames per second (fps) at a common resolution of 1920×1080 pixels. However, with current advances made in cameras, for the same resolution, the frame rate of new smartphone cameras can reach up to 960 fps. Different from VLC that uses a photodiode to process the received optical intensity, OCC is based on capturing the source using the IS, i.e., a 2D Rx containing millions of pixels, and carrying out a significant amount of image processing to acquire the information. Therefore, the data transmission rate of OCC is mostly limited to either kilobits per second (Kbps) or megabits per second (Mbps) in contrast to multi-gigabit per second (Gbps) transmission rates in Photodiode (PD)-based VLC systems.

Table 2.7: Literature survey for Optical Camera Communication and MIMO

Paper	Methodology	Related Parameters
Liu *et al.* (2022)	Optical Camera Communication (OCC) system	Communication range up to a kilometer in outdoor environments
Matus *et al.* (2021)	OCC for image capturing	Use of image processing, long sampling duration, and lenses
Wang *et al.* (2017)	Multiple photodiodes for spatial diversity	Improved spatial diversity due to NLoS channels
Cespedes and Armada (2018)	Optical adaptive precoding (OAP) scheme	Enhanced SNR and symbol interference (S/I)
Fath and Haas (2013)	MIMO techniques in Li-Fi	Spectral efficiency (SE)

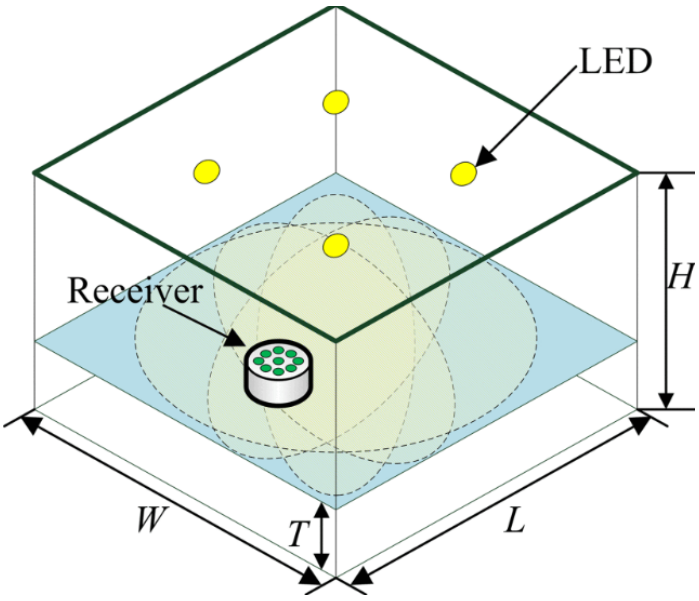

Figure 2.12: Multiple Photo-diodes for Spatial Diversity to achieve MIMO (Wang *et al.* 2017)

2.3 MIMO

In order to efficiently utilize the available Visible Light spectrum multiple LEDs can be considered as multiple transmitters but due to limited spatial diversity, the interference would be high. To eliminate this interference suitable MIMO receiver designs can be considered. The design of such MIMO receiver is a challenge and issues of the same are discussed in the following section.

2.3.1 MIMO Receiver Design

MIMO receivers can be of two types depending on what component is used at the receiver, i.e., the Photodiode or image sensor. The performance of the receiver varies based on the type of sensor and modulation technique used. Photodiode provides narrow Field-of-View (FoV) thus providing high gain but requires constraint alignment and performance degrades drastically with small misalignment. On the other hand, the image sensor uses an array of photodiodes and has large FoV which relaxes the alignment requirement. It uses a phenomenon called the rolling shutter effect to achieve a high data rate. But, individual photodiodes have low gain and complex image processing needed at the receiver, hence, they cannot be used for resource-constraint devices. A hybrid of the image sensors and photodiodes was proposed in Zeng *et al.* (2009) which had advantages of both techniques.

In Wang *et al.* (2017), a design was proposed as shown in figure 2.12 which spherically mounted photodiodes, which had improved spatial diversity due to NLoS channels but at the cost of additional hardware. For efficient utilization of spatial diversity not only the design of a suitable receiver but also sufficient precoding at the transmitter is also required. This aspect was studied in Cespedes and Armada (2018), where the proposed optical adaptive precoding scheme exploits the information of transmitted symbols to enhance the effective SNR and symbol interference (S/I).

2.3.2 Li-Fi MIMO Techniques

This subsection highlights MIMO techniques that are exploited in Li-Fi (Fath and Haas 2013).

- Repetition Code (RC): In this technique, the same signal is transmitted over all transmitters. This provides increased gain as the signals from all transmitters are reconstructed at the receiver. However, this technique provides flexibility for transmitter-receiver alignment but provides restricted spectral efficiency.

- Spatial Multiplexing (SMP): On the contrary to RC in SMP, each transmitter sends different data which acts like multiple parallel Single Input Single Output (SISO). This increases spectral efficiency but compared to RC SMP requires tighter alignment of transmitter-receiver to avoid interference however it still provides better data rates compared to RC.

- SM: In this type of MIMO technique spatial dimension is used for transmitting data as only one transmitter transmits data at any arbitrary time. Each transmitter is activated based on the assigned symbols. Based on the received signal, an estimation of which LED was activated is done which is used to reconstruct the respective symbol at the receiver. Thus it achieves higher SE compared to RC and SMP.

It was observed that the image sensor provides better SNR compared to photodiodes for SM or SMP due to its inherent feature of wider FoV and relaxed alignment (Fath and Haas 2013).

2.4 Cell Design and Deployment

In Feng *et al.* (2018), effects of inter-cell interference based on Li-Fi access point arrangements have been discussed. As the modulation techniques used show drastic degradation in the quality of signal for edge users, it is important to address the issue of inter-cell interference. Thus, a device that does not receive sufficient light due to room arrangement may experience a low data rate compared to the device which is aligned to the transmitter. In order to avoid this, several strategies are proposed like partitioned clusters (Jung *et al.* 2016), dynamic resource allocation based on uplink (Kashef *et al.* 2015), Joint Transmission (Chen *et al.* 2013) using delayed transmission and reconstruction. However, it is important to design better interference avoidance techniques to ensure high data rate communication under close deployment of receivers as the coverage of normal VLC cells is small. Table. 2.8 highlights the literature survey on cell design, deployment and handover.

2.5 Handover in VLC

An important advantage of wireless communication is freedom of movement. However, in order to serve communication for devices under motion, the connected device should be able to transfer data sessions from one access point to another. This process of switching an access point while ensuring device connectivity is called handover. In this section, handover techniques for Li-Fi and related issues are discussed. This will provide insight into which parameters for handover should be considered. The following mentioned are a few parameters that are derived from RF handover and which can also be applied to Li-Fi cell-to-cell handover.

- **Receive Signal Strength (RSS):** RSS is the amount of power received by the receiver. In Li-Fi, signal strength is dependent on the received light intensity. Hence, the RSS for Li-Fi will not only change based on mobility but also device orientation. Using RSS value device and Li-Fi access point can undergo handover from one access point to another.

- **Signal-to-Interference Ratio:** The handover can also be initiated based on Signal-to-Interference Ratio. If the interference is high compared to the received signal, then handover from one Li-Fi access point to another is initiated.

Table 2.8: Literature survey on Cell Design, Deployment, and Handover

Paper	Methodology	Related Parameters
Feng *et al.* (2018)	Effects of inter-cell interference	- Interference avoidance techniques
Jung *et al.* (2016)	Partitioned clusters	- Cell partitioning
Kashef *et al.* (2015)	Dynamic resource allocation based on uplink	- Dynamic resource allocation
Chen *et al.* (2013)	Joint Transmission (JT)	- Delayed transmission and reconstruction
Soltani *et al.* (2017)	Handover technique in Li-Fi cells	- RSS (Received Signal Strength)
Han *et al.* (2015)	Vertical handover	- Connectivity type (Li-Fi to Wi-Fi or vice versa)
Wang and Haas (2015)	Dynamic load balancing	- Load balancing between RF-based and Li-Fi-based connectivity
Wang *et al.* (2016)	Fuzzy logic for handover prediction	- Mobility prediction and handover decision-making using fuzzy logic

- **Speed of Mobile Node (MN):** Handover occurs due to the mobility of the device. The handover can be initiated by estimating future positions depending on the current speed and direction of mobility. The work in Soltani *et al.* (2017) provides insight into this problem. A mobile user can be provided with a dynamic quality of service when it is moving across heterogeneous networks.

In Soltani *et al.* (2017), a basic technique of handover in Li-Fi cells is proposed by considering the effects of device orientation and mobility. It calculates the probability of handover based on RSS by estimating it for simulated receiver movement and orientation. It uses a geometric model for receiver orientation and random way-point mode for receiver movement. However, this handover is studied for horizontal handover, i.e., Li-Fi cell to Li-Fi cell. Whereas, in vertical handover (Han *et al.* 2015) connectivity type is changed, i.e., Li-Fi to Wi-Fi or vice versa. It was observed that this technique requires additional overhead for adopting change in data frames. However, it provides more mobility and freedom of orientation compared to horizontal handover. In Dynamic load balancing (Wang and Haas 2015), a solution is proposed for better utilization of bandwidth by providing RF-based connectivity for mobile devices and Li-Fi based connectivity for almost stationary devices. An improvement over the same was proposed by using fuzzy logic for determining mobility and predicting handover with dynamic load balancing (Wang *et al.* 2016), which reduces handover overhead.

2.6 Outcome of Literature Survey

Following are the open areas for research based on the conducted study:

- **Efficient Design of Transmitters and Modulation Techniques**: As light is the fastest mode of communication, the speed of communication is only limited by the processing speed of Transmitters and Receivers. However, by tapping into different properties of light such as color, polarity, and direction of transmission, a faster and more efficient Li-Fi/VLC communication system can be achieved. The design of such a system of coordinated transmitters and the implementation of a suitable modulation scheme that could exploit these properties to enable faster and more robust communication is active research in this area.

- **Receiver Designs to Enable MIMO and Mobility**: Receivers such as cameras or Multi-directional Photo-diodes with wider FoV have been observed to provide better support for MIMO and Device Mobility. However, the issues of inter-cell interference and active noise are prevalent are such systems. Different spatial modulation techniques and 3-dimensional localization and positioning techniques have been observed to improve the performance of Li-Fi/VLC system concerning device mobility. Hence, there is a need of designing hybrid sensors which could leverage the benefits of cameras and photodiodes to develop faster, MIMO enabled and mobility-supported receivers.

- **Modulation and Receiver Design Dependent Transmitter Deployment Strategies**: The performance of various Li-Fi/VLC modulation techniques and receiver designs concerning transmitter deployment patterns have not been studied extensively. Thus providing an opportunity to explore communication performance concerning various modulation schemes and receiver designs to come up with a unified model for enhancing the overall performance.

- **Robust Load Balancing Techniques to Handle Effects of Handover** With respect to the practical deployment of Li-Fi/VLC enabled devices, it is important to understand the nature of change in network traffic and flow control when the user shifts between different networks. User mobility modeling and network load balancing is current active research in the field of handover in Li-Fi.

2.7 Summary

In this chapter, we presented the existing state-of-the-art techniques to achieve visible light communication. Further, various issues and challenges pertaining to the implementation and adoption of VLC were highlighted, specially with respect to transmitter and receiver design, modulation techniques, channel properties, MIMO, and illumination requirements. The chapter majorly highlights types of modulation techniques, such as, single carrier modulation, multicarrier modulation, and color domain modulation. The challenges and issues mentioned in this chapter will be addressed in the coming chapters. The next chapter highlights the proposed work to mitigate a challenge of lack cost efficient easy-to implement VLC testbed.

Chapter 3

Proposed Photodiode-based VLC Prototype and Simulation

In recent years, VLC/Li-Fi has garnered tremendous attention from research communities across the world. The major reason is the increased number of network-connected devices due to the emergence of IoT. Although VLC could serve as an effective complementary technology to Wi-Fi, there is a need to have accessible easy to setup low-cost VLC testbeds. Fundamental theoretical analysis of an indoor VLC system has been provided in (Komine and Nakagawa 2004), proving its feasibility. However, to build a practical communication system in conjunction with lighting, many system design issues need to be addressed, including three basic communication parts: transmitter, channel, and receiver. Thus, to implement and evaluate real-world scenarios of VLC products, extended experimental testing over testbeds is needed. This has resulted in the increasing interest of researchers in building test beds in their respective areas of research.

However, as compared to traditional radio and microwave-based wireless communication techniques, VLC has significant challenges. A few such major challenges are;

- Free space noise elimination
- Limited scope of using light features for modulation techniques
- Psycho-physical limitations (sensitivity towards flickering) of the human eye

Considering these challenges, several modulation techniques have been proposed, and continuous work is in progress to improve these modulation techniques concerning bandwidth, error rate, operational distance, spectral efficiency, and

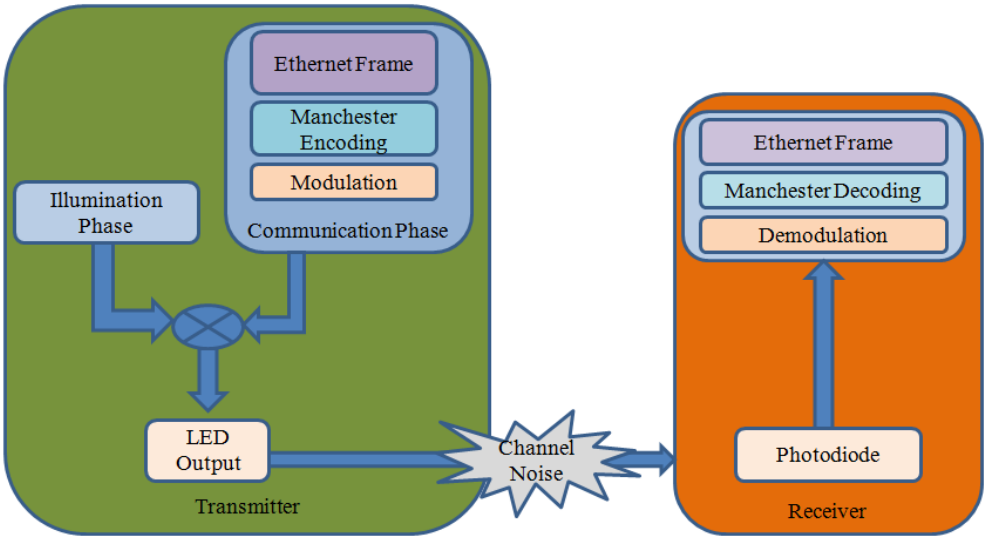

Figure 3.1: VLC Transmitter and Receiver

spatial efficiency (Oyewobi *et al.* 2022; Almadani *et al.* 2020). This chapter highlights, the design and implementation of a low-cost experimental VLC testbed and builds a system to support multimedia data transfer using the proposed testbed. The proposed testbed is evaluated based on the performance of existing OOK and Pulse Duration Modulation (PDM) modulation techniques under a controlled environment. The results of the testbed performance are then compared with the standard implementation of VLC channel simulation using Matlab. The novelty of the work is with respect to building a cost-efficient VLC testbed for performing preliminary tests on various modulation techniques. The testbed would provide practical insight into the effects of channel path loss on the performance of VLC based communication system. It would also provide a basic understanding of parameters affecting VLC performance.

A standard VLC system will consist of two modules, namely as VLC transmitter module and VLC receiver module. Figure 3.1 shows a block diagram for each module. Transmitter will operate in two alternating phases, i.e., the illumination phase and the communication phase. In the illumination phase, a steady light intensity will be maintained, while in the communication phase data will be transmitted. The overall perceivable light intensity during both phases needs to be constant to avoid visible flickering. Hence, a steady stream of alternating 0s and 1s will be sent during the illumination phase and Manchester-encoded data will be sent in the communication phase. Manchester encoding is selected to guarantee a balanced distribution of power cycles as well as to aid bit recovery.

The data to be transmitted will be encapsulated in an Ethernet frame format

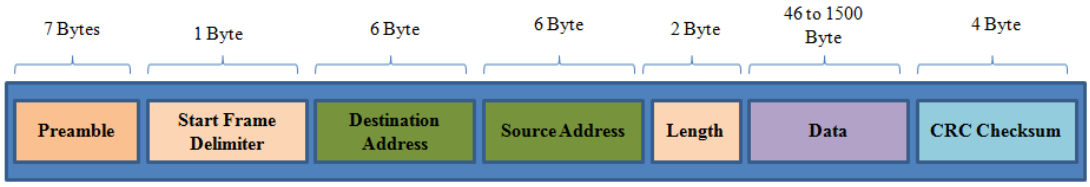

Figure 3.2: Ethernet Frame Format

as shown in figure 3.2. The ethernet frame format is selected as it is one of the simplest and most basic frame structures which is compatible with other wireless frame formats. Each bit is Manchester encoded and passed to the modulation layer as shown in figure 3.1 where depending upon the selected modulation scheme the LED light will be controlled. For the experimental evaluation of the proposed VLC test bed, OOK and PDM modulation techniques will be implemented due to similar computational requirements. Finally, by varying the parameters such as distance, angle, power, and data rates performance of each modulation scheme is evaluated based on the success of reception/accuracy. Where accuracy is the percentage of correctly received bits for thousand consecutive bits from a fixed ethernet packet and payload. Finally, the proposed system will be compared with other existing VLC testbeds (Baeza *et al.* 2015; Greives and Kulhandjian 2020) with respect to building cost.

The proposed testbed is then used for building a proposed image transmission framework to showcase multimedia data transfer over VLC. The proposed image transmission system is evaluated based on its capability of reconstructing the image at the receiver side. A custom payload is designed and a sample black and white image is used for experimentation. The performance of the proposed system is evaluated based on the size of the image, bit rate, transmission time, and accuracy.

3.1 Related Work

In paper Li *et al.* (2012), a physical layer testbed is built to verify channel characteristics under visible light spectrum for indoor environment. It was observed that achievable data rate is inversely proportional to transmission bandwidth and path loss is directly proportional to beam-angle. In Cui *et al.* (2010), a systematic design and demonstration of LoS VLC was proposed, which discusses transmitter design with illumination and communication perspectives. It also provided an insight on theoretical model for channel path loss and received optical power along with

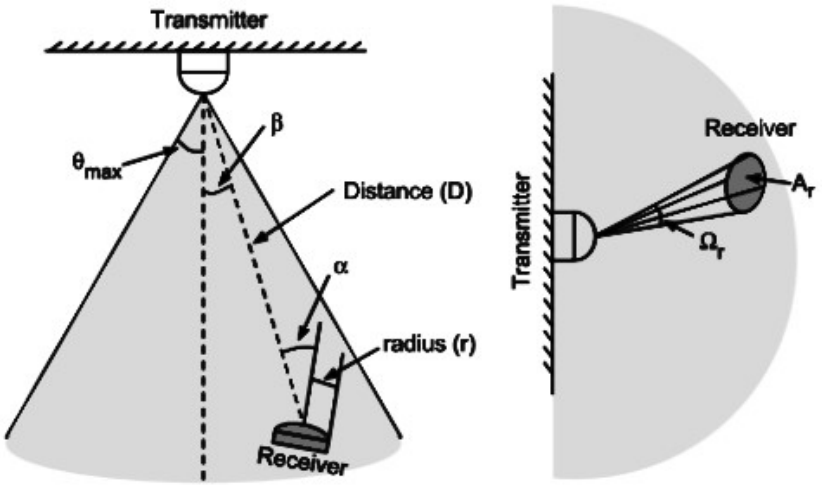

Figure 3.3: LOS Channel Model (Cui *et al.* 2010)

optimum receiver front-end design. A comparative analysis of simulations versus experimental demonstration showed validity of the theoretical model. Further, improvements were suggested in terms of adaptive thresholding and run length limiting codes for added robustness. The proposed synchronization technique discussed in paper Schmid *et al.* (2012) uses alternative cycles of illumination and communication phases. These alternative cycles can be used for obtaining light intensity threshold which is required for bit determination in an IM/DD based VLC systems. Shinwasusin *et al.* (2015) showed an analytical and simulated comparison between variation of OOK modulation and other modulations such as CSK, PWM, PPM and OFDM based on BER versus SNR. It was observed that in the simulated environment PPM provided highest data rate followed by OFDM and other modulation techniques. The design of our proposed test-bed and the evaluation metrics is inspired from these works with few major changes concerning required hardware to keep implementation cost minimum.

3.2 Proposed Work

For ease of understanding, the section is divided into three sub-sections namely, a) the channel model b) theoretical SNR measurement, and c) the proposed testbed. Table.3.1 shows the notations and semantics used for the explanation of the proposed work.

Table 3.1: Notations and semantics for the proposed work

Notation	**Semantics**
D	Distance between receiver and transmitter
r	Radius of receiver aperture
α	Angle formed by the line connecting centers of source and receiver with the receiver normal
β	Angle formed by the line connecting centers of source and receiver with the source normal
θ_{max}	LED beam maximum half angle
Ω_r	Receiver solid angle seen by the transmitter
A_r	Receiver area
I_0	Axial intensity with unit candela
$g_s(\theta)$	Normalized spatial distribution function specific to vendor
F_s	Total transmitted luminous flux
Ω_{max}	LED beam solid angle
F_r	Receiver's received luminous flux
L_L	Luminous path loss
m	Order of Lambertian emission
$\Phi_{1/2}$	Semi-angle at half illuminance of an LED
SNR	Signal-to-Noise Ratio
γ	Ratio of the received visible light power and ambient noise
$P_{rSignal}$	Received signal power
σ^2_{total}	Total noise variance
σ^2_{shot}	Shot noise variance
q	Electronic charge
B	Equivalent noise bandwidth
I_2	Noise bandwidth factor for rectangular transmitter pulse shape
$\sigma^2_{thermal}$	Thermal noise variance
T_A	Absolute temperature of the environment
G	Open-loop voltage gain
η	Fixed capacitance of photodetector per unit area
Γ	PET channel noise factor
g_m	PET transconductance
I_3	Noise bandwidth factor for full raised-cosine equalized pulse shape

3.2.1 Channel Model

A Matlab model is created as mentioned by Cui *et al.* (2010) in order to simulate the communication environment for the performance evaluation of LoS VLC system. Figure 3.3 shows a general VLC transmitter receiver scenario. Here, the distance between receiver and transmitter is D and r defines the radius of receiver aperture. The angle formed by the line connecting centers of source and receiver with the receiver normal is denoted as α and with the source normal is β. θ_{max} represents LED beam maximum half angle. Ω_r is the receiver solid angle seen by the transmitter and A_r is the receiver area. They satisfy the relation $A_r \cos\alpha \approx D2\Omega_r$.

If I_0 is the axial intensity with unit candela and $g_s(\theta)$ is the normalized spatial distribution function particular to vendor, then the spatial luminous intensity distribution of LED can be provided as product of axial intensity and spatial distribution $I_0.g_s(\theta)$ as shown in Eq.6.1.

$$F_s = \int_0^{\Omega_{\max}} I_0 g_s(\theta) d\Omega = I_0 \int_0^{\theta_{\max}} 2\pi g_s(\theta) \sin\theta d\theta \tag{3.1}$$

Luminous intensity is the power (adjusted for human eye perception called the luminosity function) of light in a unit solid angle and luminous flux is a measure of total amount of energy radiated per second from a light source in all directions. Hence, if F_s represents total transmitted luminous flux, then we have the relation as shown in Eq.6.1, where Ω_{max} is the LED beam solid angle, which is related to the θ_{max} as Ω_{max}=$2\pi.(1-\cos(\theta_{max}))$.

We denote the receiver's received luminous flux as F_r=$I_0 g_s(\beta).\Omega_r$. Thus we can express the luminous path loss as shown in Eq.3.3

$$L_L = \frac{F_r}{F_s} = \frac{I_0 g_s(\beta)\Omega_r}{I_0 \int_0^{\theta_{\max}} 2\pi g_s(\theta)\sin\theta d\theta} \tag{3.2}$$

$$\approx \frac{g_s(\beta) A_r \cos\alpha}{D^2 \int_0^{\theta_{\max}} 2\pi g_s(\theta)\sin\theta d\theta} \tag{3.3}$$

As mentioned earlier, many commercial lighting LEDs without any beam shaping component can be treated as Lambertian sources with spatial distribution function $g_s(\theta) = \cos^m(\theta)$, where m is the order of Lambertian emission and is related

to the semi-angle at half illuminance of an LED $\Phi_{1/2}$ as $m = -ln2/ln(cos\Phi_{1/2})$. If we substitute the above $g_s(\theta)$ into Eq. 3.3 and set $\theta_{max} = \pi/2$, we can simplify the integration and obtain the LOS path loss for the Lambertian source as shown in Eq.3.4:

$$L_L \approx \frac{(m+1)A_r}{2\pi D^2} \cos\alpha \cos^m(\beta) \tag{3.4}$$

3.2.2 Theoretical SNR

A Matlab simulation will be built using existing equations for theoretical evaluation of SNR based on channel characteristics, room dimension and receiver design (Seok-Ju Lee and Sung-Yoon Jung 2012). SNR is considered as measure to evaluate VLC signal quality. SNR can be expressed as the ratio of the received visible light power and ambient noise as shown in Eq.3.5:

$$SNR = \frac{\gamma^2 P_{rSignal}^2}{\sigma_{total}^2} \tag{3.5}$$

where the desired signal power $P_{rSignal}$ is as per Eq.3.6:

$$P_{rSignal} = \text{Received signal power of Light Tools} \tag{3.6}$$

In case of noise, the total noise variance becomes

$$\sigma_{total}^2 = \sigma_{shot}^2 + \sigma_{thermal}^2 \tag{3.7}$$

where σ_{shot}^2 is the shot noise variance expressed by Eq.3.8,

$$\sigma_{shot}^2 = 2q\gamma P_{rSignal} B + 2q\gamma P_{bg} I_2 B \tag{3.8}$$

Here q is the electronic charge, B is the equivalent noise bandwidth, and I_2 is the noise bandwidth factor that accounts for a rectangular transmitter pulse shape.

Eq.3.9 shows thermal noise variance $\sigma_{thermal}^2$ which is given as folows:

$$\sigma_{thermal}^2 = \frac{8\pi k T_A}{G} \eta A I_2 B^2 + \frac{16\pi^2 k T_A \Gamma}{g_m} \eta^2 A^2 I_3 B^3 \tag{3.9}$$

where T_A is the absolute temperature of the environment, G is the open-loop voltage gain, η is the fixed capacitance of photodetector per unit area, Γ is the positron emission tomography (PET) channel noise factor, g_m is the PET transconductance, and I_3 is the noise bandwidth factor that accounts for a full raised-cosine

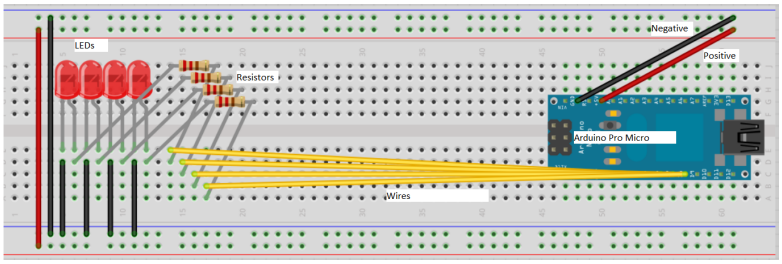

Figure 3.4: Circuit Diagram of VLC Transmitter

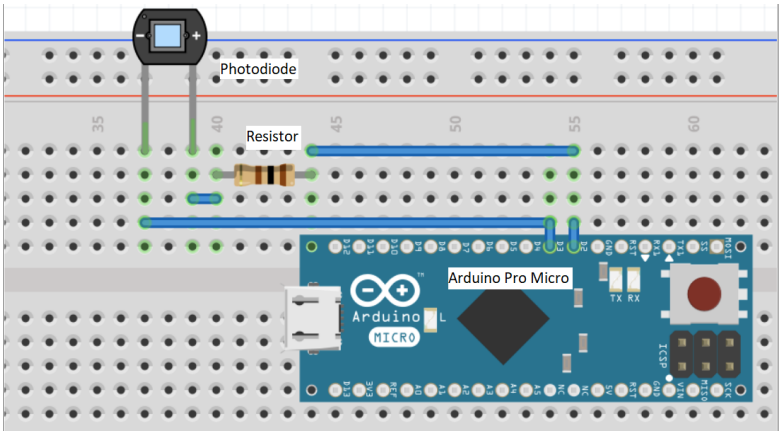

Figure 3.5: Circuit Diagram of VLC Receiver

equalized pulse shape.

3.2.3 Design of Proposed Testbed

The proposed testbed design comprises of a VLC-Tx and a VLC-Rx. The circuit diagram of VLC-Tx is as shown in Figure 3.4 where, 4 LEDs are connected to a open source programmable board Arduino micro. Resistors are connected in between the programmed pins of Arduino and LEDs to avoid damaging LEDs due over current. The 'on-off' cycles of LEDs will be controlled by programming the Arduino board.

The VLC-Rx consists of a photodiode and an Arduino micro, as shown in Figure 3.5. The board will be programmed to read the changes in the voltage values at the input pin connected to photodiode. Figure 3.6 shows the implemented VLC testbed. Figure 3.6a, shows VLC transmitter which uses for surface-mounted device (SMD) LEDs connected to Arduino micro. The entire assembly is housed inside a Poly-Vinyl-Chloride (PVC) pipe extension joint of radius 2.5cm. The transmitter module is built in the shape of lamp using PVC pipes to enable freedom for varying height.

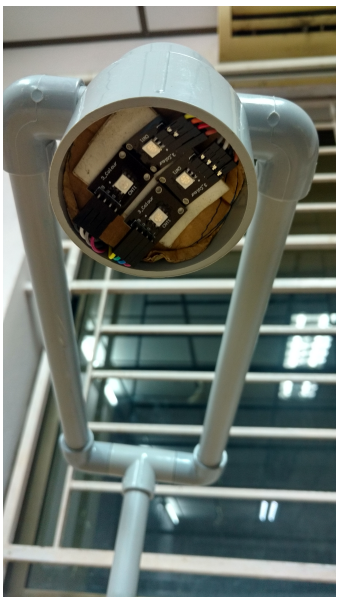

(a) Transmitter Module

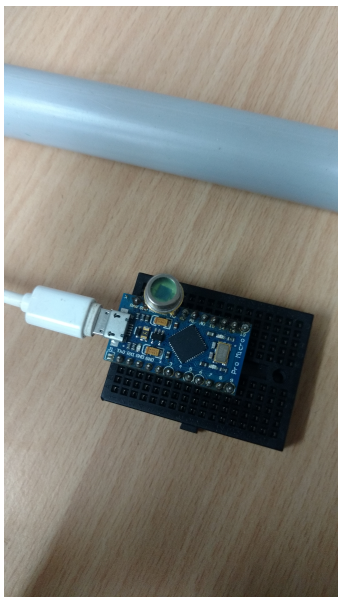

(b) Receiver Module

(c) Proposed Testbed

Figure 3.6: Implementation of proposed VLC Transmitter and Receiver

Figure 3.6b shows VLC receiver module, which has a photodiode connected to arduino. The proposed algorithms were implemented using Arduino integrated development environment (IDE). Two Arduino micros with 16 MHz clock frequency are used for implementation of transmitter and receiver. 4 SMD LEDs of 0.2W are used to provide sufficient light intensity for the experiment. These LEDs are low-cost and are operational between 3.6-6.2 v, tolerable current 60 mA, which provides luminous intensity of 250 lux. The BH1750 light intensity sensor is used to obtain intensity of light falling over sensor due to its FoV and sensitivity. BH1750 has FoV of 70 degrees and the response time is better than any regular avalanche photodiodes. PVC pipes based structure is built with freedom of variation in height for the testbed. The ambient light intensity was 135 lux while the modulation techniques were tested and, the light intensity of the 4 LEDs combine was observed to be 600 lux. Thus, the external ambient noise is minimum for the distance of 20cm between transmitter and receiver. Figure 3.6c shows the overall setup including transmitter and receiver.

3.2.4 Implementation of VLC Algorithms

This section highlights implementation of generic VLC transmitter, followed by implementation of transmitter and receiver OOK and PDM modulation. Both modulation schemes work in two phases namely as illumination phase and commu-

nication phase. Here, under illumination phase, the transmitter transmits steady set of bits which does not carry any data and it is used to maintain constant illumination and to aid threshold calibration. Whereas, during communication phase, a data is transmitted in pre-coded format as per IEEE 802.1.

3.2.4.1 Implementation of Generic VLC Transmitter

Algorithm 1 Generic VLC Transmitter(Part A)

```
1: function SETUP
2:     Set pin mode to output for all the LED connected Pins
3:     Set message
4: end function

5: function LOOP
6:     for i=0 to Count1 do
7:         if 0 <= i < Count1 then
8:             ILLUMINATION_PHASE
9:         else if Count1 <= i < Count2 then
10:            COMMUNICATION_PHASE
11:        else if i = Count2 then
12:            i = 0
13:        end if
14:    end for
15: end function
```

Algorithm 1 Generic VLC-Tx (Part A), consists of *Setup* function to initialize variables and connected pins of LEDs and *Loop* function for continuous and repeated process of switching between illumination and communication phases. It is also having user defined functions *Illumination_Phase* and *Communication_Phase* which are called within *Loop*. To enable switching between these two phases an incremental counter is used. Here *Count*1 and *Count*2 is used to compare current count for calling illumination or communication phase.

Algorithm 2 Generic VLC-Tx (Part B) shows implementation of *Illumination_Phase* and *Communication_Phase* function. *Illumination_Phase* is used to maintain steady illumination by sending a continuous bit stream of 1 for 1 byte. The received data is sent to the *Send* function under the *Communication_Phase* function.

3.2.4.2 Implementation of OOK Modulation

In this section, the implementation of OOK transmitter and receiver is discussed. The *Send* function under the communication phase of the generic transmitter is

Algorithm 2 Generic VLC Transmitter(Part B)

```
1: function ILLUMINATION_PHASE
2:     for i=0 to 7 do
3:         SEND(1)
4:     end for
5: end function
6: function COMMUNICATION_PHASE(b)
7:     SEND(Start Bit Pattern)
8:     for each byte in message do
9:         for each bit in the byte do
10:            SEND(bit)
11:        end for
12:    end for
13: end function
```

highlighted. Figure 3.7a shows a pulse shape of an OOK modulated signal.

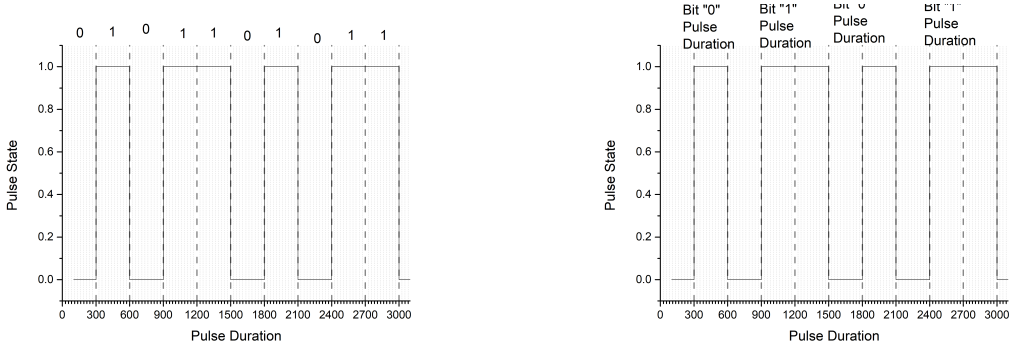

(a) OOK Modulation (b) PDM Modulation

Figure 3.7: Comparison of OOK and PDM Modulation

Algorithm 3, performs Manchester encoding and performs OOK modulation by turning LED on or off depending upon the bit value. Thus, for example, a bit stream of 1,1,1,0,0 will be converted to 0,1,0,1,0,1,1,0,1,0, Manchester code. Here, 1 is represented as 0,1 and 0 is represented as 1,0. These logical bits are mapped with LED on and off states. Figure 3.7a shows graphical representation of OOK modulated pulses. Thus, for logic 0 LED will be off and logic 1 LED will be on. It provides a steady distribution of the power cycle without any DC bias and flickering.

At the receiver side, as shown in Algorithm 4 OOK receiver initially establishes a threshold for bit determination by sampling for fixed number of samples. This is achieved by calling *Get_Intensity_Threshold* function under *Setup*. *Get_Intensity_Threshold* returns the average intensity of light for a predefined

Algorithm 3 OOK Transmitter Send Function

```
1: function SEND(a)                          ▷ Manchester encoding and LED Control
2:     if a is 1 then
3:         LED_On                                                  ▷ Signifies '1'
4:         delay(x)
5:         LED_Off                                                 ▷ Signifies '0'
6:         delay(x)
7:     else if a is 0 then
8:         LED_Off                                                 ▷ Signifies '0'
9:         delay(x)
10:        LED_On                                                  ▷ Signifies '1'
11:        delay(x)
12:    end if
13: end function
```

Algorithm 4 OOK Receiver

```
1: function SETUP
2:     Set Threshold = GET_INTENSITY_THRESHOLDS
3: end function
4: function LOOP
5:     if Current_Intensity > Threshold then
6:         Print "1"
7:     else
8:         Print "0"
9:     end if
10: end function
11: function GET_INTENSITY_THRESHOLD
12:    Compute average of Light Intensities received by photodiode for fixed num-
       ber of iterations
13:    return Average Light Intensity
14: end function
```

number of samples. This process is performed after equal interval of time to re-calibrate light intensity threshold. Inside *Loop* function, *Current_Intensity* is compared with threshold to determine received bit. At the data link layer, these decoded bits are stored in a buffer for subsequent symbol decoding and message retrieval. Start sequence is identified by performing pattern matching on the buffer and the subsequent bytes are decoded based on respective positions.

3.2.4.3 Implementation of PDM

This section highlights the implementation of PDM *Send* function under communication phase of generic transmitter and discuss the implementation of PDM Receiver.

Figure 3.7b shows graphical representation of PDM modulated pulses. Algorithm 5 PDM Transmitter (Send), show implementation of *Send* Function. Here, the generic structure of transmitter remains the same as mentioned in previous section. It accepts bit value as the parameter from the serial connection and converts it into Manchester code. Each of these expanded bits are then represented by respective pulses which are obtained by varying the duration of 'on' cycles.

Algorithm 5 Pulse-Duration-Modulation(PDM) Transmitter(Send)

```
1: function SEND(a)                          ▷ Manchester encoding and LED Control
2:     if a is 0 then
3:         ONE
4:         ZERO
5:     else if a is 1 then
6:         ZERO
7:         ONE
8:     end if
9: end function
```

Algorithm 6 Pulse-Duration-Modulation(PDM) Transmitter(Zero)

```
1: function ZERO
2:     LED_On
3:     delay(x)
4:     LED_Off
5:     delay(x)
6: end function
```

Algorithm 6 shows implementation of function *Zero* used for sending pulse corresponding to bit "0". And, Algorithm 6 shows implementation of function *One* used for sending pulse corresponding to bit "1". Here, x is an arbitrary value in microseconds, thus to send bit value of "1" the LED will be on for $2x$ duration followed by off for x duration and to send "0" the LED will be on for x duration followed by off for x duration.

On the receiver side, as shown in Algorithm 8, PDM Receiver, identification of received bit involves two phases. First phase involves estimation of intensity

Algorithm 7 Pulse-Duration-Modulation(PDM) Transmitter(One)

```
1: function One
2:     LED_On
3:     delay(2x)
4:     LED_Off
5:     delay(x)
6: end function
```

Algorithm 8 Pulse Duration Modulation(PDM) Receiver

```
1: function Setup
2:     Set pin mode to input for Photodiode connected Pin
3:     Set I_Threshld=Get_Intensity_Thresholds
4:     Set D_Threshld=Get_Duration_Thresholds
5: end function
6: function Loop
7:     if Current_Intensity > I_Threshld and Flag == 0 then
8:         Start_Timer
9:         Set Flag = 1
10:    else if Current_Intensity < I_Threshld and Flag == 1 then
11:        Stop_Timer
12:        Find Duration of Pulse
13:        if Current_Duration >= D_Thrshld then
14:            Print "1"
15:        else if Current_Duration < D_Thrshld then
16:            Print "0"
17:        end if
18:        Add Current_Duration to Duration_Array
19:    end if
20:    Increment Counter for each iteration
21:    if Counter == ResetCounter then
22:        Set Counter = 0
23:        Set I_Thrshld=Get_Intensity_Thresholds
24:        Set D_Thrshld=Get_Duration_Thresholds
25:    end if
26: end function

27: function Get_Intensity_Threshold
28:    Compute average of Light Intensities received by photodiode for fixed number of iterations
29:    return Average Light Intensity
30: end function
31: function Get_Duration_Threshold
32:    Compute average of pulse durations from Duration_Array
33:    return Average Pulse Duration
34: end function
```

threshold to detect operational status of LED. And second phase involves, threshold estimation of pulse duration. Thus, by sampling, pulse duration estimation and comparison with threshold corresponding bit is decoded. A continuous incremental counter called *ResetCounter* is also maintained to re-calibrate the system for finding both the threshold values, i.e., light intensity threshold and pulse duration threshold.

3.3 Results and Discussion

This section provides a discussion on the results of experiments conducted using the simulator and proposed testbed for OOK and PDM.

3.3.1 Results of Simulation Experiments

The results of experiments conducted based on simulation of channel characteristics and its effect on error probability are used to evaluate channel quality based on SNR under different conditions such as,

- Different room dimensions
- Different LED Power
- Different transmitter Field-of-views

Figure 3.8, shows densely distributed SNR values for smaller space compared to Figure 3.9. However, the SNR decreases with an increase in the distance in both cases as the source follows Lambertian distribution.

Figure 3.10 and Figure 3.11, shows improvement in the SNR with increase in LED power. It was also observed that based on the transmitter FOV, the SNR drastically changes. With decrease in the FOV there was improvement in SNR.

This is due to the formation of the light beam which provides better signal quality. However, it reduces the coverage area. The effects of change in transmitter FoV over SNR is shown in Figure 3.12 and Figure 3.13.

Based on the simulated channel characteristics, the error probability for OOK modulation is evaluated. As shown in Figure 3.15 and Figure 3.14, it was observed that with the increase in power the error probability decreases and the rate of decrease in error probability is inversely proportional to the distance between transmitter and receiver. It was also observed that with an increase in the distance, the error probability increases but the rate of increase in error probability is

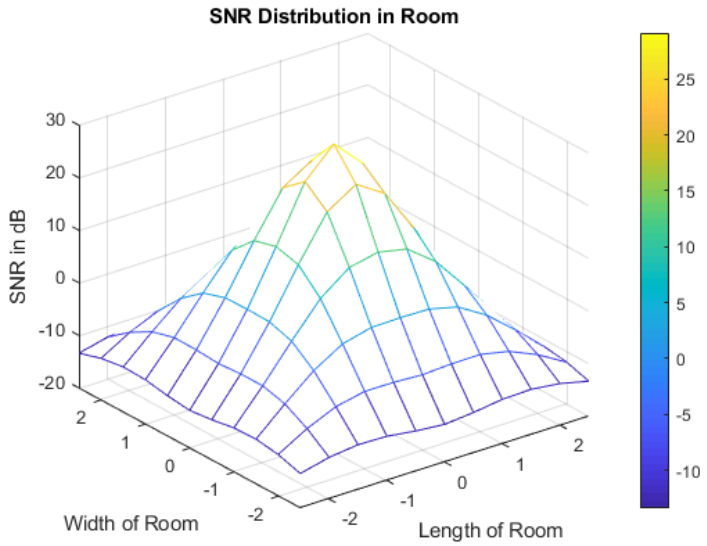

Figure 3.8: Room Width and Length 5m

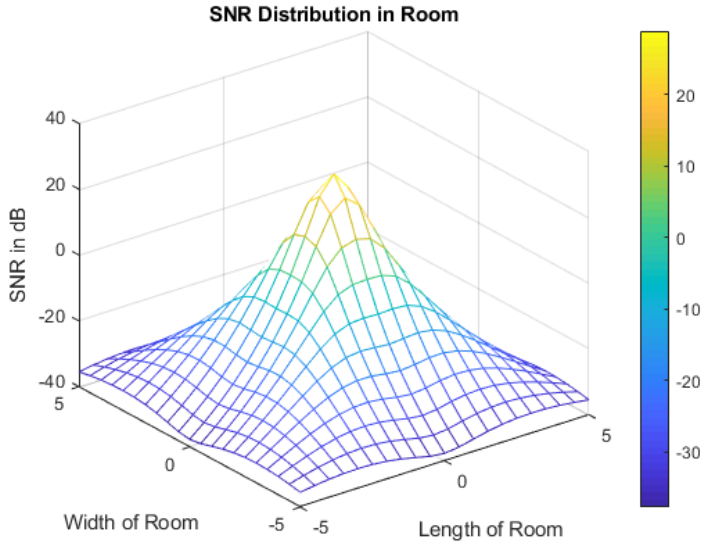

Figure 3.9: Room Width and Length 10m

inversely proportional to the power of LED. An outlier was observed at a distance of 0.1m and a power value of 15W, this is due to the sensitivity of the photodiode which fails to record any changes in the intensity as the high power source is very close to the receiver.

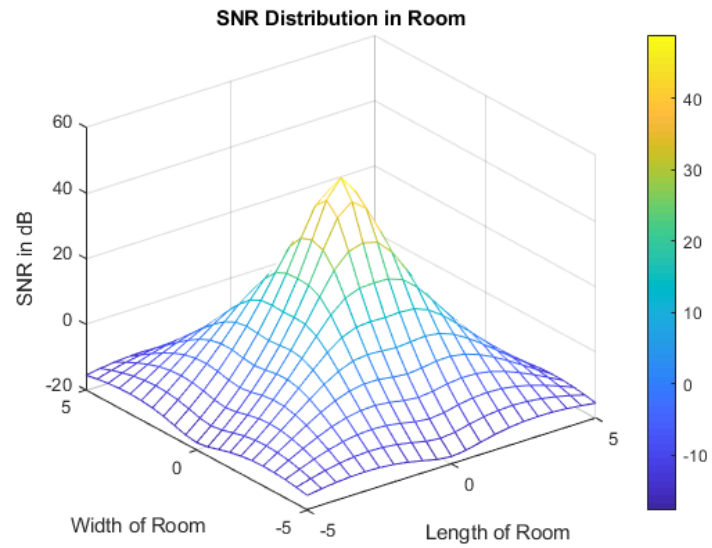

Figure 3.10: LED Power 10 Watts

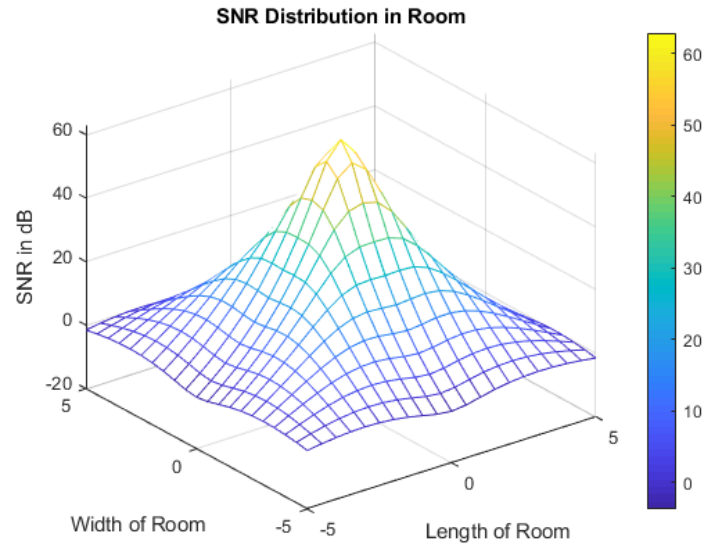

Figure 3.11: LED Power 50 Watts

3.3.2 Results of Testbed Experiments

The accuracy of each modulation technique is experimentally evaluated. Figure 3.16 shows accuracy for OOK and PDM. It was found that OOK gives maximum accuracy when the bit rate is low. However, even for a lower bit rate the accuracy observed was 57.6%.

On the other hand, PDM provided better accuracy, especially at lower bit rates. The accuracy keeps decreasing with the increase in bit-rate and distance

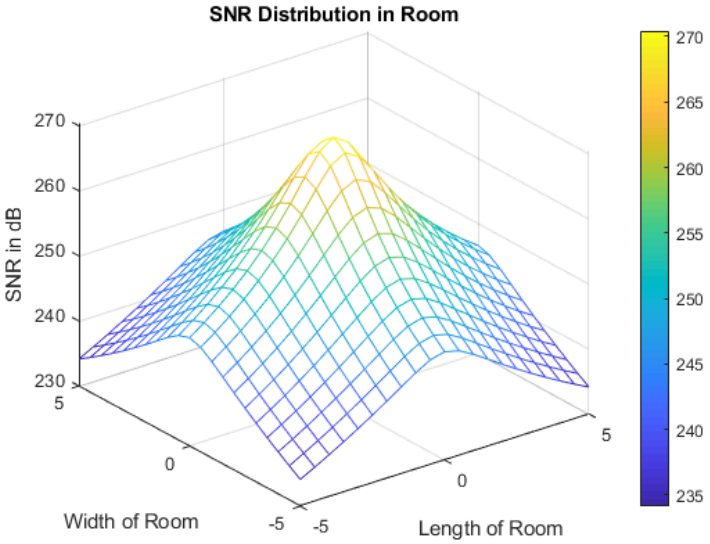

Figure 3.12: Transmitter FOV 20 Degrees

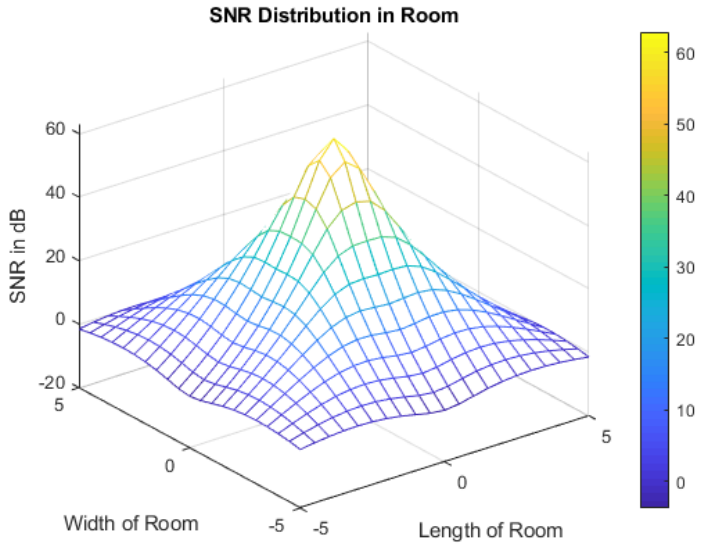

Figure 3.13: Transmitter FOV 70 Degrees

for both techniques.

The percentage improvement of PDM over OOK based on accuracy is shown in Figure 3.17. It was observed that PDM has provided many times more than 100% improvement over OOK based on accuracy. This is majorly due to two factors, firstly, OOK suffers synchronization drift due to which transmitter and receiver will be in synchronization for some time and slowly goes off-sync and again slowly comes back in sync. This happens repeatedly resulting in overall accuracy close to 50% even under the best conditions. However, PDM works in asynchronous

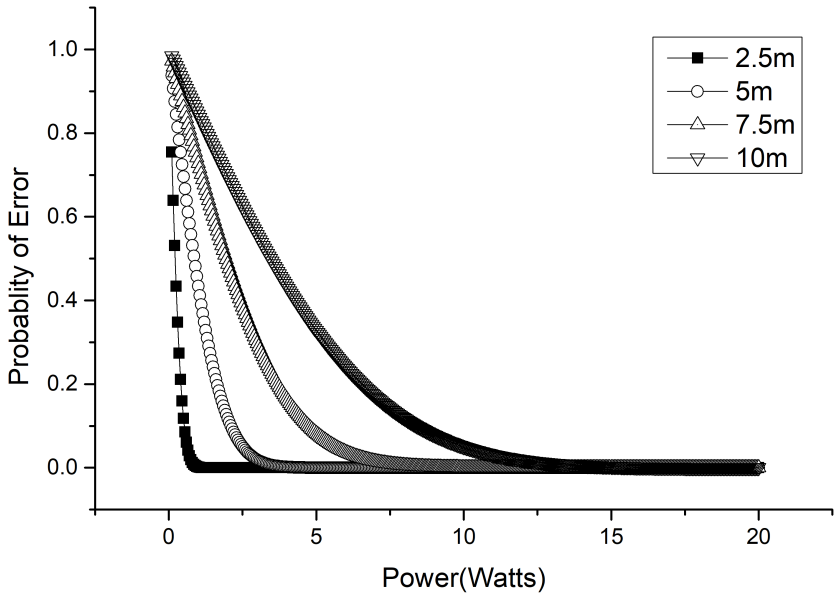

Figure 3.14: Distance vs Error Probability

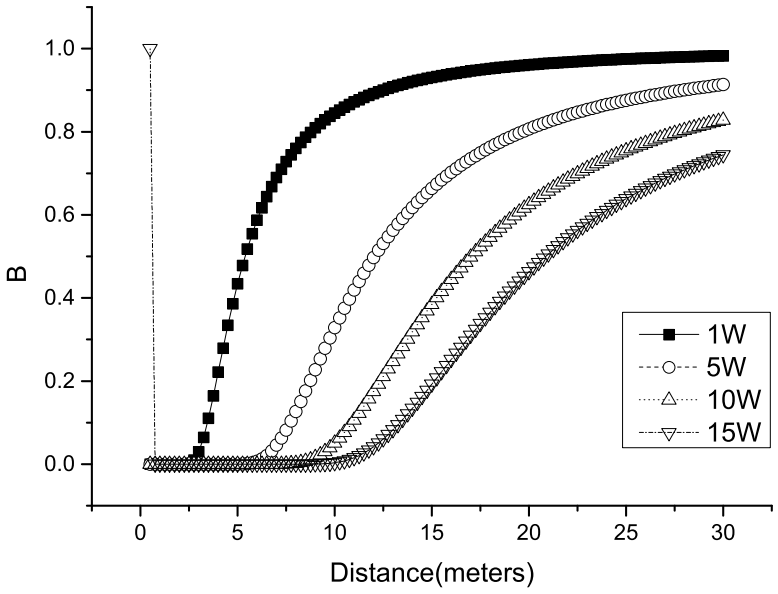

Figure 3.15: Power vs Error Probability

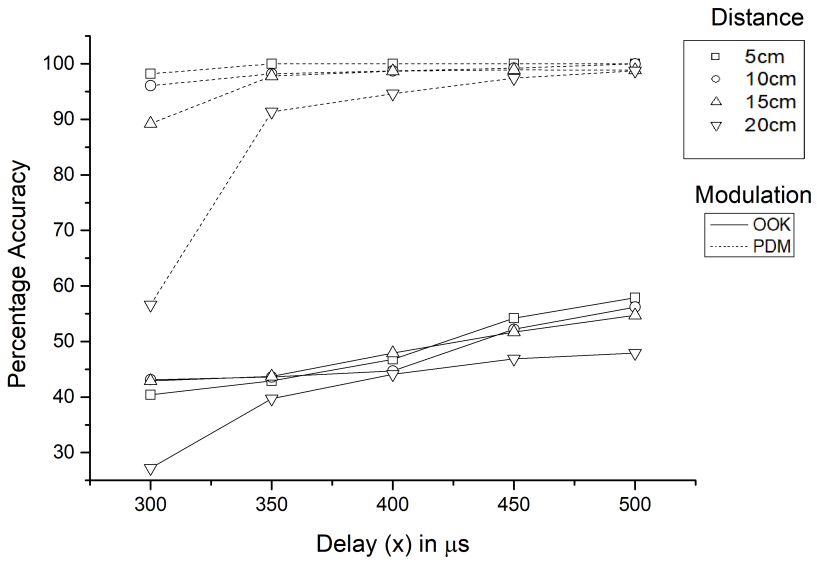

Figure 3.16: Performance Analysis of OOK and PDM Modulation

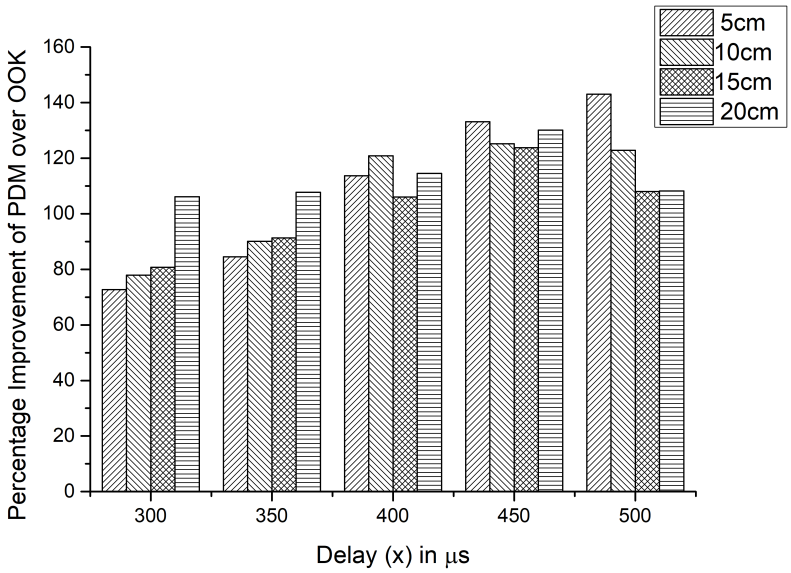

Figure 3.17: Percentage Improvement of PDM over OOK

mode, thus it provides better accuracy at the cost of reduced bandwidth. This is because the time required to transmit one-bit using PDM is more compared to using OOK. On average, three bits in OOK is equivalent to one bit in PDM thus, PDM is 3 times slower than OOK. The overall cost of implementation of the proposed VLC testbed was lower compared to testbeds showcased in (Baeza *et al.* 2015) due to the use of off-the-shelf readily available electronic components and structural elements. The trend of decline in the accuracy with the increase in distance in both the modulation techniques i.e., OOK and PDM is also similar to the observed trend using simulations. This is majorly due to the decrease in light intensity as the receiver moves away from the transmitter.

3.4 Proposed Image Transmission Technique using Low-Cost Photodiode-based VLC Testbed : An Application

This section proposes an application of image transmission based on the proposed testbed explained in Sec.3.3.2. The aim of the proposed system is to transmit a 'n x n' binary image using OOK modulation for VLC-testbed, reconstruct the image on the receiver side using custom frame format, and evaluate the accuracy of the reconstructed image across different distances.

RF technologies have facilitated communication including audio, images, video, and data transmission. However, the RF spectrum is becoming increasingly crowded, necessitating the exploration of alternative data transfer methods (Soh *et al.* 2018). Visible Light Communication (VLC) has emerged as a potential solution, leveraging optical-through-air transceiver systems for data transmission. Soh et al. implemented software-hardware co-design to achieve real-time audio transmission using VLC, verifying the system's performance through serial data and text transmission (Soh *et al.* 2018). Sandoval-Reyes developed an image transmission and reception application using VLC, utilizing a Raspberry Pi 3 computer, bright LEDs, and a light sensor. The application demonstrated acceptable image reproduction with noise resulting from environmental factors and alignment (Sandoval-Reyes 2019). Yudhabrama *et al.* (2017) designed a low-cost VLC transceiver prototype capable of real-time data and image transfer. The system achieved reliable performance within a specified distance range, acceptance angle, and baud rate, highlighting error rates for text and image transmission at different settings. These studies contribute to the understanding and practical

implementation of VLC systems for data transmission.

3.4.1 Design and Implementation

Figure 3.18, highlights various steps involved in our proposed system. Initially, the input image will be converted into a binary image. The binary image will contain only zeros and ones at the corresponding pixel position. These binarized pixels are then mapped to respective payload information. The data payload will contain information about the pixel positions which are black and represented in the frame format as shown in Figure 3.19. The symbol '#' will be used as an image delimiter. Symbol 'A' will be used as a row delimiter i.e., the data following 'A' are data related to a row. Manchester encoded binary values of '#' and 'A' are transmitted using LED's 'On/Off' states. Manchester encoding is used to evenly distribute the 'On/Off duty cycles and thus avoid flickering when continuous '1's or '0's are transmitted. The binary image will be made of binary one and binary zero. Therefore a row in a binary image will consist only of '0' or '1'. These rows will be transmitted using a LED using OOK Modulation.

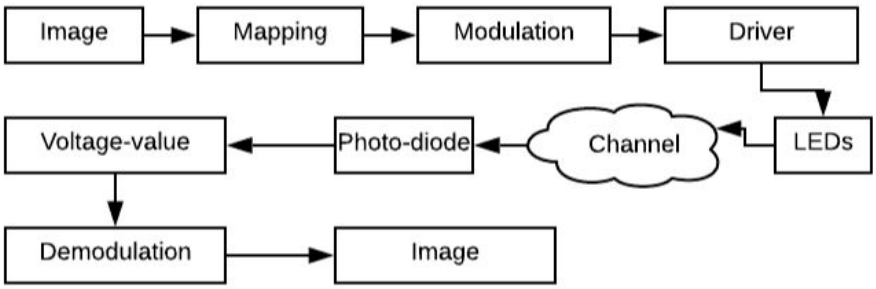

Figure 3.18: Block diagram of VLC system to transmit image

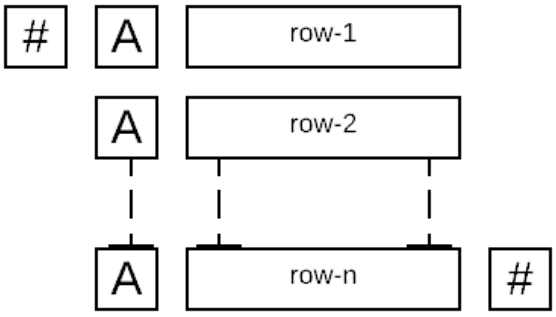

Figure 3.19: Payload Delimiter Frame Format

The LED will be in the 'Off' state when it encounters '0' and will be in the 'On' state when it encounters '1'. A 'n x n' binary image will be used for our proposed work. This payload is then modulated using OOK modulation.

At the receiver side, the photodiode will be used to detect light intensity in its environment. Photodiode will detect LED's state, i.e., 'On' or 'Off'. LED and light sensor will be synchronization by keeping the delay value constant, both for LED and light sensor. The bit will be determined by comparing the received intensity with an average light intensity as the threshold. Each bit will be appended to the previous bit to create a file of binary values. This file would then be passed to an algorithm to identify the delimiter and extract the image data.

Algorithm 9 shows the procedure for conversion of sensor values to binary values. The sensor readings are converted to binary zeros and ones. The threshold is determined using Eq.3.10.

$$threshold = \frac{\sum(values)}{no.of readings} \tag{3.10}$$

Due to a lack of synchronization, the receiver receives repeated values for a single state change at the transmitter side. Thus, to eliminate the repeated values, a second level of thresholding is performed by comparing the number of repeated '0's or '1's with the average of the repetitions. It was also observed during preliminary experiments that for a common transmitter and receiver data rate, the average of repeated states at the receiver side will also be constant. Thus, in the proposed algorithm, variables 'a' and 'b' are two constants. 'a' indicates that '0' should repeat at least 'a' times to indicate single '0' and similarly '1' should repeat at least 'b' times to represent single '1'. The final array will have binary values of delimiters and image values.

When two consecutive '#' are encountered, then it indicates that the next values are related to 'A' and the image. Then we will find the index of 'A', such that 'A' is just after the two consecutive '#'. After finding such 'A', the next 'n' values will be the data of the first row of the image. Then again 'A' will be there and then 'n' values will be of the next row and so on. Algorithm 10 shows the procedure of conversion of binary values to an image of size nxn.

Post-implementation of the testbed and proposed algorithms, an preliminary experimental setup is considered for performance evaluation of the implemented system. A 5x5 image of the letter "T" is considered as it involved the least variations in pixel positions. The size of the buffer considered was twice the size of the image to eliminate partial reception of data due to desynchronization. The

Algorithm 9 Conversion of sensor values into binary

```
1: function CON2BIN(values)
2:     binary1 = []
3:     for i in values do
4:         if i ≥ threshold then
5:             binary1.append(1)
6:         else
7:             binary1.append(0)
8:         end if
9:     end for
10:    binary2 = []
11:    count ← 1
12:    len1 ← len(binary1)
13:    for i = 1 to len1 − 1 do
14:        if binary1[i] == binary1[i − 1] then
15:            count ← count + 1
16:        else
17:            val ← 0
18:            if binary1[i − 1]==0 then
19:                val ← ⌊count/a⌋        ▷ 'a' is minimum no. of times '0' repeats to represent single '0'
20:                for j = 0 to val − 1 do
21:                    binary2.append(0)
22:                end for
23:            else
24:                val ← ⌊count/b⌋        ▷ 'b' is minimum no. of times '1' repeats to represent single '1'
25:                for j = 0 to val − 1 do
26:                    binary2.append(1)
27:                end for
28:            end if
29:            count ← 1
30:        end if
31:    end for
32:    return binary2
33: end function
```

Algorithm 10 Decoding sensor values to obtain image

```
function DECODE(values, n)
    delimiter1 = [0, 0, 1, 0, 0, 0, 1, 1]                ▷ delimiter1 is '#'
    delimiter2 = [0, 1, 0, 0, 0, 0, 0, 1]                ▷ delimiter2 is 'A'
    binary ← CON2BIN(values)
    index_del1 ← FIND_DEL(binary, delimiter1)
    index_del2 ← FIND_DEL(binary, delimiter2)
    start_delimiter2 = 0
    for i = 1 to len(index_del1) − 1 do
        if index_del1[i] - index_del1[i − 1] == 8 then
            start_delimiter2 ← index_del1[i] + 8
            break
        end if
    end for
    start_img ← 0
    for i = 0 to len(index_del2) − 1 do
        if index_del2[i] == start_del2 then
            start_img ← i
            break
        end if
    end for
    img = []
    for i = start_img to start_img + n − 1 do
        row = []
        temp ← index_del2[i] + 8
        for j = 0 to n − 1 do
            row.append(binary[temp])
            temp ← temp + 1
        end for
        img.append(row)
    end for
    return img
end function
```

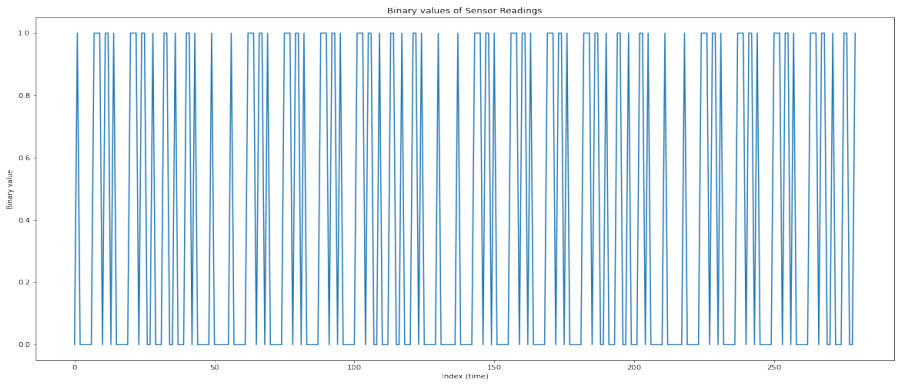

Figure 3.20: Received Bit Pattern for the Input Image "T"

accuracy of the received data at low bit rates at varying distances was considered. Figure 3.20 shows sample received data which contains delimiter codes and image data payload. The initial distance between the transmitter and receiver was kept to 10 cm which was gradually increased as per experiments.

The data of the image to be transmitted is as shown in Figure 3.21a. Each delimiter is further converted to its binary and transmitted.

3.4.2 Results and Discussion

Figure 3.21b, shows a sample binary received data after the process of sampling, thresholding, and bit determination.

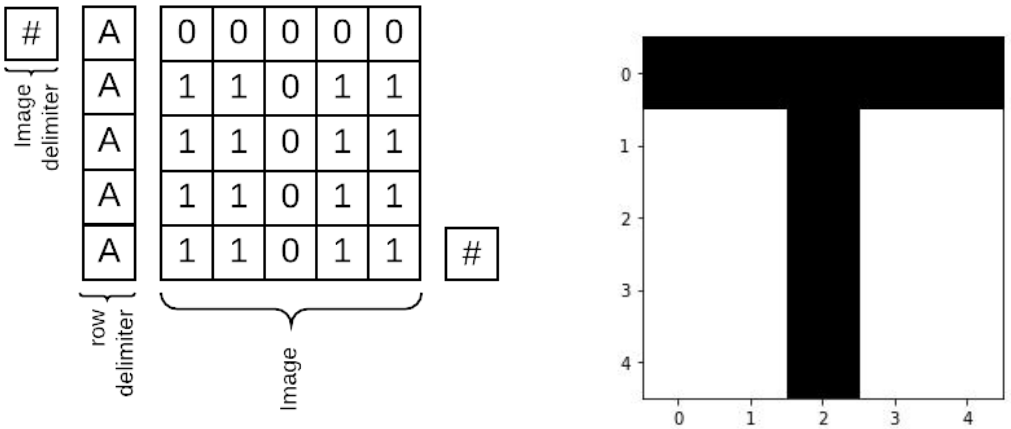

(a) Image T Payload (b) Received Image of T

Figure 3.21: Transmission and Reception of Image Data

Table 3.2: Bitrate vs Transmission Time vs Accuracy

Size of Image (bytes)	100		144		196	
Bit Rate (bps)	**Transmission Time (sec)**	**Acc. (%)**	**Transmission Time (sec)**	**Acc. (%)**	**Transmission Time (sec)**	**Acc. (%)**
2	800	100	1152	100	1568	100
4	400	100	576	100	784	100
10	160	100	230.4	100	313.6	97.2
20	80	100	115.2	98.7	156.8	93.5
100	16	99.1	23.04	95.3	31.36	89.7

Table 3.2, shows the evaluation of the system based on the parameters such as bit rate, size of the image, transmission time, and accuracy. It was observed that the system performs best for low bit rates and shorter distances. The system shows degradation in performance as the bit rate and size of the image increase. This is mainly due to synchronization drifting between sender and receiver. It was also observed that as the distance increases the more error bits get induced. This was due to the fact that as the distance increases the variations in light intensity falling over the photodiode become less distinguishable.

3.5 Summary

An experimental test-bed for evaluation of VLC modulation techniques was designed and implemented. Based on the free space optical characteristics a channel model was built and effects of various environmental parameters such as dimensions of the room, power of LED, and FoV of transmitter on the SNR were simulated and observed. The error probability was simulated based on these channel characteristics. It was observed that the simulated error probability was proportionately in line with experimentally obtained results. It was also observed that PDM Modulation performed twice as better as OOK Modulation in terms of the success of reception, however, PDM was on average three times slower than OOK.

Using the implemented testbed, an application was proposed and implemented to transfer binary images between VLC-Tx and VLC-Rx. Successful image transfer was observed for short distances, which implies a wider range of VLC applications can be implemented.

Future Works mainly include enhancing the algorithm to support for gray-scale and color images. The proposed work was limited to small distances. As a part of future work, other modulation techniques can be implemented on the proposed testbed, and performance analysis based on various parameters such as photosensors, LEDs, ambient lighting conditions, transmitter FoV and longer distances can be studied. Although a photo-diode-based VLC system can be cost-efficient, the issues such as limited FoV and the need for dedicated hardware prevent its widespread adoption amongst existing communication systems. Thus, there is a need to build VLC testbeds and applications which use readily available resources and provide easy integration with existing systems.

Chapter 4

Proposed Rolling Shutter based Optical Camera Communication using Hybrid Frequency Shift Pulse Duration Modulation

Increasing interest in VLC has led to a need to revamp the previously existing modulation techniques, posing more unique challenges specific to the nature of visible light. However, the receiver side adoption of VLC is strictly limited to the implementation based on photodiode or camera. Photodiodes are inexpensive and provide low complexity implementation for VLC as the modulation techniques are based on light intensity. In this case, achieving higher data rates is constrained to the response time of the photodiode (Nada *et al.* 2018; Shulyak *et al.* 2020; Sadat *et al.* 2022). Although other light properties such as color has shown promising results in terms of better data rate, (Chen *et al.* 2019; Singh *et al.* 2015*a*) but as photodiodes are limited to sensing only light intensities, other techniques had to be explored. Moreover, the need for additional dedicated hardware in the form of photodiodes in the existing devices is the major limitation of adapting VLC

OCC is considered one possible solution towards achieving a ready-to-use VLC system by utilizing the camera's properties, computational capacity of mobile phones, and chromaticity of the light (Aguiar-Castillo *et al.* 2021). Since such systems use existing cameras integrated into mobile phones, they need not require additional dedicated hardware like photodiode (He *et al.* 2019; Shi *et al.* 2018). These systems can be used in vehicle-to-vehicle communication, indoor localization, indoor positioning, indoor navigation and augmented reality. In a typical

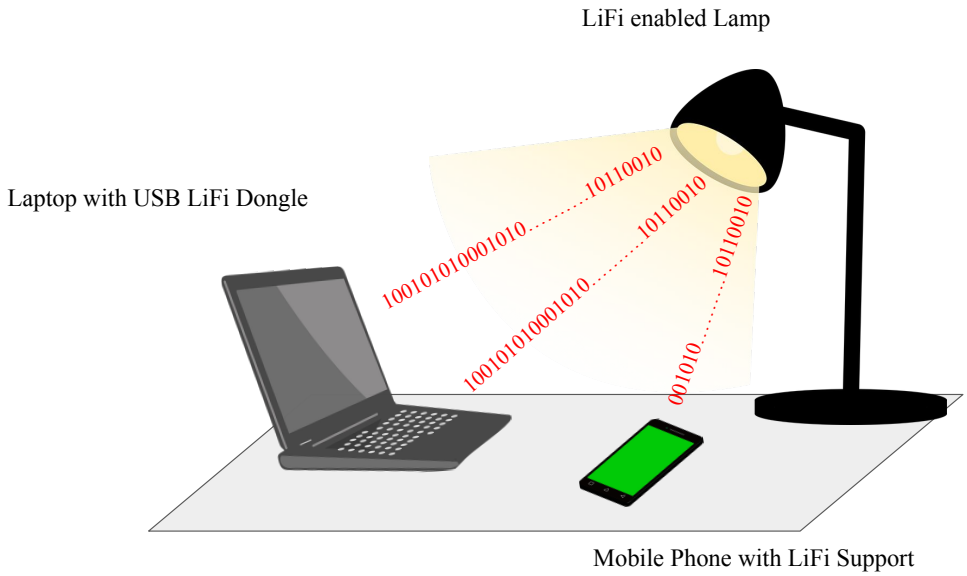

Figure 4.1: VLC enabled Lamp

indoor environment, VLC systems can be deployed as lamps or ceiling lights, as shown in Figure 4.1. However, other challenges related to the OCC-based VLC System include identifying the VLC access point, adjusting exposure, and video pre-processing. In this chapter a novel hybrid modulation technique is proposed, implemented, and evaluated in comparison with the existing two modulation techniques with similar implementation complexities. The objectives highlighted under this chapter are as follows:

- To study and experimentally evaluate thresholding techniques for OOK and Frequency Shift Keying (FSK) modulation schemes under OCC.
- To propose and implement Hybrid Frequency Shift Pulse Duration Modulation scheme for OCC.
- To evaluate the performance of the proposed technique based on BER(%), distance, and frames per bit.
- To design and implement an indoor positioning system using the HFSPDM technique testbed.

4.1 Related Work

This section highlights previous work carried out in the domain of OCC, specifically about its challenges in adopting VLC Systems, modulation techniques, and

thresholding mechanisms. In paper Nguyen *et al.* (2019*b*), the author has provided a performance analysis of OOK modulation based on different camera parameters such as frame rate, focal length, rolling rate, and shutter speed. It was observed that the pixel intensity was higher for closer distances, resulting in a high SNR and thus better data decoding. Paper Teli *et al.* (2019) shows the effects of ISO exposure values on the BER. The experimental results demonstrated that the system observed an increase in noise, directly proportional to the camera's sensitivity concerning ISO values and shutter speeds. In paper Lee *et al.* (2015), the difference between rolling shutter vs. global shutter is discussed. Issues such as mixed symbol frames, stripe width estimation, and image pre-processing are addressed by their proposed "Rolling Lights" System. These works provided sufficient insight into the relation between camera parameters and their impact on information reconstruction. It also helped to understand the "Rolling Shutter" phenomenon and techniques used for its adaptation in OCC.

In a camera-based VLC System, the captured video/images must be processed to decode the encoded data from the light blink pattern. Matlab-based digital image processing methods such as gray-scaling, histogram equalization, and high pass filters were discussed to improve signal quality in OCC System (Li *et al.* 2016*b*). Bummin Kim *et al.* (2017) provided an overview and performance evaluation of three thresholding methods, namely as Background Subtraction, Polynomial Regression, and Moving Average. The Background Subtraction method, includes masking of reference frame over current frame to identify difference in intensities. Whereas, Polynomial Regression and Moving Average thresholding method directly calculates raw intensity values. It was observed that the Background Subtraction method out performed other two techniques in terms of computational speed. These works highlighted various image processing and thresholding techniques used under OCC which inspired our proposed work.

The modulation technique is crucial in providing efficient bandwidth and data rate. Various existing modulation techniques, such as OOK, FSK, and CSK, are modified to serve OCC-based VLC systems. Thus, in a simple OOK Modulation, logic 0 means light is Off, and logic 1 means Light is On. These changes in the On-Off cycle produce black and white stripes in the captured image/video under tuned conditions (Rajagopal *et al.* 2014). However, in OCC, direct encoding data in OOK is complex due to the low frame rate of cameras and the flickering frequency of source light. Thus, the most common way to achieve OOK without flickering is to encode data bits in terms of frequencies. In paper Le *et al.* (2014) a Frequency Shift OOK (FS-OOK) Modulation technique is implemented and evaluated. It

also provides a sub-carrier frequency design based on the relationship between bit interval and sampling interval and between sub-carrier frequencies and flickering mitigation conditions. A Binary Frequency Shift OOK (BFS-OOK) (Van Thang *et al.* 2018) modulation is proposed, and experimental analysis is provided for the relation between distance and detectable stripes. The proposed system mapped each binary bit to a pair of frequencies separated by the guard band frequency, enabling the detection of data bits from the frame. In paper Roberts (2013) the OOK frequencies logic 1 and 0 are selected such that when under-sampled by a low frame rate camera, these frequencies align to low pass frequencies that can then be further decoded to the original bit values.

Modulation based on the color changes is unique to VLC and Li-Fi Systems. There are different color constellations such as 4-CSK, 8-CSK, 16-CSK depending upon the number of bits mapped to a color. An experimental demonstration of a low-cost OCC system with a 2D-constellation-assisted 4-CSK transmission scheme is proposed in paper Deng *et al.* (2019). The system could achieve a BER of 3.8×10^{-3} for the distance of 0.8m and a data rate of 10.74 kb/s. A novel CSK-based OCC system is proposed in paper(Chen *et al.* 2019), which uses an 8-CSK modulation pattern to obtain pixel efficiency of 3.75 pixels per bit. Here, pixel efficiency is a performance evaluation parameter for an OCC system, which is the minimum number of pixels required to represent a bit. In paper Hu *et al.* (2019) an LED-to-camera communication system called ColorBars is proposed, which addresses major challenges about color flicker, inter-frame data loss, and receiver diversity. It was observed that when ColorBars use lower CSK modulation, reliable communication is guaranteed due to the extremely low symbol error rate. These works aided metrics selection for performance evaluation of our proposed technique.

These works have provided us with sufficient insight and motivation to explore the OCC-based Li-Fi domain further. We have tried to contribute to this growing domain with our proposed testbed and modulation technique. Our work is inspired by these related works and attempts to extract, combine, and modify them to create a better solution.

4.2 Overview of OCC

This section highlights few issues and characteristics of the OCC based Li-Fi system while explaining the generic architecture, synchronization issues, encoding principle, decoding principle, and performance evaluation metrics.

4.2.1 Generic OCC Architecture

The Figure 4.2, shows a generalized block diagram of an OCC system. The input binary data stream is passed to Optical Signal Modulator which modulates the signal using the selected technique. The modulated signal is mapped to the LED driver which is used to control the LED. The modulated signal is transmitted over a free-space optical medium. Mobile phone cameras receive the directed light as live video. The video undergoes frame sampling and thresholding to demodulate the signal and decode the received data.

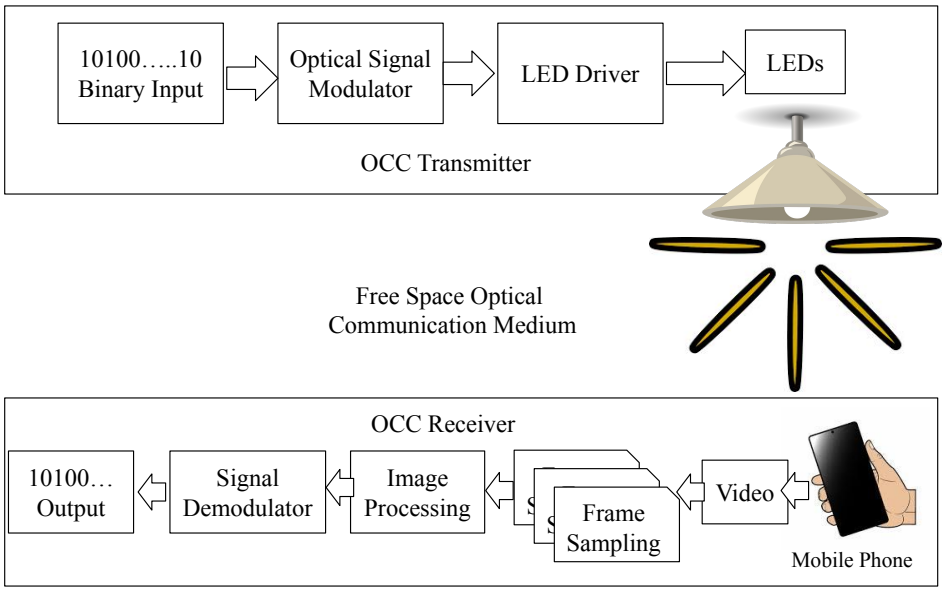

Figure 4.2: The schematic block diagram of an OCC system

4.2.2 Synchronization

The primary deployment of OCC based Li-Fi systems is typically in a broadcast environment. Thus, there is no feedback channel unlike RF communication; this limits the dynamic tuning of the receiver equipment to achieve synchronization and thus restricts achieving higher data rates. The problem of synchronization is basically due to two factors, the first being random sampling and the second being variable frame sampling intervals. If the user device starts sampling at any point during transmission, there is a possibility of losing data; this problem is called random sampling (Hasan *et al.* 2018). On the other hand, the operational performance of each image sensor varies from product to product; this results in the problem of having different frame rates for different equipment despite the same configurations.

4.2.3 Encoding Principle

The basic encoding principle in rolling shutter-based OCC remains the same, i.e., encoding data in stripes. Thus, depending upon the modulation schemes, the properties of stripes will change. For example, in direct OOK modulation, the width of stripes will change based on the bit patterns. Whereas for FSK, the modulated output would vary in the number of stripes, and for CSK, it would be colored stripes. Although the number of stripes required to represent a bit determines the efficiency of the modulation technique, it is also dependent on the size of the transmitter (Chavez-Burbano *et al.* 2021). Figure 4.3 shows sample frames from each modulation scheme. In FSK, the data is transmitted by modulating the signals in-terms of shifting frequencies, while in PDM, it is transmitted by changing the duration of pulse. The proposed modulation technique combine these two techniques to transmit the data by modulating duration of frequencies.

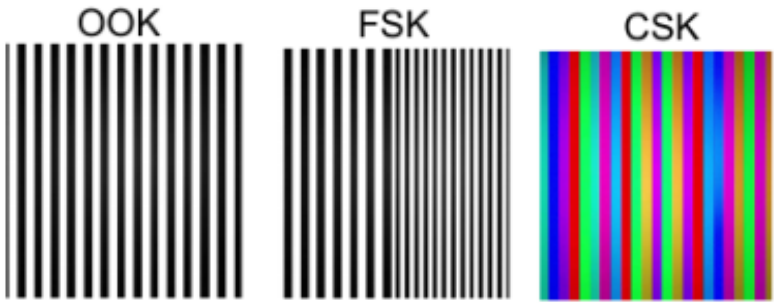

(a) OOK Modulation (b) FSK Modulation (c) CSK Modulation

Figure 4.3: Modulation Patterns

4.2.4 Decoding Principle

An image sensor is built with pixel arrays and a built-in read-out circuit. Each pixel of an image sensor acts as a photodetector. Depending upon the type of camera, these arrays are activated either at once or one by one; this is the basic working principle of the global shutter and rolling shutter. The pixels are activated together in the global shutter, whereas pixels are activated in succession in the rolling shutter. Rolling shutter enables capturing of LED states at different pixels resulting in a series of stripes as shown in Figure 5.1.

The transmitted bits are decoded using image-processing techniques as shown in Figure 4.5. The first step is detecting and tracking the transmitter from video

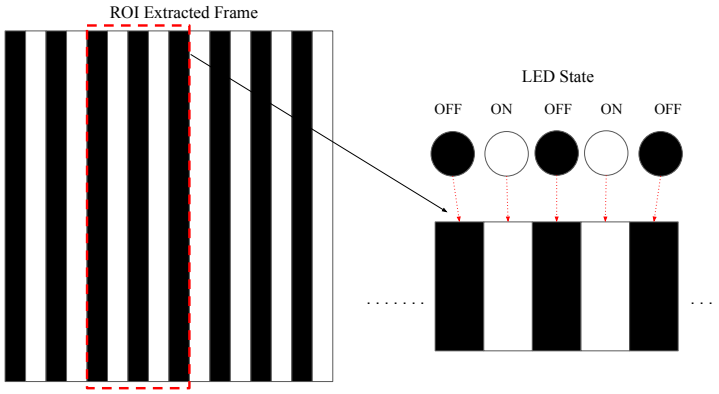

Figure 4.4: Rolling Shutter Effect

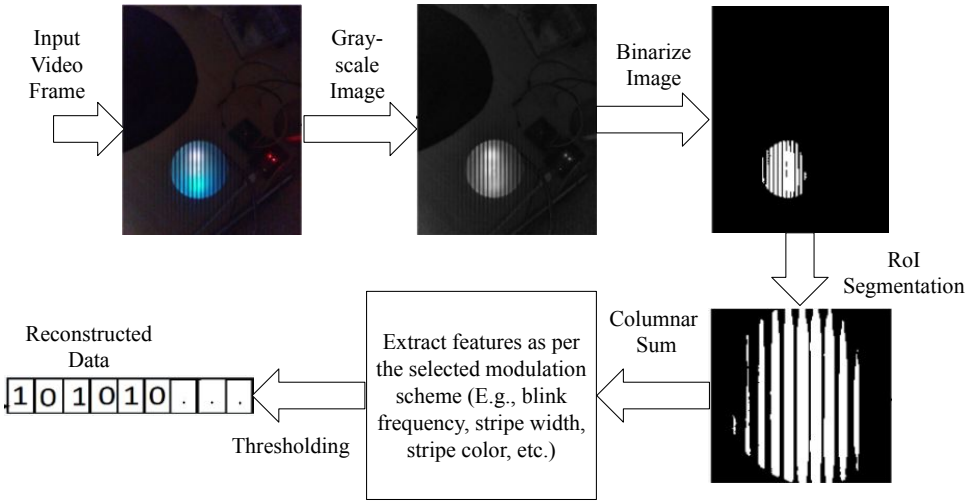

Figure 4.5: Decoding Steps

frames using computer vision algorithms to identify the Region of Interest (RoI). The RoI from the image is cropped and resized to obtain an image containing stripes. The cropped RoI further undergoes pre-processing to obtain a 2D signal using thresholding and decoding techniques. The decoded bits are used to reconstruct sent data. Details on this process are discussed in Sec.4.3.

4.2.5 Performance Evaluation Metrics

In an OCC based Li-Fi system, the number of frames required to represent a bit is the crucial factor in determining the modulation techniques' efficiency. In a typical OCC based Li-Fi system using OOK modulation, the encoded bits are observed as stripes in the image at the receiver side. Thus, the more the stripes in

the image, the more bits can be encoded. However, the width of these stripes is proportional to the LED transmitter's symbol rate. Thus, for a higher symbol rate, the corresponding bit rate will be higher, which results in an increase in number of bits per second. Each bit is represented with the smaller duration of on-off cycles causing the stripe width to become thinner. However, due to the pixel bleeding effect, the image becomes blurred and the width of the stripes becomes difficult to decode. On the other hand, if the stripe width is wider, the number of bits recovered will be less. Hence, there must be a balance between bit representation, modulation technique, image processing, and size of transmitter.

In addition to SNR and BER, frames-per-bit (He *et al.* 2019) metric will also be used to evaluate the performance of the proposed modulation technique. SNR under various ambient lighting conditions and distances will be recorded. To measure SNR the ratio of overall pixel intensity of the image before transmission and during transmission will be estimated.

4.3 Design and Implementation of Proposed HFSPDM Modulation Technique

This section highlights the design and implementation of reference modulation techniques such as OOK and BFS-OOK, and proposed HFSPDM. Table. 4.1 shows all notations and corresponding semantics used for the explanation. Discussion on each modulation is further divided into encoding and decoding steps. Since all the demodulation techniques need to undergo common pre-processing, a standard preprocessing function is implemented as shown in Algorithm 19

Algorithm 11 Common Image Preprocessing

```
Initialize a Buffer(size)
function PREPROCESSING(image)
    Convert image to grayscale
    Enhance the contrast
    Binarize the image
    Dilute the image
    Find dimensions of the brightest and largest blob
    Mask the background
    Crop the original image
    Resize the cropped image based on found ROI
    Grayscale, Enhance Contrast, and Binarize the Cropped Image
end function
```

Table 4.1: Notations and semantics for the proposed work

Notation	**Semantics**
OOK	Optical On-Off Keying
RoI	Region of Interest
VLC	Visible Light Communication
FS-OOK	Frequency Shift Keying On-Off Keying
BFS-OOK	Binary Frequency Shift On-Off Keying
PDM	Pulse Duration Modulation
FSK	Frequency Shift Keying
HFSPDM	Hybrid Frequency Shift Pulse Duration Modulation
y_i	Grayscale value of pixel at point i
$fs(i)$	Sum of the values of the last s pixels at point i
s	Number of pixels for calculating the sum
n	Index variable for sum calculation
T	Threshold in quick adaptive thresholding
r	Adjustment ratio for calculating the threshold
S	Number of pixels for calculating the threshold
i	Index variable for pixel values and calculations
$f_s(i)$	Moving average of grayscale values of the columnar sum of pixels from the cropped RoI
$value$	Value from the buffer for comparison
$Sliding\_Window\_Average$	Average value obtained by sliding window on the buffer
b_1, b_2, b_3, b_4, b_5, b_6, b_7	Binary bits representing the data
$F1, F2, F3$	Distinct frequencies used for HFSPDM modulation
$NumberOfStripes1$, $NumberOfStripes2$	Preset number of observable stripes for BFS-OOK
$Delay1, Delay2$	Delay values for controlling frequencies in BFS-OOK
C	Set of values obtained after performing column-wise sum, normalization, and binarization
$N_{Stripes}$	Number of stripes detected
m	Length of the vector C
$count_i$	Sum of consecutive non-zero values for stripe width detection
max	Maximum width of the stripe in the frame
a	Binary input value for frequency selection in BFS-OOK modulation
$Loop$	Function for repetitively transmitting start bit frequency and individual bits
$Freq1$, $Freq2$, $Freq3$	Frequencies representing the 2-bit patterns in HFSPDM modulation

4.3.1 OOK Modulation

The transmitter side implementation of an OOK modulation in OCC is similar to that of photodiode based OOK modulation. However, to achieve communication in the visible light spectrum, special care has to be taken to avoid flickering while performing data transmission. Thus, flickering issues can be tackled by having higher frequencies of 'on-off' cycles and using a suitable bit encoding technique like Manchester encoding. However, in OCC, the 'on-off' cycles cannot be directly decoded because the frame rate of a standard camera is lower than the operational flicker-free frequency of the transmitter. The sequence of activation of micro photodiodes in a camera produces images containing alternate black and white stripes. The rolling shutter phenomenon is used to address the issue of high-frequency 'on/off' cycles. The captured image is the result of serial activation of the array of micro photo-sensors of the camera. It results in registering transmitter states at different pixels at different times; which results in an image containing bands/stripes/rolls. The color of these stripes represents received bits. Dark stripes are for logic 0, and bright stripes are for logic 1. The width of dark and bright stripes will be equal, however, for Manchester encoded bits there could be maximum two consecutive 0s or two 1s which will have twice the width of one 0 or one 1 bit. For example, if the width of dark and bright bands is 10 pixels individually, then Manchester encoded bit pattern '100101' will have widths like 10, 20, 10, 10, 10 pixels.

4.3.1.1 Encoding in OOK Modulation

The algorithmic implementation of OOK Modulation using a programmable board is as shown in Algorithm 12. Here the *Setup* function is used to initialize the LED-connected pins and a predefined test message. *Loop* function is used to perform repetitive tasks, which include sending the start bit pattern for synchronization before each byte is sent, followed by transmission of each bit of a byte. Furthermore, the *Send* function encodes the received bit into Manchester format and controls the LED states, respectively. For example, if the received bit is 1, post encoding, it becomes 0,1, represented by 'off' states followed by the 'on' state of the LED. A minimum delay is decided, which should satisfy the flicker-free characteristic of light at the transmitter and the observable width of the stripe at the receiver. Depending on this value of x, the data rate and width of the observable stripes in the image are controlled. The size of the transmitter and distance from the receiver also affects the number of observable stripes.

Algorithm 12 OOK Modulation for Li-Fi Transmitter

```
1: function SETUP
2:     Set pin mode to output for all the LED-connected Pins
3:     Set message
4: end function

5: function LOOP
6:     SEND(Start Bit Pattern)
7:     for each byte in message do
8:         for each bit in the byte do
9:             SEND(bit)
10:        end for
11:    end for
12: end function

13: function SEND(a)                    ▷ Manchester encoding and LED Control
14:    if a is 0 then
15:        LED_On                                          ▷ Signifies '1'
16:        delay(x)
17:        LED_Off                                         ▷ Signifies '0'
18:        delay(x)
19:    else if a is 1 then
20:        LED_Off                                         ▷ Signifies '0'
21:        delay(x)
22:        LED_On                                          ▷ Signifies '1'
23:        delay(x)
24:    end if
25: end function
```

4.3.1.2 Decoding in OOK Modulation

Quick adaptive thresholding is used for decoding received signals. It calculates the moving average of grayscale values of the columnar sum of pixels from the cropped RoI.

The algorithm consumes least memory for hardware implementation than other thresholding techniques such as Polynomial Fitting and Iterative ThresholdingLiu *et al.* (2016). It is expressed mathematically as follows, where y_i be the grayscale value of a pixel at point i and assume $fs(i)$ be the sum of the values of the last s pixels at point i; hence it can be represented in Eq. 4.1,

$$f_s(i) = \sum_{n=0}^{s-1} y_{i-n} \tag{4.1}$$

A much faster way to calculate the weighted moving average is to subtract 1/s part of it and add the value of only the latest pixel instead of all s pixels; This is like emphasizing the grayscale values closer to the target value. Then the threshold in the quick adaptive thresholding is represented by Eq. 4.2, where r is the adjustment ratio.

$$T = \frac{r\sum_{n=0}^{S-1}(1-\frac{1}{S})^n y_{i-n}}{1}\sum_{n=0}^{S-1}(1-\frac{1}{S})^n \tag{4.2}$$

Algorithm 13 OOK Demodulation for OCC-LiFi Receiver

```
Initialize a Buffer(size)
function ImageToPulse(CroppedImage)
    Return colomwise sum
end function

function Main(video)
    for each frame in the video do
        Preprocessing(image)                          ▷ As shown in Alg.19
        ImageToPulse(CroppedImage)
        Append the obtained vector to a buffer
        if buffer size is full then
            Normalize Values in buffer
            for each value in the buffer do
                if value > Sliding Window Average then
                    decode bit as 1
                else if value < Sliding Window Average then
                    decode bit as 0
                end if
            end for
        end if
    end for
end function
```

The process of demodulation of the received OOK signal at the receiver is as shown in Algorithm 13. This process is divided into three parts, namely image preprocessing, conversion of image to pulses, and finally the main orchestrator function. In *Main* function the video stream of an active VLC transmitter is recorded which is further processed frames by frame. Each frame is passed to *Preprocessing* function, which returns the RoI identified by using image processing techniques. The returned RoI is converted to a vector under the *ImageToPulse* function. Obtained vector value is appended to a predefined buffer of arbitrary size. The

process is repeated till the size of the buffer is full. Finally, data normalization is performed on the buffer, and each value in the buffer is compared with the threshold obtained by the sliding window average. Based on the outcome of the comparison, the bit value is decoded.

4.3.2 BFS-OOK Modulation

Each bit is represented as one stripe in the captured image with OOK modulation. Although it provides a higher data rate, at the cost of increased sensitivity to noise. Additionally, the distance between the transmitter and the receiver is strictly related to the data rate. With a slight change in the distance, the number of observed stripes changes, and thus the decoded bits. Alternatively, in FS-OOK, the data is directly encoded in the form of frequencies of 'on/off' cycles. Therefore, by identifying the transmitting frequencies, the receiver can demodulate the signal. In BFS-OOK, two frequencies are used for representing logic 1 and 0 respectively.

4.3.2.1 Encoding in BFS-OOK Modulation

The steps involved in encoding data under a BFS-OOK modulation technique are as shown in Algorithm 14. Here, the *Setup* function initializes parameters such as pins connected to the microcontroller, delay values, number of stripes, and test message. $Delay1$ and $Delay2$ is used have different frequencies for 'on/off' cycles, whereas, $NumberOfStripes1$ and $NumberOfStripes2$ are used for pre-setting observable stripes at the receiver for fixed distance of 20 cm. The function $Frequency$ accepts two parameters, namely as $NumberOfStripes$ and $Delay$, based on which the frequency and number of iterations of 'on/off' cycles are decided. *Send* function accepts binary values as input, depending upon which the corresponding frequency is selected. *Loop* function is used to repetitively transmit start bit frequency followed by individual bits from the defined message.

4.3.2.2 Decoding in BFS-OOK Modulation

BFS-OOK modulation uses distinct OOK frequencies to transmit logic ones and logic zeros, respectively. Thus, the thresholding scheme used for BFS-OOK has to distinguish between these two frequencies. This can be achieved in two ways, either by finding the number of stripes in the image or by finding the width of stripes. Eq. 4.3, shows the implementation of a function to count the number of stripes from the given frame. Here, $N_{Stripes}$ represents the number of stripes, and C is the set of values obtained after performing column-wise sum, normalization,

Algorithm 14 BFS-OOK Modulation for VLC Transmitter

```
1: function SETUP
2:     Set pin mode to output for all the LED connected Pins
3:     Set Delay1 and Delay2
4:     Set NumberOfStripes1, NumberOfStripes2
5:     Set message
6: end function

7: function FREQUENCY(NumberOfStripes,Delay)
8:     for i=0 to NumberOfStripes do
9:         LED_On
10:        delay(Delay)
11:        LED_Off
12:        delay(Delay)
13:    end for
14: end function

15: function SEND(a)
16:    if a is 0 then
17:        FREQUENCY(NumberOfStripes1,Delay1)
18:    else if a is 1 then
19:        FREQUENCY(NumberOfStripes2,Delay2)
20:    end if
21: end function

22: function LOOP
23:    SEND(Start Bit Pattern)
24:    for each byte in message do
25:        for each bit in the byte do
26:            SEND(bit)
27:        end for
28:    end for
29: end function
```

and binarization. Thus C consists only of binary values, and m is the length of the vector C.

$$N_{Stripes} = \frac{\sum_{1}^{m-1} (C_i - C_{i+1})^2}{2} \tag{4.3}$$

Consider for a sample binary bit stream of $b_1, b_2, b_3, b_4, b_5, b_6, b_7$ represented by 0,0,1,1,1,0,0. Here, consecutive 1s represent a white stripe. After performing $(C_i - C_{i+1})^2$ from b_1 to b_7 the output generated is 0,1,0,0,0,1,0. After performing summation over it we get 2 which represent edges of the stripe and by dividing it by 2 we get 1 i.e., the 1 white stripe is detected. For detecting the width of stripes, Eq. 4.4 and 4.5 is used. Here, $count_i$ maintains the sum of consecutive non-zero values. Thus, bit values from $b_1 - b_7$ are represented as 0,0,1,2,3,0,0 respectively. By finding the maximum of all the values, the maximum width of the stripe in the frame is estimated.

$$count_i = \begin{cases} count_{i-1} + 1, & if max > count_i \\ 0, & \text{otherwise} \end{cases} \tag{4.4}$$

$$max = \begin{cases} max & if max > count_i \\ count_i & otherwise \end{cases} \tag{4.5}$$

Algorithm 15 shows algorithmic implementation of BFS-OOK receiver based on discussed equations. Post thresholding the value obtained is added to a buffer. Once the size of this buffer is full, data normalization is performed. Each value from the buffer is then compared with the obtained threshold from the previous function, and the respective binary value is decoded.

Algorithm 15 BFS-OOK Demodulation for VLC-OCC Receiver

```
Initialize a Buffer(size)
function CountEdges(CroppedImage)
    Perform Edge detection
    Return number of edges detected
end function

function CountWidth(CroppedImage)
    Convert to a Row Vector using Columnwise Sum
    Normalize the Row
    Binarize the row
    Find length non-zero sub-sequences
    Return average width
end function

function Main(video)
    for each frame in the video do
        Preprocessing(image)                          ▷ As shown in Alg.19
        CountEdges(CroppedImage)/CountWidth(CroppedImage)
        Append the obtained vector to a buffer
        if buffer size is full then
            Normalize Values in buffer
            for each value in the buffer do
                if value ¿ Sliding Window Average then
                    decode bit as 1
                else if value ¡ Sliding Window Average then
                    decode bit as 0
                end if
            end for
        end if
    end for
end function
```

4.3.3 Proposed HFSPDM Modulation

Figure 4.6 shows the arrangement of frequencies to distinguish data pattern from start/stop bit pattern. Here, $F1$, $F2$, and $F3$ represent three distinct frequencies that satisfy specific relations. For example, $F1 = 4 \times F3$, $F1 = 2 \times F2$ and $F2 = 2 \times F3$. Here, $F1$ represents the start bit pattern frequency. Identification of this frequency enables us to estimate the next frames. The data bit pattern is divided into two subparts to map with the desired bit pattern. The combination of two frequencies represents four 2-bit patterns such as 00, 10, 01, and 11. The

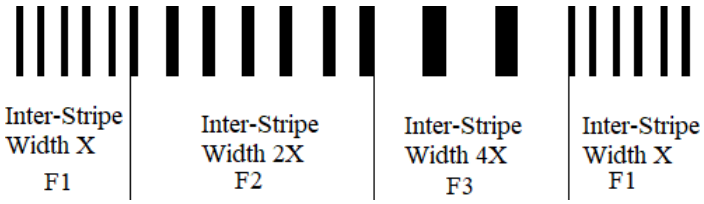

Figure 4.6: Sample Frame Format in terms of Frequency for HFSPDM

Table 4.2: HFSPDM Frequency Mapping Table

Data Bit	Frequency Distribution	Pulse Shape
00	**F2(100%)+F3(0%)**	
01	**F2(75%)+F3(25%)**	
10	**F2(25%)+F3(75%)**	
11	**F2(0%)+F3(100%)**	

data bit pattern is enclosed within two consecutive start bit patterns. Table 4.2 shows the mapping of four 2-bit patterns to their respective frequencies, duty cycles, and pulse shape. The modulation method is a hybrid of FSK and PDM since frequency duration is used for decoding bits.

4.3.3.1 Encoding in HFSPDM Modulation

The steps involved in the encoding of data bits using HFSPDM is as shown in Algorithm 16. The working of *Frequency* and *Send* functions is the same as explained in Sec. 4.3.2.1 except for a minor change with respect number of bits sent. In the proposed technique, 2 bits are passed to the *Send* function thus, the *Send* function has to handle four states. Additionally, since the start bit is represented by a different frequency, the *Send* function has to also handle the fifth case of the start bit pattern. For, the purpose of convenience each bit pair is divided into four calls to the *Frequency* function. thus, depending on the bit pair, the corresponding frequency duration can be controlled. For example, if the bit pair is 00, then $F2$ frequency i.e., $Frequency(NumOfStripes2, Delay2)$ will be called 4 times. Whereas, if the bit pair is 01, Frequency $F2$ will be called 3 times followed by Frequency $F3$ i.e.,$Frequency(NumOfStripes3, Delay3)$ which will be called only once. Typically, the encoded frequencies follow the Nyquist sampling theorem, and the relation between the number of stripes, delay, and

Algorithm 16 HFSPDM for Li-Fi Transmitter

```
1: function SEND(a)
2:     switch a do
3:         case 00
4:             4 times FREQUENCY(NumOfStripes2,Delay2)
5:         case 10
6:             FREQUENCY(NumOfStripes2,Delay2)
7:             3 times FREQUENCY(NumOfStripes3,Delay3)
8:         case 01
9:             3 times FREQUENCY(NumOfStripes2,Delay2)
10:            FREQUENCY(NumOfStripes3,Delay3)
11:        case 11
12:            4 times FREQUENCY(NumOfStripes3,Delay3)
13:        case StartBit
14:            FREQUENCY(NumOfStripes1,Delay1)
15: end function
```

frame rate is provided as follows:

$$B_r = \frac{F_r}{2} \tag{4.6}$$

$$D_1 = \frac{1}{2} \times (((1/B_r) \times 10^6)/N_{l1}) \tag{4.7}$$

$$D_2 = \frac{1}{2} \times (((1/B_r) \times 10^6)/(2 \times N_{l1})) \tag{4.8}$$

$$F_1 = \frac{1}{D_1}, (where F1 > F_{ff}) \tag{4.9}$$

$$F_2 = \frac{1}{D_2}, (where F2 > F_{ff}) \tag{4.10}$$

Here, F_r is the camera frame rate, B_r is the bit encoding rate, N_{l1} is the number of stripes expected, D_1 and D_2 is the delay between the 'On-Off' cycle, resulting into frequency F_1 and F_2. These frequencies represent logic 1 and 0. Special care should be taken while assigning the number of lines as it affects the frequency and detection of stripes. The frequency should be more than the minimum flicker-free frequency (F_{ff}), i.e., 200Hz.

4.3.3.2 Decoding in HFSPDM Modulation

Decoding of HFSPDM modulated signal requires two thresholding steps. The first thresholding is performed to identify the frequencies, while the second thresholding

is performed to identify the duration of frequencies. The first level of thresholding is performed similarly to BFS-OOK as discussed in Sec. 4.3.2.2, which provides the largest stripe width from each frame. The widest stripe from sample frames should be four times the width of the smallest stripe due to the preset relation between frequencies. However, as the practical system is prone to external noise, an error margin of 10% of the widest stripe is set. Thus, the relation between the widths of different frequencies is given as follows, where $W1$, $W2$, and $W3$ are widths of stripes in the frames for frequencies $F1$, $F2$, and $F3$, respectively.

$$W3 = 4 \times W1 \pm \frac{W1}{10} \tag{4.11}$$

Stripe width of second frequency can be estimated from W3 and W1 as shown in Eq.4.12

$$W2 = \frac{W3}{2} \pm \frac{W1}{10} \tag{4.12}$$

After finding frequency from the frames, second thresholding is applied based on Percentage Frequency Frame Ratio (PFFR). In this method, the percentage occurrence of any frequency frame out off $F2$ and $F3$ can be considered.

For example Eq.4.13 shows P_{F2} as percentage of $F2$ frequency frames. Where T_{F2} is the total number of frames between successive start frames containing $F2$ frequency and N_{Frames} is the total number of frames between successive start frames.

$$P_{F2} = \frac{T_{F2}}{N_{Frames}} \times 100 \tag{4.13}$$

The algorithmic implementation of HFSPDM is as shown in Algorithm 17. The duration of frequencies should be more than twice the frame rate of the camera for sampling. Here, assuming pre-processing is performed, a sample set of stripe widths from the video stream is created. The frames can be identified in $F1$, $F2$, and $F3$ frequency frames from the obtained widths. Finally, the bit pairs are decoded by counting the number of $F2$ and $F3$ frequency frames and comparing them with the threshold values. Here two Boolean flags are used to track start bit frequency $F1$ and count the number of $F2$ $F3$ frequency frames. $Fr2$ and $Fr3$ consist of the count of respective frequency frames and the percentage of $F2$ or $F3$ frequency is estimated. The obtained percentage is then used to decode the bit pair using percentage mapping applied during encoding.

Algorithm 17 HFSPDM Demodulation for Li-Fi Receiver

```
1: function CountFrequencyFrame(CroppedImage)
2:     W=CountWidth(CroppedImage)
3:     if W==F1 and Flag1==0 and Flag2=0 then
4:         Set Flag1=1
5:     else if W==F2 and Flag1==1 then
6:         Set Flag2=1
7:         Increment Counter for F2
8:     else if W==F3 and Flag1==1 then
9:         Set Flag2=1
10:        Increment Counter for F3
11:    else if W==F1 and Flag1==1 and Flag2==1 then
12:        Set Flag1=0
13:        Set Flag2=0
14:        Return Count of F2 and F3 Frequency containing frames
15:    end if
16: end function

17: function Main(video)
18:    for each frame in the video do
19:        Preprocessing(image)                    ▷ As shown in 19
20:        CountWidth(CroppedImage)
21:        Append the obtained value in a buffer
22:        if buffer size is full then
23:            F1=min(buffer)
24:            F3=4xF1+F1/10
25:            F2=F3/2+F1/10
26:        end if
27:    end for
28:    for each frame in the video do
29:        Fr2,Fr3=CountFrequencyFrames(CroppedImage)
30:        Compare with the threshold value
31:        Decode bit pair
32:    end for
33: end function
```

4.4 Experimental Setup

In this section, the hardware and software details used for the implementation of proposed OCC testbed and camera parameters used for testing are discussed.

4.4.1 Rolling shutter based OCC Testbed Setup

A circuit diagram for controlling LED as Li-Fi Transmitter is shown in Figure 4.7a. For building the VLC transmitter testbed an Arduino mirco programmable board is used. Three off-the-shelf multi-color LEDs are connected to the board. To avoid direct exposure to these bright lights and to have a well-defined shape transmitter a simple diffuser is used. Thus with a diffuser, the radius of the transmitter is 3cm. Figure 4.7 shows the implemented VLC Transmitter under different conditions such as b) without a diffuser, c) with a diffuser, and d) operational. Each modulation technique is tested for a variable distance between transmitter and receiver and at different frequencies. Figure 4.8 shows the experimental setup for the performance evaluation of the proposed technique.

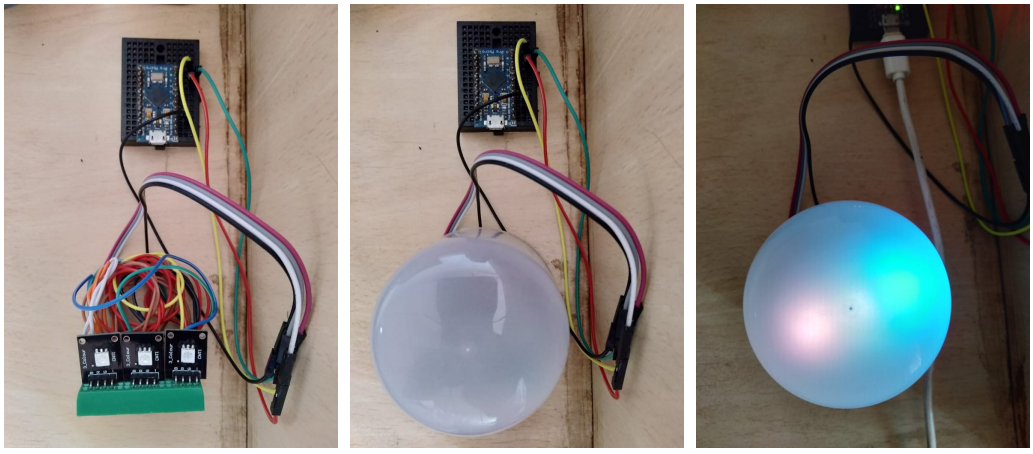

(a) VLC Transmitter (b) VLC Transmitter with Diffuser (c) Operational VLC Transmitter

Figure 4.7: Li-Fi Transmitter

The SNR was measured by keeping the brightness, contrast and exposure parameters constant under different ambient light values i.e., 50 lux and 120 lux. Eq. 5.15 gives sum of pixel intensities of the image where, P_{ij} is pixel intensity of gray scaled image at position i, j and Z_i is an image frame. As shown in Eq. 5.14 A_i is image frame containing active transmitter while B_i is image frame containing inactive transmitter. The average pixel intensity observed with transmitter 'on'

was considered as signal power while the average pixel intensity of frame with transmitter 'off' was considered as noise power to estimate SNR.

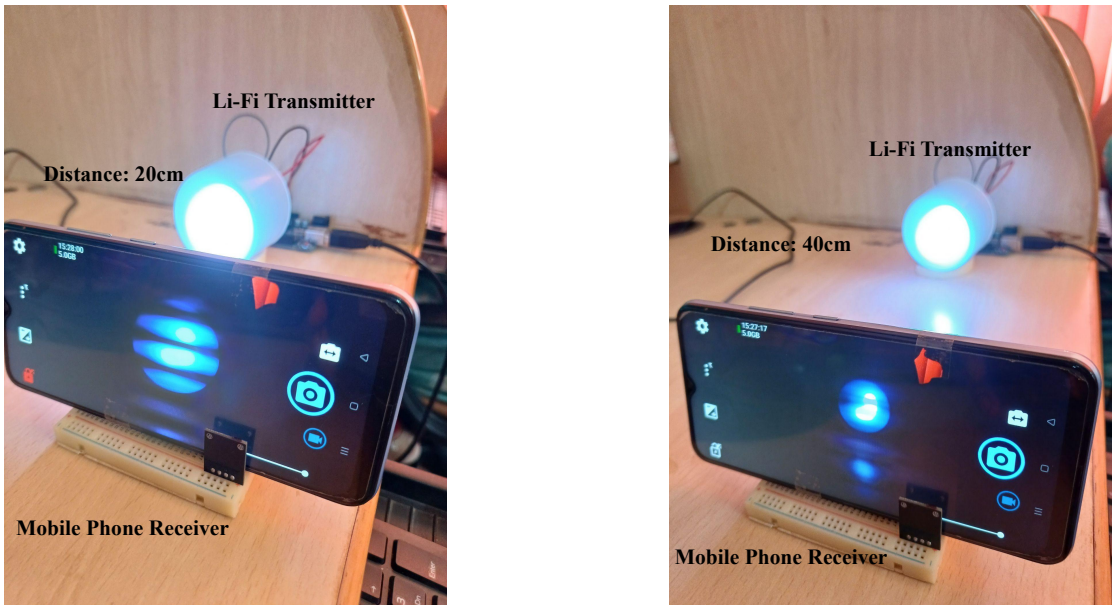

Figure 4.8: Experimental Setup with Transmitter and Receiver distances as 20cm and 40cm from left respectively

$$Z_i = \sum_{j=1}^{y} \sum_{i=1}^{x} P_{ij} \tag{4.14}$$

$$SNR_{dB} = 10 \times \log \frac{\sqrt{\frac{1}{n}\sum_{i=0}^{n-1} |A_i|^2}}{\sqrt{\frac{1}{n}\sum_{i=0}^{n-1} |B_i|^2}} \tag{4.15}$$

4.4.2 Camera Parameters

For the experimental analysis of the proposed method, a video feed from an Oppo A3S android phone camera is taken, and an application named "Open Camera" is used to adjust the exposure and frame rate. Other parameters are as shown in Table.4.3:

Table 4.3: Camera Parameter

Parameter	Value	Parameter	Value
Exposure	ISO3200	Contrast	100
Frame Rate	30FPS	Brightness	100
Resolution	160x96	Ambient Light	50-120 lux

4.5 Results and Discussion

This section discusses the results obtained from each experimental evaluation of each modulation technique.

Figure 4.9 shows that as the distance and ambient light intensity increases the SNR value decreases. Further experiments were conducted by keeping the ambient light intensity between 50-60 lux as it provided better SNR. Stress pattern of alternate 0 and 1 is used for finding BER.

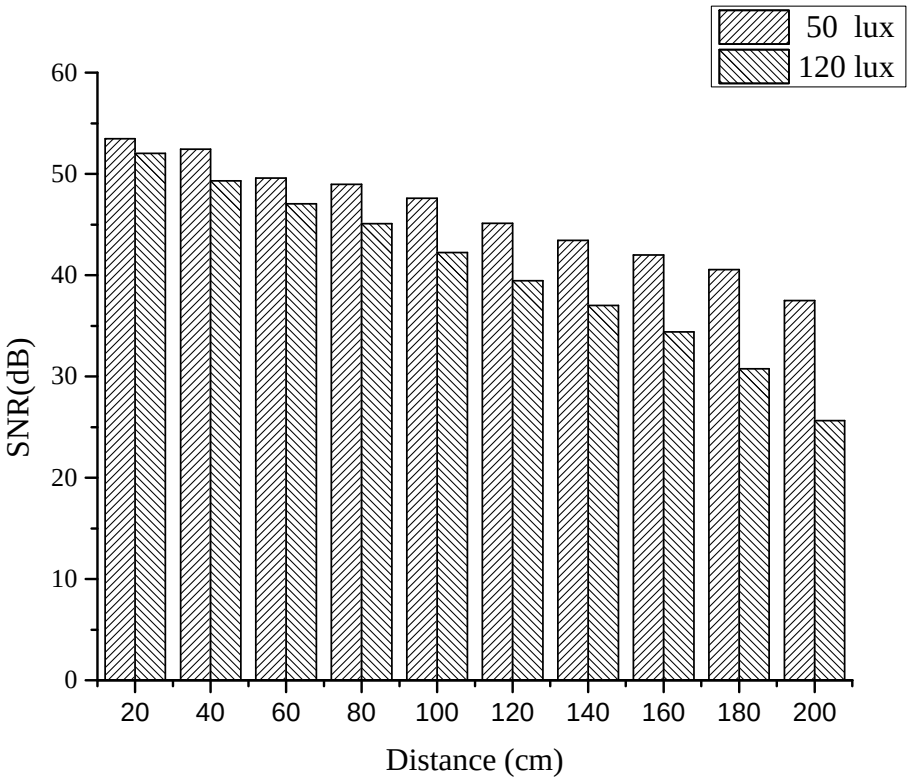

Figure 4.9: SNR vs Distance vs Ambient Light

The results for OOK, BFS-OOK, and the proposed HFSPDM modulation technique are represented in separate subsections. These results majorly show the number of detectable stripes for various frequencies at various distances. It also shows the average width of the stripe based on the corresponding frequency. Also, the result highlights the BER performance under varying distances for each implemented modulation technique. Finally, the performance of the proposed modulation technique is compared with existing techniques.

4.5.1 Results for OOK

The first experiment was to analyze the effect of OOK modulation frequency concerning distance. The number of stripes detected from the frame is the evaluation parameter. For each frequency and distance, an average of 5 tests is considered.

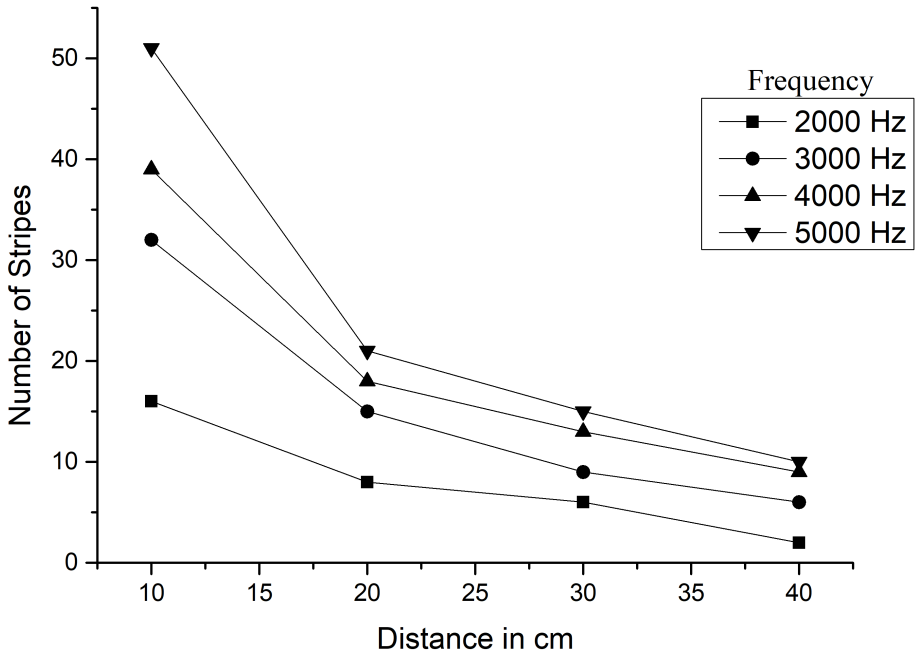

Figure 4.10: OOK Modulation Distance vs Detectable Stripes for various frequencies

As shown in Figure 4.10, it is observed that for the shorter distance, the number of stripes detected is more and drastically decreases with the increase in the distance. It is majorly because of the decrease in the RoI region while stripe width stays constant. Thus, an optimal trade-off between frequency, distance, and size of light aperture is required. The number of detectable stripes in OOK modulation is directly proportional to the data rate.

The other experiment was to analyze the relation between stripe width and distance. As shown in Figure 4.11, it was observed that stripe width is inversely proportional to frequency. However, it was also observed that there was no significant visible stripe for very low frequencies and greater distances; this is due to the size of the aperture and the number of pixels it occupied in the image/video. Here, the stripe width remains constant, but identification of RoI based on the implemented pre-processing techniques fails as the distance increases; this is majorly

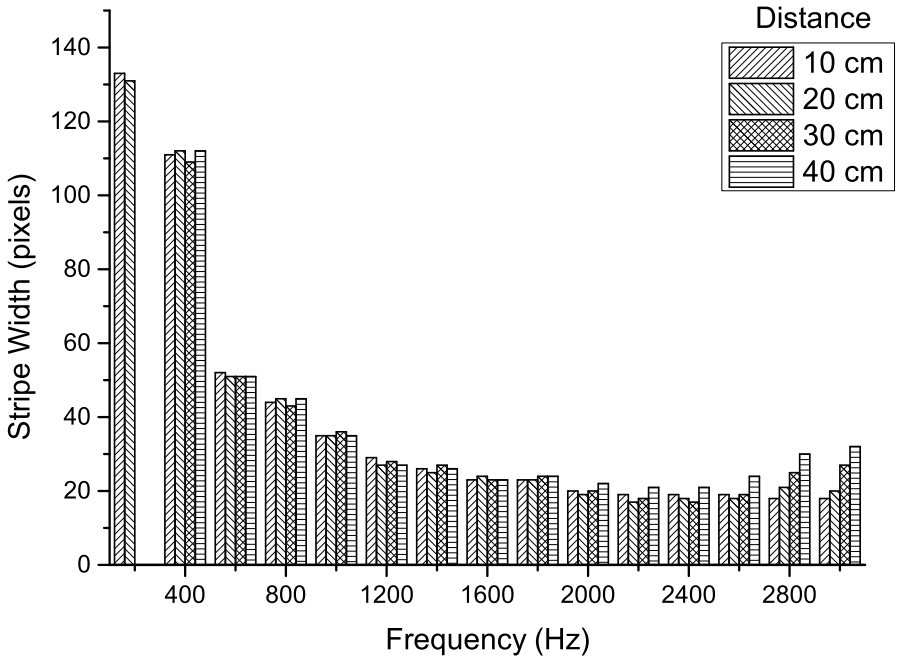

Figure 4.11: OOK Modulation Frequency vs Stripe Width

due to the absence of the brightest blob in the image as the transmitter appears to be overlapped by a dark stripe.

Also, the decrease in the size of stripe width is observed to follow the elliptic curve, where the curve reaches its minimum at the frequency of 2000Hz for a fixed distance of 20cm and starts ascending again. This behavior was observed due to the phenomenon of pixel spreading which results in stripes with smaller widths spreading and causing boundary detection error.

The steps involved in pre-processing and identification of the number of stripes and stripe width are shown in Figure 4.12. Here, two cases with the same OOK frequency but varying distances are shown. The number of stripes detected is dependent on the distance, whereas the width of the stripe remains almost identical. It was an important observation as it defined a reliable feature to identify frequencies in BFS-OOK.

Figure 4.13, shows the comparison between various window sizes for quick adaptive thresholding. It is observed via trial and error that for smaller window sizes threshold is more adaptive.

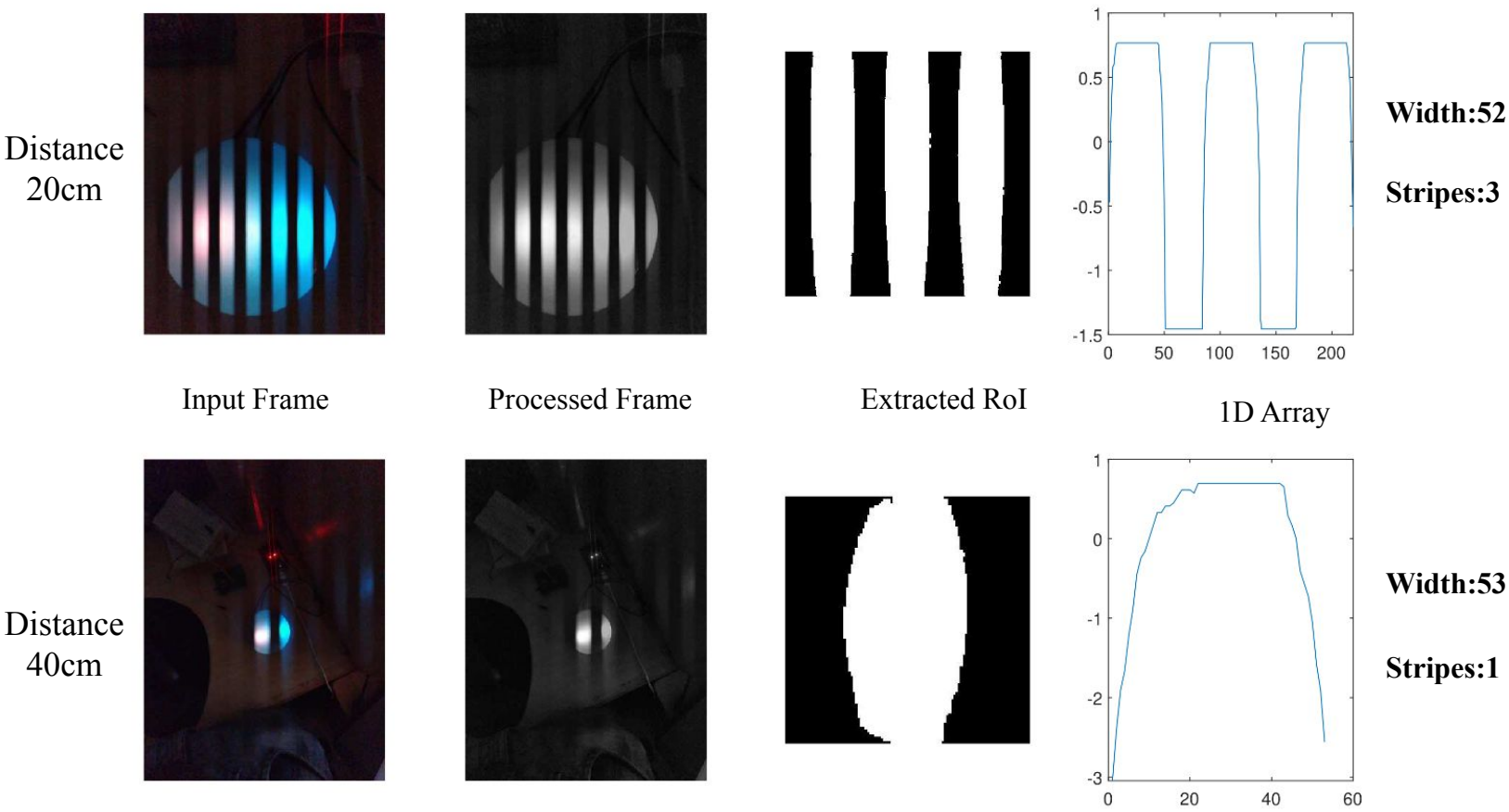

Figure 4.12: Number of Lines vs. width vs. distance

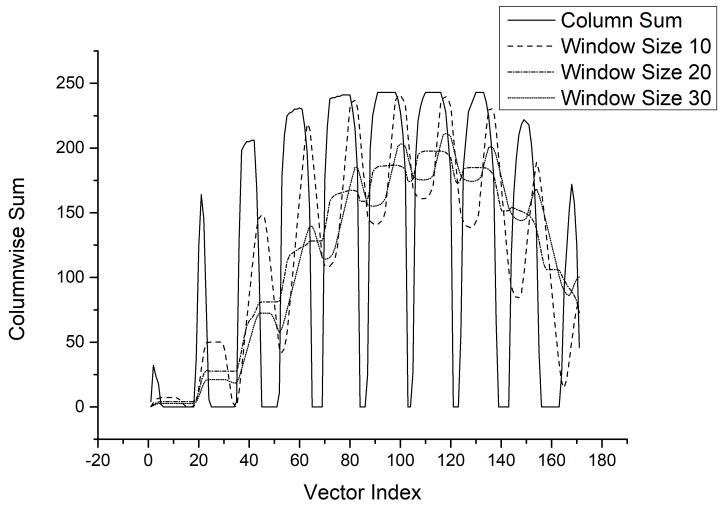

Figure 4.13: OOK Sliding Window Thresholding

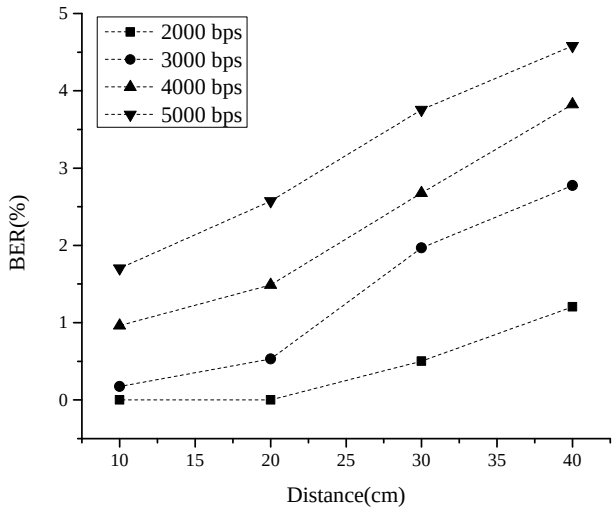

Figure 4.14: OOK BER vs Distance

Thus, by keeping the window size to 10, experiments to test the BER of OOK system are conducted. The evaluation is performed based on the percentage of wrongly received bits out of 2048 bits. As shown in Figure 4.14, it was observed that for lower bit rate, the rate of change in BER concerning distance is comparatively slower than higher frequencies; this is because detection of LED state under lower frequency is better compared to a higher frequency.

Thus, in OOK modulation, as the number of bits represented per frame is proportional to the distance between transmitter and receiver, the accuracy decreases at a higher data rate due to frame loss.

4.5.2 Results for BFSOOK

Based on the experiments conducted for OOK, it was evident that for the classification of frequencies the stripes' width is a better deciding factor than the number of stripes. Thus, the max of widths per frame is used to identify the frequency and thus determine the bit.

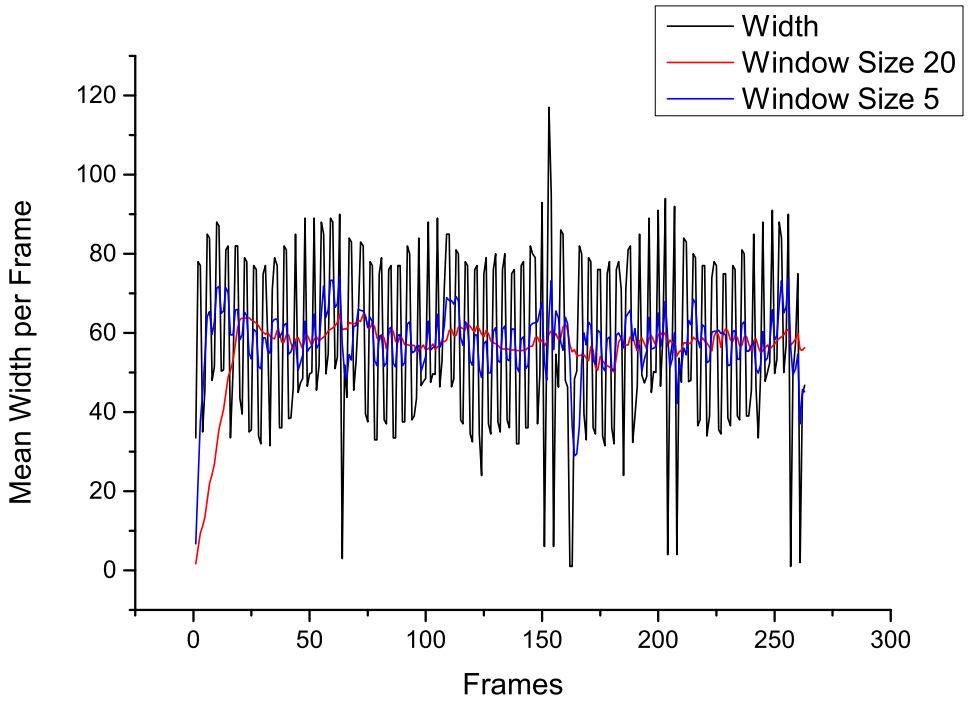

Figure 4.15: BFSOOK max widths per Frame and Thresholding Window

Figure 4.15 shows max widths of subsequent frequencies used for representing logic 0 and 1. 500Hz and 1000Hz are the two frequencies used, and the distance of 20cm is kept constant for testing the thresholding method. Figure 4.15 also shows that a sliding window size of 5 provided more adaptive thresholding for the determination of bits. Further, by keeping window size constant, the accuracy of the modulation scheme is tested. The frequencies selected follow $F2 = 2 \times F1$, to enable better classification, where $F1$ and $F2$ are frequencies for bit 0 and 1.

Figure 4.16 shows the BER in percentage considering 2048 bits at varying distances. Here, $F1$ frequency is used for representation. It is observed from the

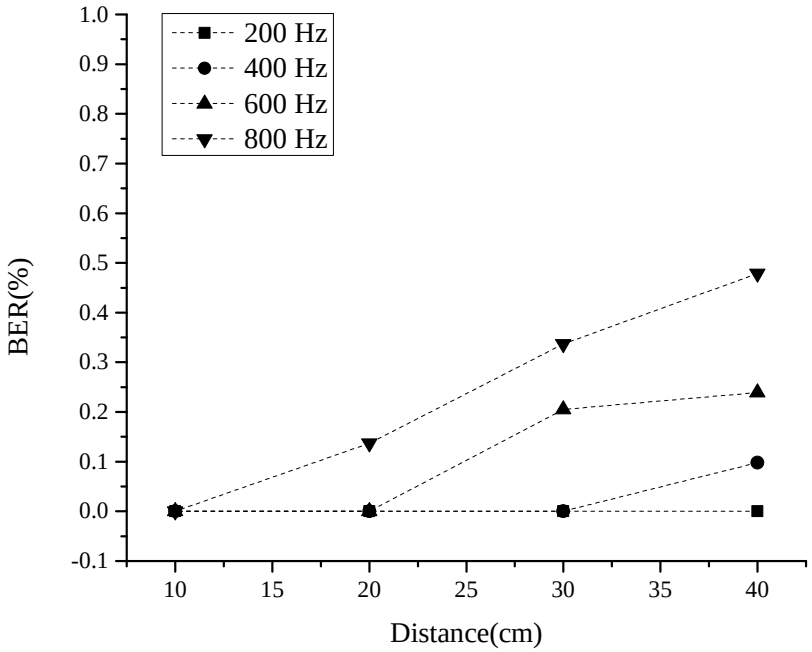

Figure 4.16: BFSOOK BER vs Distance

result that the BER(%) is 0% for $F1 = 200Hz$ viz. $F2 = 400Hz$. This is because the difference between the widths for $F1$ and $F2$ frequency is prominent and thus easy to decode. Whereas, due to the elliptic relation between width and frequency, as the frequency increases, there is a decrease in the difference between widths, making bit estimation more prone to errors resulting in an increase in BER.

BFS-OOK is more robust than OOK as the technique is inherently asynchronous and independent of distance. This modulation method provides better accuracy than OOK, even for a distance up to 40cm considering a smaller transmitter. However, the obtained data rate is lower than OOK as the number of frames required to decode the bit is higher.

4.5.3 Results for HFSPDM

The frequencies used for HFSPDM follow relation of $F3 = 2 \times F2 = 4 \times F1$. Figure 4.17 shows the obtained signal in terms of column sum for each frame. In order to provide ease of understanding and representation, the duration for each frequency is extended to multiple frames, and a repeated sequence of four 2-bit pairs is transmitted. A sliding window of size 5 is used to smoothen the obtained signal, which is then further processed to identify the frequencies.

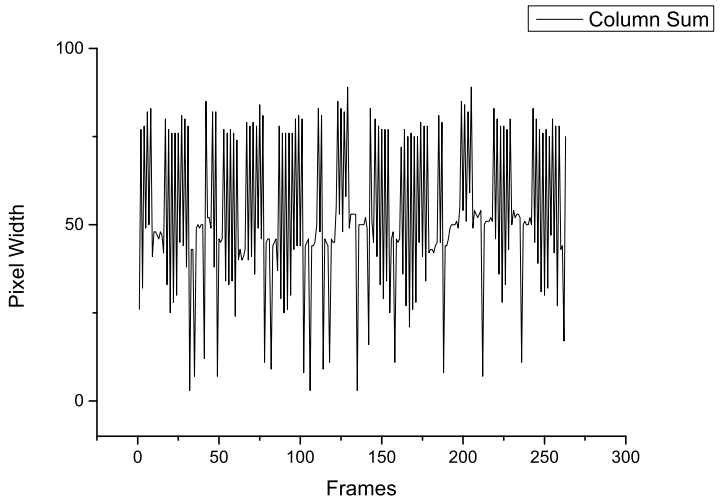

Figure 4.17: HFSPDM Signal

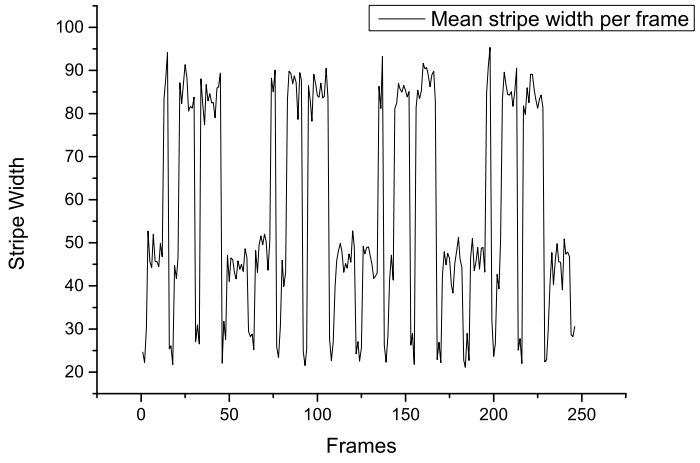

Figure 4.18: Filtered HFSPDM Signal

Figure 4.18 shows the filtered signal. Three levels can be identified from the signal; the lowermost level shows frames with stripe widths of 22 pixels approximately, the second level at a width of around 45 pixels, and the third level at a width of 80 pixels approximately. Each of these levels represents three distinct frequencies. The number of frames containing frequencies 2 and 3 between successive frequency 1 frame is identified for decoding. The final bit pair is decoded based on the percentage of frequency 2 frames. Figure 4.18 shows repeated decoding of bit patterns 00,01,10 and 11.

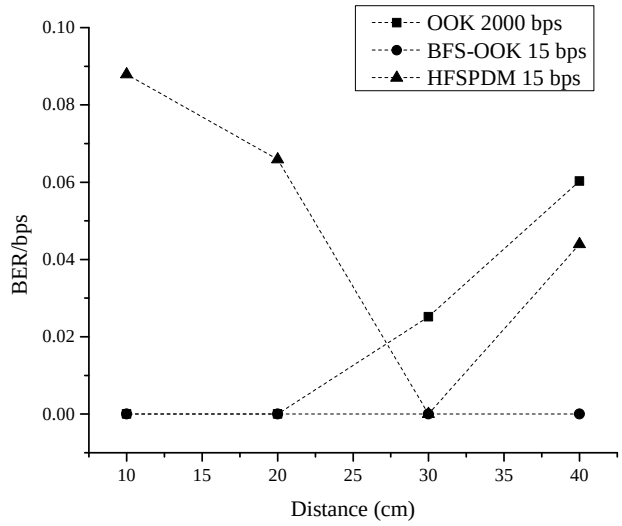

Figure 4.19: Accuracy Comparison of OOK, BFSOOK, and HFSPDM

Table 4.4: HFSPDM vs OOK vs BFSOOK

Modulation Technique	**BER/bps**	**No. of frames per bit**	**Distance (cm)**
OOK	0.06	0.05	< 20
BFSOOK	0	3	> 20
HFSPDM	**0.04**	**2.5**	> 20

An overall comparison of all three implemented techniques, i.e., OOK, BFS-OOK, and HFSPDM, is shown in Figure 4.19. The best results for each technique are compared. In general, bit rate should be kept constant for comparing BERs. However, OOK operates at very high bit rates compared to BFS-OOK and HFSPDM, thus, the ratio of BER to bit rate is used as metrics to evaluate. Hence, the lower the value better will be the performance of the technique. It was observed that BFS-OOK provided consistent BER/bits-per-second (bps) close to 0 for frequency 200Hz while our proposed HFSPDM technique has shown BER/bps closer to 0.04. However, it was also observed that in HFSPDM, the number of frames required to transmit the same amount of data as that in BFS-OOK was considerably lesser but more than OOK. This is because HFSPDM represents 2 bits per 5 frames on average, whereas BFS-OOK represents 1 bit per 3 frames. The bit to frame ratio is much higher in OOK which is of order 20 bits-per-frame; however, HFSPDM gives better BER for longer distances than OOK based on standard implementation using low-cost devices. Table 4.4 shows the relative performance of HFSPDM in comparison with OOK and BFS-OOK.

4.6 Proposed Indoor Positioning System using Rolling Shutter based OCC: An Application

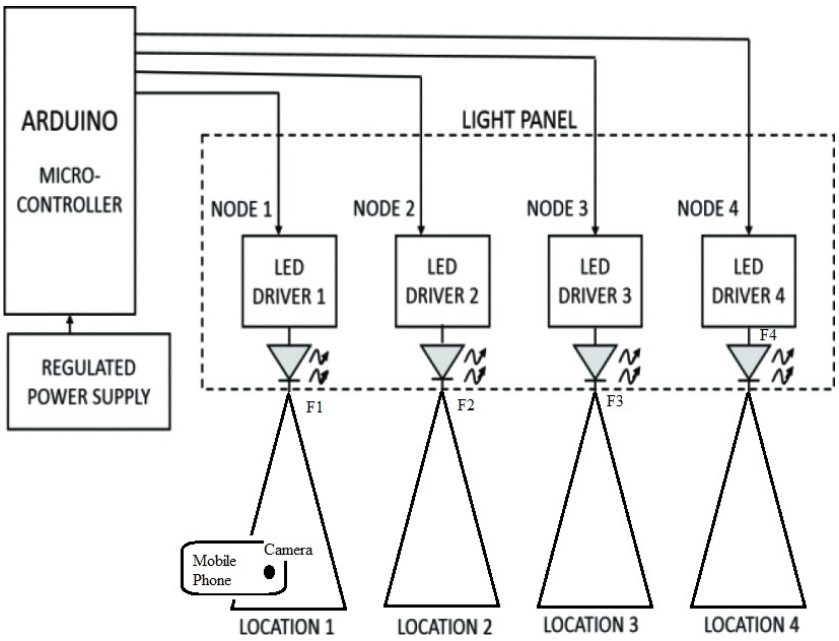

Figure 4.20: LiCamPos Block Diagram

The aim of the proposed system is to design, implement and evaluate the performance of a rolling shutter-based OCC IPS. The basic building blocks of our proposed system are as shown in Figure 4.20.

The proposed system is named as "LiCamPos" which is derived from the combination of its integral blocks, i.e., Li-Fi, camera, and positioning. It is divided into two parts namely as position beacons and receiver. Position beacons will be SMD LEDs connected to a micro-controller also called as LED-driver. One such pair of LED and its driver is called as Node. Each of these LEDs in the nodes will be programmed to blink at a very high frequency such that normal human eyes cannot see it flickering. This frequency is also called as flicker-free frequency (Marcu *et al.* 2018). All the nodes will be connected to a centralized micro-controller to assign specific flicker free frequencies to each node. These nodes will work as position beacons and OOK modulation is used to achieve to encode and broadcast the information. At the receiver side, the user will have proposed application installed in the mobile phone through which these positions will be decoded. The application requires mobile camera to identify the flickering pattern from the beacon and thus estimate the location. The aim is to harness rolling shutter phenomenon of camera to identify location and thus build an indoor positioning system.

The Li-Fi position beacons will be continuously flickering at specific frequencies. The proposed application will have a button on screen to trigger the process of finding current position. The algorithm will run in following stages on press of "Find Position" button after the mobile camera is below the beacon under FoV :

- Identify Region of Interest
- Find the number of stripes
- Find the average width of stripes
- Determine the distance between the beacon and receiver based on the number of stripes
- Determine position based on the average width of the stripes

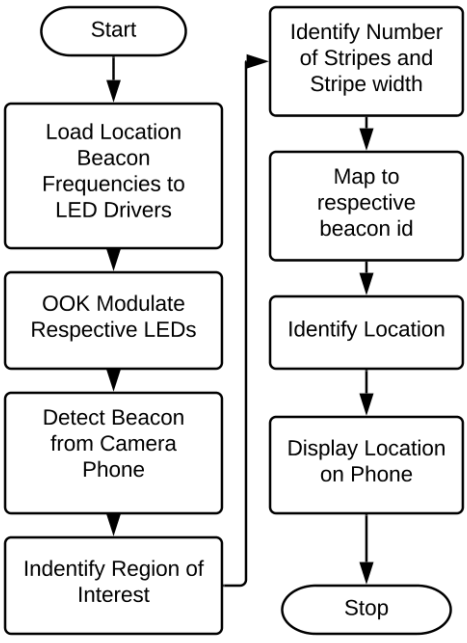

Figure 4.21: LiCamPos Block Diagram

Finally, the mobile application will get updated with the position and the same will be displayed on the mobile screen. It will use the location information to provide additional information about the location or location-specific ads. If the button is pressed when the beacon is outside the camera's FoV, then a "Location Unknown" message will appear. The proposed IPS application uses the results observed during the implementation of HFSPDM (Sec.4.5.1) to assign

beacon frequencies. The proposed application will aid most use cases that are driven by either: optimization, increased oversight, automation, or improved user experience.

Figure 4.21 shows flow of information in the proposed "LiCamPos" system. The process initiates with loading of beacon location information to LED drivers. Each beacon LED is mapped with predefined blink frequency. For example, beacon representing location "A" will blink at 800Hz. At the receiver side, user has to open the proposed mobile app and align the LED beacon in the camera FoV. When FoV of the receiver's mobile phone camera configured at 30 fps and exposure ISO3200 comes under beacon "A", it shows dark and bright stripes. The app has a button "Find Location" which starts video processing. The video is processed frame-by-frame and each frame undergoes same image processing steps as discussed in Sec. 4.2.4 which generates sequences of repeating zeros and ones. Number of zeros are counted between each successive ones to get width of stripes. All stripe widths are stored in a list over which an averaging function is applied to obtain final stripe width for corresponding frame. As this stripe width is in relation with blink frequency of "A", by identifying stripe width the location of "A" is successfully decoded. The entire image processing is implemented using OpenCV library of Python and then integrated in Andriod Studio. A key-value pair is used to provide location specific ad or message in the advertisement section of app.

Table 4.5: Experimental Setup

Parameter	**Value**
Exposure	ISO3200
Frame Rate	30FPS
Resolution	800x480
Video Bit Rate	2000Kbps

Table. 4.5 shows the camera parameter used for testing the proposed system. Open Camera App (Opencamera 2019) is used to change mobile camera characteristics. The OCC testbed setup built in Sec.4.4.1 is used to build the proposed application.

4.7 Results and Discussion

Three frequencies were selected based on clarity in observable stripe width difference to represent three locations as shown in Table.4.6.

Table 4.6: Frequency-Location Mapping

Name	**Frequency**	**Location**	**Advertisement**
F1	400Hz	A	This section shows additional information at A
F2	800Hz	B	This section shows additional information at B
F3	1200Hz	C	This section shows additional information at C

(a) Position A Distance 20 cm (b) Position B Distance 20 cm

Figure 4.22: Same distance variable position

Figure 4.22, shows screenshots of app under beacon position A and B at the distance of 20cm. Beacon A is blinking at 800Hz thus, number of stripes is less and width is more compare to beacon B. App shows decoded beacon information and distance from beacon based on stripe width and number of stripes as well as stored message specific to the location.

Figure 4.23 shows same beacon at variable distances. It shows that for beacon "A", as the distance increases the number of stripes decreases. Beacon "A" is decoded based on stripe width, while the distance is estimated based on number of stripes.

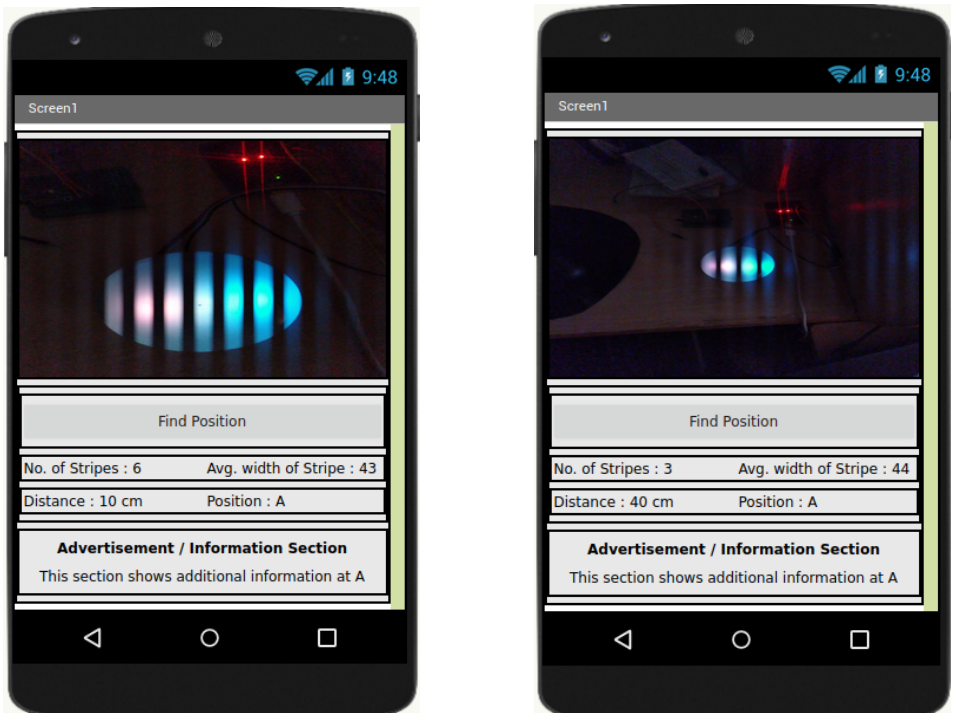

(a) Position A Distance 10 cm (b) Position A Distance 40 cm

Figure 4.23: Position A at varying distances

4.8 Summary

In this chapter, a novel rolling shutter based OCC modulation technique called HFSPDM was proposed and implemented on an in-house VLC testbed. Two other modulation techniques, OOK and BFSOOK, were implemented on the same testbed to compare their performances with the proposed technique. Through experiments, it was observed that as the distance between Tx and Rx increases the number of detectable stripes decreases independent of frequencies. It is mainly due to the decrease in size of RoI. As the distance increases RoI becomes smaller while the stripe width remains constant. These results helped in extracting distance information based on a number of detectable stripes. It was also observed that the stripe width decreases up to a certain level with an increase is frequency, however it starts increasing at higher frequencies. It is due to pixel bleeding and blurring of image which causes identification of edges difficult.

The best results for each technique were compared. It was observed that BFS-OOK provided consistent BER/bps of close to 0 for a frequency 200Hz while our proposed HFSPDM technique has shown BER/bps closer to 0.04. It was also observed that in HFSPDM, the number of frames required to transmit the same amount of data as that in BFS-OOK was considerably lesser but more than OOK;

it is due to the fact that HFSPDM represents, on average, 2 bits per 5 frames, whereas BFS-OOK represents 1 bit per 3 frames. The bit-to-frame ratio is higher in terms of OOK; however, HFSPDM gives better BER for longer distances than OOK as OOK is more sensitive to noise. Thus, it can be concluded that HFSPDM can be used in OCC applications that require low computation and high accuracy for comparatively longer distances.

As an extension to the work on HFSPDM, an IPS using VLC and OCC has been designed and implemented. In our proposed system, the use of rolling shutter phenomenon obtained images of LED beacon flickering at specific frequency with alternate bright and dark stripes. The relation between these stripe widths and frequency was used to estimate the user position, and the relation between number of stripes and distance was used to estimate distance from beacon. It was observed that the proposed IPS system works fine until the aperture size is large enough to be detected by the camera and stripe width is smaller that detected aperture. Finally, the android application housing the proposed system showed location specific messages when requested.

The proposed works used rolling shutter phenomenon to build a VLC system using readily available mobile phone camera. However, the dependence on the size of the Tx aperture, limits the achievable bandwidth and restricts the user movement. Thus, there is need to have more robust technique to achieve VLC using OCC.

Chapter 5

Proposed 2D pattern based Optical Camera Communication Techniques

Under OCC, the communication systems can be classified into rolling shutter and global shutter depending on the activation sequence of photosensors within the camera, as shown in Figure 5.1.

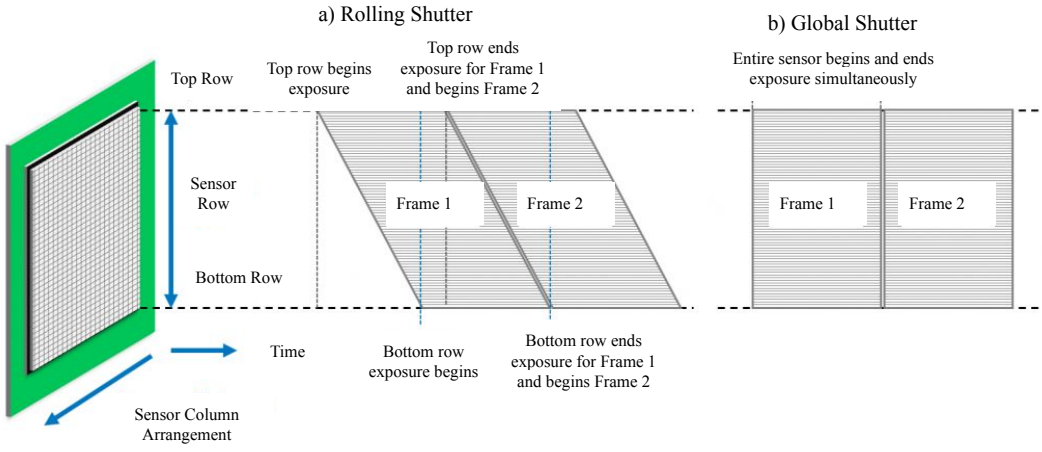

Figure 5.1: Sensor activation sequence in Rolling Shutter and Global Shutter

The rolling shutter effect is observed when the sensors are activated in row-wise or column-wise sequences one after the other within the 2D array of photosensors. While in global shutter, all the photosensors in the 2D array are activated simul-

taneously. VLC, Li-Fi, and OCC systems are inherently limited to IM/DD, which generally involves frequent switching 'on' and 'off' of LEDs. Thus, data can be modulated by controlling the parameters such as light intensity, blink frequency, and color, which can be observed by camera (Chavez-Burbano *et al.* 2017).

Although the OCC system based on rolling shutter can provide data rates up to 10-100 Kbps, the operational distance without external magnification is up to 2m and highly prone to errors (Nguyen *et al.* 2019*a*; Zinda *et al.* 2018). Thus, it is suitable only for such IoT applications that require fixed short-distance communication. However, IoT applications that require communication over larger distances and which have low data-rate demands can use global shutter or under-sampled rolling shutter-based OCC for communication.

With an aim to improve OCC communication distance and test the compatibility with IoT system, one novel pattern-based communication technique and two OCC-IoT-based applications are proposed in this chapter. A common hardware setup is used for each technique. For the proposed novel pattern-based OCC, the data to be transmitted is converted into a specially designed 8×8 pattern which is projected using 2D LED matrix. The pattern is extracted from video frames at the Rx side and compared with the dataset of patterns. A successful pattern match decodes and reconstructs data at the Rx side. The proposed technique is compared with the existing 8×8 pattern-based OCC technique with respect to the distance of communication.

Whereas for the two proposed OCC-IoT applications, the existing data representation patterns, i.e., QR-code and Aztec-code are adopted for OCC. Suitable RoI extraction and rotation compensation techniques are used to recreate the sensor data communicated by the Tx. The efficiency of the adopted patterns with each other and with previous work is compared.

The key contributions of the proposed work are:

- Design of a novel 8x8 LED pattern with balanced energy and entropy for robust long-distance detection and tolerance to minor intensity fluctuations.
- A simulation was built to evaluate and compare search algorithm speeds required for proposed pattern communication techniques by considering the distance and channel noise parameters.
- A Matlab application was built for real-time data communication using the proposed technique and its performance was evaluated based on ambient light intensity, distance, SNR, camera parameters, and BER(%).

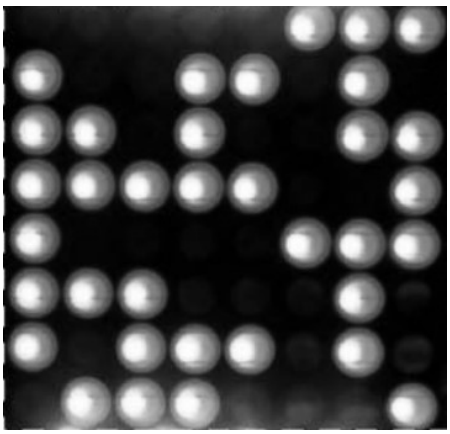

Figure 5.2: Video frame of data matrix pattern camera communication

- An IoT application was proposed, designed, implemented and evaluated using QR-code and Aztec-code patterns to communicate sensor data.

5.1 Related Work

In an OCC-based VLC system, rolling shutter-based techniques are more popular based on the amount of literature available over the internet. Rolling shutter-based modulation techniques generally involve high LED blink frequency which results in observable stripes in the video frames. Moreover, the width of these stripes can be changed based on incoming bits by controlling the delay between LED 'on/off' cycles. Thus, at the Tx side, the duration of LED 'on/off' cycle will be modulated depending on the data to be sent. While at the receiver side, the data is reconstructed by observing stripe widths and decoding the bits (Nguyen *et al.* 2016). An IPS was proposed and evaluated based on OCC-OOK modulation (Rêgo and Fonseca 2021) which encoded beacon ID. The beacon information was re-transmitted in loop fixed, and a data rate of 4 bits per frame was achieved. However, similar to other OCC-OOK system (Nguyen and Jang 2021*b*), the proposed system is vulnerable to errors, as the change in distance between transmitter and receiver changes the number of bits per frame. To overcome the limitation of direct OOK modulation, frequency-based modulation techniques such as FS-OOK (Le *et al.* 2014), BFS-OOK (Van Thang *et al.* 2018), Undersampled FS-OOK (U-FSOOK) (Roberts 2013) were proposed. Although these techniques provide more robustness and support for communication up to 2m, they are computationally more intensive and provide a low data rate than OCC-OOK. Moreover, Rolling Shutter (RS)-based OCC systems are dependent on the size of Tx aperture.

With an objective to improve the data rate and robustness of the OCC systems, active research is done in the domain of display-to-camera communication. A display screen is used to generate 2D patterns that will be captured and decoded on the Rx side. The selection of patterns that provide high information density and are detectable over the required long distance is the motivation of a few existing techniques. Several 2D data pattern representations are available; however, given the limited dimension of 2D LED array, only a few are realizable such as QR Code, Aztec code, and data matrix. Figure 5.2 shows a data matrix 8×8 LED transmitter. All the techniques require an anchoring pattern for alignment compensation at the receiver side. A data rate of 15 Kbps was achieved for multi-color 8×8 screen display (Nguyen *et al.* 2015). For the distance of 15cm, a throughput of 311.22 Kbps with an error rate of 10% was achieved for TETRIS (Stafford *et al.* 2017) using four colors, 10 fps frame rate, and 14×14 pixel color blocks. Based on similar work, the proposed system in the paper by Belyakov *et al.* (2020) demonstrated a bandwidth of 0.7 Mbps for a short distance of 20cm. Although it was observed that screen/display-to-camera communication systems provide higher data rates and robustness, they require dedicated display screens, which makes them less efficient. However, it can be used in specific application environments. Thus, to offload the requirement of dedicated high-cost displays, a relatively very low-cost LED matrix was used to achieve pattern communication (Nguyen and Jang 2021*b*). The author's proposed technique uses QR code-inspired patterns for transmitter identification and alignment, followed by an embedded data payload pattern. For a high-resolution camera, the system showcased pattern communication up to 20m distance with a low error ratio. In another work, an 8x8 LED matrix-based pattern communication technique was proposed and evaluated for inter-drone communication (Navya Deepthi *et al.* 2018). The system provided a high robustness data throughput of 64 bits per frame. A data matrix-based scalable transmitter was proposed in paper (Griffiths *et al.* 2019). The system can generate a data matrix of variable dimensions and showed BER $8.2x10^{-6}$ for 20m using a high-resolution camera. These works provided sufficient insight into the challenges, applications, and evaluation metrics for pattern-based OCC system. Various parameters such as entropy, uniformity, homogeneity, etc., were used to classify patterns and textures (Wang *et al.* 2020; Cavalin and Oliveira 2017; Hawashin *et al.* 2019).

These works provided an intuitive understanding of the proposed pattern's features. Our proposed work is inspired by these works to build a low-cost 2D LED array-based robust and long-distance supporting OCC-VLC system.

5.2 Proposed Work

The notations and their corresponding semantics which are used in the explanation of the proposed work and implementation are shown in Table.5.1.

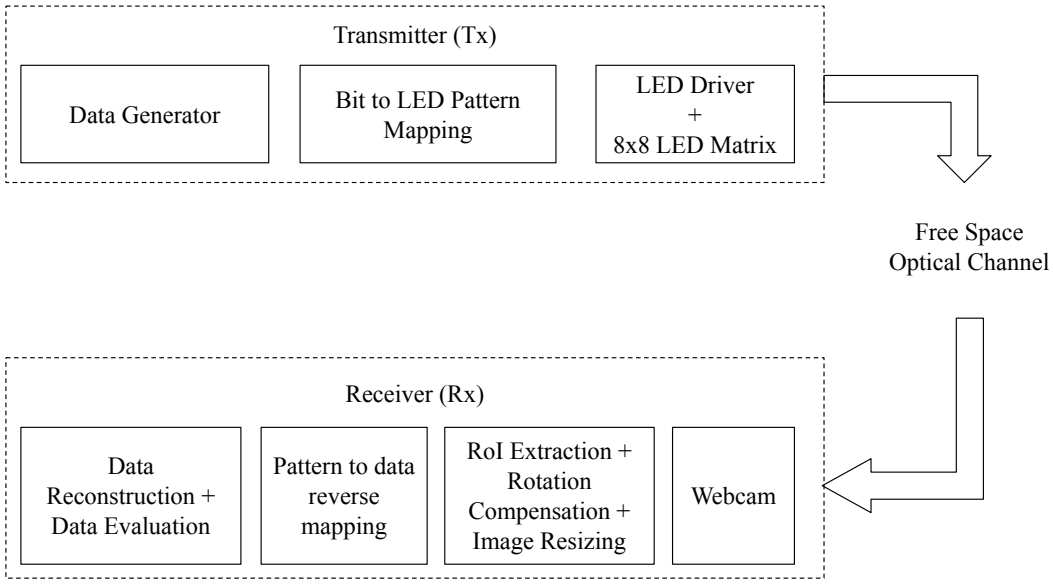

Figure 5.3: Functional block diagram of proposed system

The literature observed that recognition of images is a vital component in OCC pattern-based communication. However, as the distance between the source and camera increases, the pattern becomes less visible (Qv *et al.* 2019). Meanwhile, decoding each pattern takes more extensive computational time, which affects the achievable data rate. Hence, to achieve a high data rate by reducing computational time and longer communication distance, a texture-inspired novel, hierarchical image pattern classification-based approach for optical camera communication is proposed. The functional block diagram of the proposed system is as shown in Figure 5.3 where, the system is divided into two parts, namely as Tx and Rx. A static text file or data generator block will generate sequentially 8-bit data patterns. These patterns will be further mapped to the LEDs using a fixed rule. A single large pattern will be created using nested patterns, namely, the outer pattern (OP) and the inner pattern (IP). The mapped LEDs are then activated to transmit data. On the receiver side, images are captured at a fixed interval, and image pre-processing is performed to reconstruct data from the pattern. The pattern matching for the inner and outer patterns will be achieved in parallel by using multiple threads to reduce computational time for pattern recognition. The proposed pattern was created based on preliminary experiments on the data

Table 5.1: Notations for the proposed work

Notation	**Semantics**
OP	Outer Pattern
IP	Inner Pattern
GLCM	Gray-Level Co-occurrence Matrix
N	Number of gray levels in the image
$P_{i,j}$	Pixel intensity at position i, j
s	Size of the pattern (8, 4, or 2)
s_z	Size of the pattern dataset (2^s)
C_s	Binary representation of numbers from $2^s - 1$ to 0
D_s	Array to store the binary representation of numbers from $2^s - 1$ to 0
m	Pattern dataset matrix
m_s	Pattern dataset sub-matrix
y	Loop variable
SNR_{dB}	Signal-to-Noise Ratio in decibels
A	Signal power
B	Background noise power
n	Number of samples
P	Pixel brightness intensity
x	Number of pixel columns in the image
y	Number of pixel rows in the image
$Power$	Power of the image
N_{Err}	Number of error bits
N_{bits}	Total number of bits transmitted
BER	Bit Error Rate
$P1$, $P2$, $P3$, etc.	Positions in the 8×8 pattern matrix where 2×2 patterns are placed
N	2×2 matrix of 0s representing inactive LEDs
$L0$, $L1$, $L2$, $L3$, $L4$	2×2 binary patterns representing active LEDs mapped to bit "0" and corner patterns mapped to bit "1"
Example Pattern	Example pattern generated from the 8-bit data stream 10110111
Overall Pattern	Overall pattern matrix obtained by placing 2×2 patterns at fixed positions in an 8×8 binary matrix
Linear Search	A search technique where the complete 8×8 pattern is matched against a dataset of pre-generated images using all possible 8-bit combinations
Binary Search	A search technique where the pattern is divided into outer and inner patterns, which are matched separately against a dataset of pre-generated 4-bit patterns

Table 5.2: Comparison of Data Matrix Pattern vs Proposed Pattern

Parameter	Data Matrix	Proposed Pattern
Energy	0.2678	0.4399
Entropy	2.0028	1.6403

matrix pattern. Gray level Co-occurrence Matrix (GLCM) was used to evaluate the energy and entropy of the patterns as shown in Equations 6.1 and 5.2. Here, N is the number of gray levels in the image as specified by a number of levels under quantization, and $P_{i,j}$ is pixel intensity at position i, j.

The results in Table 5.2 show that, although the data matrix pattern can accommodate more information compared to the proposed pattern, however, the proposed pattern has higher energy than the data matrix, thus making the proposed pattern more clearly visible from long distances. The proposed pattern is described in detail as follows.

$$Energy = \sum_{i,j=0}^{N-1} (P_{i,j})^2 \tag{5.1}$$

$$Entropy = \sum_{i,j=0}^{N-1} -\ln(P_{i,j})\, P_{i,j} \tag{5.2}$$

5.2.1 Encoding of Bit Pattern

A base 2×2 pattern will be set at particular positions to obtain the final 8×8 pattern. The pattern and position of the base pattern will be determined based on the bit value and its index in a byte. Eight 2×2 binary patterns are positioned across an 8×8 binary matrix. 2×2 Binary patterns are named N, $L0$, $L1$, $L2$, $L3$, and $L4$, as shown in Eq. 5.3. Here, N is a 2×2 matrix of 0s implying inactive LEDs and inactive position, and $L0$ is a 2×2 pattern of 1s implying active LEDs mapped to bit "0". $L1$, $L2$, $L3$, and $L4$ are corner 2×2 patterns for top-left, top-right, bottom-left and bottom-right corners, respectively, mapped to bit "1".

$$N = \begin{bmatrix} 0 & 0 \\ 0 & 0 \end{bmatrix}, L0 = \begin{bmatrix} 1 & 1 \\ 1 & 1 \end{bmatrix}, L1 = \begin{bmatrix} 1 & 1 \\ 1 & 0 \end{bmatrix}$$

$$L2 = \begin{bmatrix} 1 & 1 \\ 0 & 1 \end{bmatrix}, L3 = \begin{bmatrix} 1 & 0 \\ 1 & 1 \end{bmatrix}, L4 = \begin{bmatrix} 0 & 1 \\ 1 & 1 \end{bmatrix} \tag{5.3}$$

In an 8×8 matrix, eight positions are fixed for setting the 2×2 patterns. The

eight positions are $P1$, $P2$, $P3$, $P4$, $P5$, $P6$, $P7$, and $P8$. The overall pattern appears as shown in Eq. 5.4

$$OverallPattern = \begin{bmatrix} P1 & N & N & P2 \\ N & P5 & P6 & N \\ N & P7 & P8 & N \\ P3 & N & N & P4 \end{bmatrix} \tag{5.4}$$

Where N is 2×2 non-active or zeros, 2×2 pattern $L0$ can be placed at any position depending on the position of 0 in an 8-bit binary stream. However, 2×2 patterns such as $L1$ can be placed only at $P1$ and/or $P5$, $L2$ can be placed at $P2$ and/or $P6$, $L3$ can be placed at $P3$ and/or $P7$, $L4$ can be placed at $P4$ and/or $P8$.

For example if the 8 bit data stream is 10110111, then its corresponding pattern would look like as shown in Eq. 5.5

$$ExamplePattern = \begin{bmatrix} L1 & N & N & L0 \\ N & L0 & L2 & N \\ N & L3 & L4 & N \\ L3 & N & N & L4 \end{bmatrix} \tag{5.5}$$

thus the corresponding of 8×8 binary matrix will look like

$$ExamplePattern = \begin{bmatrix} 1 & 1 & 0 & 0 & 0 & 0 & 1 & 1 \\ 1 & 0 & 0 & 0 & 0 & 0 & 1 & 1 \\ 0 & 0 & 1 & 1 & 1 & 1 & 0 & 0 \\ 0 & 0 & 1 & 1 & 0 & 1 & 0 & 0 \\ 0 & 0 & 1 & 0 & 0 & 1 & 0 & 0 \\ 0 & 0 & 1 & 1 & 1 & 1 & 0 & 0 \\ 1 & 0 & 0 & 0 & 0 & 0 & 0 & 1 \\ 1 & 1 & 0 & 0 & 0 & 0 & 1 & 1 \end{bmatrix} \tag{5.6}$$

Here $[P1,P2,P3,P4,P5,P6,P7,P8]=[1,0,1,1,0,1,1,1]$. Position $P2$ and $P5$ have 0; thus, the corresponding 2×2 binary pattern will be $L0$. Since the rest of the positions have binary 1, it is replaced with its corresponding 2×2 pattern. Such as $P1$ is replaced by $L1$, $P3$ by $L3$, $P4$ by $L4$, $P6$ by $L2$, $P7$ by $L3$, and $P8$ by $L4$. The outer positions $P1$, $P2$, $P3$, and $P4$ correspond to the first 4 bits of the 8-bit data stream, while inner positions $P5$, $P6$, $P7$, and $P8$ correspond to the remaining 4 bits of the 8-bit data stream. Binary 1 represents the LED 'on' state,

whereas binary 0 represents the LED 'off' state. The overall steps involved in encoding via simulator are described in detail in the Section 5.2.3. The generated pattern layered with noise and background for the simulator is stored in a folder. In contrast, while sending the same via hardware, the matrix is provided as input at the transmitter side, which is then mapped to an 8×8 LED matrix. A connected Arduino board controls the active state of LEDs.

5.2.2 Decoding of Bit Pattern

For decoding, a comparison has to be drawn between two search techniques, i.e., linear search and binary search. The dataset for linear pattern search will be a set of pre-generated images using all possible 8-bit combinations. In comparison, the dataset for binary pattern search will be all possible 4-bit combinations. Thus, linear search will have 256 8×8 binary matrices to search from, while binary search will have 16 4×4 binary matrices to search. The binary search will match the pattern separately for the 4×4 outer and inner pattern, whereas the linear search will match the complete 8×8 pattern. For instance, considering the above example of $[P1,P2,P3,P4,P5,P6,P7,P8]$=[1,0,1,1,0,1,1,1], the received pattern will be as shown in Eq. 5.6. The pattern will be at the 183rd index in the linear search dataset. After conversion to binary, this index produces back the transmitted 8-bit data. On the other hand, in level 1 binary search, the same pattern will be divided into two subpatterns, OP and IP. Thus, after removing the N from the example pattern as shown in Eq. 5.5, the OP will be as shown in Eq. 5.7, and the IP will be as shown in Eq. 5.8

$$OP = \begin{bmatrix} L1 & L0 \\ L3 & L4 \end{bmatrix} = \begin{bmatrix} 1 & 1 & 1 & 1 \\ 1 & 0 & 1 & 1 \\ 1 & 0 & 0 & 1 \\ 1 & 1 & 1 & 1 \end{bmatrix} \tag{5.7}$$

$$IP = \begin{bmatrix} L0 & L2 \\ L3 & L4 \end{bmatrix} = \begin{bmatrix} 1 & 1 & 1 & 1 \\ 1 & 1 & 0 & 1 \\ 1 & 0 & 0 & 1 \\ 1 & 1 & 1 & 1 \end{bmatrix} \tag{5.8}$$

These patterns will be parallelly searched by two separate threads and using a shared dataset of all 4×4 pre-generated patterns. Thus, the outer pattern will be found at the 11th index and the inner pattern at the seventh index. The outer pattern will be decoded to produce the first 4 bits of the data, i.e., 1011, whereas

the inner pattern will produce the remaining 4 bits of the data, i.e., 0111. Finally, the decoded data from outer and inner patterns will be combined to produce 8-bit data, i.e., 10110111. Similarly, in level 2 binary search, eight threads will be spawned for one 2×2 position; however, decoding requires only one comparison with $L0$.

The decoding process will be standard for hardware as well as simulation. However, for simulation, the input will be a folder containing code-generated images, while for hardware, the camera will capture pics of the transmitter in real-time. To test the performance of the proposed technique, a comparison between linear search and binary search will be drawn based on the time taken to identify the patterns. Based on these results, the performance of proposed BHIPC-based OCC techniques will be evaluated. Experiments will be conducted to record intensity profiles of the pattern from various distances; this would provide an intuitive understanding of how effectively the pattern can be decoded.

The decoding process will be standard for hardware as well as simulation. However, for simulation, the input will be a folder containing code-generated images, while for hardware, the camera will capture pics of the transmitter in real-time. To test the performance of the proposed technique, a comparison between linear search and binary search will be drawn based on the time taken to identify the patterns. Based on these results, the performance of proposed BHIPC-based OCC techniques will be evaluated. Experiments will be conducted to record intensity profiles of the pattern from various distances; this would provide an intuitive understanding of how effectively the pattern can be decoded.

Furthermore, experiments will be conducted to understand the effects of camera parameters on SNR. This would provide optimal parameter values for the best SNR, set for further experiments. BER of the proposed technique is recorded at various distances, following which for a fixed optimal distance, BER is evaluated for various data rates compared to linear search. Finally, the BER of the proposed technique is compared with existing techniques for a fixed resolution of 160×120 at varying distances. The percentage improvement is evaluated as per Eq. 5.9, where BER_e is BER for the existing technique and BER_p is BER for the proposed technique.

$$\%improvement = \frac{BER_e - BER_p}{BER_p} \times 100 \tag{5.9}$$

The proposed technique is implemented using simulation and hardware.

5.2.3 Simulation Implementation

For implementing transmitter and receiver simulation, a licensed Matlab R2019a tool was used on the system with configuration as Intel-i7-770 CPU and 16GB RAM. The detailed flowchart is as shown in Figure 5.4. Here, a text file containing random data is provided as input. This file is opened and read to extract the contents one byte at a times. Each bit of the byte is mapped with a pattern and position as discussed in Section 5.2.1. This would generate a 2D 8×8 binary matrix which is converted to an image. The image is then overlayed over a predefined camouflage image to simulate real world transmitter background. A fixed Gaussian noise is added to the image to simulate channel noise. The conversion of read data to the simulated image is repeated ten times. A counter is maintained; as soon as the count reaches ten, a predefined image is transmitted to aid RoI extraction, and the counter is reset. The coordinates of the extracted RoI are used for each successive RoI extraction directly. The final generated image is stored at a fixed location with a naming convention as "img_xxx.jpg". Where 'xxx' is the image number, for example, "img_012.jpg". This naming convention is helpful while reading the images from the folder during the simulation of the receiver. The process stops once the file is completely read. The transmitter simulation is initiated as soon as the process of the simulated receiver ends.

The flowchart for the simulated transmitter is as shown in Figure 5.5. On the transmitter side, the process starts with input as the folder's location where all the converted images are stored. A loop will run for the total number of files in the folder. For each iteration, a Gaussian filter is applied to remove noise. Initial few iterations will be used to identify the base pattern to set the RoI bounding box. Once the base pattern is identified and RoI coordinates are extracted, RoI from each next image will be directly cropped. This image will then be resized to 8×8 and binarized. The obtained 8×8 binary matrix will then be searched from the dataset based on the searching technique selected. The dataset is generated as per Algorithm 18 after the selection of the searching technique, i.e., linear, binary level 1, or binary level 2. For linear, the pattern size will be 8×8; hence s is set to 8; similarly, for binary level 1 and level 2, s will be set to 4 and 2, respectively. All the patterns generated will be stored in the form of a 3 dimensional (3D) matrix.

Thus, for linear search, the dataset is of dimension $8 \times 8 \times 256$, while for binary level 1, it is $4 \times 4 \times 16$, and for binary level 2, it is $2 \times 2 \times 4$. The reconstruction method of a byte is different for each selected search option. For linear search, the index of the matched pattern is directly converted to 8 bits. At the same time, for

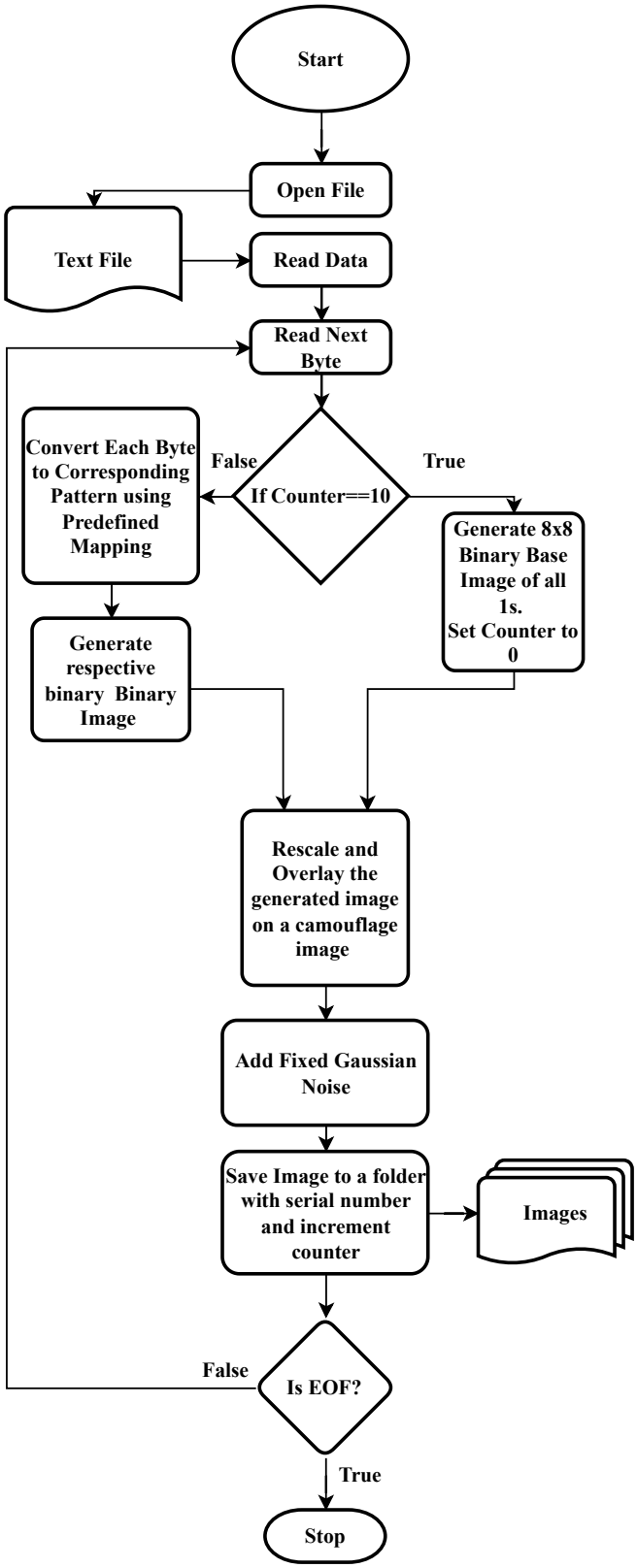

Figure 5.4: Flowchart of simulated proposed 2D pattern based OCC Encoding

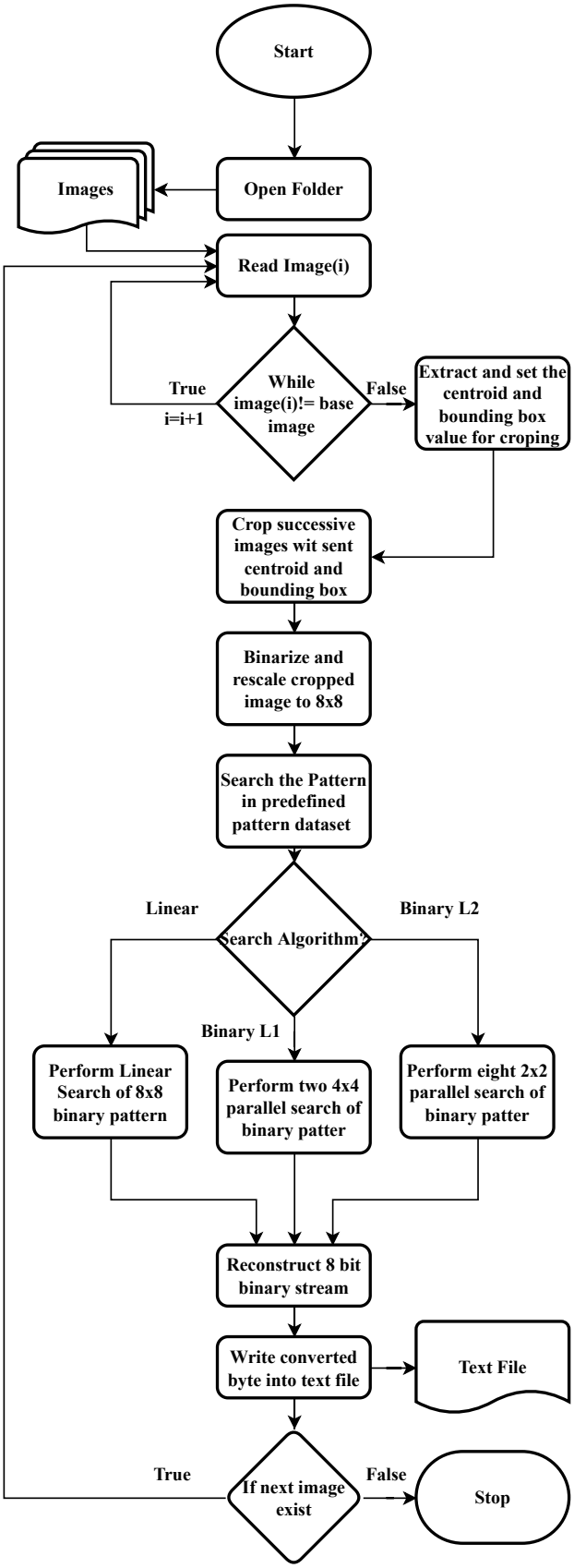

Figure 5.5: Flowchart of simulated proposed 2D pattern based OCC Encoding

binary level 1, it is obtained as a concatenation of converted binary indices of the outer and inner pattern. 8 bits generated by binary level 2 is the concatenation of critical indices for each 8 position.

The simulation does not consider the errors introduced due to asynchronous transmitter frame rate and receiver transmission rate. Thus, 100% accuracy is expected for complete data transfer. However, to prove that the proposed pattern with binary search provides faster results, the time taken for each search based on the selected search technique is maintained. A comparison is drawn between linear, binary level 1, and binary level 2.

Algorithm 18 Pattern Dataset Generator

Require: $s = 8, 4, 2$
Ensure: $m = zeros(s, s, 2^s)$
  $s_z = 2^s$
  $C_s = dec2bin(2^s - 1 : -1 : 0) -' 0'$
  $D_s = zeros(1, s)$
  for $y = s_z : -1 : 1$ **do**
    $D_s = C_s(y, :)$
    $m_s(1:2, 1:2, (s_z + 1) - y) = state(D_s(1), 1)$
    if $s > 1$ **then**
      $m_s(1:2, s-1:s, (s_z + 1) - y) = state(D_s(2), 2)$
      if $s > 2$ **then**
        $m_s(s-1:s, 1:2, (s_z + 1) - y) = state(D_s(3), 3)$
        $m_s(s-1:s, s-1:s, (s_z + 1) - y) = state(D_s(4), 4)$
        if $s > 2$ **then**
          $m_s(s/2-1:s/2, s/2-1:s/2, (s_z + 1) - y) = state(D_s(3), 3)$
          $m_s(s/2-1:s/2, s/2+1:s/2+2, (s_z + 1) - y) = state(D_s(4), 4)$
          $m_s(s/2+1:s/2+2, s/2-1:s/2, (s_z + 1) - y) = state(D_s(3), 3)$
          $m_s(s/2+1:s/2+2, s/2+1:s/2+2, (s_z+1)-y) = state(D_s(4), 4)$
        end if
      end if
    end if
  end for

5.2.4 Hardware Implementation

The hardware requirement for the implementation of the proposed technique is shown in Table 5.3. Like the simulated transmitter, byte by byte data is converted to an 8×8 pattern at the transmitter side.

An Arduino Uno connected to an 8×8 LED matrix is used to activate specific LEDs per the required pattern. The delay between successive pattern projections

Table 5.3: Hardware Requirements

Hardware	Model	Use
Programmable Board	Arduino UNO	To convert incoming data into 8x8 binary and map to 2D LED Array
8x8 LED Array	WS2812B-64	To illuminate LEDs based on the received pattern
Webcam	Logitech c270	To record video and decode patterns.

can be changed, and thus, the transmission data rate can be controlled. For example, if the delay is kept at 1000 milliseconds, the transmission data rate is 8 bits per second.

Algorithm 19 Common Image Preprocessing

1: Convert image to grayscale
2: Enhance the contrast
3: Binarize the image
4: Dilute the image
5: Find dimensions of the brightest and largest blob
6: Mask the background
7: Crop the original image
8: Apply rotation compensation using Feature Matching
9: Resize the cropped image to 8x8 based on found ROI
10: Grayscale, Enhance Contrast and Binarize the Cropped Image

The camera is set to continuously capture images with a delay value satisfying the Nyquist Sampling requirement at the receiver side. The selected camera provides a maximum resolution of 720p and supports up to a 30 FPS frame rate. However, the resolution is set to the lowest 160×140 pixels for the experiments. Each captured image frame undergoes pre-processing as shown in Algorithm 19 and provides an 8×8 binary matrix. This binary matrix is then searched across the dataset per the selected searching technique and reconstructed data. The reconstructed data is stored in a file. The received data and transmitted data are compared to identify errors. Based on the number of error bits at the receiver and the total number of bits transmitted BER is evaluated as shown in Eq. 5.10. Here, N_{Err} is the number of error bits, and N_{bits} is the total number of bits transmitted.

$$BER(\%) = \frac{N_{Err}}{N_{bits}} \tag{5.10}$$

To evaluate the signal quality under various conditions SNR_{dB} is calculated as

per Eq. 5.11, where, A is the signal power and B is background noise power, n is the number of samples.

$$SNR_{dB} = 10 \times \log \frac{\sqrt{\frac{1}{n}\sum_{i=0}^{n-1} |A_i|^2}}{\sqrt{\frac{1}{n}\sum_{i=0}^{n-1} |B_i|^2}} \tag{5.11}$$

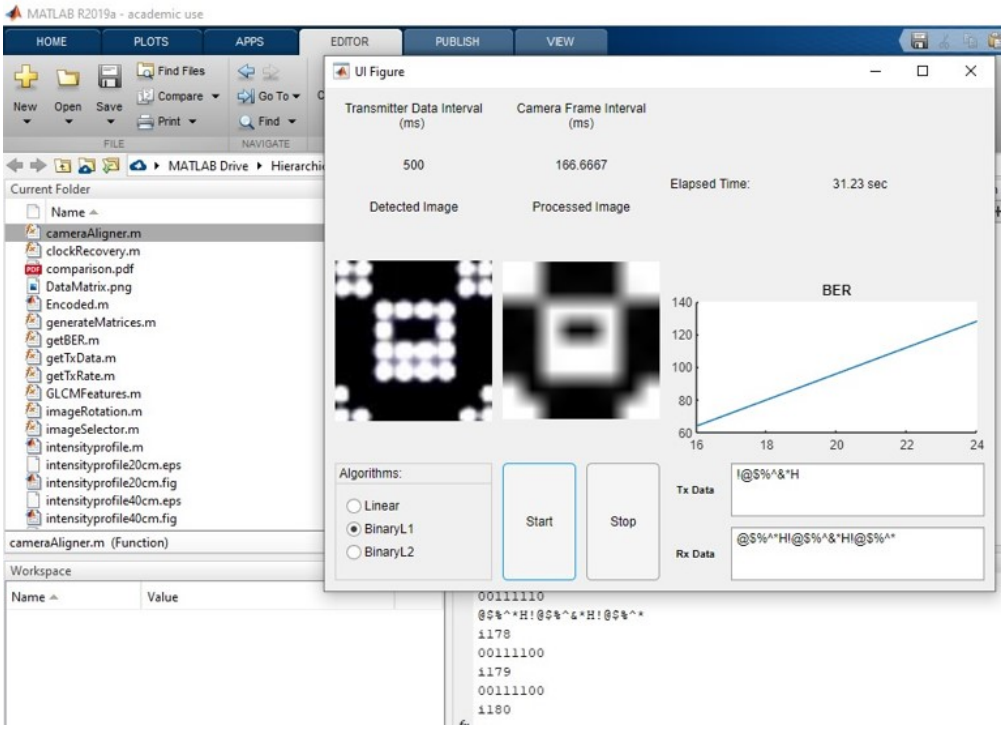

Figure 5.6: Screenshot of Matlab application built for conduction of experiments and evaluation of proposed technique.

The signal and noise power are estimated as the vector sum of pixel intensities for each column for a grayscaled image as shown in Eq. 5.12; here, P is the pixel brightness intensity, and x and y are the numbers of pixel columns and rows in the image. Thus, when the transmitter is activated, the overall power will be higher compared to when it is inactive.

$$Power = \sum_{j=1}^{y}\sum_{i=1}^{x} P_{ij} \tag{5.12}$$

A front end is created using Matlab app as shown in Figure 5.6 for ease of conducting experiments. It provides options for selecting search algorithms and displays raw and processed images, frame rate, transmission rate, transmitted data, received data, the time elapsed, and BER.

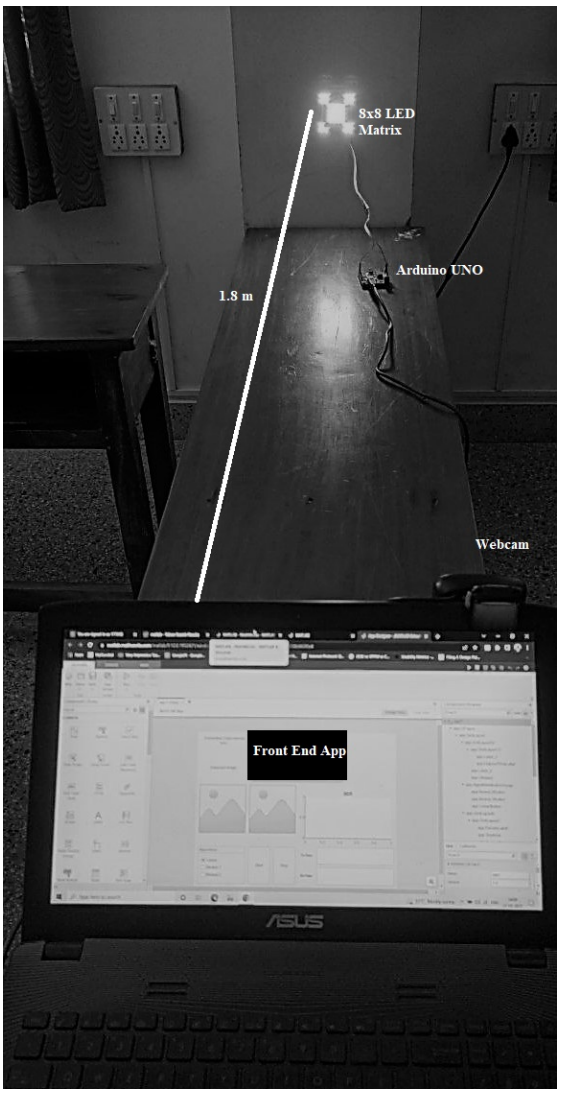

Figure 5.7: Experimental Setup, with 8x8 LED Matrix, Arduino UNO, Webcam and App Front end.

The transmitter is mounted on a wall; the receiver is positioned perpendicular to the wall at LoS distance, as shown in Figure 5.7

A comparison between the simulated results and implemented hardware is drawn for testing the proposed system. The parameters like computational time of decoding, BER, and distance are considered for evaluation.

5.3 Results and Discussion

In this section, the experimental results are discussed. Experiments are categorized into subsections based on stages of implementation of the proposed technique. These sub-sections are distance vs. intensity profile, performance evaluation of

search techniques, camera parameters vs. SNR, BER evaluation of the proposed technique, and comparison with existing techniques.

5.3.1 Distance vs Intensity Profile

An experiment was conducted to observe the intensity profile of the transmitter at various distances. Figure 5.8 shows the images of the transmitter after pre-processing. It can be observed that with the increase in distance for a selected fixed resolution, the image quality degrades.

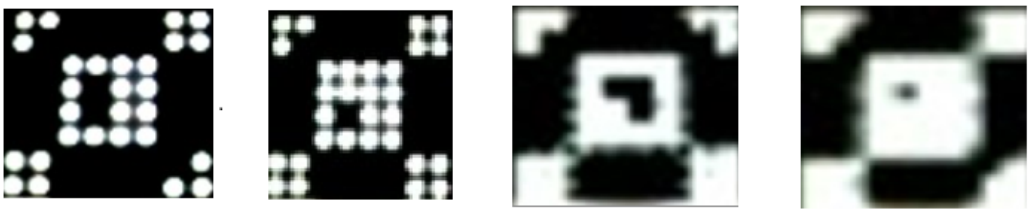

Figure 5.8: Final cropped transmitter image at distances 20cm, 40cm, 100cm and 200cm respectively (left to right)

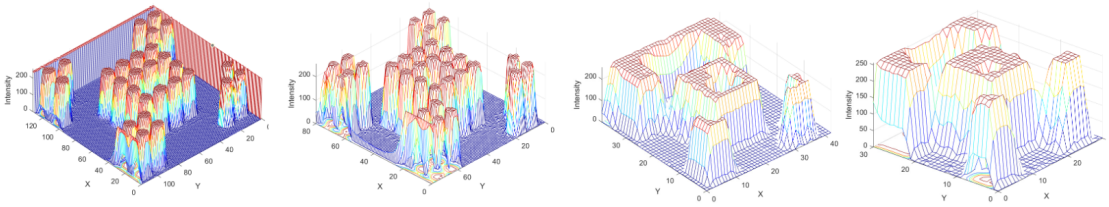

Figure 5.9: Intensity Profile of transmitter at distances 20cm, 40cm, 100cm and 200cm respectively (left to right)

It was also observed from Figure 5.9 that pixel intensity becomes more scattered and overlaps with neighboring pixel intensity. It leads to incorrect resizing of the image to an 8×8 binary matrix. Further experiments were conducted to analyze the impact of this limitation on BER.

5.3.2 Performance Evaluation of Search Techniques

Figure 5.10 shows the comparison of computational time for searching 2D 8×8 patterns from the dataset using the selected technique using simulation. All possible 8-bit patterns were generated from '00000000' to '11111111' and searched individually. The time taken for each key search was recorded and plotted. As the key becomes more extensive, the computational time for linear search increases,

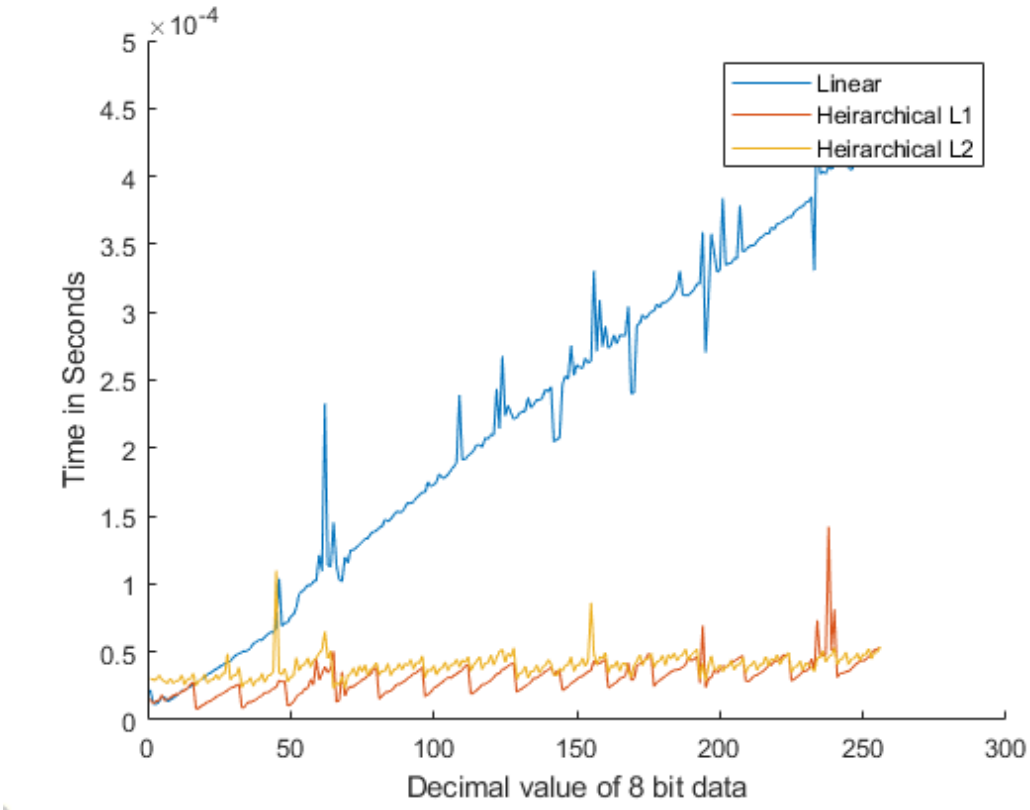

Figure 5.10: Comparison between Linear, Binary Level 1 and Binary Level 2 algorithms based computational time for searching a 2D 8X8 patterns using Simulation

while the computational time for binary level 1 and level 2 search techniques remains minimum. It was also observed that between binary level 1 and level 2 algorithms, level 1 provides faster decoding. It could be that level 2 requires more time to decompose the pattern and reconstruct it from 8 threads. The reason can also be justified based on the initial key search results,i.e., for keys 1-5, where level 2 under-performs compared to the other two techniques.

Similar experiment was performed using hardware, where data was read from a file, transmitted, received, and decoded. The computational time for searching each pattern was recorded and plotted as shown in Figure 5.11. It was observed that linear search shows drastic changes in the search times, and it is consistently higher than binary level 1 and level 2 search. It was also observed that binary level 2 shows a spike during initial searches and then drops to a minimum and is consistent. However, Binary level 1 provided a more stable and low computational search than the other two. These experiments established that the proposed technique provides better results with respect to computational time. Thus, further experiments were conducted on the impact of camera parameters and environment

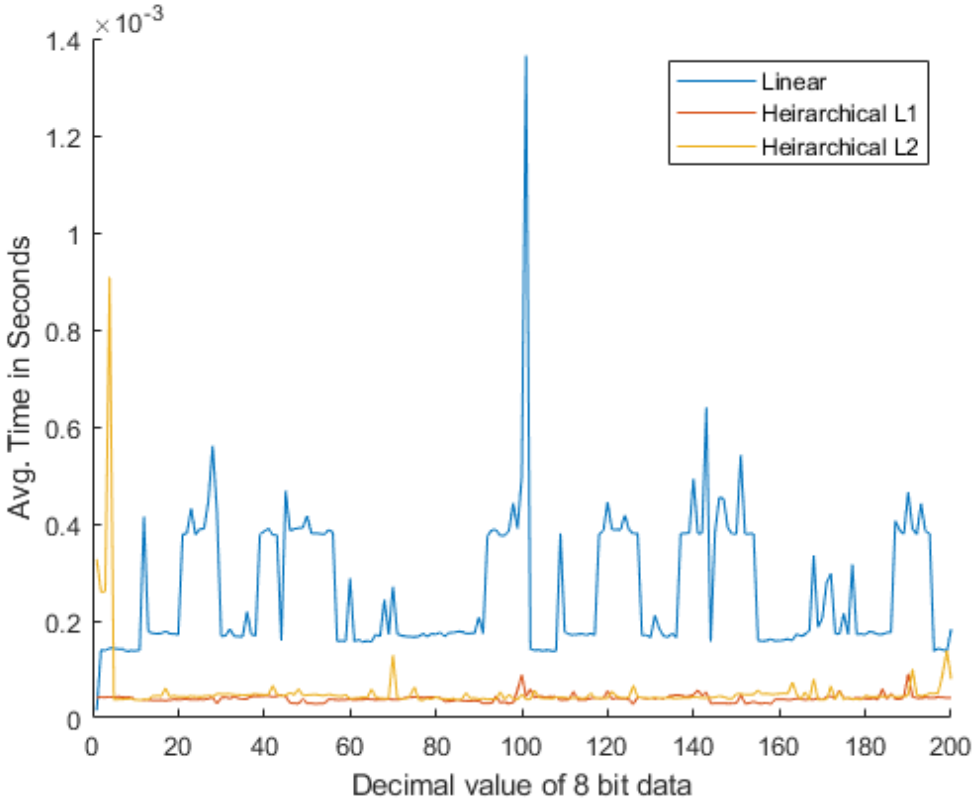

Figure 5.11: Comparison between Linear, Binary Level 1 and Binary Level 2 algorithms based computational time for searching a 2D 8X8 patterns using Hardware.

on BER.

5.3.3 Camera Parameters vs SNR

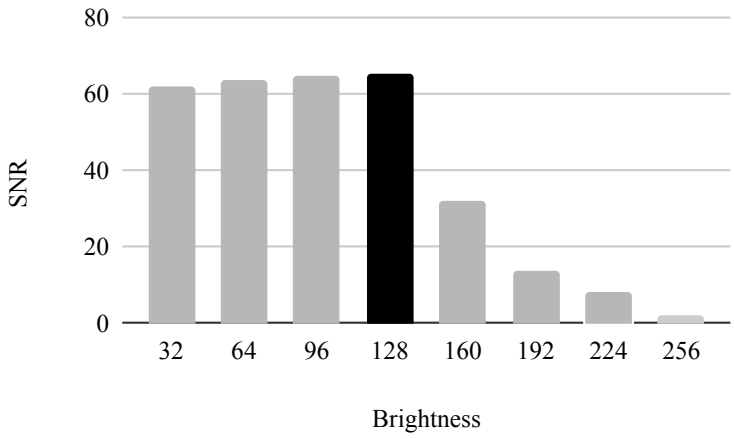

Figure 5.12: For the fixed distance of 20 cm and ambient light intensity of 12 lux the SNR value drastically drops beyond the brightness parameter 148.

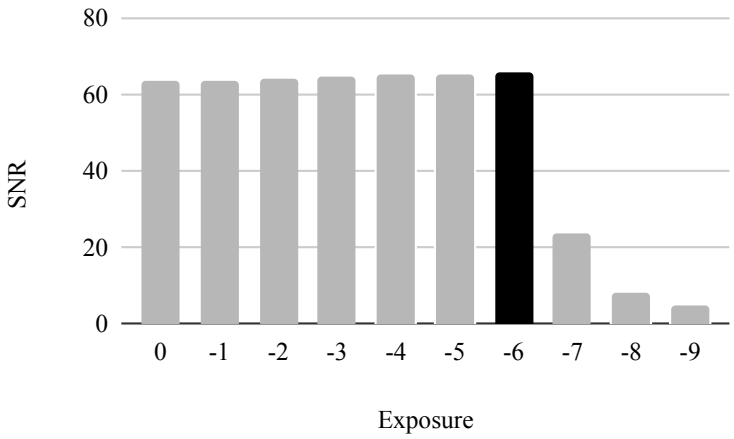

Figure 5.13: For the fixed distance of 20 cm, ambient light intensity of 12 lux and brightness parameter as 128 the SNR value drastically drops beyond the exposure parameter -6

Before evaluating BER, experiments were conducted to select optimal camera parameter values. The ambient light intensity was 10-20 lux during the conduction of all experiments. A darker shade of grey is used to depict the optimal value in the following results.

The Matlab webcam object supports brightness levels between 0-255. Figure 5.12 shows that initially, the SNR was increasing till it reached the maximum at 128; however, a sudden drop in SNR value is observed, which continues to drop further with an increase in brightness value. As the brightness value increases, the overall image intensity increases; thus, the difference between signal and background noise power decreases. Thus, the brightness value is 128 for further experiments since it provided maximum SNR.

Further, experiments were conducted to select the optimal exposure value. Matlab webcam supports exposures in the range of 0 to -9. Figure 5.13 shows the results of the experiment. It was observed that an exposure value of -6 provides maximum SNR and it drops drastically after -7 because of decreasing difference between signal and noise power.

A similar experiment was conducted to identify the optimal contrast value. Matlab webcam object supports contrast levels from 0 to 255. Figure 5.14 shows the results of the experiment. It was observed that for contrast level 96, the setup provides maximum SNR. SNR remains almost constant for any further increase in contrast level.

Finally, experiments were conducted to identify the optimal distance. Figure 5.15 shows the results of the experiments, where other camera parameters are set

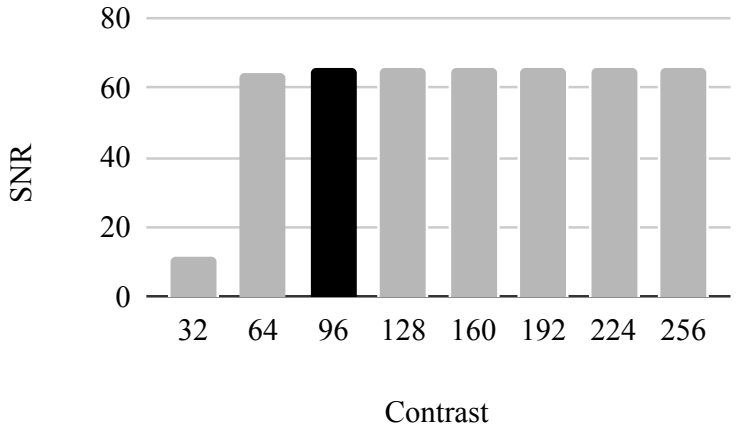

Figure 5.14: For distance=20 cm, ambient light intensity = 12 lux, brightness parameter=128 and exposure=-6 highest observed SNR was for contrast parameter 96.

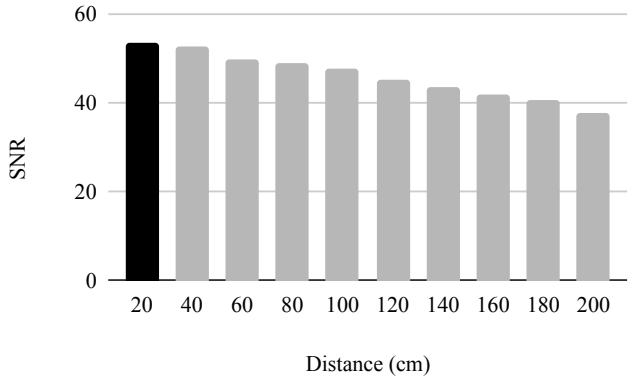

Figure 5.15: For ambient light intensity = 12 lux, brightness parameter=128, exposure=-6, contrast=96. the highest SNR was observed at 20cm and gradually drops with increasing distance.

as per the results of previous experiments. At a distance of 20 cm, the setup provides maximum SNR and decreases gradually as the distance increases. At a shorter distance, the transmitter size to image size ratio is more; thus, the signal power is high.

5.3.4 BER Evaluation

BER is measured for all three search algorithms: linear, binary level 1, and binary level 2. The results are as shown in Figure 5.16. It was observed that the search algorithm provided better results for lower transmission rates as the BER(%) was low. It was also observed that binary level 1 and level 2 search algorithms showed

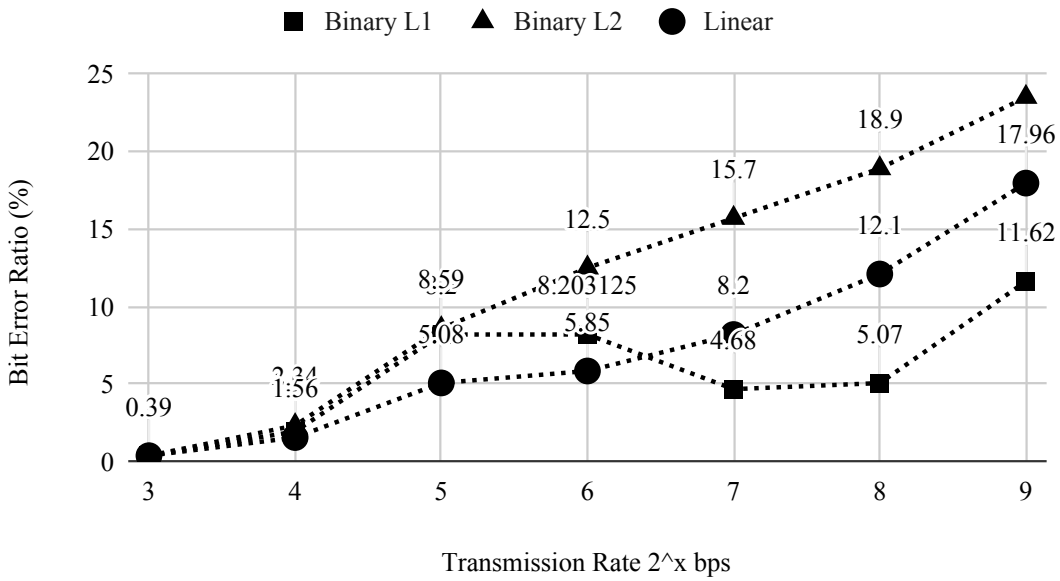

Figure 5.16: For ambient light intensity = 12 lux, brightness parameter=128, exposure=-6, contrast=96 and distance 100 cm, Binary L1 shows better performance for higher bit rates.

higher BER than linear for low transmission rates. The linear algorithm performs faster decoding for a fixed set of inputs. Here, since the given input was a text from a file, the linear algorithm has to search for a maximum of 176 keys. Binary level 2 consistently provided higher BER, which kept increasing with the transmission data rate. It is assumed to be due to the additional computational overhead of fragmenting the pattern into eight threads and combining it. An interesting result was observed for binary level 1 for a higher transmission data rate. At the data rate of 128 bps, binary level 1 outperforms the other two search techniques and consistently gives better performance than linear and binary level 2. This behavior shows that although binary level 1 provided faster search results for a low bit rate, it performed the exact key searches multiple times due to high delay between successive frames. However, as the transmission data rate increased, the inter-frame delay was reduced; due to this, the number of repeated searches was reduced, providing faster search results.

Similarly, linear search shows poor performance for higher data rates as the average search time for each key is higher than the inter-frame delay. Thus, when the search result of one key is received, a few frames are already dropped, which increases BER. The proposed pattern communication technique works well with binary level 1 search for higher data rates.

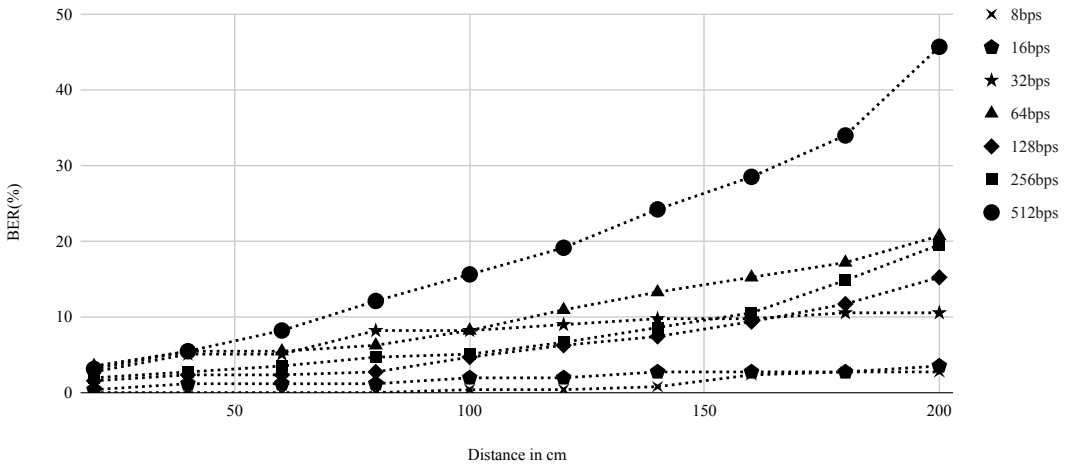

Figure 5.17: BER vs Distance vs Transmission Data Rate of Binary Level 1 Search for proposed pattern communication

Based on the observations, an experiment was conducted to test the performance of the proposed pattern communication with binary level 1 search at varying distances for different transmission data rates. The results of the experiment are as shown in Figure 5.17. The proposed hierarchical pattern communication technique works best with binary search level 1 for low data rates up to 2m distance. The optimal BER for maximum distance and bit rate is observed for 200 m and 256 bps. For higher bps, the system shows degrading performance.

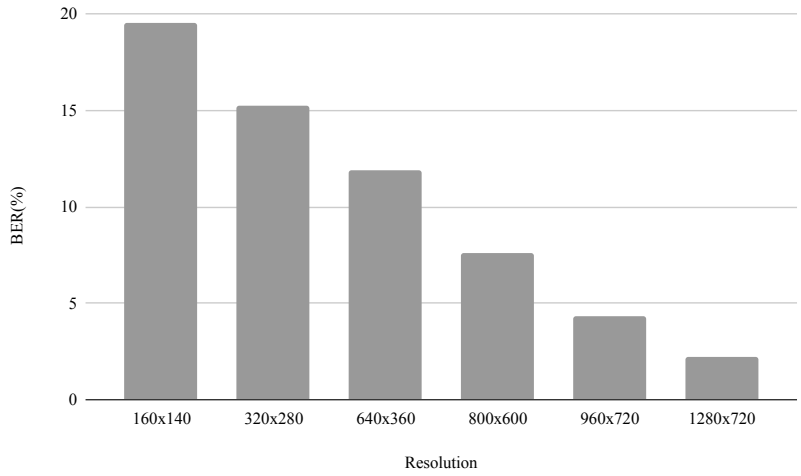

Figure 5.18: For distance of 2m, the graph shows BER(%) for various resolutions

Since the selected resolution was 160 × 140 for all the experiments, an experiment was conducted to analyze the impact of higher resolution on the BER of

the proposed technique. Figure 5.18 shows the observed results, which imply that for higher camera resolution, the BER experiences improvement. It is mainly because the pattern in the RoI extracted image becomes sharper as the resolution increases. Thus, a communication distance of more than 2m can be achieved with more accurate RoI detection techniques.

5.3.5 Performance Comparison

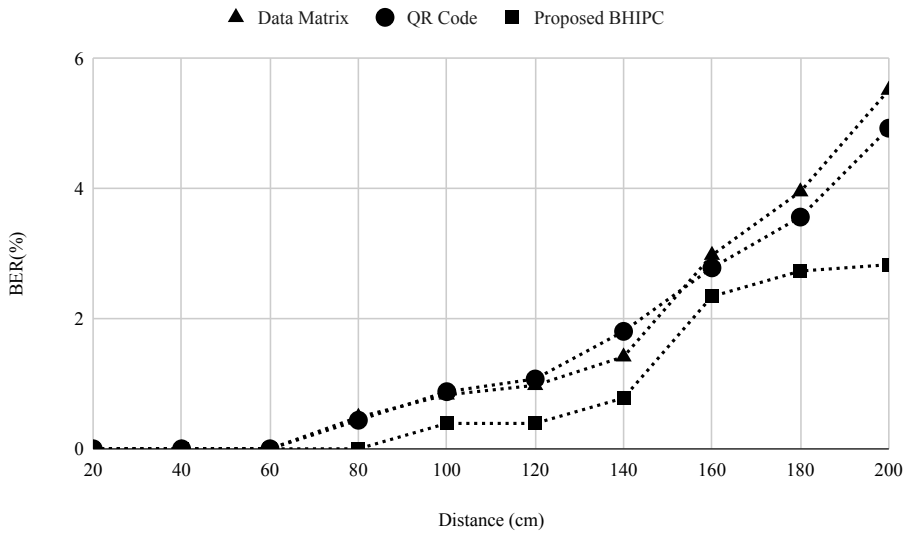

Figure 5.19: Proposed pattern communication technique is compared with existing pattern communication techniques.

Finally, the proposed technique was compared with data matrix and QR code pattern communication techniques by keeping the resolution to 160x140 for varying distances. BER(%) was compared between each technique, and obtained results are as shown in Figure 5.19. For the distance of 2m, the proposed pattern communication technique provided 48.6% and 42.5% improvement in BER compared to data matrix and QR code pattern-based communication techniques, respectively. Due to the close arrangement of active LEDs in the data matrix and QR code pattern, it causes pixel blurring and thus, contributes to quantization error while resizing the image to an 8×8 binary matrix. However, it must also be noted that since the data matrix and QR code pattern accommodate considerably more bits per image frame compared to the proposed technique, BER is more sensitive to quantization errors.

5.4 Applications

In this section, the experimental setup built for BHIPC, is used to implement and evaluate two proposed applications to showcase integration of pattern-based OCC with IoT. QR code and Aztec code patterns are used to communicate sensor data using proposed frame formats between IoT device (Tx) and camera (Rx). The discussion is divided into 6 subsections, namely as, overall system architecture, anchor points, frame format, decoding and evaluation metrics.

5.4.1 Overall System Architecture

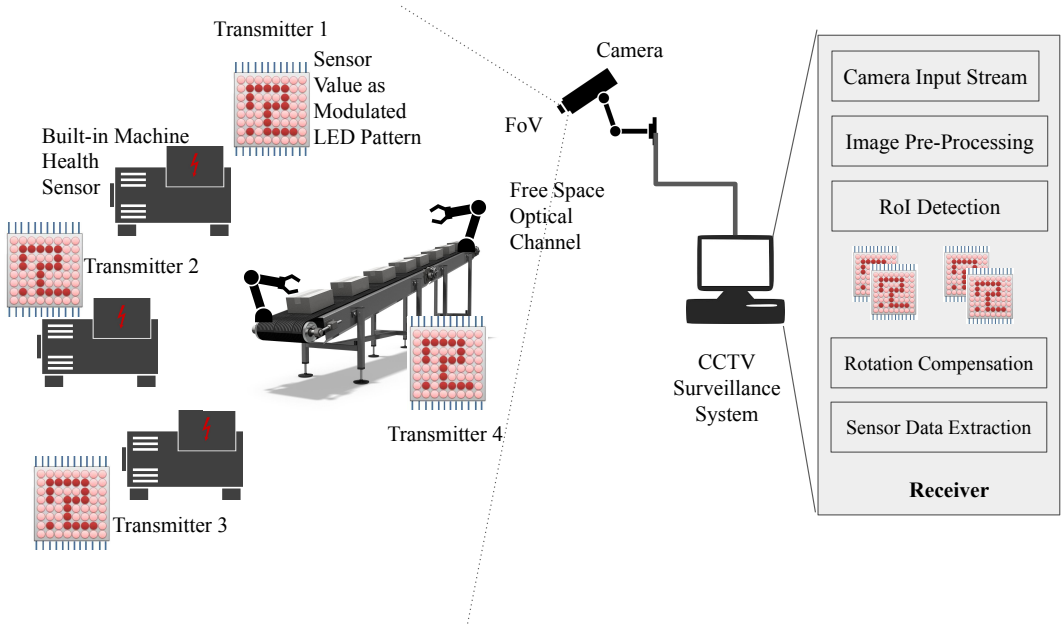

Figure 5.20: Proposed LiCamIoT System

The overall proposed architecture of both the techniques are similar with respect its integral modules. However, the arrangement data payload in the 8×8 pattern differs.

Figure 5.20 shows the division of proposed system into two parts, i.e., Tx and Rx, separated by the free-space optical communication channel. The left part of the figure shows various industrial machines with inbuilt sensors. The reading from these sensors will be converted to an 8×8 LED pattern based on the proposed frame format. Each machine can be identified using a unique ID pattern. Assuming that the industrial area is under CCTV surveillance, a camera will capture frames of the environment as per its FoV, including the LED matrix. The captured image will undergo image pre-processing for RoI extraction. The

extracted RoI will be rotated if needed to fit the bounding box. Finally, the rotated image will be cropped and resized to 8×8 matrix for pattern matching and decoding. The decoded bits will be combined to reconstruct the transmitted data. The complete process detail is mention in the upcoming sections.

5.4.2 Anchor Points

Anchor points in a pattern are fixed set of points which are used for aligning the pattern before decoding. The proposed 8×8 pattern for QR code will be divided into 4 regions as shown in Figure 5.21. Each region is having its corresponding importance. The region colored in green represent anchoring pattern. This pattern will be used to locate transmitter from the image and perform rotation compensation for alignment. Its aim is to provide robustness and aid in decoding.

$$L1 = L2 = L3 = \begin{bmatrix} 1 & 1 & 1 \\ 1 & 0 & 1 \\ 1 & 1 & 1 \end{bmatrix}, L4 = \begin{bmatrix} 0 & 0 & 0 \\ 0 & 1 & 1 \\ 0 & 1 & 1 \end{bmatrix} \tag{5.13}$$

The 3×3 corner anchoring patterns are shown in Eq.5.13. Pattern $L4$ is unlike $L1$, $L2$ and $L3$. It will provide a fixed region along which the pre-processed image will be rotated. Similarly, in proposed Aztec code based pattern communication, the 6×6 anchoring pattern is highlighted with green color as shown in Figure 5.22. The sub-matrix of each frame will be matched with an anchoring pattern after pre-processing from the video stream. Bit position at location 2×2 will be used for rotation compensation. If all the cells of the processed image match with the anchoring pattern, further processing will be initiated, including data extraction. Sensor type, fragment number, and data occupy 6, 6, and 16 bits, respectively. Thus, all 28 bits will be transmitted per frame. The pre-processed image will be rotated till it matches with the corner element or four rotations are completed. The frame will be dropped if the anchor pattern is unrecognized.

5.4.3 Frame Format

The frame format for both the proposed systems is same and as shown in Figure 5.23. 28 bits frame is divided into 3 sub frames. Sensor type and fragment number are 6 bit sub-frames which will provides type of sensor and current fragment number respectively. The fragment number sub-frame will be used for sensor values which require more that 16 bits for representation. The number of fragments required will be fixed as per sensor type. The final 16 bit sub frame will provide

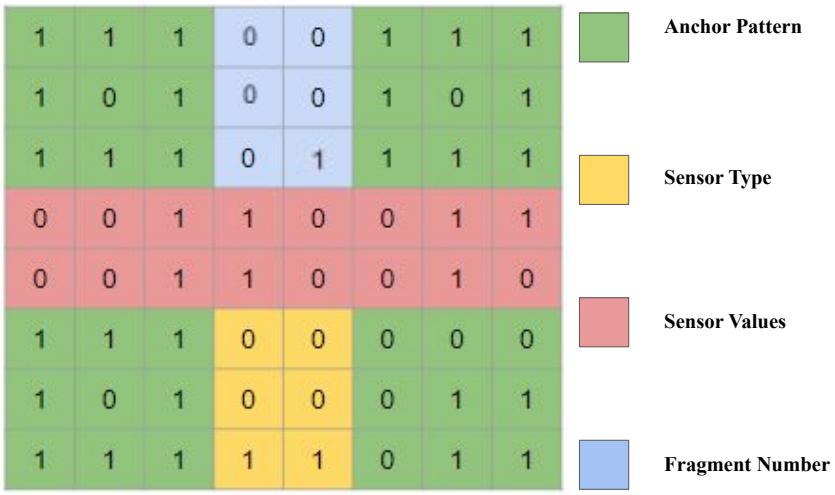

Figure 5.21: Proposed QR Code 8x8 Pattern Format

sensor value. In case of fragmented data, the fragments will be merged to provide final sensor value.

5.4.4 Decoding

On the receiver side, a continuous video will be captured at a low frame rate. Image frames will be separated from the video and each image frame will undergo pre-processing to extract encoded information. The steps involved in decoding will be as shown in Figure 5.24. The input colored image will be converted to grayscale. The brightest pixel intensity will be extracted to provide binary thresholding. The RoI will be extracted by cropping bounding box created around the largest blob from the binarized image. The RoI will be rotated to align and fit the bounding box. The aligned RoI will be resized to 8×8 binary matrix which will under anchor point extraction and rotation. Finally, information such as sensor type, fragment number and sensor data will be extracted to reconstruct transmitted data.

5.4.5 Evaluation Metrics

Performance of both the proposed systems will be evaluated based on SNR at various distance under different ambient lighting conditions. SNR is the ratio of signal power to background noise as given in Eq. 5.14. Here, A is the signal power and B is back ground noise power. In the proposed systems, signal is encoded as image, thus sum of pixel intensities when transmitter is transmitting is considered as A and sum of pixel intensities when transmitter is not transmitting is considered

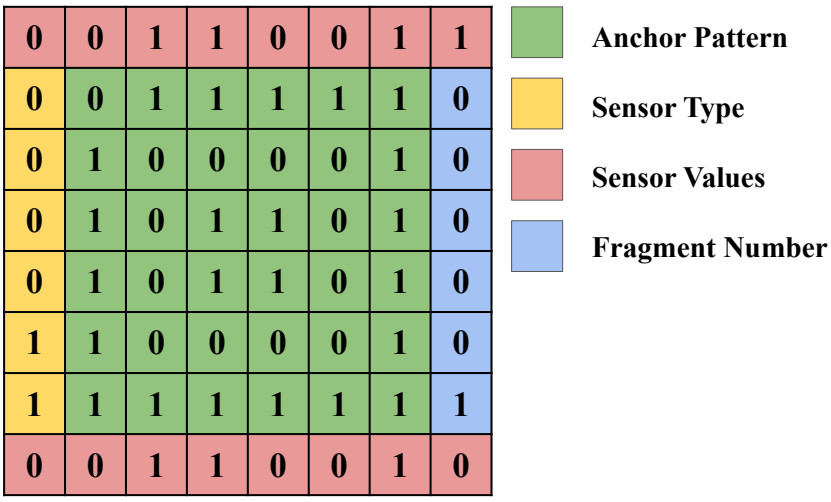

Figure 5.22: Proposed Aztec Code 8x8 Pattern Format

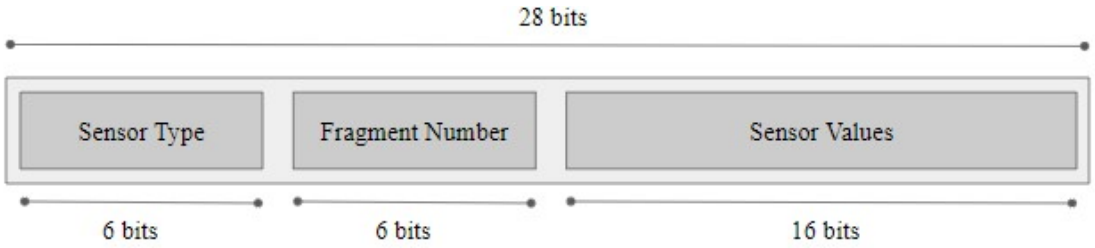

Figure 5.23: Frame Format for Proposed System

as B. The equation for power calculation is given by Eq. 5.15

$$SNR_{dB} = 10 \times \log \frac{\sqrt{\frac{1}{n}\sum_{i=0}^{n-1}|A_i|^2}}{\sqrt{\frac{1}{n}\sum_{i=0}^{n-1}|B_i|^2}} \tag{5.14}$$

$$Power = \sum_{j=1}^{y}\sum_{i=1}^{x} P_{ij} \tag{5.15}$$

The proposed systems will not transmit data bit by bit, instead it will transmit packets. Thus, Packet Error Ratio (PER) will be used to measure the performance of proposed system for various distances. PER is the percentage of error packets received to total packets transmitted as given in Eq. 5.16.

$$PER(\%) = \frac{Packets_{Err}}{Packets_{total}} \tag{5.16}$$

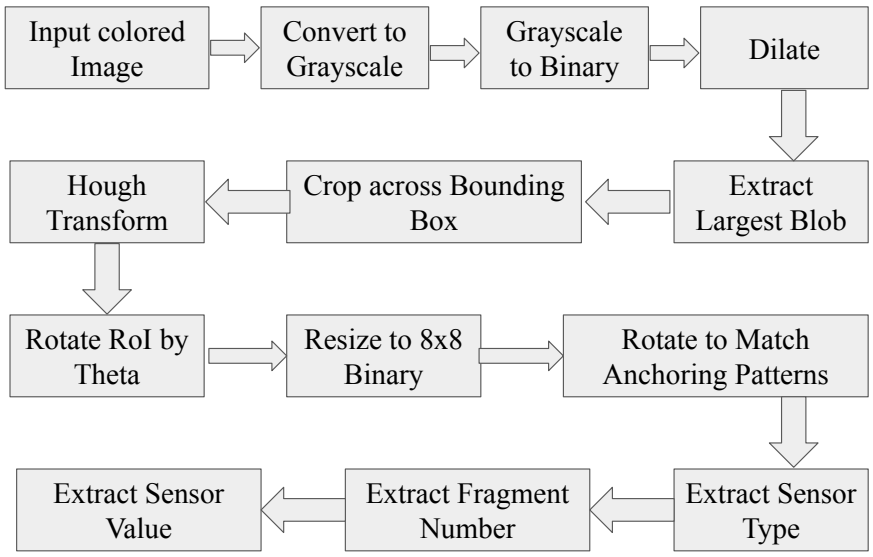

Figure 5.24: Steps Involved in Decoding

5.5 Requirements and Implementation

In this section hardware and software required for implementation of the proposed systems and its integration is discussed. Table 5.4 enlists the components used and its corresponding role in the proposed system.

Table 5.4: Required Hardware Components

Hardware	Model	Use
Temperature Humidity Sensor	DHT11	To convert sensed humidity and temperature from physical environment to deigital
Programmable Board	Arduino UNO	To convert incoming data into 8x8 binary and map to 2D LED Array
8x8 LED Array	WS2812B-64	To illuminate LEDs based on the received pattern
Webcam	Logitech c270	To record video and decode patterns.

The circuit diagram for the proposed QR code and Aztec code based systems is as shown in Figure 5.25. An Arduino UNO programmable board is used to read the input from temperature and humidity sensor(DHT11). The read sensor data, sensor type and fragment number are mapped to specific LEDs as per proposed frame format. The delay between each successive frame can be varied to provide

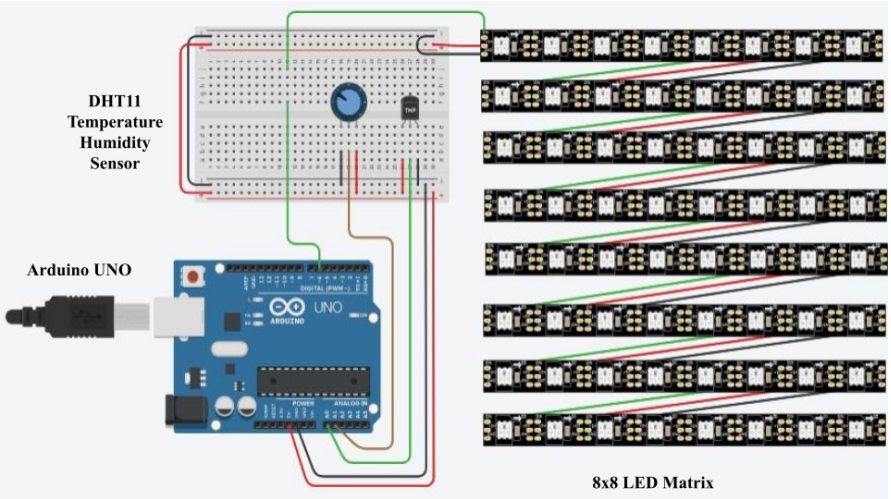

Figure 5.25: Circuit Diagram for Proposed Transmitter

different Packet Rates.

Figure 5.26 and Figure 5.27 shows implementation of proposed systems transmitting DHT sensor data using proposed frame formats and receiver camera capturing data and decoding it in real time.

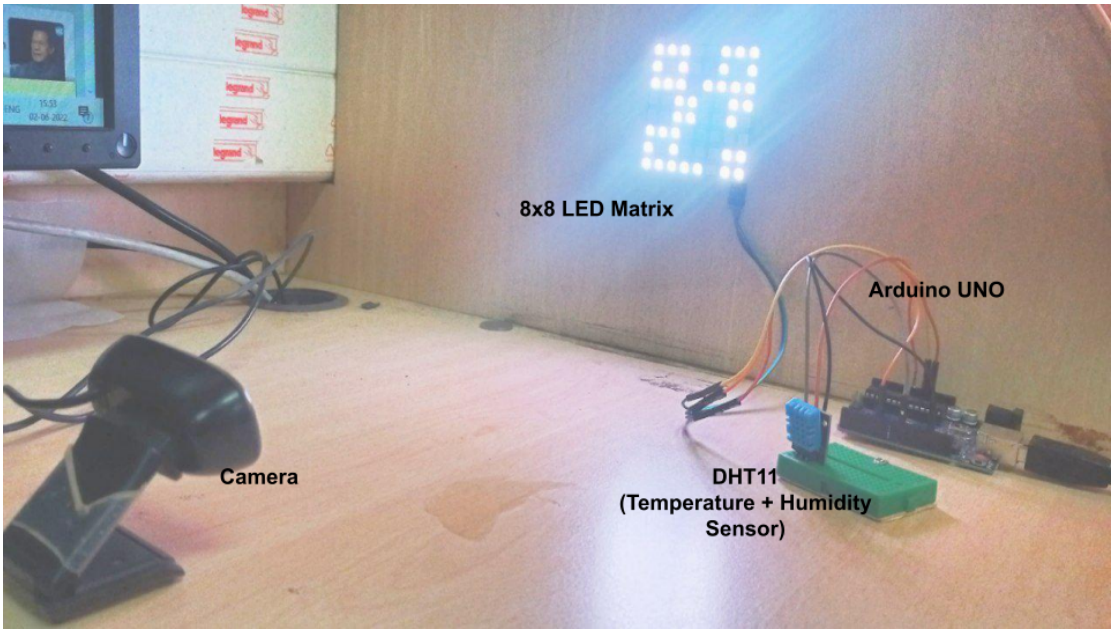

Figure 5.26: Implementation of QR code based system

5.5.1 RoI Extraction

On the receiver side, the captured raw image undergoes pre-processing to extract the encoded bit. The steps involved are as follows:

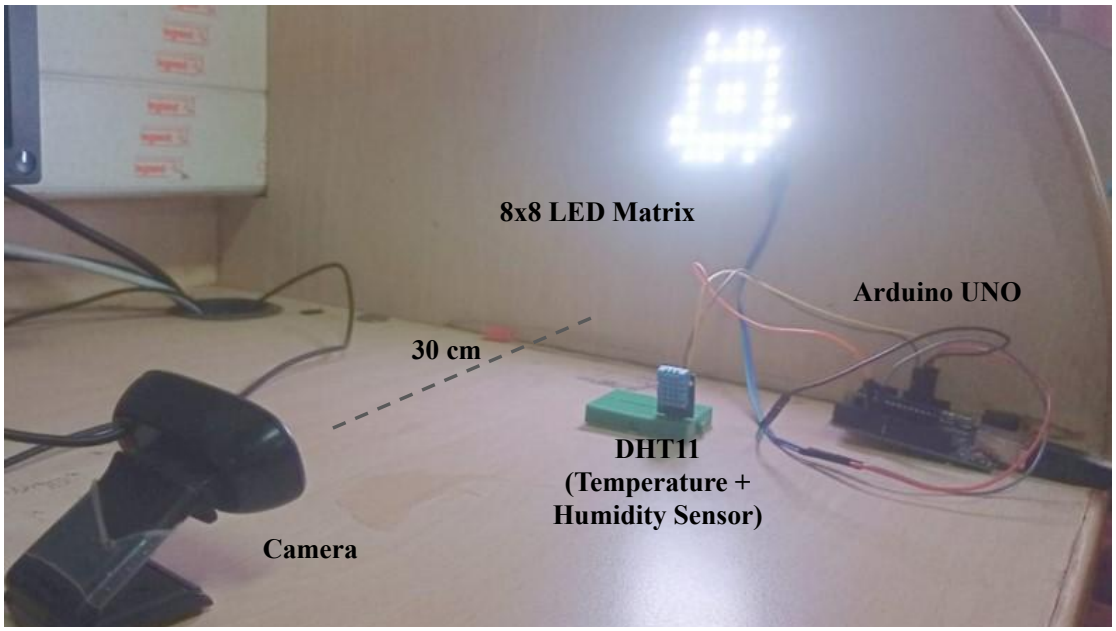

Figure 5.27: Implementation of Aztec code based system

5.5.1.1 Step 1: RGB to Grayscale Conversion

$$Gray_{i,j} = 0.299 * R_{i,j} + 0.587 * G_{i,j} + 0.114 * B_{i,j} \tag{5.17}$$

The process of data extraction involves sequential steps starting with image grayscaling. The three-channel colored input image is converted to a grayscale image by using Eq. 5.17. Here $R_{i,j}$, $G_{i,j}$, and $B_{i,j}$ are color channels of the given image and $Gray_{i,j}$ is generated image. The coefficients of each variable are set as per the conversion standard.

5.5.1.2 Grayscale Binarization

In this step, initially, the brightest pixel from the grayscaled image is selected as per Eq. 5.18. Here, $Gray_{i,j}$ is grayscaled image. max_j provides an array of maximum pixel intensities across columns. max_i provides maximum value from the array. $Intensity_{max}$ is maximum pixel intensity from given grayscaled image.

$$Intensity_{max} = max_i(max_j(Gray_{i,j})) \tag{5.18}$$

All the pixels except the brightest ones are rounded to 0 and a 2D binary image $B_{i,j}$ is generated as shown in Eq. 5.19.

$$B_{i,j} = Gray_{i,j} < Intensity_{max} - 1 \tag{5.19}$$

The obtained binarized image undergoes image dilation to increase the bright region. A structural element as shown in Eq. 5.20 is used to perform dilation. Here, $strel_n$ is square structuring element and n is dimension of unity matrix. Binary image dilation is performed as per Eq. 5.21.

$$strel_n = \begin{bmatrix} 1_{1,1} & .. & .. & 1_{n,n} \\ .. & .. & .. & .. \\ .. & .. & .. & .. \\ 1_{n,1} & .. & .. & 1_{n,n} \end{bmatrix} \tag{5.20}$$

$$B_{i,j} \oplus strel = \left\{ z | (\hat{strel}_z \cap B^c_{i,j} \neq \phi) \right\} \tag{5.21}$$

5.5.1.3 Mask and Crop RoI

The areas of all blobs from the dilated image are added to a list BA. BM is the largest blob from the list as shown in Eq. 6.18. The overlapping area of BM and $Gray_{i,j}$ is cropped to provide RoI as shown in Eq. 6.19

$$BM = max(BA_i) \tag{5.22}$$

$$RoI = \{p_{i,j} | Gray_{i,j} \cap BM_{i,j}\} \tag{5.23}$$

5.5.2 Rotation Compensation and Resizing

Algorithm 20 Rotation Compensation and Resizing for RoI

Require: Binary RoI Image
Ensure: BW=edge(RoI,'canny')
  [H,T,R]=hough(BW)
  Peak=houghpeaks(H,1), angle=T(P(1,2))
  areaRatio=blobArea/bBoxArea, areaRatios=[]
  while i<10 **do**
    angle=angle+i
    areaRatio=blobArea/bBoxArea
    areaRatios=[areaRatios areaRatio]
    i=i+1
  end while
  [M,I]=max(areaRatios), BW=rotate(RoI,angle+I), RS=resize(BW,[8,8])
  return RS

The rotation compensation and resizing of the RoI is performed as shown in Algorithm 20. A bounding box is drawn to fit the obtained RoI. A Hough

transform is performed on the RoI to obtain orientation angle. The image is rotated as per the obtained angle. The obtained image is further rotated till the ratio of area of blob to area of bounding box is maximum. The final adjusted image is the resized to 8x8 binary matrix.

Algorithm 21 QR Code-Anchor Identification and Pattern Decoding

Require: Resized Image $RS_{i,j}$
Ensure: SensorVal=[], count=1
Ensure: L1,L2,L3 and L4 are initialized
  [P1,P2,P3,P4]=extractAnchorPosition($RS_{i,j}$)
  while P1!=L1 & P2!=L2 & P3!=L3 & P4!=L4 or count==4 **do**
    $RS_{i,j}$=Swap($RS_{i,j}$,$RS_{j,i}$), $RS_{i,j}$=Swap($RS_{i,j}$,$RS_{i,N-1-j}$)
    count=count+1
  end while
  if count==4 **then**
    break
  else
    count=1
  end if
  S_{Type},F_t=extractSensorType($RS_{i,j}$)
  F_c=bin2dec([$RS_{1,4}$ $RS_{1,5}$ $RS_{2,4}$ $RS_{2,5}$ $RS_{3,4}$ $RS_{3,5}$])
  SV_t=zeros(1,16*F_t)
  while count¡=F_t **do**
    i=F_c
    x1=8i-7, y1=8i+7, x2=16i-7, y2=16i+7
    $SV_{[x1:y1]}$ = [$RS_{4,1}$ $RS_{4,2}$ . . . $RS_{4,8}$
    $SV_{[x2:y2]}$ = [$RS_{5,1}$ $RS_{5,2}$ . . . $RS_{5,8}$]
    F_{c+1}=bin2dec([$RS_{1,4}$ $RS_{1,5}$ $RS_{2,4}$ $RS_{2,5}$ $RS_{3,4}$ $RS_{3,5}$])
    if F_c!=F_{c+1} **then**
      F_c=F_{c+1}
      count=count+1
    else
      $SV_{[x1:y2]}$ = zeros(1,16);
    end if
  end while
  for j=1:2*count **do**
    x3=8j-7, y3=8j+7
    SensorVal=[SensorVal bin2dec($SV_{[x3:y3]}$)]
  end forreturn SensorVal

The 8×8 resized image undergoes anchor identification and pattern decoding as shown in Algorithm 21. For proposed QR code-based communication technique, input 8 × 8 binary matrix is extracted including corner 3 × 3 positions. These

sub-matrices are then compared with $L1$, $L2$, $L3$ and $L4$.

Algorithm 22 Aztec Code-Anchor Identification and Pattern Decoding

Require: Resized Image $RS_{i,j}$
Ensure: SensorVal=[], count=1
Ensure: Anchor pattern(A_P) initialization
  A_E=extractAnchorPosition($RS_{i,j}$)
  while A_E!=A_P or count==4 **do**
    $RS_{i,j}$=Swap($RS_{i,j}$,$RS_{j,i}$)
    $RS_{i,j}$=Swap($RS_{i,j}$,$RS_{i,N-1-j}$)
    count=count+1
  end while
  if count==4 **then**
    break
  else
    count=1
  end if
  S_{Type},F_t=extractSensorType($RS_{i,j}$)
  F_c=bin2dec([$RS_{2,8}$ $RS_{3,8}$ $RS_{4,8}$ $RS_{5,8}$ $RS_{6,8}$ $RS_{7,8}$])
  SV_t=zeros(1,16*F_t)
  while count¡=F_t **do**
    i=F_c
    x1=8i-7, y1=8i+7, x2=16i-7, y2=16i+7
    $SV_{[x1:y1]}$ = [$RS_{1,1}$ $RS_{1,2}$ . . . $RS_{1,8}$
    $SV_{[x2:y2]}$ = [$RS_{8,1}$ $RS_{8,2}$ . . . $RS_{8,8}$]
    F_{c+1}=bin2dec([$RS_{2,8}$ $RS_{3,8}$ $RS_{4,8}$ $RS_{5,8}$ $RS_{6,8}$ $RS_{7,8}$])
    if F_c!=F_{c+1} **then**
      F_c=F_{c+1}
      count=count+1
    else
      $SV_{[x1:y2]}$ = zeros(1,16);
    end if
  end while
  for j=1:2*count **do**
    x3=8j-7, y3=8j+7
    SensorVal=[SensorVal bin2dec($SV_{[x3:y3]}$)]
  end forreturn SensorVal

In Aztec code-based pattern technique, the anchor pattern is identified, and the pattern is decoded from the 8×8 binary matrix using Algorithm 22. The corner pixel at position $RS_{2,2}$ is used for comparison. If zero, no rotation is applied to the 8x8 binary matrix, and the data extraction process is initiated. However, if it is one, the matrix is rotated by 90 degrees, using transpose and swap functions. A 90 degree matrix rotation is performed until the pattern matches or 4 rotations

are completed. If the positions match then sensor type, fragment number and sensor value are extracted, else the packet is dropped.

Algorithm 23 Extraction Sensor Type and Total Fragments - QR Code Pattern

Require: $RS_{i,j}$
Ensure: S_{Type}=Null, F_t=0
  if $RS_{4,8}$==1 & $RS_{5,8}$==1 **then**
    S_{Type}=Temperature, F_t=2
  else if $RS_{4,7}$==1 & $RS_{5,7}$==1 **then**
    S_{Type}=Humidity, F_t=1
  else if $RS_{4,6}$==1 & $RS_{5,6}$==1 **then**
    S_{Type}=None, F_t=0 ▷ End Frame
  end ifreturn S_{Type}, F_t

Algorithm 24 Extraction Sensor Type and Total Fragments -Aztec Code Pattern

Require: $RS_{i,j}$
Ensure: S_{Type}=Null, F_t=0
  if $RS_{1,7}$==1 & $RS_{1,6}$==1 **then**
    S_{Type}=Temperature, F_t=2
  else if $RS_{1,5}$==1 & $RS_{1,4}$==1 **then**
    S_{Type}=Humidity, F_t=1
  else if $RS_{1,3}$==1 & $RS_{1,2}$==1 **then**
    S_{Type}=None, F_t=0 ▷ End Frame
  end ifreturn S_{Type}, F_t

The sensor type is extracted from the QR-code pattern using Algorithm 23 while Algorithm 24 is used to extract same information using Aztec-code pattern. The sensor type and total fragments is used to compare and count number fragments decoded. For sensor type null, the previous fragment is merged to obtain final sensor value. The pattern with sensor type null works as delimiter between successive packets.

5.6 Experimental Setup and Results

In this section, various experiments to evaluate the performance of proposed systems and its corresponding results is discussed. Table 5.5 shows the system configuration of the receiver and camera parameters.

The first experiment was conducted to check the validity of the implemented system. The receiver and transmitter were kept at 50cm distance from each other

and real-time data from digital humidity temperature (DHT11) sensor was transmitted using proposed pattern communication technique. The ambient light intensity was between 5-10 lux. The processed binary matrix was successfully decoded to provide 100% reconstruction of transmitted packet at the receiver side as shown in Figure 5.28.

Table 5.5: Camera and System Configuration

Camera Parameters		**System Configuration**	
Contrast	96	**CPU**	Intel(R) Core(TM) i7-7700
Brightness	128		
Exposure	-6		
Resolution	320x280	**RAM**	16 GB

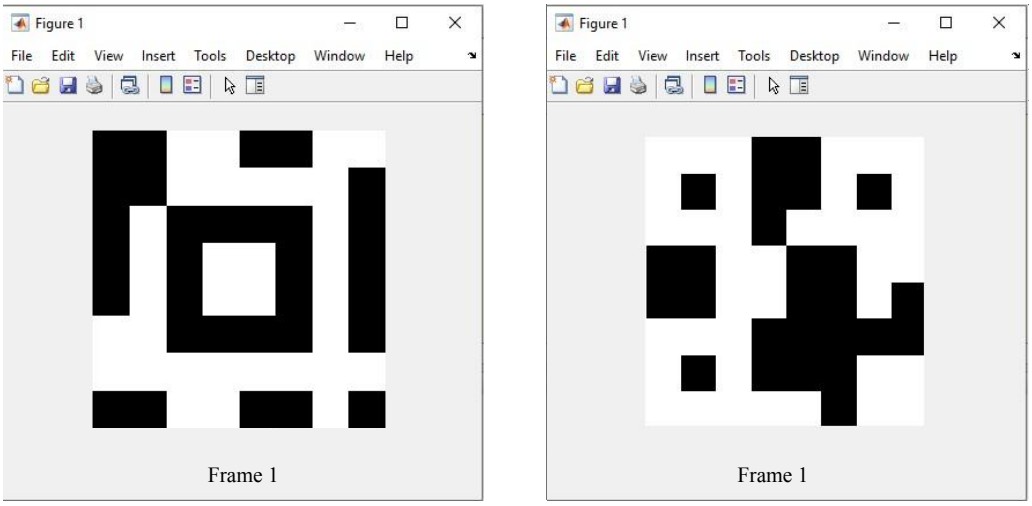

(A) Aztec Code Pattern **(B) QR Code Pattern**

Figure 5.28: Decoded 8x8 patterns for transmitted sensor data

The second experiment was conducted to observe the impact of distance on LED light intensity and blurring. Figure 5.29 and Figure 5.30 shows that as the distance increase, the light from neighboring LEDs overlap producing a blurring effect. Red colored peaks in Figure 5.29(A) are overlapping indicating the brightness intensity being blurry from a distance of 100 cm. However, in contrast, the red-colored peaks in Figure 5.29(b) are not overlapping indicating the brightness intensity being clear from a distance of 50 cm.

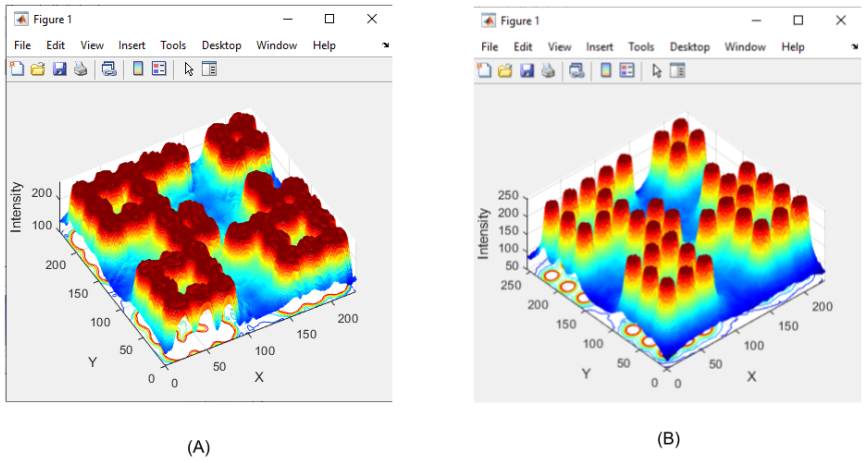

(A) (B)

Figure 5.29: QR code-Intensity Profiles at distances at (A) 100cm and (B) 50cm

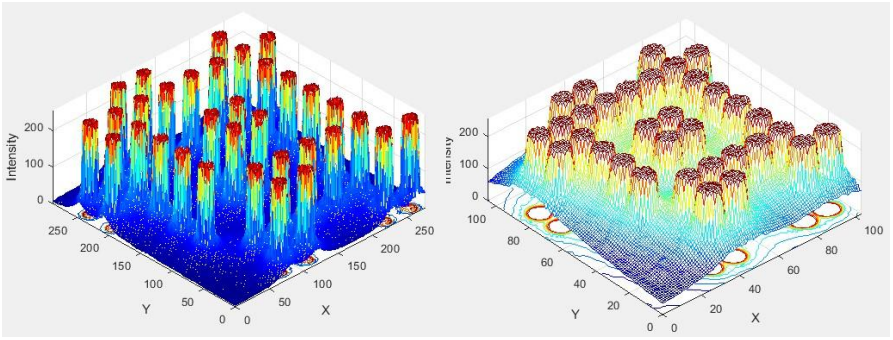

(A) (B)

Figure 5.30: Aztec code-Intensity Profiles of Frame 1 at distances at (A) 50cm and (B) 100cm

In the third experiment, SNR is measured at 50cm and 100cm distances. To calculate SNR, the overall image intensity of active transmitter was compared with overall image intensity of inactive transmitter.

Figure 5.31 shows the steps involved in SNR measurement of both the proposed pattern-based camera communication systems. Both systems showed similar trend with respect to change in SNR with change in distance as shown in Figure 5.32. It was observed that for the fixed ambient light condition, the SNR decreases with increase in distance. This is due to the fact that, as the distance increases the overall image intensity reduces causing the ratio to drop. It was also observed that as the ambient light intensity increases the difference between background noise and active signal reduces causing degradation in channel quality.

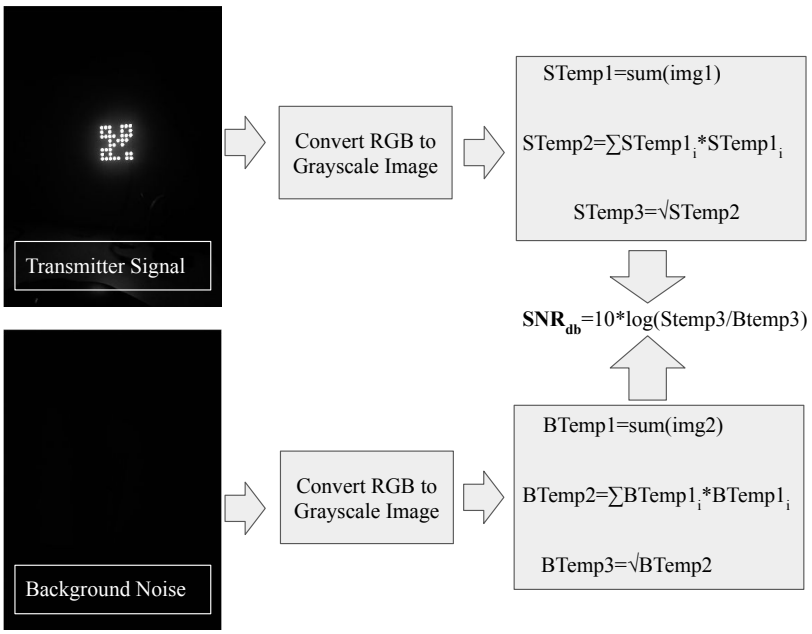

Figure 5.31: SNR Measurement

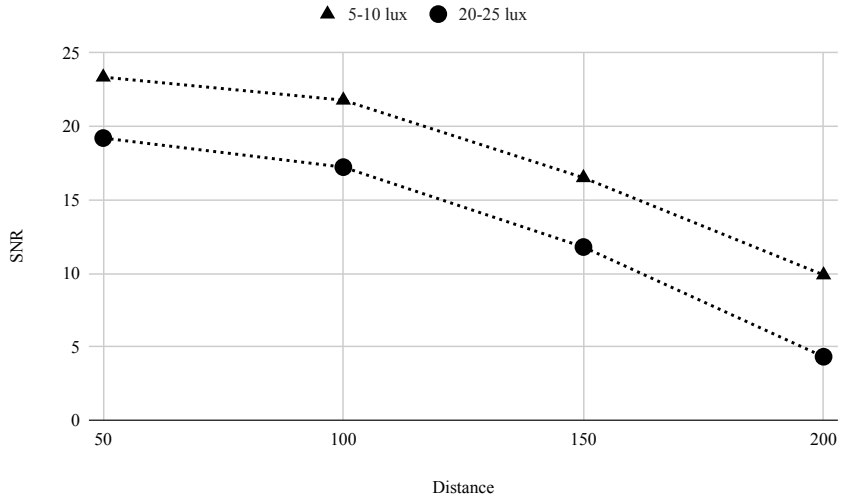

Figure 5.32: SNR vs Distance vs Ambient Light Intensity

The final experiment evaluated and compared the PER(%) of the proposed Aztec pattern-based vs. QR code-based system. The percentage of error packets received or dropped out of a total of 2000 packets was used to evaluate PER. Figure 5.33 shows the increase in percentage error as the distance increases for the proposed and reference system. Two packet rates, i.e., 2 Pps and 4 Pps, are used to evaluate Packet Rates' performance. The proposed system provides consistently better PER(%) than the reference system, even with the change in packet rate.

Both systems provide data rates of 28 bits per frame and have similar imple-

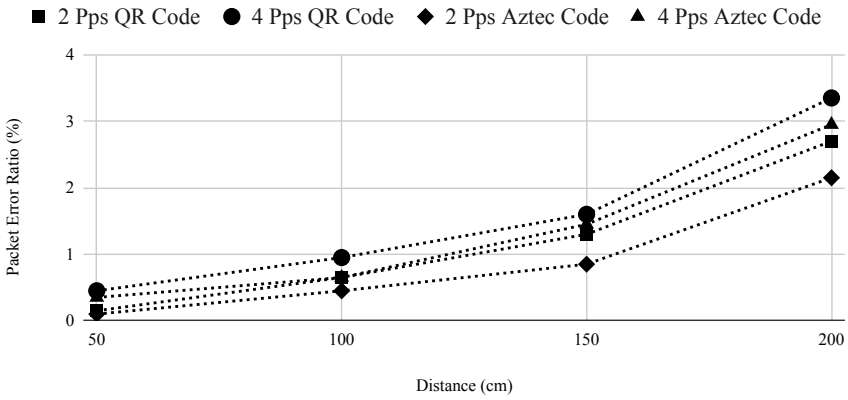

Figure 5.33: PER vs Distance vs Pps

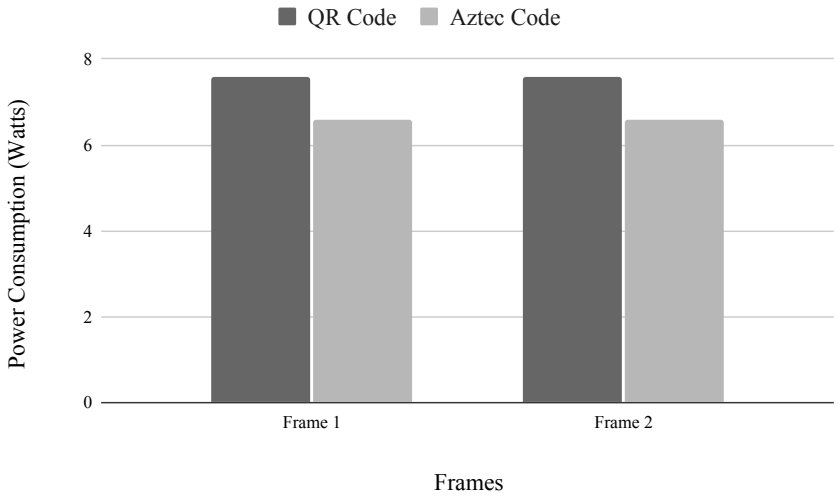

Figure 5.34: Power Consumption Comparison of QR Code vs Aztec Code

mentation complexity. The power requirement for the proposed Aztec code-based system is lesser than QR code-based system due to the lesser number of LEDs used for pattern construction. Figure 5.34 shows the power used for frames 1 and 2 where single LED uses 0.2 Watts/second.

5.7 Summary

In this chapter, a novel 2D LED matrix pattern inspired by nested textures and two OCC-IoT applications were proposed. The existing 2D data matrix-based camera communication system provides a maximum data rate of up to 1960 bps; however, as the distance between transmitter and receiver increases, the pixels become a blur. Thus, the system suffers degradation in BER. To mitigate this

problem, a concept inspired by the domain of texture feature analysis and classification was used to build a pattern that could be detected from longer distances using regular cameras. The proposed pattern is nested in nature, providing inherent support for hierarchical pattern classification. The incoming bit sequence was mapped to an 8×8 pattern. A Tx and Rx simulation was built using Matlab to compare linear and binary search computational time. It was observed from the simulation results that the multi-threaded binary search performed better than the linear search. Thus, further experiments were conducted on a hardware prototype. Experiments concerned with optimal camera parameter selection were conducted. Intensity profiles of transmitter patterns were measured at various distances to understand the blurring of pixel intensities. Experiments were conducted to evaluate the performance search techniques concerned with BER and distance. It was observed that the proposed pattern provides faster decoding for multi-threaded binary search compared to linear search for data rates higher than 256 bps. It was also observed that binary search provided the best performance with 20% BER at 2m distance and 256 bps. An experiment was conducted to test the impact of camera resolution on BER; thus, for a fixed distance of 2m, it was observed that BER improves with an increase in camera resolution. The proposed technique is suitable for an indoor industrial environment where a video feed from a camera can monitor machine health parameters without using RF-based communication.

The focus of the proposed technique was to provide faster pattern recognition for higher data rates and distances up to 2m low-resolution camera without external magnification. The system's performance can further be improved in terms of distance by using a high-resolution camera and external magnification. The data rate can also be improved by integrating other multiple nested patterns and colors.

Using the insight from the implementation of proposed nested pattern based OCC, two applications were proposed to showcase the integration of IoT and 2D pattern based OCC. The proposed patterns use QR-code and Aztec-code inspired patterns to enable rotation compensation and to provide ease of detection. A DHT11 sensor was used to provide temperature and humidity values from the surrounding environment. These sensed values were transmitted using the proposed QR-code and Aztec-code-inspired patterns and decoded using a camera on the receiver side. SNR of the proposed system was evaluated based on frame intensities at various distances. It was observed that out of the two proposed systems, Aztec-code-based pattern-to-camera communication is more power-efficient and provides better PER(%) for multiple distances and packet rates as compared to

the QR-code pattern-based system. Both the proposed systems can be used to enhance any existing indoor infrastructure with the camera to provide non-RF-based data communication.

The proposed OCC systems discussed in this chapter used single color for generating 2D patterns and thus, provide a single channel for communication. However, the chromaticity of light in conjunction with the spetialty of 2D transmitter can improve the performance of the proposed technique to provide higher bandwidth and support MIMO.

Chapter 6

Quantum Chromodynamics Inspired Optical Camera Communication with User Centric MIMO

In OCC, the Tx is typically based on LEDs, which support a range of chromatic values, thus providing access to the visible light spectrum for modulation. The signal is modulated using light properties like intensity, blink frequency, polarity, chromaticity, and spatiality (Hasan *et al.* 2018). On the Rx side, depending on the modulation scheme, these features are extracted from the video stream, and corresponding signal demodulation and data reconstruction are performed. In an environment where the distance and orientation between Tx and Rx are constant, the demodulation is performed using preset RoI extraction (Nguyen *et al.* 2021). However, support for variable distance and orientation is required for a practical system.

Moreover, as the signal is demodulated using image frames, the frame rate of the camera defines the data rate and throughput of the OCC link (Preda *et al.* 2021). Although higher frame rate cameras can provide higher data rates, they are costlier than regular cameras, which restricts their deployment to a few specific use cases. Considering these limitations, the performance of an OCC can be improved by using spatially arranged multiple neopixel LEDs (Jung and Kim 2021) or display screens (Bao *et al.* 2021).

6.1 Related Works

The major challenges of an OCC system are Tx detection, MIMO, the distance of communication, and rotation mitigation or tolerance. The Tx in OCC can be identified using the luminance characteristics or the shape of the Tx aperture. Do and Yoo (2019) proposed a simple LED panel detection algorithm that identifies the brightest pixel and performs convex fill to obtain RoI. The simulated results show decreasing accuracy in RoI identification with increasing distance. However, the proposed system was not tested under practical scenarios where multiple bright pixels might exist. The author of the paper Guan *et al.* (2019) introduced the Convolutional Neural Networks (CNN) for RoI detection; however, the Tx and Rx are restricted to be arranged in parallel without any rotation or skew. Sun *et al.* (2021) proposed a hybrid technique for LED panel detection using a modified YOLOv5 object detection model. Although the proposed technique provides high accuracy for rotated and skewed normal and blurry images, it is compute-intensive. Non-flickering OCC Tx has been proposed, but most have distance limitations due to the relation between Tx size, distance, and throughput (Teli *et al.* 2020*a*; Zinda *et al.* 2018). Thus, IEEE 802.15.7-2018 standard has specified clauses for OCC modulation techniques that allow flickering and provide Kbps data rates using dedicated LED panels and displays. Moreover, these transmitters can also offer MIMO for IoT devices in an indoor environment.

In an OCC system, MIMO can be provisioned using frequency or color-based modulation techniques. Nguyen and Jang (2021*a*) proposed and demonstrated MIMO-OFDM using two Tx sources and achieved a combined throughput of 3.840 Kbps for a fixed distance. However, the system does not support rotation as the spatial arrangement of multiple Txs induces error in the demodulation. To provide rotation support in a flicker-free RS-OCC system, Teli *et al.* (2020*b*) proposed an RS-MIMO for IoT using grouped LED arrays as a transmitter. The maximum throughput of 1.9 and 0.9 Kbps was obtained for 0-degree and 50-degree rotations; however, the throughput was also dependent on the distance between Tx and Rx. LED array-based active marker design was proposed by Gorse *et al.* (2018) to provide efficient marker detection for augmented reality and positioning applications under low ambient light conditions. In Nguyen *et al.* (2021) a 2D LED array-based OCC system with rotation support and MIMO was proposed. The system provided BER of 10^{-4} for 11 dB SNR however, the throughput can further be enhanced by using chromatic features of light (Nguyen and Jang 2016; Hao *et al.* 2012).

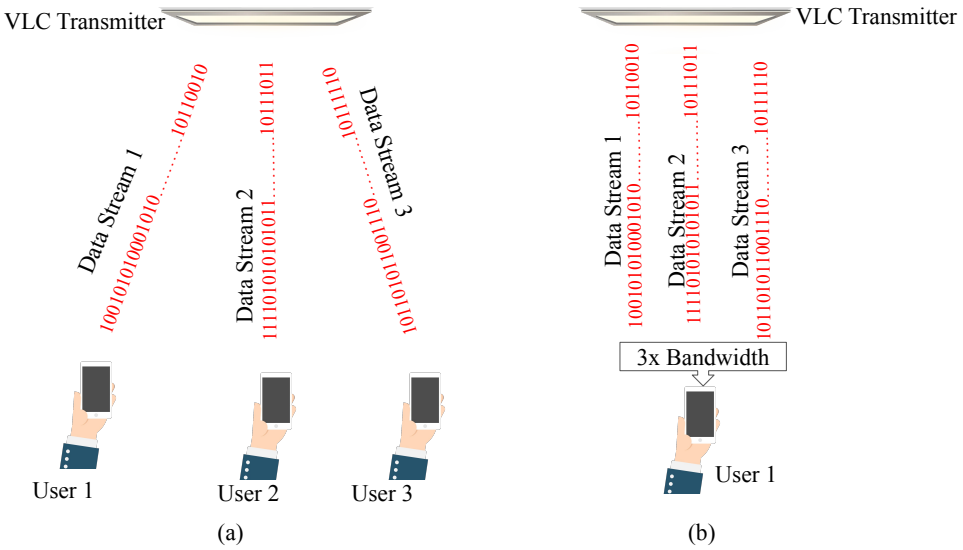

Figure 6.1: User centric MIMO under OCC Access Point (a) 3 user devices 1x bandwidth (b) 1 user device 3x bandwidth

User-centric MIMO provides variable bandwidth depending upon the number of devices under the VLC access point (Han and Zhao 2022; Chen *et al.* 2020). Figure 6.1a, and 6.1b show the bandwidth distribution for three OCC Rx devices and one Rx device, respectively. OCC-MIMO can be achieved by modulating signals using color mapping techniques. However, few phenomenons in nature exist that inherently showcase changes in color based on changes in its underlying composition.

QCD is a branch of Quantum Physics under which the chromatic properties of quantum particles are studied (Olsen *et al.* 2018). Recent discoveries in the field of quantum physics have revealed that the sub-atomic particle neutron and proton are composed of hadrons which consist of quarks held together by the strong force produced during the exchange of gluons. Depending upon the number of quarks in a hadron, the hadron is classified into Baryons and Mesons. Baryons consist of 3 quarks, while Meson consists of a pair of quarks and antiquarks (Gallmeister and Mosel 2022; Ahmed *et al.* 2020). In Baryons, the quarks are held together by exchanging gluons, keeping the overall hadron stable. Loosely inspired by the Baryons gluon exchange model, this paper proposes a 2D 8×8 neopixel LED matrix for an OCC. The major contributions of this work are as follows:

- Proposes quantum chromodynamics principles for data to color mapping using an 8×8 LED matrix.
- Proposes a rotation support technique for the OCC using a QR code-inspired

anchoring pattern.

- Design and development of simulator for proposed QCD-inspired OCC modulation with rotation support and MIMO
- Design and development of a low-cost prototype of the proposed QCD-OCC system and compare the success of reception(%) with the proposed simulator.
- Performance evaluation of the proposed system based on metrics such as SNR, the success of reception(%), intensity profile, throughput, and BER.

6.2 Proposed Work

The previous section briefly introduced the concept of QCD. This section provides a detailed explanation of the proposed modulation technique inspired by the behavior of sub-atomic particles. Table. 6.1, shows all the notations and corresponding semantics used in the explanation of the proposed work and its implementation.

6.2.1 Proposed Technique

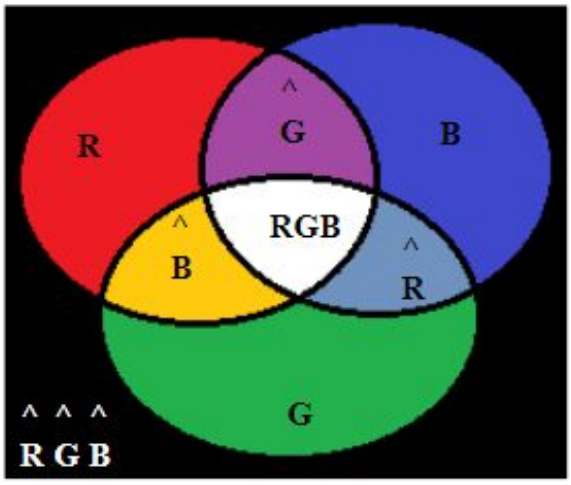

Figure 6.2: Gluon exchange-based color changes in Quarks. Baryons Model

At the sub-atomic level, the exchange of gluons between quarks creates a strong force that keeps the Hadron stable which is the composition of neutrons and protons. Baryon, a type of Hadron, is generally represented with white(W) color to

Table 6.1: Table of Notations used in Proposed Work and Implementation

Notation	Semantics
R, G, B	Red, Green, Blue
$\hat{R}$, $\hat{G}$, $\hat{B}$	Anti-Red, Anti-Green, Anti-Blue
$\oplus$	Dilation operation
A_i^{Tx}	Aligned Transmitter
A_i	Anchor position
$B_{x,y}$	Binarized pixel at position (x,y)
BM	Blob with the maximum area
D_G	Generated binary data stream
D_i	Data position
D_t	Data throughput
E_b	Number of error bits
fps	Frame rate of Rx camera
$Gr_{x,y}$	Grayscale value at position (x, y)
I_{in}, I_{ac}	Images containing inactive Tx, active Tx
I_{peak}	Peak value of pixel intensity
L_{max}	Maximum stream length
L_1, L_2, L_3	Lengths of data streams in file 1, 2, and 3
L_i^{new}	Length of the new data stream in file i
$N_{AnchorLEDs}$	Number of LEDs used for anchor pattern
$N_{ColorBits}$	Number of bits required to represent color
N_{LEDs}	Number of LEDs on Tx panel
N_F	Total number of frames required to transmit each file
N	Length of the data stream
O_{8x8}^{Rx}	Rotated matrix
O_{8x8x3}^{Tx}	8x8x3 matrix obtained by multiplexing color channels
P	Pseudo-random number between 0 and 1
R_{8x8}^{Rx}, G_{8x8}^{Rx}, B_{8x8}^{Rx}	Binary matrices after channel separation
R_{8x8}^{Tx}, G_{8x8}^{Tx}, B_{8x8}^{Tx}	8x8 matrices from file frames
RoI	Region of Interest
S	Size limit
$strel_n$	Square structural element of size n
T_b	Total number of transmitted bits
T	Threshold for binarization
U_1, U_2, U_3	User 1, User 2, User 3
Z_i	Number of zeros to be padded in file i

indicate its stability. The quarks are represented by the colors red(R), green(G), and blue(B), as shown in Figure 6.2. Cyan, violet, and yellow are used to describe the absence of red, green, and blue from white. These also represent anti-red($\hat{\text{R}}$), anti-green($\hat{\text{G}}$), and anti-blue($\hat{\text{B}}$). Thus, combining the original color and its complement always produce white, showcasing a stable hadron as shown in Eq. 6.1.

$$R + \hat{R} = G + \hat{G} = B + \hat{B} = W \tag{6.1}$$

Inspired by this analogy, our proposed technique will assign a color to an LED in an 8x8 LED matrix based on the absence or presence of a bit in the set of 3-bits. Table 6.2 shows the color mapping for an LED in the resultant output. These groups of 3-bits can be generated either by using three separate binary data streams or by using a single data stream divided into groups of 3-bits.

Considering three data streams to be transmitted for users U_1, U_2 and U_3, three colors will be assigned such that, $R \implies U_1$, $G \implies U_2$ and $B \implies U_3$. Thus, from Eq. 6.1 the relation between user data streams and respective assigned colors can be shown as: $R+G \implies U_1+U_2 \implies \hat{B}$, $G+B \implies U_2+U_3 \implies \hat{R}$, $R+B \implies U_1+U_3 \implies \hat{G}$, and $R+G+B \implies U_1+U_2+U_3 \implies W$. For example, if U_1 data bit is zero, and U_2 and U_3 data bits are one, then $\hat{R}$ color would be set at the respective position of an LED in 8×8 neopixel LED matrix.

Table 6.2: Bits to color mapping using Baryons additive color model

Bits	**Color**	**Bits**	**Color**
000	$\hat{\text{R}}\hat{\text{G}}\hat{\text{B}}$=Black	111	RGB = White
001	B = Blue	110	$\hat{\text{B}}$ = Yellow
010	G = Green	101	$\hat{\text{G}}$ = Violet
100	R = Red	011	$\hat{\text{R}}$ = Cyan

6.2.2 Overview of Proposed Communication System

The proposed Quantum Chromodynamics based OCC (QCD-OCC) system is divided into two parts, namely as Tx and Rx, separated by free space channel as shown in Figure 6.3.

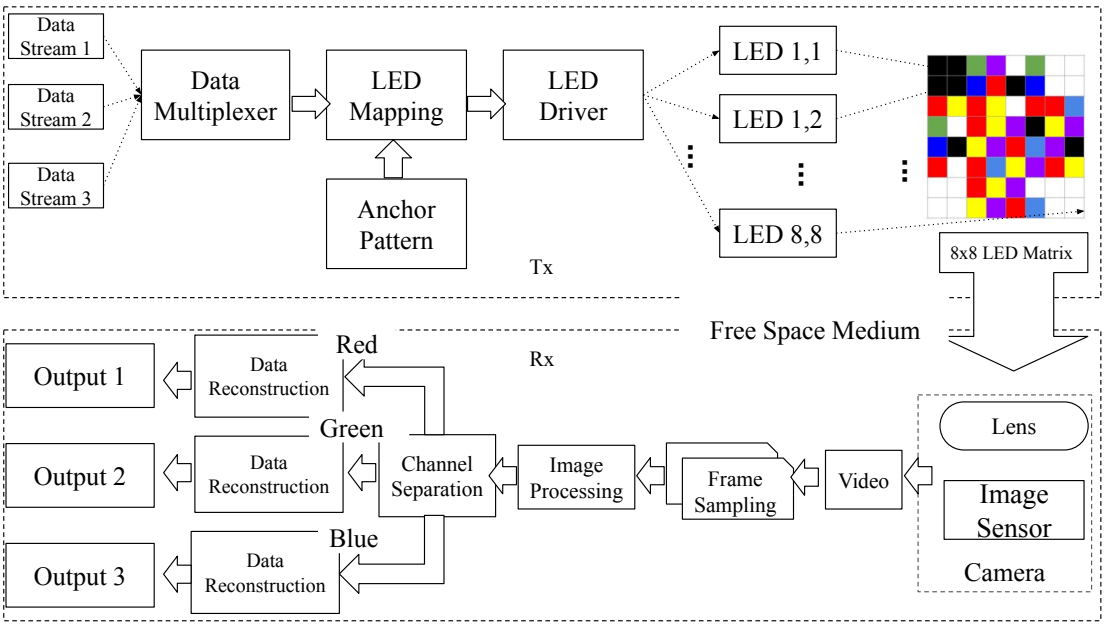

Figure 6.3: Overview of Proposed QCD-OCC System

On the transmitter side, the data to be transmitted can be in two formats as follows where $(R, G, B)_{i=1}^{48}$ is an array of size 48 containing color information for respective indices of three individual/one single datastream/s:

- **Format 1:** In this format, three separate binary data streams $D1$, $D2$ and $D3$ of variable lengths for user $U1$, $U2$ and $U3$ will be used to generate 3D matrix of size $1 \times 48 \times 3$ as shown in Eq. 6.2, where matrix R,G, and B are sub-matrices along Z-axis at indices 1, 2 and 3 respectively.

$$(R, G, B)_{i=1}^{48} = (D1_i, D2_i, D3_i) \tag{6.2}$$

- **Format 2:** In this format, a single binary data stream D will be folded to obtain a 3D matrix of size 1x48x3 as shown in Eq. 6.3.

$$(R, G, B)_{i=1}^{48} = (D_i, D_{48+i}, D_{96+i}) \tag{6.3}$$

Representation of data in format 1 enables MIMO and supports simultaneous communication with three users, while format 2 provides 3x bandwidth as compared to format 1 directed for one user. Format 1 is used throughout this paper for ease of understanding.

Each matrix of size $1 \times 48 \times 3$ obtained post multiplexing will be reshaped into corresponding $6 \times 8 \times 3$ matrices. These $6 \times 8 \times 3$ matrices will be converted to

$8 \times 8 \times 3$ matrices by integrating anchor patterns. Anchor patterns are corner 2×2 sub-matrices that will be used to retrieve orientation information from the image at the receiver side. The resultant $8 \times 8 \times 3$ matrix will be converted to an 8×8 color image using bit color mapping as per Table 6.2. Color from each resultant cell will be mapped to LEDs based on color value and position in the matrix. An LED driver will control the status of LEDs as per the input from mapping and produce an 8×8 multicolor LED output.

A continuous video capturing the transmitter LED panel will be recorded on the receiver side. The video will be processed frame-by-frame to extract the transmitter's position using the image processing technique. The detected RoI will be resized and converted to an $8 \times 8 \times 3$ image which undergoes channel separation and provides three 8×8 binary matrices. The data will be regenerated at the receiver sides after the removal of anchor patterns.

A simulator and prototype of the proposed QCD-OCC system will be implemented, and their performance will be evaluated. The performance of the system will be evaluated based on Peak Signal to Noise Ratio (PSNR), data throughput, the success of reception(%), and BER at various distances and under different ambient lighting conditions. PSNR serves as a metric for evaluating channel quality. It will be computed using the Mean Squared Error (MSE) between the images containing inactive Tx(I_{in}) and active Tx(I_{ac}) (Huynh-Thu and Ghanbari 2012). Eq. 6.4 shows the computation of MSE where $Rows$ and $Cols$ are the height and width of input images in terms of pixels, respectively.

$$MSE(I_{in}, I_{ac}) = \frac{1}{Rows \times Cols} \sum_{i=1}^{Rows} \sum_{j=1}^{Cols} (I_{in}(i,j) - I_{ac}(i,j))^2 \tag{6.4}$$

The peak value of the pixel intensity(I_{peak}) in the received image I_{ac} will be computed as per the Eq.6.5

$$I_{peak} = max_{Rows}(max_{Cols}(I_{ac})) \tag{6.5}$$

From Eq. 6.4 and 6.5 PSNR can be expressed as:

$$PSNR((I_{in}, I_{ac}) = 10 \log_{10}(I_{peak}^2 / MSE((I_{in}, I_{ac})) \tag{6.6}$$

The data throughput(D_t) for the proposed system will be evaluated as per Eq. 6.7 where N_{LEDs} is number LEDs on Tx panel, $N_{ColorBits}$ is number of bits required to represent color $N_{AnchorLEDs}$ is number LEDs used for anchor pattern,

and fps is frame rate of Rx camera.

$$D_t = (N_{LEDs} * N_{ColorBits} - N_{AnchorLEDs}) * \frac{fps}{2} \tag{6.7}$$

The percentage success of reception will be calculated as per Eq. 6.8 where T_b is the total number of transmitted bits, and E_b is the number of error bit

$$Successof Reception(\%) = \frac{T_b - E_b}{T_b} * 100 \tag{6.8}$$

6.2.3 Implementation of Proposed QCD-OCC Transmitter Simulation

A simulator is proposed to study challenges for the practical implementation of the proposed QCD-OCC system. Similar to the proposed system, the simulator will have Tx and Rx. Figure 6.4 shows the components of Rx simulation. A random binary data generator function generates binary streams of variable lengths. For example, if P is a pseudo-random number between 0 and 1 and S is the size limit, then the data generated D_G will be as shown in Eq. 6.9, where

$$D_G = [x_1, x_2, x_3, ..., x_N] \tag{6.9}$$

where $N = \lceil P \times S \rceil$ and

$$x = \begin{cases} 1, & \text{if } 0.5 > P \\ 0, & \text{otherwise} \end{cases}$$

These streams are written into three files to simulate three individual data sources. The maximum stream length (L_{max}) across the three files is computed as per Eq. 6.10, where L_1, L_2, L_3 are lengths of data stream in file 1, 2 and 3 respectively.

$$L_{max} = \max(L_1, L_2, L_3) \tag{6.10}$$

The lengths of each data stream are made equal by padding 0s. The number of zeros(Z_i) to be padded is determined as per the Eq. 6.11 where i is file number.

$$Z_i = (48 \times \lceil \frac{L_i}{48} \rceil) - (L_{max} \mod 48) \tag{6.11}$$

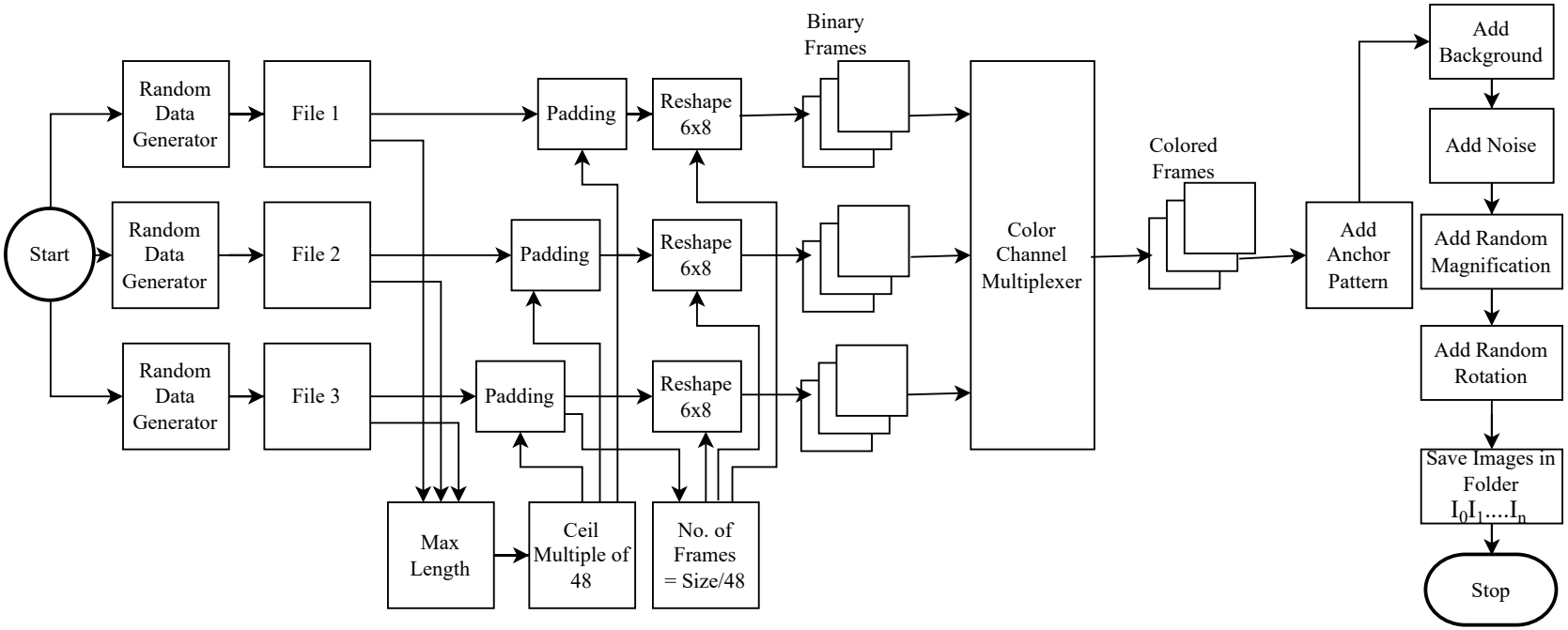

Figure 6.4: Block diagram of the proposed QCD-OCC Transmitter Simulator

The individual data streams are appended with the corresponding number of zeros to obtain new data streams of lengths L_i^{new}, where $L_i^{new} = L_i + Z_i$. The lengths of the resultant data streams are equal and multiple of 48. The total number frames (N_F) required to transmit each file is $L_1^{new} \div 48$. Thus, each frame consists of 48 bits for individual files.

The scalar 1×48 is vectorized into 6×8 binary matrices. These 6×8 matrices are further converted to 8×8 matrices as per the proposed Tx frame format shown in Figure 6.5a, where A_i and D_i are anchor and data positions, respectively. The corner 2×2 matrices are zeros and overwritten by anchor pattern post multiplexing. Each frame with common indices is forwarded to a color channel multiplexer, where an 8x8 matrix from three file frames, namely as R_{8x8}^{Tx}, G_{8x8}^{Tx} and B_{8x8}^{Tx} are multiplexed into a single $8 \times 8 \times 3$ matrix O_{8x8x3}^{Tx}.

Figure 6.5b represents steps involved in color channel multiplexing. An 8×8 anchoring pattern is added across three channels obtaining the output $8 \times 8 \times 3$ matrix. The anchor pattern values is assigned as $[A_1,A_2,A_3,A_4]$=[0,0,0,0] and $[A_5,...,A_{16}]$=[1,...,1]. In the next step, the colors for each cell of the final 8×8 matrix are defined as per the Baryons color model inspired bit color mapping table.

As an 8×8 size image is a very small size in terms of pixels, the image is rescaled to 64×64. The final generated colored image is overlapped on a camouflage base image size $1920 \times 1080 \times 3$ using sub-matrix substitution, and a Gaussian noise is added to simulate the process involved in RoI extraction. A magnification factor is integrated to simulate the change in Tx size as per distance from Rx. The resultant image undergoes rotation of 45 or 90 degrees to verify the rotation support of the proposed system. Each image is named as per the frame number and stored in a folder.

6.2.4 Implementation of Proposed QCD-OCC Receiver Simulation

The steps involved in receiver simulation are shown in Figure6.6. The process starts with accessing the folder containing images generated by the Tx simulator. Each image is processed sequentially as per the naming convention. However, since in a practical system, there will be a probability of packet drop due to frame sampling error,

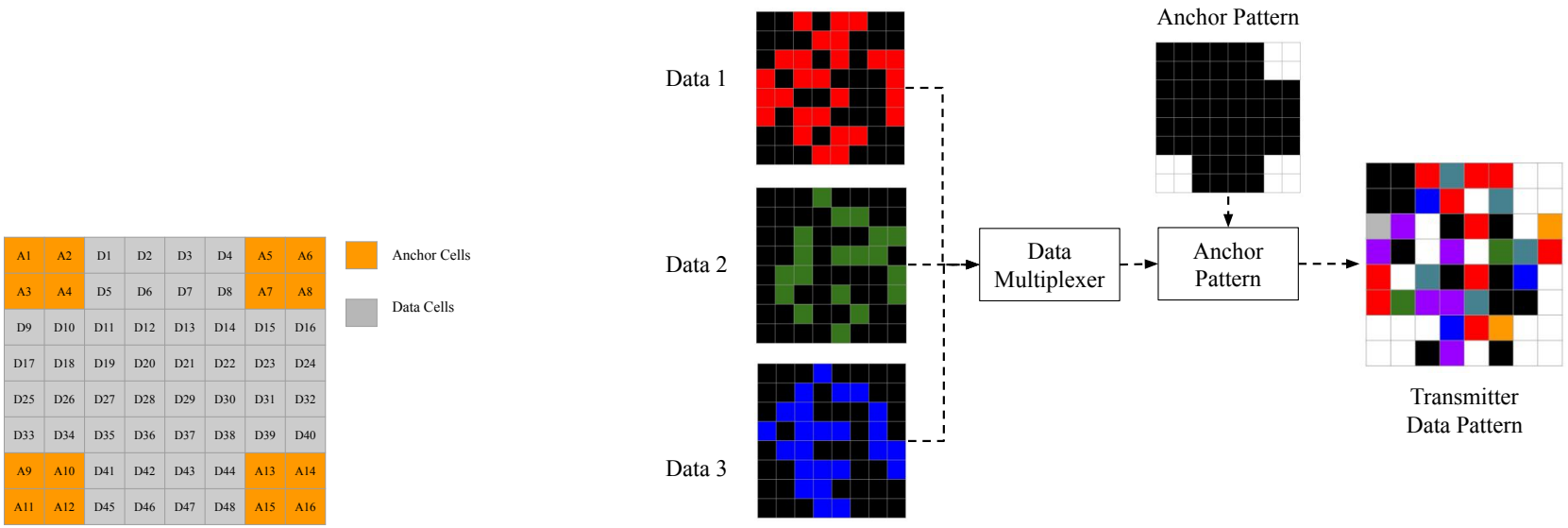

(a) Proposed Tx Frame Format

(b) Color Channel Multiplexer

Figure 6.5: Proposed OCC Modulation Scheme Frame Format and Color Channel Multiplexing Process

thus a simulation of this error resulting in skipping of image($S(i)$) is implemented as:

$$S(i) = \begin{cases} i, & if P < 1 - (F_r/48/3/D_r) \\ 0 \end{cases} \tag{6.12}$$

where i is an image from the folder, F_r is the frame rate of the camera, and D_r is the transmitter data rate. The probability of packet drop for the selected image decreases with an increase in camera frame rate and/or decrease in transmitter data rate. The selected image undergoes noise removal using a Wiener filter. The extraction of RoI from the first image is a sequence of pre-processing steps. The input colored image is converted into grayscale(Gr) as per the Eq.6.13 where x and y are the rows and columns of pixels in the image, and R, G and B are color channels.

$$Gr_{x,y} = 0.299 * R_{x,y} + 0.587 * G_{x,y} + 0.114 * B_{x,y} \tag{6.13}$$

A threshold(T) for binarization is estimated as per Eq.6.14 where maximum grayscaled pixel intensity is used as the threshold. Eq. 6.15 provides binarized image(B)

$$T = max_x(max_y(Gr_{x,y})) \tag{6.14}$$

$$B_{x,y} = Gr_{x,y} < T - 1 \tag{6.15}$$

A square structural element($strel$) of size n as given in Eq.6.16 is used to dilate the binarized image. Eq.6.17 provides dilated binary image.

$$strel_n = \begin{bmatrix} 1_{1,1} & .. & .. & 1_{n,n} \\ .. & .. & .. & .. \\ .. & .. & .. & .. \\ 1_{n,1} & .. & .. & 1_{n,n} \end{bmatrix} \tag{6.16}$$

$$B_{i,j} \oplus strel = \left\{ z | (\hat{strel}_z \cap B^c_{i,j} \neq \phi) \right\} \tag{6.17}$$

Out of the n blobs from the dilated image, the blob with the maximum area(BM) is selected as per Eq.6.18 where BA_n is the area of blob n.

$$BM = max(BA_n) \tag{6.18}$$

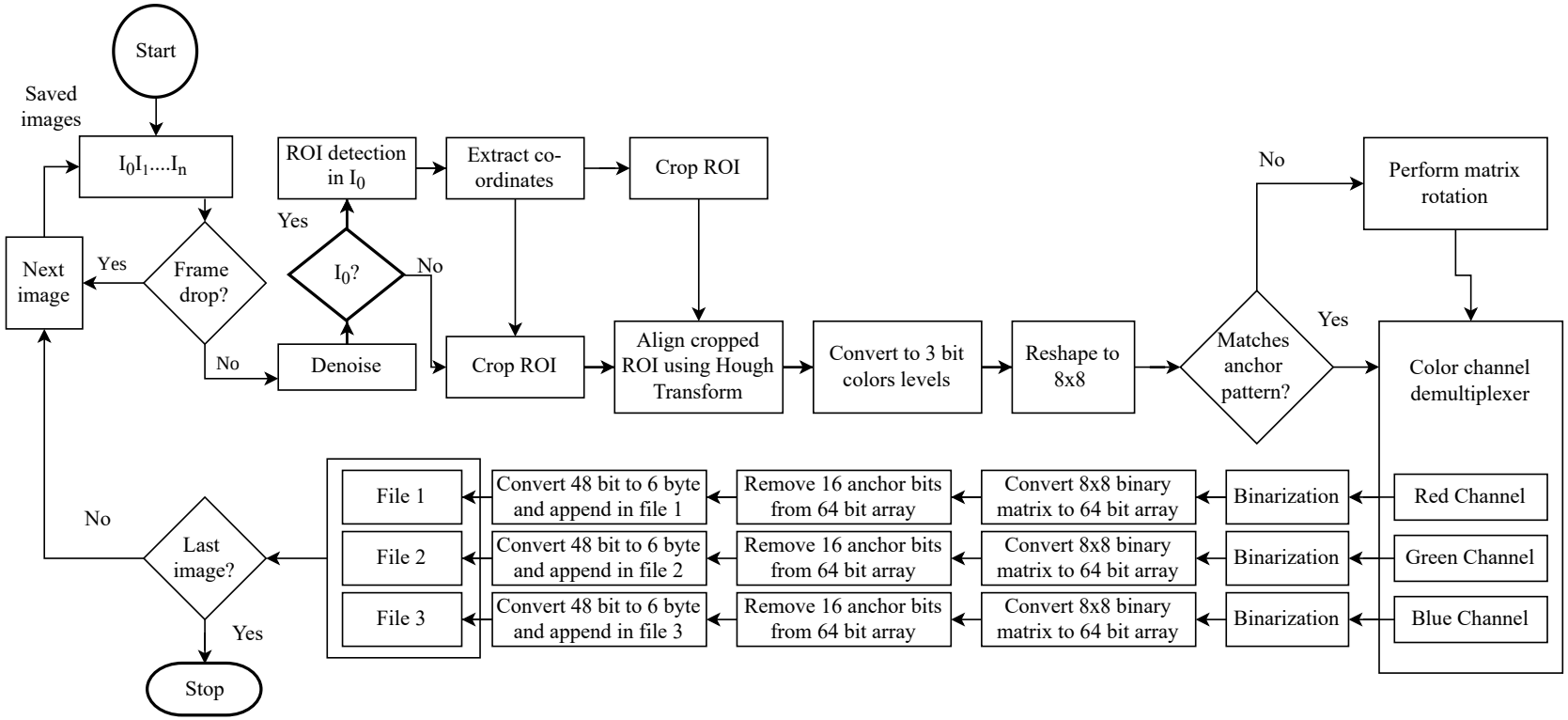

Figure 6.6: Block diagram of the proposed QCD-OCC Receiver Simulator

The coordinates of BM are extracted from each channel to provide RoI as shown in Eq. 6.19 where $p_{x,y}$ is the pixel at position x and y.

$$RoI = \{p_{x,y}|(R_{x,y} \cap BM_{x,y}) + (G_{x,y} \cap BM_{x,y}) + (B_{x,y} \cap BM_{x,y})\} \tag{6.19}$$

The coordinates of extracted RoI are applied to all the subsequent images to crop Tx. It is assumed that subsequent images have the same Tx position and magnification in the image as the first reference image. A square bounding box is drawn around the Tx. The area of the bounding box is compared with the area of the blob in RoI, and RoI rotation is performed to align RoI with the bounding box. A Hough transform is applied to identify the angle(θ) by which Tx is rotated, and an opposite direction rotation of Tx is performed. Thus, the aligned Tx (A_i^{Tx}) from cropped RoI of i^{th} image can be expressed as shown in Eq. 6.20, where, H_T is Hough transform.

$$A_i^{Tx} = rotate(RoI_i, -(H_T(RoI_i))) \tag{6.20}$$

The aligned RoI of Tx will further be quantized to 3-bit color, and a reshaping function is applied to covert the resultant image into an $8 \times 8 \times 3$ matrix. The values from anchoring positions are extracted and compared with expected values. An anti-clockwise matrix rotation is performed till all the anchor values match or four iterations are over. The rotated matrix(O) can be expressed as shown in Eq. 6.21 where T_r is transpose operation and C_r is column reverse operation.

$$O_{8x8}^{Rx} = C_r(T_r(A_{8x8})) \tag{6.21}$$

Each cell in the resultant matrix O_{8x8}^{Rx} consists of RGB values. By undergoing channel separation O_{8x8x3}^{Rx} is converted to three 8×8 matrices R_{8x8}^{Rx}, G_{8x8}^{Rx} and B_{8x8}^{Rx}. Each matrix is binarized, and the resultant 8×8 binary vector is converted to 64-bit streams. The anchor values from these three streams are removed from corresponding positions to provide the final 48 bits per stream. The values are written in separate output files, and the entire process repeats for the next image till no more images exist in the input folder to read. The output of each iteration is written in append mode in respective files.

Figure 6.7a shows the image generated by the simulated transmitter, which consists of a simulated Tx LED panel and background. Figure 6.7b shows a screenshot of the Rx simulator during demodulation steps which consist of cropped RoI, channel-separated binary matrices, PSNR, and decoded data.

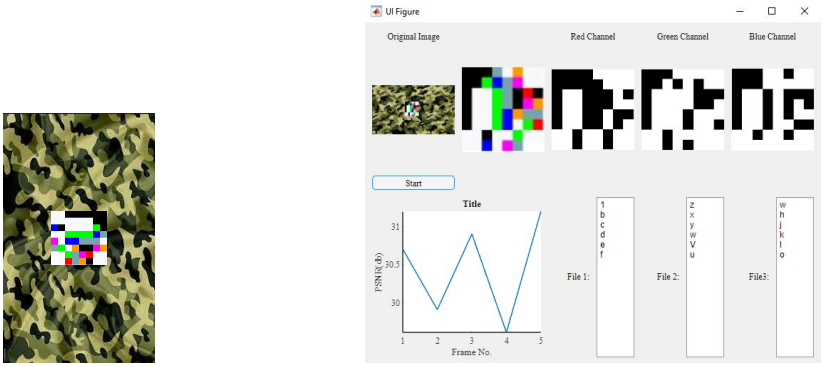

(a) Tx Simulator Generated Image (b) Rx Simulator Demodulation

Figure 6.7: Tx and Rx Simulator Screenshots of Proposed QCD-OCC System

6.2.5 Implementation of Proposed QCD-OCC System Prototype

The proposed QCD-OCC system prototype consists of a programmable board (Arduino Uno) controlled 8×8 neopixel LED matrix (Adafruit WS2812B) as Tx and a webcam (Logitech C310) attached computer as the Rx. This circuit diagram and implemented Tx is as shown in Figure 6.8a and 6.8b.

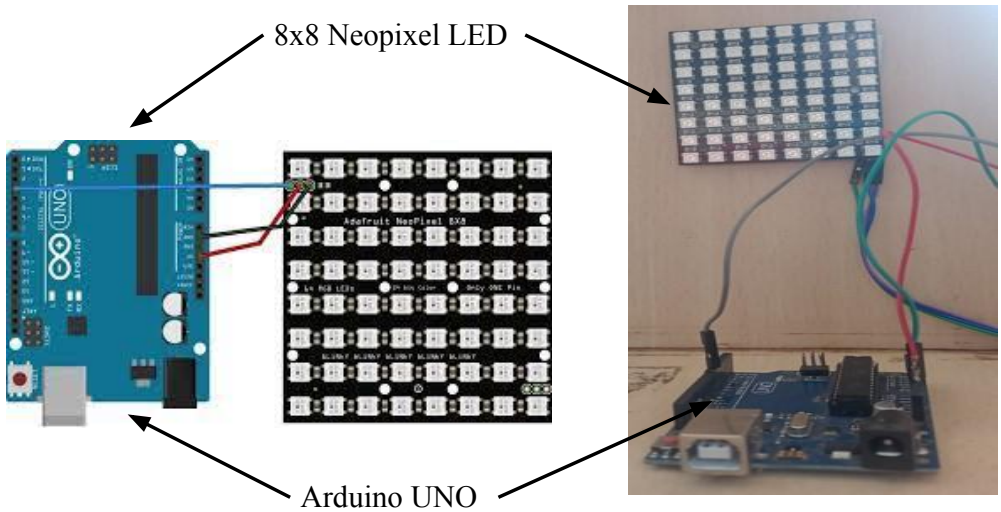

Figure 6.8: Implementation of Proposed Tx (a)Circuit Diagram (b) Connected Hardware Components

Pins v+, v-, and in of LED matrix are connected to 5v, ground(GND), and digital pin 6 of the Arduino board in the same order. Pin 6 is set to output using $pinMode(6, OUTPUT)$ command. Algorithm 25 shows the steps involved

in transmitting data using QCD-OCC Tx. Three individual predefined message strings, namely $F1$, $F2$, and $F3$, are used as input. M is the maximum length of these three strings, computed using *length* and *max* functions. N_{frames} is the number of frames required to transmit overall data. $frame_i$ is initialized to 0 and is used to track the current frame number. $Adafruit\_Neopixel$ is a class of Adafruit library that provides access to functions used for controlling neopixel LED. *pix* is an object of $Adafruit\_Neopixel$ class, and the constructor accepts the number of LEDs(64), connected pin number(6), and the type of the neopixel LED($NEO\_GRB+NEO\_KHZ800$) as its parameters. The $delayVal$ is the delay between successive Tx frames. Thus, if Tx_{frames} is 5 per second, then $delayVal$ will be 200 ms. The *Loop*(10) function sets anchor pattern(1), top 2×4 data pattern(1), bottom 2×4 data pattern(1), and middle 4×8 data pattern(1) of the Tx frame as per input characters.

Algorithm 25 QCD-OCC for Transmitter

Initialize strings $F1$,$F2$, and $F3$
$M = max(F1.length(), max(F2.length(), F3.length()))$
$N_{frames} = ceil((m \times 8) \div 48)$
$frame_i = 0$
$Adafruit\_NeoPixelpix = Adafruit\_NeoPixel(64, 6, type)$
$delayVal = 1000/Tx_frames$
function SETUP
    Set pin mode to output for pin 6
end function
function LOOP
    SetAnchorPattern()
    SetTopDataPattern($frame_i$)
    SetBottomDataPattern($frame_i$)
    SetMidDatatPattern($frame_i$)
    pix.show()
    delay($delayVal$)
    $frame_i++$
    if mod $(frame_i, N_frames) == 0$ **then**
        $frame_i = 0$
    end if
end function

Algorithm 26 Supporting Functions: SetAnchorPattern

function SETANCHORPATTERN
    $A_1(2,2) = 0, A_2(2,2) = 1, A_3(2,2) = 1, A_4(2,2) = 1$
end function

Algorithms 26, 27, 28 and 29 shows the implementation of supporting functions. The *SetAnchorPattern* function sets the pattern for the four corner 2×2 positions as zero or unity matrices per the Tx frame format. Each Tx frame represents 6 bytes per channel. The function *bitRead* is used to read the bit value of a byte at the specific input index.

Algorithm 27 Supporting Functions: SetTopDataPattern

function SETTOPDATAPATTERN($frame_i$)
$charF1c1 = F1.charAt(6 \times frame_i)$
$charF2c1 = F2.charAt(6 \times frame_i)$
$charF3c1 = F3.charAt(6 \times frame_i)$
for $(i = 2; i < 6; i++)$ **do**
$T_D(0, i) = pix.setPixelColor(i, pixels.Color(255 * bitRead(F1c1, 7-(i-2)), 255 * bitRead(F2c1, 7-(i-2)), 255 * bitRead(F3c1, 7-(i-2))))$
end for
for $(i = 10; i < 14; i++)$ **do**
$T_D(1, i-8) = pix.setPixelColor(i, pix.Color(255 * bitRead(F1c1, 3-(i-10)), 255 * bitRead(F2c1, 3-(i-10)), 255 * bitRead(F3c1, 3-(i-10))))$
end for
end function

Algorithm 28 Supporting Functions: SetBottomDataPattern

function SETBOTTOMDATAPATTERN($frame_i$)
$charF1c1 = F1.charAt(6 \times frame_i + 1)$
$charF2c1 = F2.charAt(6 \times frame_i + 1)$
$charF3c1 = F3.charAt(6 \times frame_i + 1)$
for $(i = 51; i < 54; i++)$ **do**
$B_D(6, i-49) = pix.setPixelColor(i, pixels.Color(255 * bitRead(F1c1, 7-(i-51)), 255 * bitRead(F2c1, 7-(i-51)), 255 * bitRead(F3c1, 7-(i-51))))$
end for
for $(i = 58; i < 62; i++)$ **do**
$B_D(7, i-56) = pix.setPixelColor(i, pix.Color(255 * bitRead(F1c1, 3-(i-58)), 255 * bitRead(F2c1, 3-(i-58)), 255 * bitRead(F3c1, 3-(i-58))))$
end for
end function

The function *SetTopDataPattern* converts the first byte of each frame per channel into the top 2×4 LED color matrix. The color for each LED is computed as the product of bit value and 255. Thus, for bit value 1, the respective color will be 255 and 0 for bit value 0. *pixColor* accepts parameters as R, G, and B values from 0-255. For, example $pixColor(255, 255, 255)$ represent whit color. Function *setPixelColor* set the color for corresponding LED number. Similar to

Algorithm 29 Supporting Functions: SetMidDataPattern

function SETMIDDATAPATTERN($frame_i$)
  for $(j = 2; j < 6; j++)$ **do**
    $charF1c1 = F1.charAt(6 \times frame_i + j)$
    $charF2c1 = F2.charAt(6 \times frame_i + j)$
    $charF3c1 = F3.charAt(6 \times frame_i + j)$
    for $(i = 7; i > 0; i--)$ **do**
      $M_D(2 + j, 7 - i) = pix.setPixelColor$
      $(i, pixels.Color(255 * bitRead(F1c1, i),$
      $255 * bitRead(F2c1, i),$
      $255 * bitRead(F3c1, i)))$
    end for
  end for
end function

SetTopDataPattern, the function *SetBottomDataPattern* converts the second byte of each Tx frame per channel into the bottom 2×4 LED color matrix. The function *SetMidDataPattern* is used to convert the remaining 4 bytes of each Tx frame per channel into the middle 4×8 LED color matrix.

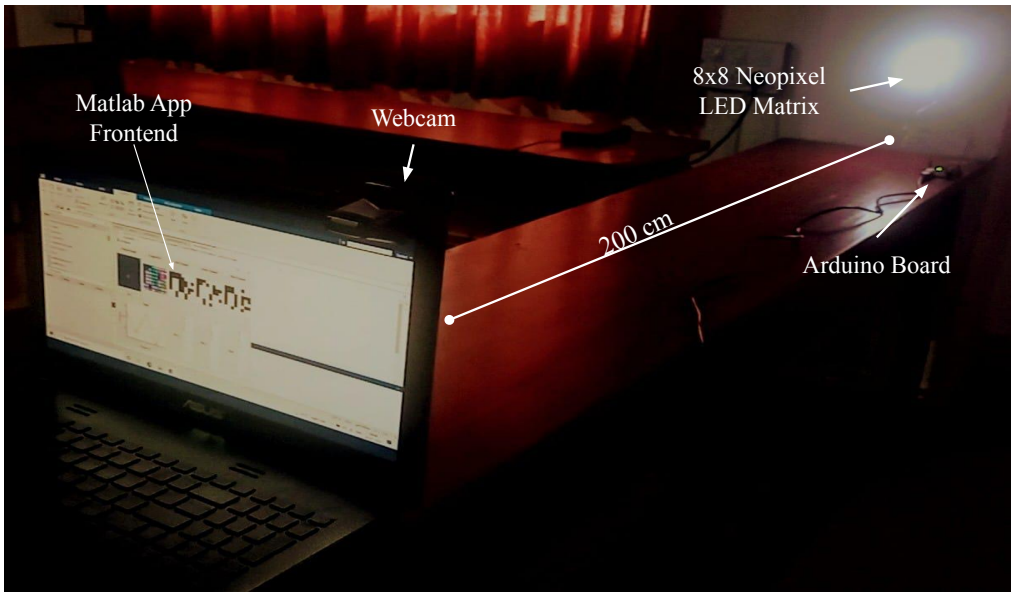

Figure 6.9: Implemented QCD-OCC Prototype System

The implementation of the proposed prototype Rx is similar to the performance of the proposed Rx simulator. The only change is concerning input and removal of the frame drop function. In the prototype Rx, the input will be a direct camera feed for which the image capture rate is controlled using the delay function. Figure 6.9 shows the hardware implementation of the proposed QCD-OCC system, and

components like Rx Camera, 8×8 LED Tx, Arduino uno, and Matlab-based app front end are highlighted.

6.3 Results and Discussion

Table 6.3: Parameter of the Experiment Setup

Parameter	**Value**	**Parameter**	**Value**
Tx Dimension	6.5 cm x 6.5 cm	CPU	i7-700 3.6GHz
Tx Model	WS2812B-64 8x8 LED Matrix	RAM	16 GB
Transmission Data Rates	720 bps, 1440 bps, 2160 bps, 2880 bps, 3600 bps, 4320 bps	File Sizes	File 1: 97 bytes, File 2: 123 bytes, File 3: 109 bytes
Camera Frame Rate	30 fps 1/1500s	Distances	50 cm, 100 cm, 150 cm, 200cm
Camera Resolution	1920x1080 pixels	Ambient light	27 lux, 149 lux 304 lux
Exposure	ISO100	Rotation Angle	0, 45, 90

Table 6.3 shows the parameters and their corresponding values used during the performance evaluation of the proposed system. Preliminary experiments were conducted to study the impact of distance on the pixel intensity of Tx. Figure 6.10 shows the original Tx and its corresponding side and top views of intensity profiles at distances of 50, 100, and 200 cm. It was observed that for L = 50 cm and 100 cm, there was the least significant difference with respect to pixel density in the RoI. It was also observed that intensities for white, red, and yellow color LEDs were more prominent across three images. The colors such as blue, green, and cyan had comparatively less intensity. At L = 200 cm, the intensity of cyan color becomes negligible, resulting in faulty decoding of bits.

The success of reception at a distance of 50 cm for varying Tx data-rate was evaluated for the proposed QCD-OCC simulator and proposed QCD-OCC prototype. The magnification factor for simulated Tx was kept at 0.9 to match the size of prototype Tx at a 50 cm distance. The ambient light intensity for the prototype was ≈27-31 lux. The mean of 10 iterations per data rate was used to generate a comparison. Figure 6.11 shows the obtained results. It was observed that the success of the reception of the proposed QCD-OCC prototype drops drastically after the point where the Tx frame rate becomes greater than 15. It is mainly due to sampling error which results in capturing Tx images during frame transitions.

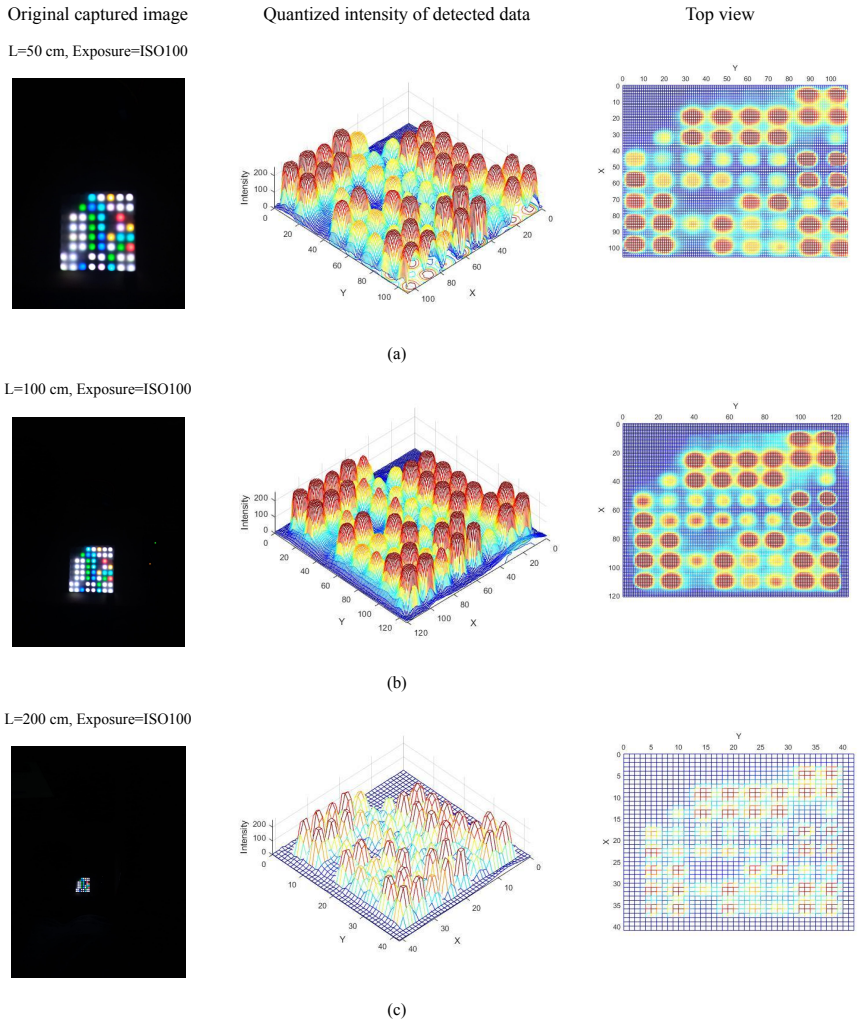

Figure 6.10: Tx intensity profile at distances L=50 cm, 100 cm and 200 cm

Since the proposed equation used for simulation of frame drop does not handle the condition of Tx data rate $> fps/2$ separately, the figure shows a linear drop in the success of the reception.

The results of the evaluation of PSNR under various lighting conditions are shown in Figure 6.12. It was observed that with the increase in distance, the PSNR value decreases irrespective of lighting conditions. It was also observed that the PSNR value was highest for the least ambient light intensity and decreased gradually with the increase in ambient light intensity. As distance and ambient light intensity increase, the difference between the reference image and Tx image decreases, directly proportional to PSNR. Figure 6.13 shows the success of reception at various distances under different lighting conditions. The average of 10 samples per distance per lighting condition is plotted.

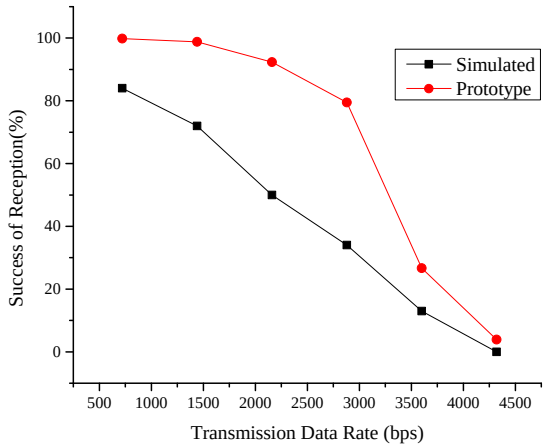

Figure 6.11: Comparison of success of reception (%) between implemented proposed QCD-OCC simulator and proposed QCD-OCC prototype

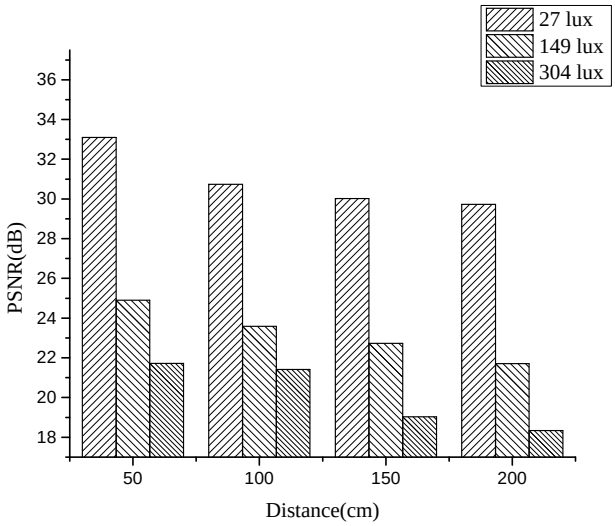

Figure 6.12: Evaluation of proposed prototype-PSNR at distances 50, 100, 150, and 200 cm under different ambient lighting conditions.

It was observed that for ambient light ≈27 lux, reception success is ≈100% at distances 50, 100, 150, and 200 cms. The success rate gradually decreases with an increase in ambient light and distance. These results show that the proposed system performs well even under low light conditions.

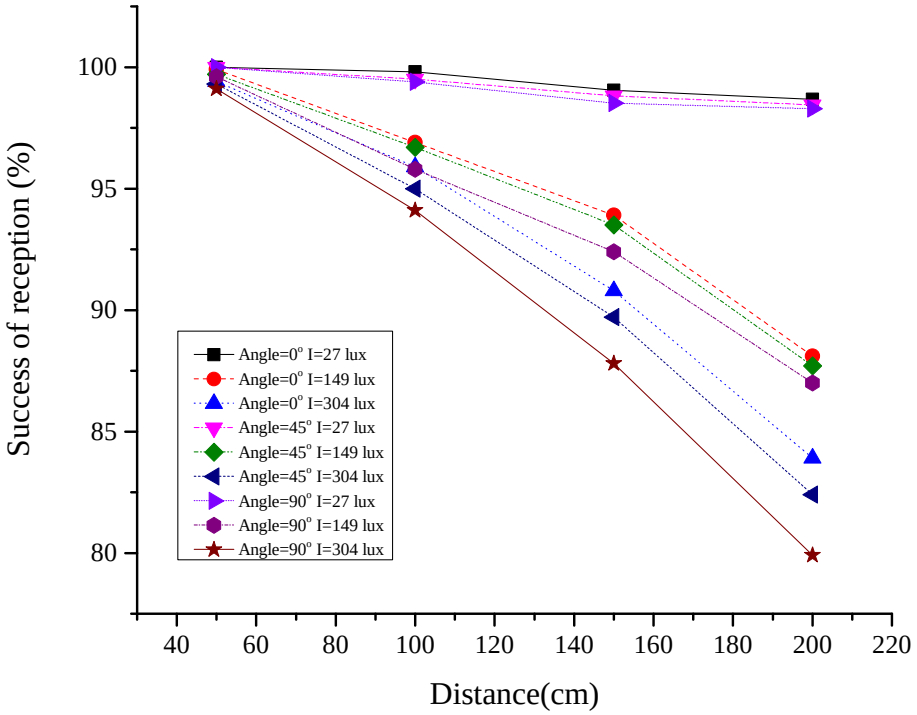

Figure 6.13: Evaluation of proposed prototype-the success of reception (%) at distances 50, 100, 150, and 200 cm under different ambient lighting conditions.

The BER of the proposed prototype was evaluated under the low light condition of ≈27-30 lux at distances of 50, 100, 150, and 200 cms for Tx data rates 720, 1440, 2160, 2880, 3600, and 4320 bps. As shown in Figure 6.14, it was observed that the proposed system delivers its minimum BER of 1.37×10^{-5} at a distance of 50 cm and Tx data rate of 720 bps. Since, for IoT applications, BER of 10^{-3} is sufficient for communication, the BER of 1.21×10^{-3} for 2880 bps at a distance of 200 cm is sufficient for IoT applications. It was also observed that the performance of the system deteriorated with an increase in Tx data rate and distance. Increasing data rate adds more sampling errors, whereas increasing distance adds to frame drops due to incorrect detection of LEDs from the group of interfering LEDs.

The performance of the proposed system with respect to throughput and rotation support was compared with other existing similar OCC techniques, which used an 8×8 LED panel as Tx and a 30 frames per second (FPS) camera as Rx for their implementation, as shown in Figure 6.15 where T is the angle of rotation by which Rx is rotated.

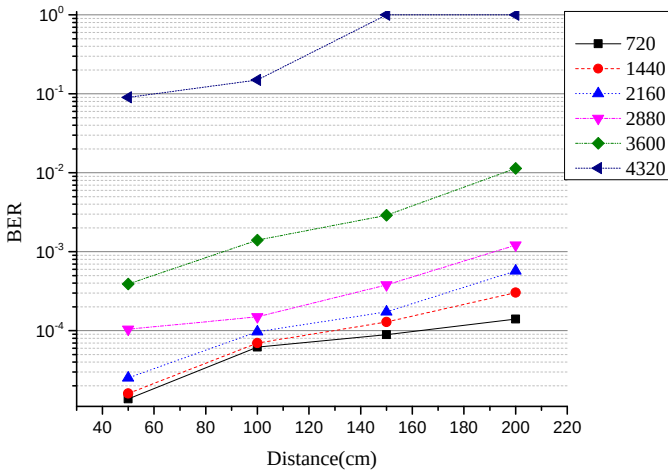

Figure 6.14: Performance evaluation of proposed prototype-BER vs. Distance vs. Tx data rate,

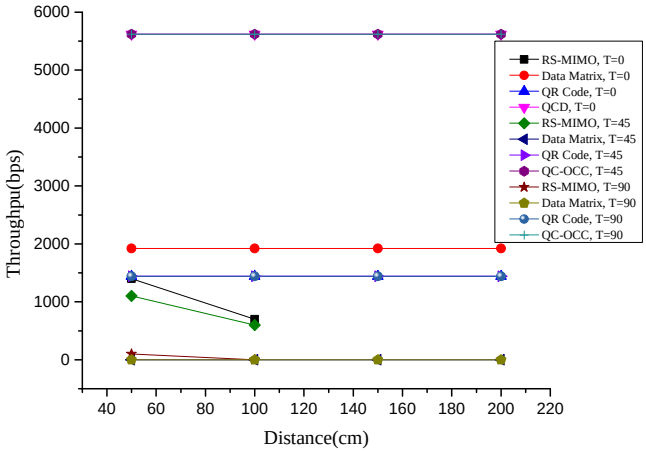

Figure 6.15: Performance evaluation of proposed prototype-Data throughput of other similar systems

RS-based OCC systems provide high throughput for a fixed short distance, but as the distance increases, the throughput drops. Also, RS-based systems offer limited support for rotation. The data matrix system provides a throughput of 1.92×10^3 bps for zero degrees rotation. QR Code-inspired system provides rotation support; however, with the throughput of 1.44×10^3 bps, it is lower than the data matrix system as few LEDs are constantly used for representing anchor positions.

Table 6.4: Performance Comparison

Technique	**Tx Device**	**Camera FPS**	**Dist ance**	**Flicker**	**Rotation Support**	**Type of Camera**	**Number of Links**	**BER**	**Throu-ghput**
RS-OCC-MIMO Teli *et al.* (2020*a*)	8x8 LED Panel	30	<1.5m	No	No	RS	1	$> 10^{-4}$	1.4 Kbps
Data Matrix	8x8 LED Panel	30	<2m	Yes	No	GS	1	$> 10^{-3}$	1.9 Kbps
QR Code (Single Color)	8x8 LED Panel	30	<3m	Yes	Yes	GS	1	-	1.44 Kbps
QR Code (Multi-Color) Nguyen and Jang (2016)	LCD Display	60	<3m	Yes	Yes	RS+GS	Multiple	$> 10^{-4}$	5.4 Kbps
Proposed QCD-OCC	8x8 LED Panel	30	<3m	Yes	Yes	RS+GS	Multiple	$> 10^{-4}$	4.32 Kbps

The proposed QCD-OCC system uses 16 LEDs to represent anchor positions and 3-bit colors to send data, thus achieving a throughput of 4.32×10^3 bps with rotation support.

Table 6.4 shows the comparison of the proposed system with existing systems based on parameters like type of Tx device, Rx camera FPS, maximum distance with tolerable BER, flickering, rotation support, type camera, MIMO support, BER, and throughput. It was observed that the proposed QCD-OCC showcases support for rotation, compatibility with RS and Global Shutter (GS) cameras, allows multiple links, and provides a combined throughput of 2160 bps.

In a similar system, the multicolor QR code showcased better performance compared to the proposed QCD-OCC system as it uses 4 LEDs for rotation compensation; however, the system uses an LCD which consumes more power compared to an 8x8 LED panel and 60 fps camera at the Rx side.

As shown in Table. 6.5, the proposed QCD-OCC method stands out among the other methods listed in the table for several advantages it offers. Unlike the previous works, QCD-OCC combines the use of the "Brightest Object" and "Shape Detection" techniques, allowing it to detect and analyze both the brightest objects and their shapes simultaneously. This provides a more comprehensive approach to RoI detection. Furthermore, QCD-OCC supports multiple bright sources and handles RoIs that are rotated or skewed. It also exhibits high computational efficiency, as it does not require intensive computing resources. Additionally, QCD-OCC is not dependent on the distance between the RoI and the detection system, ensuring consistent performance regardless of the proximity. These advantages make QCD-OCC a promising method for RoI detection, offering a robust and versatile solution for various applications.

6.4 Summary

A novel Quantum Chromodynamics inspired 8x8 multicolor LED panel-to-camera communication was proposed, implemented, and evaluated. A Baryon's gluon exchange color model was used to provide the mapping between sets of 3 bits and respective colors. QR code-inspired anchoring patterns was introduced to provision rotation support and thus offered more robustness. The Tx and Rx simulations of the proposed system were implemented to simulate processes involved in converting data to LED mapping and reconstructing data from images. Two strategies were proposed to achieve user-centric MIMO. Three different files were

Table 6.5: Method Comparison

Previous Work	**RoI Detection Method**	**Support for**			**Compute Intensive**	**Dependent on Distance**
		Multiple Bright Sources	**Rotation or Skew**	**MIMO**		
(Do and Yoo 2019)	Brightest Pixel	No	No	No	No	Yes
(Guan *et al.* 2019)	CNN, LoS	Yes	No	No	Yes	No
(Sun *et al.* 2021)	YOLOv5, Shape Detection	Yes	Yes	No	Yes	No
(Nguyen and Jang 2021*a*)	CNN	Yes	No	Yes	Yes	No
(Teli *et al.* 2020*b*)	Brightest Pixel	No	Yes	Yes	No	Yes
(Nguyen *et al.* 2021)	YOLOv5, Shape Detection	Yes	Yes	No	Yes	No
Proposed QCD-OCC	Brightest Object, Shape Detection	Yes	Yes	Yes	No	No

used to simulate MIMO at the Tx side, which was further decoded and logged into three output files. The content from input files and output files were compared to the evaluated success of the reception of the implemented simulator. A function is dependent on the camera frame rate and Tx data rate was used to simulate frame drop. A low-cost prototype was built using 8x8 neopixel LEDs and a webcam to test the proposed QCD-OCC system. The intensity profiles for the Tx at various distances were compared to study the impact of color intensity for successful decoding. The success of reception was compared between the simulator and prototype. The prototype provided 100% success of reception and maximum PSNR of ≈33 dB at the distance of 50 cm and for Tx data rate of 720 bps and ambient light intensity ≈27 lux. The proposed prototype demonstrated the least BER of 1.37×10^{-5} for 50 cm and 720 bps Tx data rate; however, the maximum allowable BER of 1.13×10^{-2} was observed at a maximum distance of 200 cm, and the maximum data rate of 3600 bps. The proposed system supported MIMO and showcased a combined throughput of 2.16 Kbps with rotation support up to 90 degrees and a maximum communication distance of <3 m.

The performance of the prototype Rx can be further improved by using a specialized lens to support longer distances of communication and high frame rate cameras. Usage of 16×16 and 32×32 LED panels would provide higher throughput. The performance of the simulator can be improved by integrating LED light spreading characteristics.

Chapter 7

Conclusions and Future Work

OWC is an emerging domain of wireless communication that has potential to serve as various bandwidth intensive applications. Visible light communication and optical camera communications are two sub-domains under OWC, that uses the available unlicensed visible light spectrum to enable data transfer. These technologies can be integrated in the existing network architecture and can serve as the possible solution for communication under non-RF zones, such as hospitals, and military areas. In this thesis, various design architectures of VLC and OCC systems are proposed, implemented and evaluated to improve over existing systems. The motivation of the work was to design and develop an efficient modulation technique for visible light communication in indoor environment with respect to data rate, error rate, and distance for IoT applications. The defined objectives included, design and implementation of VLC and OCC modulations techniques that addresses the existing challenges and issues. The integration of proposed techniques with IoT architecture is also explored in thesis by implementing few IoT applications on the experimental testbeds built during testing of proposed modulation techniques. A detailed literature survey was carried to understand about the domain, its challenges and to get familiarized with various implementation and evaluation aspects of the VLC/OCC systems. It also helped to identify the research gaps to align with the proposed objectives.

The first set of contributions addresses the need for having an easy-to-setup VLC testbed using off-the-shelf components. An experimental testbed was designed and implemented to analyze VLC modulation techniques. the channel model was built and based on the free space, the effect of various environmental parameters such as room dimensions, LED and transmitter FoV in SNR was simulated and observed. optical properties. The error probability was simulated using the channel characteristics. It turned out that the simulated error proba-

bility was relatively consistent with the experimentally obtained results. It was also found that of the two modulation techniques applied on the proposed test platform, PDM modulation performed twice as well as OOK modulation in terms of reception success, but PDM was on average three times slower than OOK modulation due to its underlying nature. Using the implemented test platform, an application to transfer binary images from VLC-Tx to VLC-Rx was proposed and implemented. 100 % reception success was observed at a short distance, which showed the integrability of the VLC system with IoT applications. The work is limited by the need for separate hardware to match existing VLC devices. Since the introduction of new hardware components into existing devices would require investments and additional research by companies, the planned work is limited to laboratory environments, where the operation of VLC systems is demonstrated and modular techniques are tested.

The second set of contributions address the practical limitations of photdiode based VLC systems, by proposing a camera based modulation technique. It provides cameras for existing devices that can be converted to VLC compatible devices. A new rolling window-based OCC modulation technique called HFSPDM was proposed and implemented in an in-house VLC test system. Two other modulation techniques, OOK and BFS-OOK, were implemented on the same testbed to compare their performance with the proposed technique. In all experiments, it was observed that when the distance between Tx and Rx increases, the number of detectable lines decreases, regardless of the modulation frequencies. This is mainly due to the decrease in the size of RoI. As the distance increases, RoI decreases, while the track width remains unchanged. These results helped to extract the distance information based on the multiple traced lines. It was also observed that as the modulation frequency increases, the path width decreases to a certain level and starts to increase at higher modulation frequencies. This is due to pixel leakage and blurring of the image, making it difficult to detect edges. Compared to two other benchmark modulation techniques, BFS-OOK was found to provide consistent near-zero BER/bps at 200 Hz, while our proposed HFSPDM technique showed BER/bps closer to 0.04. It was also observed that the number of frames to transmit the same amount of data in HFSPDM as in BFS-OOK was significantly lower, but higher than OOK; that's because HFSPDM represents an average of 2 bits per 5 frames, while BFS-OOK represents 1 bit per 3 frames. The bitframe ratio is higher than OOK; however, HFSPDM gives a better BER than OOK at longer distances because OOK is more sensitive to noise. Thus, it can be concluded that HFSPDM can be used in OCC applications that require little

computation and high accuracy over relatively long distances.

As an extension to the work on HFSPDM, an IPS using VLC and OCC has been designed and implemented. In our proposed system, the use of rolling shutter phenomenon obtained images of LED beacon flickering at specific frequency with alternate bright and dark stripes. The relation between these stripe widths and frequency was used to estimate the user position, and the relation between number of stripes and distance was used to estimate distance from beacon. It was observed that the proposed IPS system works fine until the aperture size is large enough to be detected by the camera and stripe width is smaller that detected aperture. Finally, the android application housing the proposed system showed location specific messages when requested.

The proposed works used rolling shutter phenomenon to build a VLC system using readily available mobile phone camera. However, the dependence on the size of the Tx aperture, limits the achievable bandwidth and restricts the user movement. Thus, there is need to have more robust technique to achieve VLC using OCC.

The third set of contributions is with respect to 2D pattern-based OCC. A novel 2D LED matrix pattern to camera communication was proposed to provide non-RF-based long-distance communication for Industrial IoT applications. The current 2D data matrix based camera communication system offers a maximum transfer rate of up to 1960 bps; however, as the distance between the transmitter and receiver increases, the pixels become imprecise resulting into BER degradation. To alleviate this problem, a concept inspired by texture feature analysis and classification was proposed to create a pattern that can be detected by conventional cameras at longer distances. The proposed model is nested in nature, which provides inherent support for hierarchical pattern classification. The incoming bit sequence was mapped into an 8x8 pattern. A simulation of Tx and Rx was built in Matlab to compare linear and binary search times. Based on the simulation results, it was found that multi-threaded binary search performs better than linear search. Thus, additional tests were performed on the hardware prototype. Experiments were conducted on the optimal choice of camera parameters. Experiments were conducted to evaluate BER and remote sensing techniques. The proposed model was found to provide faster decoding for multi-threaded binary search compared to linear search at data rates above 256 bps. The binary search gave the best performance of 20% BER at 2 m distance and 256 bps. It was also observed that the BER improves as the camera resolution increases.

Two applications to demonstrate the integration of IoT and 2D pattern-based

OCC were proposed. The proposed patterns were inspired by QR codes and Aztec codes. A DHT11 sensor was used to provide ambient temperature and humidity readings. The sensor data was transmitted using the proposed techniques and decoded using the receiving camera. SNR of the proposed applications were evaluated based on the visibility and correctness of decoding data at different distances. Of the two proposed systems, the Aztec code-based pattern-to-camera communication was more energy efficient. Both proposed systems can be used to extend existing indoor infrastructure with cameras to provide non-RF based data communication. It was observed that the performance of the proposed system can be improved further by including chromaticity of light in conjunction with the spatiality of the 2D transmitter to provide higher bandwidth and MIMO support.

In another proposed 2D pattern-based OCC system, a novel Quantum Chromodynamics inspired 8x8 multicolor LED panel-to-camera communication was proposed, implemented, and evaluated. The Tx and Rx simulations of the proposed system were implemented to simulate processes involved in converting data to LED mapping and reconstructing data from images. A function is dependent on the camera frame rate and Tx data rate was used to simulate frame drop. A low-cost prototype was built using 8x8 neopixel LEDs and a webcam to test the proposed QCD-OCC system. The success of reception was compared between the simulator and prototype. The prototype provided 100% success of reception and maximum PSNR of ≈33 dB at the distance of 50 cm and for Tx data rate of 720 bps and ambient light intensity ≈27 lux. The proposed prototype demonstrated the least BER of 1.37×10^{-5} for 50 cm and 720 bps Tx data rate; however, the maximum allowable BER of 1.13×10^{-2} was observed at a maximum distance of 200 cm, and the maximum data rate of 3600 bps. The proposed system supported MIMO and showcased a combined throughput of 2.16 Kbps with rotation support up to 90 degrees and a maximum communication distance of <3 m.

The performance of the prototype Rx can be further improved by using a specialized lens to support longer distances of communication and high frame rate cameras. Usage of 16×16 and 32×32 LED panels would provide higher throughput. The performance of the simulator can be improved by integrating LED light spreading characteristics.

Considering the limitations of the proposed work, the future directions would be with respect to improvement in achieving longer distance communication using photodiodes. The limited FoV of photodiode can be addressed by combining mul-

tiple directed photodiodes. Further modulation techniques can be implemented and tested on the proposed photodiode based VLC testbed.

Further new RS-based modulation techniques can implemented and tested using the proposed testbed. The performance of the proposed HFSPDM technique can be improved by using color based modulation. The proposed pattern based modulation techniques were tested for a short distance, further experiments can be conducted using external magnification to increase distance of communication.

Publications based on Research Work

Journal Publications

1. S. Salvi and V. Geetha, "*An Optical Camera Communication using Hybrid Frequency Shift and Pulse Width Modulation Technique for Li-Fi*" MDPI Computation Volume 10 Issue 7, Page No. 110; https://doi.org/10.3390/computation10070110 [Scopus, ESCI]

2. S. Salvi and V. Geetha, "*A Nested Texture Inspired Novel Image Pattern Based Optical Camera Communication*", in IEEE Access, vol. 10, pp. 109056-109067, 2022, doi: 10.1109/ACCESS.2022.3213701. [Scopus, SCIE]

3. S. Salvi and V. Geetha, "*Quantum Chromodynamics Inspired Optical Camera Communication for User-Centric MIMO*" Special Issue on Optical Camera Communication, MDPI Applied Sciences, Volume 12(20), 10204; https://doi.org/10.3390/app122010204 [Scopus, SCIE]

Conference Publications

1. S. Salvi and V. Geetha, "*Design and Implementation of a Lowcost Testbed for LiFi Modulation Techniques and Experimental Evaluation using Matlab Simulation*" ISBM ICT4SD 2023 Bangkok [Scopus] (Submitted)

2. S. Salvi and V. Geetha, "From Light to Li-Fi: Research Challenges in Modulation, MIMO, Deployment Strategies and Handover," 2019 International Conference on Data Science and Engineering (ICDSE), Patna, India, 2019, pp. 107-119. doi: 10.1109/ICDSE47409.2019.8971475 [Scopus]

3. S. Salvi, V. Geetha, and S. Sowmya Kamath, “Jamura: A Conversational Smart Home Assistant Built on Telegram and Google Dialogflow,” TENCON 2019 - 2019 IEEE Region 10 Conference (TENCON), Kochi, India, 2019, pp. 1564-1571. doi: 10.1109/TENCON.2019.8929316 [Scopus]

4. S. Salvi, V. Geetha, H. Maru, N. Kumar and R. Ahmed, “An Image Transmission Technique using Low-Cost Li-Fi Testbed,” 2021 2nd International Conference on Secure Cyber Computing and Communications (ICSCCC), 2021, pp. 114-119, doi: 10.1109/ICSCCC51823.2021.9478124. [Scopus]

5. S. Salvi, V. Geetha, K. Praveen, K. C and V. J. Nayaka, “LiCamPos: An Indoor Positioning System using Light to Camera Communication,” 2021 2nd International Conference on Secure Cyber Computing and Communications (ICSCCC), 2021, pp. 261-266, doi: 10.1109/ICSCCC51823.2021.9478134. [Scopus]

6. S. Salvi and G. V, ”LiCamIoT: An 8x8 LED Matrix Pattern to Camera Communication for LiFi-IoT Applications,” 2022 IEEE Silchar Subsection Conference (SILCON), Silchar, India, 2022, pp. 1-6, doi: 10.1109/SILCON55242.2022.10028869. [Scopus]

7. S. Salvi and G. V, ”A Novel 2D LED Matrix and Aztec Pattern Inspired Optical Camera Communication for Industrial IoT,” 2022 IEEE 19th India Council International Conference (INDICON), Kochi, India, 2022, pp. 1-6, doi: 10.1109/INDICON56171.2022.10040141 [Scopus]

Bibliography

Aguiar-Castillo, L., V. Guerra, J. Rufo, J. Rabadan, and R. Perez-Jimenez (2021). "Survey on Optical Wireless Communications-Based Services Applied to the Tourism Industry: Potentials and Challenges". *Sensors*, 21(18), 6282.

Ahmed, M. F., M. K. Hasan, M. Shahjalal, M. M. Alam, and Y. M. Jang (2020). "Experimental Demonstration of Continuous Sensor Data Monitoring Using Neural Network-Based Optical Camera Communications". *IEEE Photonics Journal*, 12(5), 1–11.

Ahn, K. and J. K. Kwon (2012). "Color Intensity Modulation for Multicolored Visible Light Communications". *IEEE Photonics Technology Letters*, 24(24), 2254–2257.

Albraheem, L. I., L. H. Alhudaithy, A. A. Aljaser, M. R. Aldhafian, and G. M. Bahliwah (2018). "Toward Designing a Li-Fi-Based Hierarchical IoT Architecture". *IEEE Access*, 6, 40811–40825.

Ali, M. O., M. M. Alam, M. F. Ahmed, and Y. M. Jang (2021). "A New Smart-Meter Data Monitoring System based on Optical Camera Communication". *2021 International Conference on Artificial Intelligence in Information and Communication (ICAIIC)*, IEEE, Jeju Island, Korea (South), 477–479.

Almadani, Y., D. Plets, S. Bastiaens, W. Joseph, M. Ijaz, Z. Ghassemlooy, and S. Rajbhandari (2020). "Visible Light Communications for Industrial Applications—Challenges and Potentials". *Electronics*, 9(12), 2157.

Atta, M. A. and A. Bermak (2018). "A Polarization-Based Interference-Tolerant VLC Link for Low Data Rate Applications". *IEEE Photonics Journal*, 10(2), 1–11.

Baeza, V. M., M. Sánchez-Fernández, A. G. Armada, and A. Royo (2015). "Testbed for a LiFi system integrated in streetlights". *2015 European Conference on Networks and Communications (EuCNC)*, IEEE, Paris, France, 517–521.

Bao, X., J. Pan, Z. Cai, J. Li, X. Huang, R. Chen, and J. Fang (2021). "Real-time display camera communication system based on LED displays and smartphones". *Opt. Express*, 29(15), 23558–23568.

Belyakov, N. A., A. I. Borodkin, I. S. Polukhin, D. S. Shiryayev, O. A. Kozyreva, and V. E. Bougrov (2020). "Nearfield Free-Space Visible Light Communication System via Smartphone Screen". *2020 International Conference Laser Optics (ICLO)*, IEEE, St. Petersburg, Russia, 1–1.

Bian, R., I. Tavakkolnia, and H. Haas (2019). "15.73 Gb/s Visible Light Communication With Off-the-Shelf LEDs". *Journal of Lightwave Technology*, 37(10), 2418–2424.

Bummin Kim, Hyunha Park, Yusung Kim, and Ikjun Yeom (2017). "Decoding method comparisons in Light-to-Camera communication". *2017 International Conference on Information Networking (ICOIN)*, IEEE, Da Nang, Vietnam, 80–82.

Cavalin, P. and L. S. Oliveira (2017). "A Review of Texture Classification Methods and Databases". *2017 30th SIBGRAPI Conference on Graphics, Patterns and Images Tutorials (SIBGRAPI-T)*, IEEE, Niteroi, Brazil, 1–8.

Cespedes, M. M. and A. G. Armada (2018). "On the optimality of multiple photodiode receivers using precoding schemes for visible light communications". *2018 Global LIFI Congress (GLC)*, IEEE, Paris, France, 1–4.

Chavez-Burbano, P., V. Guerra, J. Rabadan, and R. Perez-Jimenez (2017). "Optical camera communication for smart cities". *2017 IEEE/CIC International Conference on Communications in China (ICCC Workshops)*, IEEE, Qingdao, China, 1–4.

Chavez-Burbano, P., J. Rabadan, V. Guerra, and R. Perez-Jimenez (2021). "Flickering-Free Distance-Independent Modulation Scheme for OCC". *Electronics*, 10(9), 1103.

Chen, C., D. Tsonev, and H. Haas (2013). "Joint transmission in indoor visible light communication downlink cellular networks". *2013 IEEE Globecom Workshops (GC Wkshps)*, IEEE, Atlanta, GA, USA, 1127–1132.

Chen, C., H. Yang, P. Du, W.-D. Zhong, A. Alphones, Y. Yang, and X. Deng (2020). "User-Centric MIMO Techniques for Indoor Visible Light Communication Systems". *IEEE Systems Journal*, 14(3), 3202–3213.

Chen, H., S. Hu, J. Ding, S. Bian, H. Wu, P. Hua, S. You, X. Li, Q. Yang, and M. Luo (2017). "Performance comparison of visible light communication systems based on ACO-OFDM, DCO-OFDM and ADO-OFDM". *2017 16th International Conference on Optical Communications and Networks (ICOCN)*, IEEE, Wuzhen, China, 1–3.

Chen, H., S. Wen, X. Wang, M. Liang, M. Li, Q. Li, and Y. Liu (2019). "Color-Shift Keying for Optical Camera Communication Using a Rolling Shutter Mode". *IEEE Photonics Journal*, 11(2), 1–8.

Chen, W., Z. Li, and M. Jiang (2018). "Color-and-Intensity Shift Keying for Visible Light Communication". *IEEE Communications Letters*, 22(9), 1790–1793.

Chowdhury, M. Z., M. T. Hossan, A. Islam, and Y. M. Jang (2018). "A Comparative Survey of Optical Wireless Technologies: Architectures and Applications". *IEEE Access*, 6, 9819–9840.

Cui, K., G. Chen, Z. Xu, and R. D. Roberts (2010). "Line-of-sight visible light communication system design and demonstration". *2010 7th International Symposium on Communication Systems, Networks Digital Signal Processing (CSNDSP 2010)*, IEEE, Newcastle Upon Tyne, UK, 621–625.

David Quilindo-Méndez, C., E. F. Hoyos-Zúñiga, and A. F. Escallón-Portilla (2020). "M-QAM modulation technique effect for an OFDM-RoF/XGS-PON converged network". *2020 IEEE Latin-American Conference on Communications (LATINCOM)*, IEEE, Santo Domingo, Dominican Republic, 1–6.

Dehghani Soltani, M., A. A. Purwita, I. Tavakkolnia, H. Haas, and M. Safari (2019). "Impact of Device Orientation on Error Performance of LiFi Systems". *IEEE Access*, 7, 41690–41701.

Deng, R., L. Liu, Y. Shao, and L. Chen (2019). "2D-Constellation-Assisted CSK transmission over OCC system under low-level illuminance". *2019 24th OptoElectronics and Communications Conference (OECC) and 2019 International Conference on Photonics in Switching and Computing (PSC)*, IEEE, Fukuoka, Japan, 1–3.

Do, T.-H. and M. Yoo (2019). "A simple LED panel dection algoritum for Optical Camera Communication systems". *2019 International Conference on Information and Communication Technology Convergence (ICTC)*, IEEE, Jeju, Korea (South), 747–749.

Fath, T. and H. Haas (2013). "Performance Comparison of MIMO Techniques for Optical Wireless Communications in Indoor Environments". *IEEE Transactions on Communications*, 61(2), 733–742.

Feng, L., R. Q. Hu, J. Wang, and Y. Qian (2018). "Deployment Issues and Performance Study in a Relay-Assisted Indoor Visible Light Communication System". *IEEE Systems Journal*, 1–9.

Fujimoto, N. and H. Mochizuki (2013). "477 Mbit/s visible light transmission based on OOK-NRZ modulation using a single commercially available visible LED and a practical LED driver with a pre-emphasis circuit". *Optical Fiber Communication Conf./Nat. Fiber Optic Engineers Conf.*, IEEE, Anaheim, CA, USA, 1–3.

Galati, A. and C. Greenhalgh (2010). "Human Mobility in Shopping Mall Environments". *Proceedings of the Second International Workshop on Mobile Opportunistic Networking*, Association for Computing Machinery, New York, NY, USA, 1–7.

Gallmeister, K. and U. Mosel (2022). "Hadronization and Color Transparency". *Physics*, 4(2), 440–450.

Gancarz, J. E., H. Elgala, and T. D. Little (2015). "Overlapping PPM for band-limited visible light communication and dimming". *Journal of Solid State Lighting*, 2(1), 3.

Garg, N. and J. Parikh (2017). "Wireless transceiver design for visible light communication". *2017 International Conference on Inventive Computing and Informatics (ICICI)*, IEEE, Coimbatore, India, 509–511.

Ghassemlooy, Z., F. Ebrahimi, S. Rajbhandari, S. Olyaee, X. Tang, and S. Zvanovec (2017). "Visible light communications with hybrid OFDM-PTM". *2017 13th International Wireless Communications and Mobile Computing Conference (IWCMC)*, IEEE, Valencia, Spain, 894–898.

Gorse, L., C. Löffler, C. Mutschler, and M. Philippsen (2018). "Optical Camera Communication for Active Marker Identification in Camera-based Positioning Systems". *2018 15th Workshop on Positioning, Navigation and Communications (WPNC)*, IEEE, Bremen, Germany, 1–6.

Greives, W. and H. Kulhandjian (2020). "Design and Experimentation of a Low-cost Receiver for Visible Light Communications". *2020 IEEE Latin-American*

Conference on Communications (LATINCOM), IEEE, Santo Domingo, Dominican Republic, 1–6.

Griffiths, A. D., J. Herrnsdorf, M. J. Strain, and M. D. Dawson (2019). "Scalable visible light communications with a micro-LED array projector and high-speed smartphone camera". *Opt. Express*, 27(11), 15585–15594.

Guan, W., J. Li, S. Wen, X. Zhang, Y. Ye, J. Zheng, and J. Jiang (2019). "The Detection and Recognition of RGB-LED-ID Based on Visible Light Communication using Convolutional Neural Network". *Applied Sciences*, 9(7), 1400.

Haas, H., L. Yin, Y. Wang, and C. Chen (2016). "What is LiFi?". *Journal of Lightwave Technology*, 34(6), 1533–1544.

Han, H., L. He, and Q. Li (2015). "Vertical handover in optical wireless heterogeneous networks". *2015 IEEE International Conference on Communication Software and Networks (ICCSN)*, IEEE, Chengdu, China, 427–431.

Han, T. and D. Zhao (2022). "Energy Efficiency of User-Centric, Cell-Free Massive MIMO-OFDM with Instantaneous CSI". *Entropy*, 24(2), 234.

Hao, T., R. Zhou, and G. Xing (2012). "COBRA: Color Barcode Streaming for Smartphone Systems". *Proceedings of the 10th International Conference on Mobile Systems, Applications, and Services*, Association for Computing Machinery, New York, NY, USA, 85–98.

Haruyama, S. (2013). "Visible light communication using sustainable LED lights". *2013 Proceedings of ITU Kaleidoscope: Building Sustainable Communities*, IEEE, Kyoto, Japan, 1–6.

Hasan, M. K., M. Z. Chowdhury, M. Shahjalal, V. T. Nguyen, and Y. M. Jang (2018). "Performance Analysis and Improvement of Optical Camera Communication". *Applied Sciences*, 8(12), 2527.

Hawashin, B., A. Mansour, J. Abukhait, F. Khazalah, S. AlZu'bi, T. Kanan, M. Obaidat, and M. Elbes (2019). "Efficient Texture Classification Using Independent Component Analysis". *2019 IEEE Jordan International Joint Conference on Electrical Engineering and Information Technology (JEEIT)*, IEEE, Amman, Jordan, 544–547.

He, J., Y. Zhou, R. Deng, J. Shi, J. He, Z. Jiang, and Q. Tang (2019). "Efficient Sampling Scheme Based on Length Estimation for Optical Camera Communication". *IEEE Photonics Technology Letters*, 31(11), 841–844.

Hu, P., P. Pathak, H. Zhang, Z. Yang, and P. Mohapatra (2019). "High Speed LED-to-Camera Communication using Color Shift Keying with Flicker Mitigation". *IEEE Transactions on Mobile Computing*, 1–1.

Huang, W., C. Gong, and Z. Xu (2014). "Visible light communication based on wavelet packet division multiplexing". *2014 Sixth International Conference on Wireless Communications and Signal Processing (WCSP)*, IEEE, Hefei, China, 1–5.

Huynh-Thu, Q. and M. Ghanbari (2012). "The accuracy of PSNR in predicting video quality for different video scenes and frame rates". *Telecommunication Systems*, 49(1), 35–48.

IEEE (2018). "IEEE Draft Standard for Local and metropolitan area networks - Part 15.7: Short-Range Optical Wireless Communications". *IEEE P802.15.7/D3, August 2018*, IEEE, 1–412.

Islam, R. and M. R. H. Mondal (2019). "Hybrid DCO-OFDM, ACO-OFDM and PAM-DMT for dimmable LiFi". *Optik*, 180, 939 – 952.

Islim, M. S., D. Tsonev, and H. Haas (2015). "Spectrally enhanced PAM-DMT for IM/DD optical wireless communications". *2015 IEEE 26th Annual International Symposium on Personal, Indoor, and Mobile Radio Communications (PIMRC)*, IEEE, Hong Kong, China, 877–882.

Jeganathan, J., A. Ghrayeb, and L. Szczecinski (2008). "Spatial modulation: optimal detection and performance analysis". *IEEE Communications Letters*, 12(8), 545–547.

JEITA (2007*a*). "JEITA CP-1221 Standards Book". Online. URL https://www.jeita.or.jp/japanese/standard/book/CP-1221/#target/page_no=1. Accessed: June 15, 2023.

JEITA (2007*b*). "JEITA CP-1222 Standards Book". *JEITA*. URL https://www.jeita.or.jp/japanese/standard/book/CP-1222/#target/page_no=1. (15.9.2018).

JEITA (2013). "JEITA CP-1223 Standards Book". *JEITA*. URL https://www.jeita.or.jp/japanese/standard/book/CP-1223/#target/page_no=1. (15.9.2018).

Jovicic, A., J. Li, and T. Richardson (2013). "Visible light communication: opportunities, challenges and the path to market". *IEEE Communications Magazine*, 51(12), 26–32.

Jung, H. and S.-M. Kim (2021). "Experimental Demonstration of 3 × 3 MIMO LED-to-LED Communication Using RGB Colors". *Sensors*, 21(14), 4921.

Jung, S., D. Kwon, S. Yang, and S. Han (2016). "Reduction of inter-cell interference in asynchronous multi-cellular VLC by using OFDMA-based cell partitioning". *2016 18th International Conference on Transparent Optical Networks (ICTON)*, IEEE, Trento, Italy, 1–4.

Kashef, M., M. Abdallah, K. Qaraqe, H. Haas, and M. Uysal (2015). "Coordinated interference management for visible light communication systems". *IEEE/OSA Journal of Optical Communications and Networking*, 7(11), 1098–1108.

Kharraz, O. and D. Forsyth (2013). "Performance comparisons between PIN and APD photodetectors for use in optical communication systems". *Optik - International Journal for Light and Electron Optics*, 124, 1493–1498.

Komine, T. and M. Nakagawa (2004). "Fundamental analysis for visible-light communication system using LED lights". *IEEE Transactions on Consumer Electronics*, 50(1), 100–107.

Le, N.-T., T. Nguyen, and Y. M. Jang (2014). "Frequency shift on-off keying for optical camera communication". *2014 Sixth International Conference on Ubiquitous and Future Networks (ICUFN)*, IEEE, Shanghai, China, 22–25.

Lee, H.-Y., H.-M. Lin, Y.-L. Wei, H.-I. Wu, H.-M. Tsai, and K. C.-J. Lin (2015). "RollingLight: Enabling Line-of-Sight Light-to-Camera Communications". *Proceedings of the 13th Annual International Conference on Mobile Systems, Applications, and Services*, Association for Computing Machinery, New York, NY, USA, 167–180.

Lee, K. and H. Park (2011). "Modulations for Visible Light Communications With Dimming Control". *IEEE Photonics Technology Letters*, 23(16), 1136–1138.

Lee, S. C. J., S. Randel, F. Breyer, and A. M. J. Koonen (2009). "PAM-DMT for Intensity-Modulated and Direct-Detection Optical Communication Systems". *IEEE Photonics Technology Letters*, 21(23), 1749–1751.

Li, C., H. Lu, T. Lu, W. Tsai, B. Chen, C. Chu, C. Wu, and C. Liao (2016*a*). "A 100m/40Gbps 680-nm VCSEL-based LiFi transmission system". *2016 Conference on Lasers and Electro-Optics (CLEO)*, IEEE, San Jose, CA, USA, 1–2.

Li, S., A. Balatsoukas-Stimming, and A. Burg (2022). "Device-free Movement Tracking using the UWB Channel Impulse Response with Machine Learning". *2022 IEEE 23rd International Workshop on Signal Processing Advances in Wireless Communication (SPAWC)*, IEEE, Oulu, Finland, 1–5.

Li, Y., J. Han, and X. Zhao (2019). "Performance Investigation of DFT-Spread OFDM Signal for Short Reach Communication Systems Beyond NG-PON2". *IEEE Access*, 7, 27426–27431.

Li, Y., L. Wang, J. Ning, K. Pelechrinis, S. V. Krishnamurthy, and Z. Xu (2012). "VICO: A framework for configuring indoor visible light communication networks". *2012 IEEE 9th International Conference on Mobile Ad-Hoc and Sensor Systems (MASS 2012)*, IEEE, Las Vegas, NV, USA, 136–144.

Li, Z., Z. Zhang, Q. Yuan, Y. Qiao, K. Liao, and H. Yu (2016*b*). "Digital image processing in led visible light communications using mobile phone camera". *2016 IEEE International Conference on Network Infrastructure and Digital Content (IC-NIDC)*, IEEE, Beijing, China, 239–243.

Lian, J. and M. Brandt-Pearce (2018). "Clipping-Enhanced Optical OFDM for IM/DD Communication Systems". *2018 IEEE International Conference on Communications Workshops (ICC Workshops)*, IEEE, Kansas City, MO, USA, 1–6.

Lian, J. and M. Brandt-Pearce (2019). "Clipping-Enhanced Optical OFDM for Visible Light Communication Systems". *Journal of Lightwave Technology*, 37(13), 3324–3332.

Lian, J., Y. Gao, and D. Lian (2019). "Variable Pulse Width Unipolar Orthogonal Frequency Division Multiplexing for Visible Light Communication Systems". *IEEE Access*, 7, 31022–31030.

Liang, X., M. Yuan, J. Wang, Z. Ding, M. Jiang, and C. Zhao (2017). "Constellation Design Enhancement for Color-Shift Keying Modulation of Quadrichro-

matic LEDs in Visible Light Communications". *Journal of Lightwave Technology*, 35(17), 3650–3663.

Librino, F. and P. Santi (2021). "The Complexity–Performance Tradeoff in Resource Allocation for URLLC Exploiting Dynamic CSI". *IEEE Internet of Things Journal*, 8(17), 13266–13277.

Lifi-Lighting (2017). "Oledcomm Products". *Lifi Lighting*. URL https://www.oledcomm.net/products/. (15.9.2018).

Liu, A., W. Shi, M. Ouyang, and W. Liu (2022). "Characterization of Optical Camera Communication Based on a Comprehensive System Model". *Journal of Lightwave Technology*, 40(18), 6087–6100.

Liu, Y., C.-W. Chow, K. Liang, H.-Y. Chen, C.-W. Hsu, C.-Y. Chen, and S.-H. Chen (2016). "Comparison of thresholding schemes for visible light communication using mobile-phone image sensor". *Opt. Express*, 24(3), 1973–1978.

Long, S., P. Tsai, Y. Huang, and I. Lai (2017). "Trellis coded generalized spatial modulation with spatial multiplexing". *2017 Asia-Pacific Signal and Information Processing Association Annual Summit and Conference (APSIPA ASC)*, IEEE, Kuala Lumpur, Malaysia, 832–837.

Lu, H., C. Li, H. Chen, C. Ho, M. Cheng, Z. Yang, and C. Lu (2017). "A 56 Gb/s PAM4 VCSEL-Based LiFi Transmission With Two-Stage Injection-Locked Technique". *IEEE Photonics Journal*, 9(1), 1–8.

Mao, T., Z. Wang, Q. Wang, S. Chen, and L. Hanzo (2017). "Dual-Mode Index Modulation Aided OFDM". *IEEE Access*, 5, 50–60.

Marcu, A. E., R. A. Dobre, and M. Vlădescu (2018). "Flicker Free Visible Light Communication Using Low Frame Rate Camera". *2018 International Symposium on Fundamentals of Electrical Engineering (ISFEE)*, Bucharest, Romania, 1–4.

Matus, V., V. Guerra, C. Jurado-Verdu, S. Zvanovec, J. Rabadan, and R. Perez-Jimenez (2021). "Design and Implementation of an Optical Camera Communication System for Wireless Sensor Networking in Farming Fields". *2021 IEEE 32nd Annual International Symposium on Personal, Indoor and Mobile Radio Communications (PIMRC)*, IEEE, Helsinki, Finland, 1–6.

Miller, A. B., M. E. Sears, L. L. Morgan, D. L. Davis, L. Hardell, M. Oremus, and C. L. Soskolne (2019). "Risks to Health and Well-Being From Radio-Frequency

Radiation Emitted by Cell Phones and Other Wireless Devices". *Frontiers in public health*, 7, 223–223.

Monteiro, E. and S. Hranilovic (2014). "Design and Implementation of Color-Shift Keying for Visible Light Communications". *Journal of Lightwave Technology*, 32(10), 2053–2060.

Moreolo, M. S., R. Munoz, and G. Junyent (2010). "Novel Power Efficient Optical OFDM Based on Hartley Transform for Intensity-Modulated Direct-Detection Systems". *Journal of Lightwave Technology*, 28(5), 798–805.

Nada, M., Y. Yamada, and H. Matsuzaki (2018). "Responsivity-Bandwidth Limit of Avalanche Photodiodes: Toward Future Ethernet Systems". *IEEE Journal of Selected Topics in Quantum Electronics*, 24(2), 1–11.

Namei Yin, C. Guo, Y. Yang, P. Luo, and Chunyan Feng (2017). "Asymmetrical and direct current biased optical OFDM for visible light communication with dimming control". *2017 IEEE International Conference on Communications Workshops (ICC Workshops)*, IEEE, Paris, France, 23–28.

Navya Deepthi, V., C. Banerjee, and S. Saxena (2018). "Dynamic 2-D Pattern-Based Passive Communication in Swarm Agents". *Advances in Electronics, Communication and Computing*, Springer Singapore, Singapore, 713–722.

Nguyen, H. and Y. M. Jang (2021*a*). "Design and Implementation of Rolling Shutter MIMO-OFDM scheme for Optical Camera Communication System". *2021 International Conference on Information and Communication Technology Convergence (ICTC)*, IEEE, Jeju Island, Korea (South), 798–800.

Nguyen, H. and Y. M. Jang (2021*b*). "Design of MIMO C-OOK using Matched filter for Optical Camera Communication System". *2021 International Conference on Artificial Intelligence in Information and Communication (ICAIIC)*, IEEE, Jeju Island, Korea (South), 474–476.

Nguyen, H., V. Nguyen, C. Nguyen, V. Bui, and Y. Jang (2021). "Design and Implementation of 2D MIMO-Based Optical Camera Communication Using a Light-Emitting Diode Array for Long-Range Monitoring System". *Sensors*, 21(9), 3023.

Nguyen, H., T. L. Pham, H. Nguyen, and Y. M. Jang (2019*a*). "Trade-off Communication distance and Data rate of Rolling shutter OCC". *2019 Eleventh International Conference on Ubiquitous and Future Networks (ICUFN)*, IEEE, Zagreb, Croatia, 148–151.

Nguyen, H., M. D. Thieu, T. L. Pham, H. Nguyen, and Y. M. Jang (2019*b*). "The Impact of Camera Parameters on Optical Camera Communication". *2019 International Conference on Artificial Intelligence in Information and Communication (ICAIIC)*, Okinawa, Japan, 526–529.

Nguyen, T., M. A. Hossain, and Y. M. Jang (2016). "Design and Implementation of a Novel Compatible Encoding Scheme in the Time Domain for Image Sensor Communication". *Sensors*, 16(5), 736.

Nguyen, T., A. Islam, T. Yamazato, and Y. M. Jang (2018). "Technical Issues on IEEE 802.15.7m Image Sensor Communication Standardization". *IEEE Communications Magazine*, 56(2), 213–218.

Nguyen, T. and Y. M. Jang (2016). "Novel 2D-sequential color code system employing Image Sensor Communications for Optical Wireless Communications". *ICT Express*, 2(2), 57–62.

Nguyen, T., N. T. Le, and Y. M. Jang (2015). "Practical design of Screen-to-Camera based Optical Camera Communication". *2015 International Conference on Information Networking (ICOIN)*, IEEE, Cambodia, 369–374.

Nishikawa, S. (1973). "Sequential M-ary PAM System". *IEEE Transactions on Communications*, 21(1), 22–33.

Noshad, M. and M. Brandt-Pearce (2014). "Hadamard coded modulation: An alternative to OFDM for wireless optical communications". *2014 IEEE Global Communications Conference*, IEEE, Austin, TX, USA, 2102–2107.

Noshad, M. and M. Brandt-Pearce (2016). "Hadamard-coded modulation for visible light communications". *IEEE Transactions on Communications*, 64(3), 1167–1175.

Ohtsuki, T., I. Sasase, and S. Mori (1993). "Overlapping multi-pulse pulse position modulation in optical direct detection channel". *Proceedings of ICC '93 - IEEE International Conference on Communications*, IEEE, Geneva, Switzerland, 1123–1127.

Okumura, J., Y. Kozawa, Y. Umeda, and H. Habuchi (2018). "Hybrid PWM/D-PAM Dimming Control for Digital Color Shift Keying Using RGB-LED Array". *IEEE Journal on Selected Areas in Communications*, 36(1), 45–52.

Olsen, S. L., T. Skwarnicki, and D. Zieminska (2018). "Nonstandard heavy mesons and baryons: Experimental evidence". *Reviews of Modern Physics*, 90(1).

Omura, N., A. Higashi, J. Yabuuchi, T. Iwamatsu, and S. Oshiba (2018). "Experimental Demonstration of OFDM Based WDM-MIMO Visible Light Communication System". *2018 Asia-Pacific Microwave Conference (APMC)*, IEEE, Kyoto, Japan, 872–874.

Opencamera (2019). "Open Camera". *Opencamera*. URL https://opencamera.org.uk/. (16.2.2019).

Oyewobi, S. S., K. Djouani, and A. M. Kurien (2022). "Visible Light Communications for Internet of Things: Prospects and Approaches, Challenges, Solutions and Future Directions". *Technologies*, 10(1), 28.

Pang, G., Ka-Lim Ho, T. Kwan, and E. Yang (1999). "Visible light communication for audio systems". *IEEE Transactions on Consumer Electronics*, 45(4), 1112–1118.

Pathak, P. H., X. Feng, P. Hu, and P. Mohapatra (2015). "Visible Light Communication, Networking, and Sensing: A Survey, Potential and Challenges". *IEEE Communications Surveys Tutorials*, 17(4), 2047–2077.

Preda, R.-O., R.-A. Dobre, and R. A. Badea (2021). "Influence of Camera Framerate Variations on an Optical Camera Communication System". *2021 44th International Conference on Telecommunications and Signal Processing (TSP)*, IEEE, Brno, Czech Republic, 316–319.

Purelifi (2016). "Home - pureLiFi - Connectivity is evolving". *pureLiFi*. URL https://purelifi.com/. (15.9.2018).

Purwita, A. A., M. Dehghani Soltani, M. Safari, and H. Haas (2018). "Impact of terminal orientation on performance in LiFi systems". *2018 IEEE Wireless Communications and Networking Conference (WCNC)*, IEEE, Barcelona, Spain, 1–6.

Qv, R., L. Feng, A. Yang, P. Guo, B. Lin, and H. Huang (2019). "A High Efficient Code for Visible Light Positioning System Based on Image Sensor". *IEEE Access*, 7, 77762–77770.

Rajagopal, N., P. Lazik, and A. Rowe (2014). "Hybrid Visible Light Communication for Cameras and Low-Power Embedded Devices". *Proceedings of the 1st*

ACM MobiCom Workshop on Visible Light Communication Systems, Association for Computing Machinery, New York, NY, USA, 33–38.

Rajagopal, S., R. D. Roberts, and S. Lim (2012). "IEEE 802.15.7 visible light communication: modulation schemes and dimming support". *IEEE Communications Magazine*, 50(3), 72–82.

Rajesh Kumar, C. and R. K. Jeyachitra (2017). "Power Efficient Generalized Spatial Modulation MIMO for Indoor Visible Light Communications". *IEEE Photonics Technology Letters*, 29(11), 921–924.

Roberts, R. D. (2013). "Undersampled frequency shift ON-OFF keying (UFSOOK) for camera communications (CamCom)". *2013 22nd Wireless and Optical Communication Conference*, IEEE, Chongqing, China, 645–648.

Roberts, R. D., S. Rajagopal, and S.-K. Lim (2011). "IEEE 802.15.7 physical layer summary". *2011 IEEE GLOBECOM Workshops (GC Wkshps)*, IEEE, 772–776.

Rêgo, M. and P. Fonseca (2021). "OCC Based Indoor Positioning System Using a Smartphone Camera". *2021 IEEE International Conference on Autonomous Robot Systems and Competitions (ICARSC)*, IEEE, Santa Maria da Feira, Portugal, 31–36.

S, P., J. D.K., S. H.S., and H. Y. Shin D.J. (2007). "Information broadcasting system based on visible light signboard". *Proc. Wireless Opt. Commun.*, 311—-313.

Saadi, M. and L. Wuttisittikulkij (2019). "Visible Light Communication – The Journey So Far". *Journal of Optical Communications*, 40(4), 447–453.

Sadat, H., M. Abaza, A. Mansour, and A. Alfalou (2022). "A Survey of NOMA for VLC Systems: Research Challenges and Future Trends". *Sensors*, 22(4), 1395.

Sandoval-Reyes, S. (2019). "Image Transmission and Reception Using Visible Light". *2019 IEEE International Fall Meeting on Communications and Computing (ROC and C)*, IEEE, Acapulco, Mexico, 5–8.

Sarbazi, E., M. Uysal, M. Abdallah, and K. Qaraqe (2014). "Indoor channel modelling and characterization for visible light communications". *2014 16th International Conference on Transparent Optical Networks (ICTON)*, IEEE, Graz, Austria, 1–4.

Schmid, S., G. Corbellini, S. Mangold, and T. R. Gross (2012). "An LED-to-LED Visible Light Communication system with software-based synchronization". *2012 IEEE Globecom Workshops*, IEEE, Anaheim, CA, USA, 1264–1268.

Seok-Ju Lee and Sung-Yoon Jung (2012). "A SNR analysis of the visible light channel environment for visible light communication". *2012 18th Asia-Pacific Conference on Communications (APCC)*, IEEE, Jeju, South Korea, 709–712.

Sevincer, A., A. Bhattarai, M. Bilgi, M. Yuksel, and N. Pala (2013). "LIGHTNETs: Smart LIGHTing and Mobile Optical Wireless NETworks — A Survey". *IEEE Communications Surveys Tutorials*, 15(4), 1620–1641.

Shi, J., J. He, J. He, Z. Jiang, Y. Zhou, and Y. Xiao (2018). "Enabling user mobility for optical camera communication using mobile phone". *Opt. Express*, 26(17), 21762–21767.

Shi, M., C. Wang, H. Guo, Y. Wang, X. Li, and N. Chi (2016). "A high-speed visible light communication system based on DFT-S OFDM". *2016 IEEE International Conference on Communication Systems (ICCS)*, IEEE, Shenzhen, China, 1–5.

Shinwasusin, E., C. Charoenlarpnopparut, P. Suksompong, and A. Taparugssanagorn (2015). "Modulation performance for visible light communications". *2015 6th International Conference of Information and Communication Technology for Embedded Systems (IC-ICTES)*, IEEE, Thailand, 1–4.

Shulyak, V., M. M. Hayat, and J. S. Ng (2020). "Sensitivity Calculations of High-Speed Optical Receivers Based on Electron-APDs". *Journal of Lightwave Technology*, 38(4), 989–995.

Siddique, A. B. and M. Tahir (2014). "Bandwidth efficient multi-level MPPM encoding decoding algorithms for joint brightness-rate control in VLC systems". *2014 IEEE Global Communications Conference*, IEEE, Austin, TX, USA, 2143–2147.

Singh, R., T. OFarrell, and J. P. R. David (2014). "An Enhanced Color Shift Keying Modulation Scheme for High-Speed Wireless Visible Light Communications". *Journal of Lightwave Technology*, 32(14), 2582–2592.

Singh, R., T. O'Farrell, and J. P. R. David (2015*a*). "Higher Order Colour Shift Keying Modulation Formats for Visible Light Communications". *2015 IEEE 81st Vehicular Technology Conference (VTC Spring)*, IEEE, Glasgow, UK, 1–5.

Singh, S., G. Kakamanshadi, and S. Gupta (2015*b*). "Visible Light Communication-an emerging wireless communication technology". *2015 2nd International Conference on Recent Advances in Engineering Computational Sciences (RAECS)*, IEEE, Chandigarh, India, 1–3.

Soh, M. Y., W. Xian Ng, Q. Zou, D. Lee, T. H. Teo, and K. Seng Yeo (2018). "Real-Time Audio Transmission Using Visible Light Communication". *TENCON 2018 - 2018 IEEE Region 10 Conference*, IEEE, Jeju, Korea (South), 2223–2226.

Soltani, M. D., H. Kazemi, M. Safari, and H. Haas (2017). "Handover Modeling for Indoor Li-Fi Cellular Networks: The Effects of Receiver Mobility and Rotation". *2017 IEEE Wireless Communications and Networking Conference (WCNC)*, IEEE, San Francisco, CA, USA, 1–6.

Soltani, M. D., A. A. Purwita, Z. Zeng, H. Haas, and M. Safari (2019). "Modeling the Random Orientation of Mobile Devices: Measurement, Analysis and LiFi Use Case". *IEEE Transactions on Communications*, 67(3), 2157–2172.

Stafford, M., A. Rogers, S. Wu, C. Carver, N. S. Artan, and Z. Dong (2017). "TETRIS: Smartphone-to-Smartphone Screen-Based Visible Light Communication". *2017 IEEE 14th International Conference on Mobile Ad Hoc and Sensor Systems (MASS)*, IEEE, Orlando, FL, USA, 570–574.

Standards, I. (2011). "IEEE Standard for Local and Metropolitan Area Networks–Part 15.7: Short-Range Wireless Optical Communication Using Visible Light". *IEEE Std 802.15.7-2011*, 1–309.

Standards-IEEE (2018*a*). "IEEE 802.15 WPAN 15.7 Amendment Study Group". *IEEE802.org*. URL https://www.ieee802.org/15/pub/IEEE%20802_15%20WPAN%2015_7%20Revision1%20Task%20Group.htm. (15.9.2018).

Standards-IEEE (2018*b*). "IEEE SA - IEEE 802.15.7-2011". *IEEE Standards Association*. URL https://standards.ieee.org/ieee/802.15.7/5154/. (15.9.2018).

Sun, X., W. Shi, Q. Cheng, W. Liu, Z. Wang, and J. Zhang (2021). "An LED Detection and Recognition Method Based on Deep Learning in Vehicle Optical Camera Communication". *IEEE Access*, 9, 80897–80905.

Taherkhani, N. and K. Kiasaleh (2018). "Reed Solomon Encoding for the Mitigation of Clipping Noise in OFDM-Based Visible Light Communications". *2018 International Conference on Computing, Networking and Communications (ICNC)*, IEEE, Maui, HI, USA, 285–289.

Tanaka, Y., T. Komine, S. Haruyama, and M. Nakagawa (2001). "Indoor visible communication utilizing plural white LEDs as lighting". *12th IEEE International Symposium on Personal, Indoor and Mobile Radio Communications. PIMRC 2001. Proceedings*, IEEE, San Diego, CA, USA, F–F.

Teli, S. R., V. Matus, S. Zvanovec, R. Perez-Jimenez, S. Vitek, and Z. Ghassemlooy (2020*a*). "Optical Camera Communications for IoT–Rolling-Shutter Based MIMO Scheme with Grouped LED Array Transmitter". *Sensors*, 20(12), 3361.

Teli, S. R., S. Zvanovec, and Z. Ghassemlooy (2019). "The first tests of smartphone camera exposure effect on optical camera communication links". *2019 15th International Conference on Telecommunications (ConTEL)*, IEEE, Graz, Austria, 1–6.

Teli, S. R., S. Zvanovec, R. Perez-Jimenez, and Z. Ghassemlooy (2020*b*). "Spatial frequency-based angular behavior of a short-range flicker-free MIMO–OCC link". *Appl. Opt.*, 59(33), 10357–10368.

Tsonev, D., S. Sinanovic, and H. Haas (2012). "Novel Unipolar Orthogonal Frequency Division Multiplexing (U-OFDM) for Optical Wireless". *2012 IEEE 75th Vehicular Technology Conference (VTC Spring)*, IEEE, Yokohama, Japan, 1–5.

Tsonev, D., S. Videv, and H. Haas (2014). "Light fidelity (Li-Fi): towards all-optical networking". *Broadband Access Communication Technologies VIII*, SPIE, Spain, 900702.

Van Thang, N., N. T. Le, T. L. Vu, M. D. Thieu, and Y. M. Jang (2018). "An Implementation of Binary Frequency Shift On-Off Keying Modulation for Optical Camera Communication". *2018 Tenth International Conference on Ubiquitous and Future Networks (ICUFN)*, IEEE, Prague, Czech Republic, 121–125.

Vappangi, S. and V. V. Mani (2019). "Performance Analysis of DST-Based Intensity Modulated/Direct Detection (IM/DD) Systems for VLC". *IEEE Sensors Journal*, 19(4), 1320–1337.

Vasconcelos, C. K. H., A. N. Barreto, and D. A. A. Mello (2014). "Quadrature diversity combining for pulse-amplitude modulated DMT in IM/DD channels". *2014 IEEE Global Communications Conference*, IEEE, Austin, USA, 2090–2095.

Vucic, J., C. Kottke, S. Nerreter, K. Habel, A. Buttner, K.-D. Langer, and J. W. Walewski (2009). "125 Mbits over 5 m wireless distance by use of OOK-Modulated phosphorescent white LEDs". *2009 35th European Conference on Optical Communication*, IEEE, Vienna, Austria, 1–2.

Wang, J., Y. Zhou, and Y. Yang (2020). "Three-Dimensional Shape Detection for Non Uniform Reflective Objects: Combination of Color Light Projection and Camera's Exposure Adjustment". *IEEE Sensors Journal*, 20(19), 11474–11483.

Wang, Q., C. Qian, X. Guo, Z. Wang, D. G. Cunningham, and I. H. White (2015). "Layered ACO-OFDM for intensity-modulated direct-detection optical wireless transmission". *Opt. Express*, 23(9), 12382–12393.

Wang, T., Y. Hou, and M. Ma (2018*a*). "A Novel Receiver Design for HACO-OFDM by Time-Domain Clipping Noise Elimination". *IEEE Communications Letters*, 22(9), 1862–1865.

Wang, T., F. Yang, L. Cheng, and J. Song (2018*b*). "Spectral-Efficient Generalized Spatial Modulation Based Hybrid Dimming Scheme With LACO-OFDM in VLC". *IEEE Access*, 6, 41153–41162.

Wang, T. Q., C. He, and J. Armstrong (2017). "Performance Analysis of Aperture-Based Receivers for MIMO IM/DD Visible Light Communications". *Journal of Lightwave Technology*, 35(9), 1513–1523.

Wang, Y. and H. Haas (2015). "Dynamic Load Balancing With Handover in Hybrid Li-Fi and Wi-Fi Networks". *Journal of Lightwave Technology*, 33(22), 4671–4682.

Wang, Y., X. Wu, and H. Haas (2016). "Fuzzy logic based dynamic handover scheme for indoor Li-Fi and RF hybrid network". *2016 IEEE International Conference on Communications (ICC)*, IEEE, Kuala Lumpur, Malayasia, 1–6.

Wikipedia (2018*a*). "International Commission on Illumination". *Wikipedia*. URL https://en.wikipedia.org/wiki/International_Commission_on_Illumination#/media/File:CIExy1931.png. (15.09.2018).

Wikipedia (2018*b*). "Photophone". *en.wikipedia.org*. URL https://en.wikipedia.org/wiki/Photophone. (15.09.2018).

Wikipedia (2018*c*). "Semaphore Telegraph/ Optical Telegraph". *en.wikipedia.org*. URL https://en.wikipedia.org/wiki/Optical_telegraph. (15.09.2018).

Wong, K. M., J. Wu, T. N. Davidson, and Q. Jin (1997). "Wavelet packet division multiplexing and wavelet packet design under timing error effects". *IEEE Transactions on Signal Processing*, 45(12), 2877–2890.

Yesilkaya, A., E. Basar, F. Miramirkhani, E. Panayirci, M. Uysal, and H. Haas (2017). "Optical MIMO-OFDM With Generalized LED Index Modulation". *IEEE Transactions on Communications*, 65(8), 3429–3441.

Yi, L. and S. G. Lee (2014). "Performance Improvement of Dimmable VLC System with Variable Pulse Amplitude and Position Modulation Control Scheme". *2014 International Conference on Wireless Communication and Sensor Network*, IEEE, Wuhan, China, 81–85.

Yudhabrama, N., I. Wijayanto, and S. Hadiyoso (2017). "Low cost visible light communication transceiver prototype for real time data and images transfer". *2017 International Conference on Control, Electronics, Renewable Energy and Communications (ICCREC)*, IOP, Yogyakarta, Indonesia, 7–10.

Zafar, F., D. Karunatilaka, and R. Parthiban (2015). "Dimming schemes for visible light communication: the state of research". *IEEE Wireless Communications*, 22(2), 29–35.

Zeng, L., D. C. O'Brien, H. L. Minh, G. E. Faulkner, K. Lee, D. Jung, Y. Oh, and E. T. Won (2009). "High data rate multiple input multiple output (MIMO) optical wireless communications using white led lighting". *IEEE Journal on Selected Areas in Communications*, 27(9), 1654–1662.

Zeng, Y., Y. Chen, H. Zhao, and X. Wang (2015). "Multiple pulse amplitude and position modulation for optical wireless channel". *2015 Seventh International Conference on Ubiquitous and Future Networks*, IEEE, Sapporo, Japan, 132–134.

Zhang, M. and Z. Zhang (2014). "An Optimum DC-Biasing for DCO-OFDM System". *IEEE Communications Letters*, 18(8), 1351–1354.

Zhang, S.-z., C.-t. Zheng, Y.-t. Li, W.-l. Ye, and Y. Liu (2012). "Design and experiment of post-equalization for OOK-NRZ visible light communication system". *Optoelectronics Letters*, 8(2), 142–145.

Zhang, T., Y. Zou, J. Sun, and S. Qiao (2018). "Design of PAM-DMT-based Hybrid Optical OFDM for Visible Light Communications". *IEEE Wireless Communications Letters*, 1–1.

Zhou, I., I. Makhdoom, N. Shariati, M. A. Raza, R. Keshavarz, J. Lipman, M. Abolhasan, and A. Jamalipour (2021). "Internet of Things 2.0: Concepts, Applications, and Future Directions". *IEEE Access*, 9, 70961–71012.

Zhou, J. and W. Zhang (2018). "A Comparative Study of Unipolar OFDM Schemes in Gaussian Optical Intensity Channel". *IEEE Transactions on Communications*, 66(4), 1549–1564.

Zinda, T., K. Ito, and W. Chujo (2018). "Rolling-Shutter-Based Optical Camera Communication Using Distributed LED Array". *2018 11th International Symposium on Communication Systems, Networks and Digital Signal Processing (CSNDSP)*, IEEE, Budapest, Hungary, 1–4.

Bio-data

Name:	Salvi Sanket Sarang
Address:	Research Scholar Hs. No. 8, DRT Colony, Subhash Road, Parbhani, Maharashtra, India
Email:	sanketsalvi.salvi@gmail.com
Mobile No:	+91 7559373238
Qualification:	Ph.D. in Information Technology, Department of Information Technology, National Institute of Technology Karnataka, Surathkal, Mangalore, India
	M.Tech. in Computer Networks Engineering, Department of Information Science Engineering, Nitte Meenakshi Institute of Technology, Bangalore, India
	B.E. in Computer Science Engineering, Department of Computer Science Engineering, VPCOE, Baramati, Pune
Research Areas:	Visible Light Communication, Optical Camera Communication, Internet of Things